University of Naples *"Federico II"*

Ph.D. thesis

Comparison and Analysis of Chemical Models, methodologies and parameters in Hypersonic Rarefied Flows

by

Luigi Morsa

Coordinator: *Prof. Antonio Moccia*

Tutor: *Prof. Gennaro Zuppardi*

2010

TABLE OF CONTENTS

List of Nomenclature

Constants

k	Boltzmann constant [k=1.38×10^{-23} J/K]
N_A	Avogadro number [6.0225×10^{26} 1/kmoles]

Acronyms

CFD	Computational Fluid-Dynamics
DSMC	Direct Simulation Monte Carlo
FNUM	number of simulated molecules representative of real molecules
mcs	mean collision separation [m]
VFD	Vibration Favoured Dissociation

Latin Symbols

a_d	dynamic factor
A_i	coefficient in equilibrium constant, i=1,…,5
c_p	constant pressure heat coefficient
c_v	constant volume heat coefficient
C_1,C_2	constants in the calculation of Z_v
C_f	friction coefficient or pre-exponential factor in the forward rate equation [m^3/molecule/s]
C_p	pressure coefficient
C_r	pre-exponential factor in the backward rate equation [m^3/molecule/s], [m^6/$molecule^2$/s]
C_A	axial force coefficient
C_D	drag force coefficient
C_L	lift force coefficient
C_{Mcg}	pitching moment coefficient around the gravity center
$C_{m,0}$	pitching moment coefficient around the nose
C_N	normal force coefficient
D	cylinder diameter [m] or capsule base diameter [m]
$D_{i,j}$	diffusivity of species i with respect to species j [m^2/s]
D_{mix}	self-diffusivity of a mixture [m^2/s]
E	energy [J] or fraction of molecules specularly reflected
E_{af}	activation energy for forward reaction [J/kg]
E_{ar}	activation energy for reverse reaction [J/kg]
F_i	impact stress [$kg^{1/2}$m/s]
F_b	dynamic breaking strength of the chemical bond [$kg^{1/2}$m/s]
F_v	stress originated from vibration [$kg^{1/2}$m/s]

g	gravity acceleration [m/s^2]
G	generic macroscopic quantity
h	thermodynamic enthalpy [J/kg], slab height [m], altitude [m]
H	total enthalpy [J/kg]
i	quantum level
k_f	forward rate coefficient [m^3/molecule/s]
k_r	reverse rate coefficient [m^3/molecule/s] or [m^6/$molecule^2$/s]
K_e	equilibrium constant [$K_e = k_f / k_r$]
K	conductivity [W/m/K]
Kn	Knudsen number
Kn_D	Knudsen number based on the diameter
L	length [m] or geometrical characteristic dimension [m]
Le	Lewis number
L_s	length of the stagnation line across the shock layer [m]
L_x, L_y	dimensions of computing region along x and along y [m]
m	mass [kg]
m_r	reduced mass [kg]
M	Mach number
M_i	molecular mass of i^{th} species [kg/kmoles]
n	temperature exponent in the rate equation, local normal
N	number density [$1/m^3$]
p	pressure [N/m^2]
P	probability or breakdown parameter
Pr	Prandtl number
R	random number or gas constant [J/kg/K]
Re	Reynolds number
$Re_{2,D}$	Reynolds number behind a normal shock wave based on the cylinder diameter
s	entropy [J/K] or intrinsic abscissa in the stream direction [m]
Sc	Schmidt number
S_t	Stanton number
S_∞	molecular speed ratio
t_s	simulation time [s]
T	temperature [K]
T_r	rotational temperature [K]
T_v	vibrational temperature [K]
T_c	temperature controlling the reaction [K]
T_w	wall temperature
T_0	stagnation temperature
u	velocity component tangential to the surface [m/s]
v	specific volume [m^3/kg]
V	velocity [m/s]
x, y	Cartesian axes
x_{cg}	center of gravity along the x-axis
x_{cp}	location of the pressure center along the x-axis
Z	Fan-Shen parameter

Z_v relaxation vibrational number

Greek Symbols

α molar fraction or angle of attack
α_N molar fraction of atomic Nitrogen
γ ratio of specific heats
Γ gamma function
δ non-equilibrium parameter from the Crocco theorem
ε symmetry factor
ζ number of internal degrees of freedom
η temperature exponent in the Arrhenius equation
ϑ angle [rad.]
ϑ_r rotational non equilibrium parameter
ϑ_v vibrational non equilibrium parameter
Θ characteristic temperature [K]
λ mean free path [m]
Λ Arrhenius constant
ρ density [kg/m^3]
σ collision diameter [Å]
σ_R reaction cross-section [m^2]
σ_T total collision cross-section [m^2]
τ viscous stress [N/m^2]
φ phase angle of vibration or rolling angle
Φ dimensionless function in the Wilke rule
ω exponent of the viscosity power law
$\Omega^{(1,1)}$ diffusion collision integral
$\Omega^{(2,2)}$ viscosity collision integral

Superscript, subscripts and special symbols

a activation
c collision
cont continuum
d dissociation or dissipative
f forward
D/Dt lagrangian derivative, $\partial/\partial t + \underline{V}\cdot\underline{\nabla}$
fm free molecular
mix mixture
r rotational or reverse
ref reference

rel	relative
s	slip
t	translational
v	vibrational
w	wall
ϕ	exponent in average temperature
∞	free stream
*	non-dimensional quantity
$\bar{}$	arithmetic average
$\underline{}$	vector
$\lfloor . \rfloor$	truncated value
(0)	at the cylinder stagnation point
$\underline{\nabla}$	nabla operator, $\underline{i}\partial/\partial x + \underline{j}\partial/\partial y$
$\times$	vectorial product
$\underline{\underline{U}}$	unitary matrix
$\underline{\underline{\tau}}$	stress tensor [N/m^2]

CHAPTER I

Introduction

1.1 Motivation

With a renewed desire to send humans back to the Moon and beyond, there is a need for accurate studies of the flow behavior over hypersonic vehicles to precisely determine how they will perform when entering an atmosphere. The ending of the Space Shuttle program has led to a greater interest in the design of the future hypersonic vehicles for reentering Earth's atmosphere. There has also been a growing interest in the entry of other planetary atmospheres, such as Mars.

The design of hypersonic vehicles requires accurate prediction of the surface quantities. These quantities are typically the heat flux, pressure and shear stress, from which the aerodynamic forces and moments can be calculated. These variables govern not only the aerodynamic performance of the vehicle, but also determine the selection and sizing of the thermal protection system (TPS), which protects the vehicle from the extreme temperatures encountered at hypersonic velocities.

Unfortunately, it is very difficult and expensive to reproduce in ground based experiments and flight tests the conditions met from a vehicle during re-entry. For this reason, computational methods have played a prominent role in hypersonic research. These methods facilitate the early stages of design and analysis, reducing the need for extensive experimentation and decreasing the risk in flight tests. Hence, there is a greater need for the development of accurate computational methods for the design of hypersonic vehicles.

1.2 Hypersonic Reentry Flows

In gas dynamics studies, the basic criterion of the flow regime is the Knudsen number:

$$\mathrm{Kn} = \frac{\lambda}{\mathrm{L}} \tag{1.1}$$

where λ is the mean free path and L is a characteristic length of flow field. The flow-regime is continuum when a Knudsen number tends to zero. While studying the gas flow in this regime, one can disregard its microscopic structure and consider only its macro-parameters such as density, velocity, or temperature. For a Knudsen number tending to infinity the flow regime can be considered as free-molecular. In this case, particle collisions with the body surface play the determining role.

There is a transitional regime between the free-molecular and continuum regimes, where not only gas-surface collisions but also intermolecular collisions are important. Free-molecular and transitional regimes are the subject of Rarefied Gas Dynamics. Besides viscosity and other important viscous effects (including heat conduction, relaxation, diffusion, and irreversible chemical reactions), strong thermal non-equilibrium of the flow is an important feature of rarefied hypersonic flows. That is to say, the velocity distribution function is substantially non-Maxwellian.

A hypersonic vehicle, entering an atmosphere, will go through many different flow regimes due to the change in atmospheric density with altitude. These regimes are characterized by Knudsen number, as shown in Fig. 1.1. This figure gives four regimes and indicates the numerical methods that are accurate for each regime. The Boltzmann equation is valid for all flow regimes, from continuum to free molecular flow.

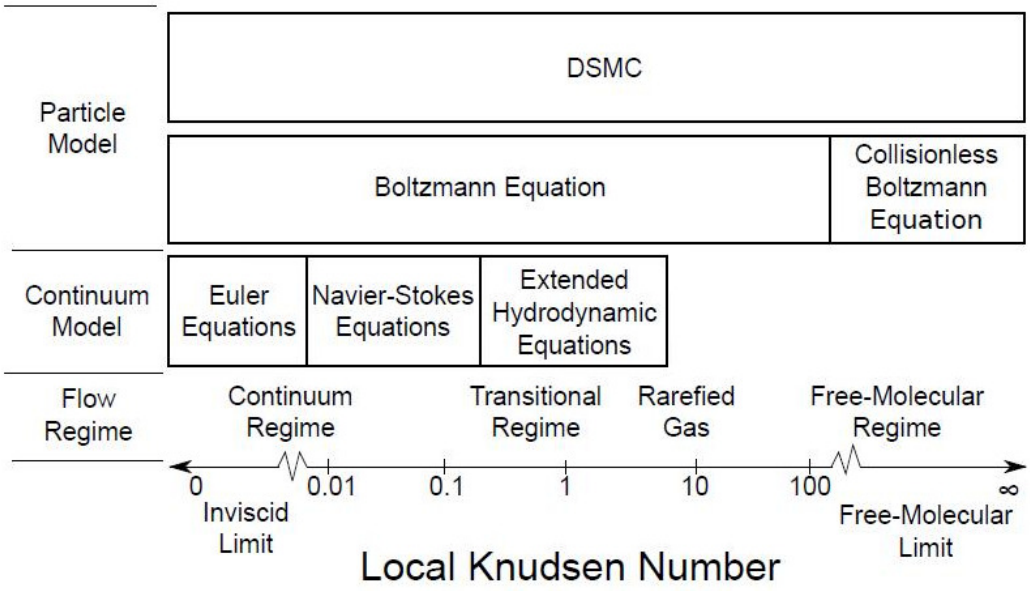

Figure 1.1 The Knudsen number limits for each method

The Navier-Stokes equations are valid in the continuum regime, below the generally accepted, but often argued, limit of a Knudsen number of 0.01. The extended hydrodynamic equations can

be utilized into the transitional regime, but these methods have not been developed as much and it is not clear how far into the transitional regime they can be utilized. The direct simulation Monte Carlo (DSMC) method [1], which has been shown to converge to solutions of the Boltzmann equation [2], can also be utilized over all flow regimes.

At lower altitudes where the density is high and the Knudsen number is low, flows should be simulated using traditional computational fluid dynamics (CFD) techniques by numerically solving the Navier-Stokes equations. However, when the Knudsen number becomes larger, the continuum assumption in the Navier-Stokes equations starts to breakdown. This is due to the fact that these equations are derived from kinetic theory based on the assumption of small perturbations from an equilibrium velocity distribution function [3]; therefore CFD only works in near equilibrium flows.

At low Knudsen numbers, the no-slip boundary conditions hold. At higher Knudsen numbers, there are insufficient collisions near the wall and the flow is not able to equilibrate with the wall, hence the no-slip condition is invalidated. The use of slip boundary conditions in the CFD method can extend the validity of this approach further into the transitional flow regime.

At higher altitudes, in the rarefied flow regime, only a non-continuum technique can be used, such as the DSMC method, that is particle method for simulating non-equilibrium gas flows. DSMC is required for accurate flow analysis of hypersonic rarefied flows where the continuum flow equations are invalid, and can be utilized in any dilute gas flow. Unfortunately, DSMC is about an order of magnitude more expensive than CFD methods and becomes prohibitively expensive at low Knudsen numbers. Note that, even though the global flow behaves as a continuum, there may still be parts of the flow that locally act as a rarefied flow, if the local length scale is very small or the local density is low. For example, a hypersonic blunt body can create a locally rarefied flow in the shock, in the boundary layer and in the wake of the body. As a result, neither CFD nor DSMC can provide a complete computational model across all regimes of a hypersonic flow.

Currently, a possible solution to this problem of continuum breakdown, is a hybrid code [4.5] that utilizes CFD and DSMC methods to accurately and efficiently simulate a hypersonic flow. This hybrid code can solve the Navier-Stokes equations when the flow is considered to be a continuum, but can switch to a DSMC method when the flow is considered rarefied such as in a shock.

1.3 Scope of the Current Work

The aim of the present thesis is the study of some problems of hypersonic rarefied Aerodynamics. More specifically the subjects here considered are:

a) **Development of a new parameter to detect non-equilibrium region.** As already pointed out, the identification of non-equilibrium regions is important for an accurate solution of a flow field. More specifically an hybrid code needs a parameter to determine what method (DSMC or CFD), has to be used in the solution of the flow field. In this thesis, a new parameter to detect the non equilibrium region is proposed. This parameter is based on the Crocco theorem. The assumption on which the new parameter relies is that a theoretical relation, based on the hypotheses of equilibrium, as the one of the Crocco theorem, is not verified in non-equilibrium. The new parameter has been computed as the difference of the terms forming the Crocco theorem equation. Thus, one can expect that the higher is non-equilibrium, the larger is the mismatch between the terms and therefore the higher is the parameter.

b) **Improvement of approximate methods (bridging formulae) for the evaluation of aerodynamic coefficients of a re-entry vehicle in high altitude flight.** At the first stage of a design of a re-entry vehicle it could be important to determine in a fast way the aerodynamic forces coefficient. The achieve this goal the well known “bridging formulae” are used. In this thesis a “new” methodology (here called “new” bridging formula) has been developed. The “new” bridging formula, has been successfully tuned to sphere and it has been also tested on two current capsules: EXPERT and ORION.

c) **Analysis and comparison of several chemical models: 1) peculiar of a DSMC approach such as quantic models (classic and new), Fan-Shen and Bird, 2) “classic” models such as the Gupta and Park models with and without ionization reactions.** It is well known that one of the most important problems in the design of a capsule is the evaluation of heat flux during the re-entry. This evaluation has to provide information about the design of the Thermal Protection System (TPS). To this regard it is important to underline that due to the endothermic characteristic of the reactions, the chemical model affects the computation of the heat flux. A very deep analysis about the difference in the computation of heat flux between a direct simulation Monte Carlo code (DS2V) and a computational fluid dynamics code (H3NS) has been carried out. To this purpose a method to implement the Park model in a DSMC code has been developed.

d) **Application of DSMC codes to evaluate the aerodynamic coefficients of a current capsule (EXPERT) and a future aerospace vehicle (FAST20XX).** For the EXPERT capsule computer tests have been carried out in the altitude flight with particular attention to the longitudinal stability of the capsule. As for as FAST20XX, the demonstration and validation of the numerical tools able to predict aero-thermal loads on a space re-entry vehicle at high altitude conditions has been carried out. This goal is fulfilled by the characterization of the DLR low density wind tunnel V2G and by an aerodynamic analysis of the available model of a lifting body.

CHAPTER II

Simulation of Hypersonic Gas Flow

2.1 Introduction

The basic difference between "classic" Aerodynamics and molecular Aerodynamics is that the first one studies a flow field by the evolution of macroscopic parameters representing the state of a fluid, such as velocity, temperature, density and so on. Molecular Aerodynamics studies a flow field by the evolution of velocity, position and internal state of each molecule. Thus, molecular Aerodynamics provides a deeper and therefore a more precise description of a fluid-dynamic system. Even though the molecular approach is of general validity, however from an applicative point of view, it is aimed to study rarefied (i.e. free molecules, transition and low density continuum), high velocity regimes, as per those met by a space vehicle at high altitude along the re-entry path.

As well known, the Navier-Stokes equations are not suitable in rarefied regimes because of:

(a) failure of the phenomenological equations of Newton, Fourier and Fick,
(b) non-equilibrium (translation, rotational and vibrational temperatures are different),
(c) anisotropy (components of translational temperature and of pressure are different along the three space directions).

Nowadays, the solution of rarefied flow fields relies on molecular methods such as Molecular Dynamics and specially Direct Simulation Monte Carlo (DSMC). Both Molecular Dynamics and DSMC are computational (non numerical) methods. In fact, they do not rely on integration of differential equations. These methods consider the gas as made up of molecules, whose evolution (movement, collisions with other molecules and with a body surface, activation of internal degrees of freedom) is simulated in a computer. The difference between the methods is that: Molecular Dynamics is deterministic, DSMC is statistic. In fact, the number of simulated molecules in Molecular Dynamics is the same like the number of real molecules, while the number of simulated molecules in DSMC is much smaller than the number of real molecules,

thus the simulated molecules represent a sample of real molecules. The Boltzmann* equation should be able, in principle, to solve every flow field from free molecule to low density continuum regimes. But this is not yet possible because this equation, as shown later, is an integral-differential equation and its solution shows overwhelming theoretical-numeric difficulties; the scientific community is still searching for a solution. Even though, it has to be pointed out that some researchers, using simplifying hypotheses and/or particular computing procedures, found solution of simple problems. For this reason the Boltzmann equation is of scarce interest from an engineering point of view, also considering that the solution of rarefied flow fields is successfully fulfilled currently by DSMC. However the Boltzmann equation is very important from a theoretical point of view. In fact it is possible to demonstrate [6,7,8,9] the link between the Boltzmann equation and other equations valid in several rarefaction levels, quantified by the Knudsen number (Kn):

(a) Maxwell equation, $Kn \gg 1$ (free molecule flow),

(b) Burnett equations, $Kn \cong 1$ (transitional regime),

(c) Navier Stokes equations, $Kn \ll 1$ (continuum),

(d) Euler equations, $Kn = 0$ (continuum, non diffusive).

Therefore the Boltzmann equation can be considered as origin or "mother" of all these equations.

2.2 Boltzmann Equation

The Boltzmann equation, in the unknown function f, states a relationship between the distribution function f and the variables $\underline{V}$, $\underline{r}$ and t. This equation, derived in 1872, is a more operative version of the Liouville equation; the Liouville equation is written in terms of probability density while the Boltzmann equation is written in terms of distribution function.

The Boltzmann equation relies on the following hypotheses:

* Ludwig Eduard Boltzmann was born in Wien on Feb. 20, 1844. He is one of the most important theoretical physicist in the history for his founding contributions in the field of kinetic theory, statistical mechanics and statistical thermodynamics. He is also one of the most important advocate for atomic theory. In 1869, at age 25, he was appointed full Professor in Mathematical Physics at the University of Graz. In 1869 he spent several months in Heidelberg working with Robert Bunsen and Leo Königsberger and then in 1871 he was working with Gustav Kirchhoff and Hermann von Helmholtz in Berlin. In 1872 he obtained his famous equation. In 1873 he joined the University of Wien as Professor in Mathematics and there he stayed until 1876. He died suicide in Duino on Sep. 5, 1906.

1. Gas is dilute. By definition, a gas is dilute if the molecular spacing δ ($\delta=n^{-1/3}$) is much greater than the molecular diameter (d): $\delta/d>>1$. This hypothesis implies that the collisions are only bi-molecular and involve only weak intermolecular forces.
2. Intermolecular collisions are perfectly elastic. A collision is elastic if: i) there is no exchange of energy between traslational degree of freedom (kinetic energy) and rotational and vibrational degrees of freedom (internal energy), ii) there is no chemical reaction (dissociation, recombination and exchange), iii) post-collisional momentum is equal to pre-collisional momentum. These points imply that molecules can be considered as rigid spheres.
3. "Molecular chaos". This hypothesis relies on the concept of stochastic independence; the distribution function of a generic molecule is independent of the distribution function of other molecules. This means that, chosen randomly two molecules 1 and 2 in the phase space, the distribution function, providing the probability that molecule 1 is in the position $\underline{r}_1$ with velocity $\underline{V}_1$ and molecule 2, is in the position $\underline{r}_2$ with velocity $\underline{V}_2$ is given by the product of the single distribution functions:

$$f\left(\underline{r}_1,\underline{r}_2,\underline{V}_1,\underline{V}_2,t\right)=f\left(\underline{r}_1,\underline{V}_1,t\right)f\left(\underline{r}_2,\underline{V}_2,t\right) \tag{2.1}$$

   Therefore, knowledge of the distribution function of a single molecule is sufficient to characterize the distribution function of the whole system.

The Boltzmann equation is made of four terms, providing the change of the number of molecules in the phase space. The unknown distribution function f is both in derivative and in integral; therefore the Boltzmann equation is an integral-differential equation. As said before, its solution presents overwhelming theoretical and numerical difficulties. A mixture of gases, made up by s chemical species, requires a distribution function, different for each species. In this case, the Boltzmann equation becomes a system of s independent equations:

$$\frac{\partial f_p}{\partial t}+\underline{V}_p\cdot\frac{\partial f_p}{\partial \underline{r}}+\underline{F}\cdot\frac{\partial f_p}{\partial \underline{V}}=\sum_{q=1}^{s}N_q\int_{-\infty}^{+\infty}\int_{0}^{4\pi}\left(f_p^*f_{1q}^*-f_pf_{1q}\right)V_{rpq}\sigma_{pq}d\Omega dV_{1q}\quad p=1,\ldots,s \tag{2.2}$$

where p and q represent particular species.

The internal degrees of freedom require a distribution function, characterized by a number of dimensions greater than the one of the phase space. Furthermore, the collision cross section of non-symmetric molecules is a function of the molecule orientation, therefore the cross sections change in time, due to rotation of the molecules in the collisions.

2.3 Philosophy of the Direct Simulation Monte Carlo Method

The gas is considered made of hundred thousands or millions of simulated molecules, each one representing a number (as per of the order of 10^{15}) of real molecules. Evolution of each molecule (from which "Direct Simulation"), in a simulated physical space, is produced by collisions with other molecules and with the body, in both cases exchanging momentum and energy. Velocity changes in modulus and in direction. Excitation of rotational and vibrational degrees of freedom and chemical reactions are also taken into account. The method is statistical and stochastic: i) statistical because the computed macroscopic thermo-fluid-dynamic quantities (velocity, temperature, density, etc.) are averages of microscopic (or molecular) quantities, ii) stochastic because its procedure relies on sampling probability functions by means of random numbers (from which "Monte Carlo").

The simulated volume, including the body, is discretized in cells. Each cell is divided in turn in sub-cells. Position, velocity and internal state of each molecule in the cells are computed concurrently. DSMC uses the cells only for sampling the macroscopic properties and for selecting the colliding molecules. Use of sub-cells allows an effective selection of collision pairs by the logic of the "nearest neighbor". Thermo-fluid-dynamic quantities are computed in each cell and located in its center. Each dimension of a cell must be smaller than the local mean free path ($\Delta x, \Delta y, \Delta z < \lambda$) as well as the distance over which there is a significant change of flow properties. Also the typical dimension of the sub-cells has to be less than the local mean free path. Furthermore, movement of each molecule from a cell to another one is the product of the velocity (that is the resultant of convective and thermal velocities) and a prefixed time step (Δt). In order to uncouple molecular motion and collisions, the time step has to be less than the mean collision time (Δt_c), or the time interval between two successive collisions.

DSMC is a very smart computer implementation of formulas from the kinetic theory of gases and has to be considered just a computer method, not a numerical method. In fact, it does not rely on any numerical procedures as per, solution of differential equations, integration, interpolation and so on. The most important advantage is that it does not suffer from numerical instabilities and does not rely on the classification of the flow field (sub/super-sonic, viscous/non-viscous, etc.) or on knowledge of similarity parameters (Mach number, Reynolds number and so on). Shortcoming is that it is always unsteady; steady flow is achieved after a long enough simulated time and therefore it requires high processing velocity to reach steady conditions. Moreover, the computer core storage has to be large enough for simulating an

appropriate number of molecules. Computation, associated with the direct physical simulation, becomes feasible when the gas density is sufficiently low. On the other hand, possible statistical fluctuations and statistical errors, due to the replacement of a very high number of real molecules with a much smaller number of simulated molecules, have to be taken also into account.

2.4 Sophisticated DSMC Method

The computer implementation of the DSMC procedures can be considerably improved in terms of accuracy of the results as well as of computational efficiency. According to what reported by Bird [10, 11] when these procedures are implemented, the DSMC method is called "sophisticated". The following procedures are implemented practically in all current most advanced DSMC codes like DS2V/3V by Bird [12, 13], SMILE by Ivanov [14], DAC by LeBeau [15]. More precisely, the description of the procedures is related to the codes DS2V/3V:

1) Automatic setting of the computational parameters: cells and molecules,
2) Cell adaptation,
3) Collision Cell System and Sampling Cell System,
4) Nearest neighbor procedure,
5) Automatically adaptive time step,
6) Radial weighting factor.

1. Automatic Setting of the Computational Parameters

The sophisticated codes are able to set automatically the proper number of cells and elements, according to the input number of megabytes to be used in the calculation and to the free stream density.

2. Cell Adaptation

The current DSMC codes discretize the computational domain in a system of rectangular divisions and each division in rectangular elements (Fig. 2.1(a)), or parallelepiped divisions and elements for 3-D domains. As a typical example, Fig. 2.1(a) shows a bounding rectangle defining the computational domain, divided into 20 (4×5) divisions, each one into 36 (6×6) elements. The number of elements per division is such that the number of all elements

approximates the number of simulated molecules. At beginning of computation, the divisions play the role of the cells, the elements play the role of the sub-cells.

The adaptation process consists in forming a cell by clustering, around a node, the elements nearest to that node, in such a way that each adapted cell contains a desired number of molecules (N_a), independently of the division to which the element belongs. The number of adapted cells (or nodes, N_n) is given by the ratio of simulated molecules (N_s) by N_a: $N_n=N_s/N_a$. The shape of an adapted cell could be similar to that shown in Fig. 2.1(b). As said before, initially, the cell nodes are set at the center of the divisions, then they are distributed in the computational domain in such a way that the probability of the location of a given node is proportional to the average number density in the division at that location.

Due to the odd shape of the adapted cell, the check for the correctness of the results (see point 7 of section 3.2) is provided by the ratio of the mean separation of the colliding molecules (mcs) to the local mean free path (mcs/λ). For correct results, the value of the parameter mcs/λ has to be less than 1.0, more specifically, Bird [10, 11] suggests a limit value of 0.2. The value of this parameter is indicative of the proper number of simulated molecules and therefore of the quality of the computation.

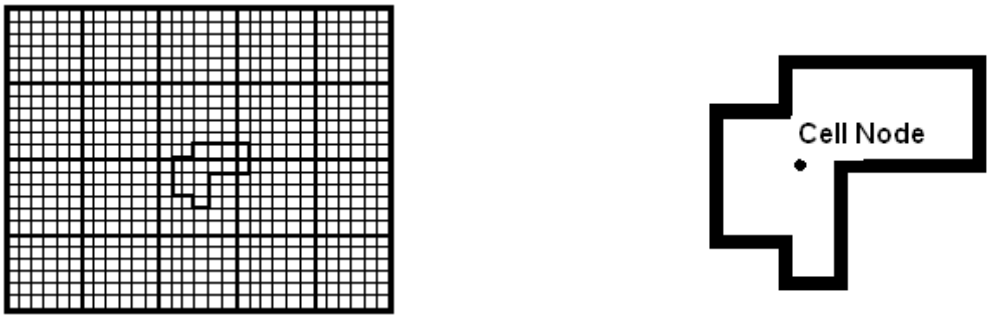

(a) (b)

Figure 2.1 Discretization of the computational domain in divisions and elements (a), adapted cell (b)

3. Collision and Sampling Cell Systems

In order to improve the computational efficiency, the "sophisticated" codes use two separated cell systems: i) collision cells and ii) sampling cells. The first one is characterized by a space resolution much higher than the second one. On the other hands, computing the macroscopic flow quantities at the same resolution like the collision cell system should be impractical.

DS2V/3V codes suggest a number of molecules, to adapt collision cells, of $N_a=8$. The "lucky" value of $N_a=8$ was found by Bird [10, 11], by several tests involving the analysis of the heat flux at the stagnation point of circular cylinder.

4. Nearest Neighbor Procedure

The essential requirement, for correct DSMC results, is linked to the condition that the colliding molecules have to be as close as possible to each other. For this reason, the sub-cells system was introduced. An improvement of the sub-cell concept is obtained by introducing the "virtual sub-cell system" and "transient sub-cell system" procedures.

The procedure of "virtual sub-cells" consists in a direct selection of the second collision partner. This means that, as said before, once the first molecule is chosen randomly in the cell, the collision partner is the nearest molecule. For this reason, it is not longer necessary to divide the cell in sub-cells, from which the label "virtual sub-cells".

The procedure of "transient sub-cells" consists in placing, on each cell, a sub-cells system, peculiar to that cell. The number of sub-cells is about equal to the number of simulated molecules, included in that cell. For instance, if the cell contains N_s simulated molecules, the sub-cell system is made of a grid $\mathrm{INT}(\sqrt{N_s})\times\mathrm{INT}(\sqrt{N_s})$. For instance if N_s=50, the grid is made of 7×7 sub-cells. Figure 2.2 shows a typical sub-cell system, placed on the cell shown in Fig. 2.1(a), supposing that the cell contains, for instance, 18 simulated molecules, the method places, on the cell, a system of 4×4 sub-cells. The molecules are indexed to this "transient" grid.

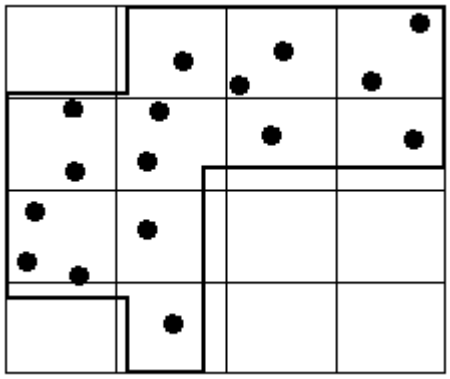

Figure 2.2 Transient sub-cells system

Based on the computing velocity, Bird [10, 11] suggests to use the "virtual sub-cells" procedure when the number of simulated molecules per cell is less than 35 and the "transient sub-cells" when N is greater than 35. Obviously, if the cells are adapted with N_a=8, the "virtual sub-cells" procedure is automatically used.

A problem, linked to the nearest neighbor procedures, is that it could happen that the second molecule, chosen as a collision partner, has been already involved in the immediately previous collision with the same molecule. This is physically impossible, because a collision moves far

the molecules. The current, sophisticated codes record the molecule of previous collision partner of each molecule, thus a second closest molecule is chosen.

It has to be pointed out that current DSMC codes do not provide, indeed, a fully nearest-neighbor capability, because it could happen that for molecules close to the boundary of a cell, the nearest one is in another cell and then it cannot be selected as a collision partner.

5. Automatically adaptive time step

Using a single, constant value of the time step (Δt) in every collision cell is not efficient. In fact, Δt could be too short for cells where density is low and too long for cells where density is high. The adaptive procedure of time step consists in fixing, in each cell, a local time step (Δt_l) as a fraction of the local collision time (Δt_c), typically: $\Delta t_l = \Delta t_c/5$. This value is used to compute the number of collisions in each cell. Flow time of the whole fluid-dynamic system is advanced in steps equal to the smallest value of Δt_l, in the whole computational domain.

6. Radial Weighting Factor

If the problem is 2-D and axi-symmetric and the cells are evenly spaced in the radial direction, the cells closer to the axis are smaller (Fig. 2.3, the filled circle is a section of the body). Being the molecules distributed uniformly in the azimuthal plane, the number of simulated molecules in each cell decreases from the cells farer from the axis to the cells closer to the axis.

The radial weighting factor, defined as the ratio of the radial position r of a molecule to the reference radius r_{ref}: r/r_{ref}, tends to equalize the number of simulated molecules in each cell layer. Thus, the number of real molecules represented by each simulated molecule (W) is:

$$W = F_N \qquad \text{if } r \le r_{ref} \tag{2.3}$$

$$W = \frac{r}{r_{ref}} F_N \qquad \text{if } r > r_{ref} \tag{2.4}$$

Furthermore, a simulated molecule moving toward the axis has some probability to be duplicated and a molecule moving away from the axis has some probability to be removed, according to its radial position: if $r<r_{ref}$ then probability to be duplicated increases, if $r>r_{ref}$ probability to be removed increases. This probability is computed as the ratio of the minimum weighting factor in the cell $(r/r_{ref})_{min}$ to the weighting factor of the molecule:

$$P = \frac{(r / r_{ref})_{min}}{r / r_{ref}} \tag{2.5}$$

P is processed by the accepted/rejection procedure.

Bird [1] verified that using the same weighting factor for all molecules in the same cell, besides simplifying the computing procedure, has only negligible effects on the flow field. In order to avoid problem linked to the occurrence of identical molecules in a cell, due to duplication, the duplication process is fulfilled by imposing a time delay. If a molecule is duplicated, the newly created molecule is stored in a buffer. Then it is selected randomly and entered in the flow,

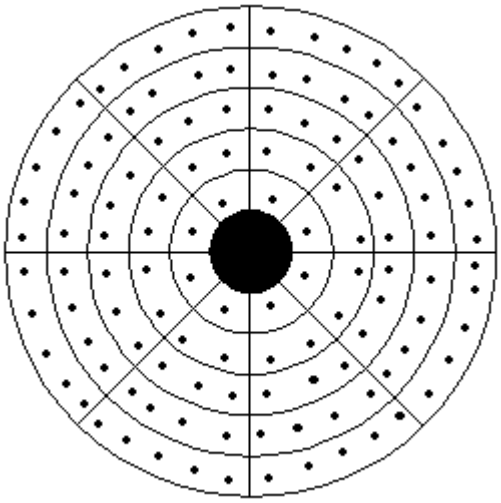

Figure 2.3 Cross section in the azimuthal plane of an axi-symmetric flow field

2.5 Computational Codes

A. DS2V and DS3V codes

DS2V and DS3V are very advanced DSMC code. Both codes are widely tested and worldwide accepted. These codes are able to consider a number of built-in gases, including also air plasma. The built-in chemical model relies on the chemical reactions from the Gupta model [16].

All procedures, making a DSMC code "sophisticated", are implemented by Bird in these codes. DS2V simulates 2-D plane/axi-symmetric flow fields, while DS3V simulates 3-D flow field. The run can be checked on line by three displays, each one related, respectively, to:

i) run parameters such as simulation time, the maximum and averaged value of mcs/λ, number of simulated molecules, number of collisions and so on.. A graphic shows the time history of the number of molecules. Fluctuations are indicative of a stabilization of the run.

ii) 2-D plots of flow field parameters: velocity, density, pressure, mcs/λ, gas composition and so on.

iii) Plots of surface parameters of heat flux, slip velocity, pressure and so on, as functions of curvilinear abscissa.

The input operation is also easier, with respect to the previous versions, thanks the use of graphical facilities.

B. H3NS code

The CFD code H3NS [17], developed by the Italian Aerospace Research Center (CIRA), solves full Reynolds averaged Navier–Stokes equations and considers air made up of the five above mentioned chemical species in thermo-chemical non-equilibrium. The code implements the Park chemical model [18, 19, 20].

H3NS is based on a finite volume approach with a cell-centered formulation. The inviscid fluxes are computed by a flux difference splitting scheme. A second-order approximation is obtained with an essentially non-oscillatory reconstruction of interface values. H3NS ran by an explicit multistage Runge–Kutta algorithm, coupled with an implicit evaluation of the source terms.

In order to take into account the effects of rarefaction, H3NS can implement, as boundary conditions, the slip velocity (u_s) and the slip temperature (T_s). Among the many available formulations of this kind of conditions, the ones proposed by Kogan [21] are usually used:

$$u_s = 1.012\lambda\left(\frac{\partial u}{\partial n}\right)_w \tag{2.6}$$

$$T_s = T_w + 1.73\frac{\gamma}{\gamma\ 1}\frac{\sqrt{\pi}}{4}\lambda\left(\frac{\partial T}{\partial n}\right)_w \tag{2.7}$$

where: u is the tangential component of velocity, γ is the specific heat ratio, n is the local normal and w stands for wall.

CHAPTER III

Evaluation of non-equilibrium by the Crocco theorem

3.1 Introduction

Prediction of non-equilibrium regions is important for an accurate solution of a flow field both by Computational Fluid-Dynamics (CFD), for the identification of regions where the flow field can be considered or not isentropic and by Direct Simulation Monte Carlo method (DSMC) for the identification of regions where the number of molecular collisions should be more or less high. More specifically, the higher is non-equilibrium the larger should be the number of molecular collisions. Non equilibrium is encountered especially in super/hypersonic rarefied flows and more precisely in the core of the shock waves. A number of papers have been written on this subject, see for instance the paper by Chigullapalli et al. [22] and related references. In these works, entropy generation rate is used as a measure of non-equilibrium. In fact, thermodynamic equilibrium is characterized by zero entropy generation and non-equilibrium is identified by a positive entropy generation. As non-equilibrium is peculiar of rarefied flows, the computation of entropy rate relies on the Boltzmann equation and, more specifically, on a discrete version of the Boltzmann's H-theorem.

The thermodynamic non-equilibrium is produced by different values of the translational, rotational and vibrational temperatures. The anisotropy is produced by different spatial components of the molecular thermal velocity and therefore by different values of the components of: translational temperature, pressure tensor, diffusion velocity of a chemical species. To consider these effects, Candler et al. [23] developed new continuum conservation equations for low density non-equilibrium hypersonic flows based on a continuum multiple translational temperature model. Candler applied this model to solve the flow field in a one-dimensional shock wave.

According to Candler [23], the physical process, generating anisotropy and thermodynamic non-equilibrium, is due to the free stream kinetic energy that is primarily converted, by means of molecular collisions, to the thermal energy in the direction perpendicular to the shock wave. The thermal energy is then transferred, by subsequent collisions, to the parallel directions to the shock wave and finally to the interior degrees of freedom (rotation and vibration) of the

molecules. The components of the translational temperature, of the pressure tensor and also of the diffusion velocity of a chemical species are different (anisotropy). As well as, the rotational and the vibrational temperatures are different from each other and from the translational one (thermodynamic non-equilibrium). Anisotropy and thermodynamic non-equilibrium increase with rarefaction. In fact, restoring equilibrium occurs only through molecular collisions; thus as rarefaction increases, the molecular collision rate decreases leading to a higher level of thermodynamic non-equilibrium and anisotropy. Therefore the continuum and the free molecular regimes can be considered as extreme cases of equilibrium and non-equilibrium, respectively.

Zuppardi [24] quantified:

(d) anisotropy both by the difference between the maximum values of the profiles of the temperature components and by the difference between the maximum values of the profiles of the modulus of the diffusion velocity components of a chemical species,
(e) thermodynamic non-equilibrium by the difference between the maximum values of the profiles of the translational, rotational and vibrational temperatures.

Bird [12] quantifies, in each cell of the computing dominion:

(a) anisotropy by the percentage variation of the translational temperature components,
(b) thermodynamic non-equilibrium by the percentage variation of rotational and vibrational temperatures with respect to the translational one.

Thermodynamic non-equilibrium and anisotropy are two aspects of non-equilibrium. Having a single parameter, for the evaluation of "global" non-equilibrium that includes both thermodynamic non-equilibrium and anisotropy could be interesting and useful from an operative point of view. In the present paper a method is proposed for the definition of a "new" single parameter. The method relies on the assumption that a theoretical relation, based on the hypotheses of equilibrium, is not verified in non-equilibrium. For this purpose, the Crocco theorem equation has been considered and the new parameter has been computed as the difference of the terms forming the Crocco theorem equation. Thus, one can expect that the higher is non-equilibrium, the larger is the mismatch between the terms and therefore the higher is the parameter. The proposed method is similar to the entropy generation rate, because relying on a single parameter, but completely different in principle.

As non-equilibrium is produced mostly by a shock wave, in order to enhance the phenomenon under study or to increase the non-equilibrium effects, a slab normal to the free stream velocity has been considered as test case. The analysis has been carried out in the whole transitional

regime, from the continuum low density to the free molecular flow regimes. The present work that has to be considered as a preliminary analysis of the new parameter, the results have been compared only with the ones by the Bird parameters. The new parameter showed to be able to detect in a more efficient way the position of non-equilibrium regions both inside and outside the shock wave.

3.2 The Crocco Theorem

As well known, the Crocco theorem is a "classical" topic in compressible Aerodynamics [25, 26, 27]; it relates the enthalpy gradient and the vorticity of the rotational, inviscid flow to the entropy gradient. The theorem provides also a useful description for a number of types of rotational flows encountered in practical applications such as the flow field in rotors of turbo machines [27].

The theorem represents a different formulation of the momentum balance equation:

$$\rho \frac{D\underline{V}}{Dt} - \underline{\nabla} \cdot \underline{\underline{\tau}} = \rho \underline{g} \tag{3.1}$$

where the stress tensor $\underline{\underline{\tau}}$ includes the dissipative ($\underline{\underline{\tau}}_d$) and the conservative ($p\underline{\underline{U}}$) contributions: $\underline{\underline{\tau}} = \underline{\underline{\tau}}_d - p\underline{\underline{U}}$. The Lagrangian derivative of velocity can be written as:

$$\frac{D\underline{V}}{Dt} = \frac{\partial \underline{V}}{\partial t} + (\underline{V} \cdot \underline{\nabla})\underline{V} = \frac{\partial \underline{V}}{\partial t} + \underline{\nabla}\left(\frac{V^2}{2}\right) + (\underline{\nabla} \times \underline{V}) \times \underline{V} \tag{3.2}$$

Considering a steady, non viscous flow field and neglecting the gravity effects, Eq.3.1 becomes:

$$\underline{\nabla}\left(\frac{V^2}{2}\right) + (\underline{\nabla} \times \underline{V}) \times \underline{V} = -\frac{1}{\rho}\underline{\nabla} p \tag{3.3}$$

By the hypothesis of local equilibrium, the differential Gibbs equation for a non-reactive gas:

$$dh = Tds + \frac{1}{\rho} dp \tag{3.4}$$

can be generalized along a space direction:

$$\underline{\nabla}h = T\underline{\nabla}s + \frac{1}{\rho}\underline{\nabla}p \tag{3.5}$$

therefore, by the definition of total enthalpy ($H=h+V^2/2$), Eq. 3.5 provides the formulation of the Crocco theorem:

$$\underline{\nabla}H + (\underline{\nabla}\times\underline{V})\times\underline{V} = T\underline{\nabla}s \tag{3.6}$$

The entropy gradient, under the same assumptions on which the Crocco theorem relies, can be computed by:

$$\underline{\nabla}s = c_v\frac{\underline{\nabla}p}{p} + c_p\frac{\underline{\nabla}v}{v} \tag{3.7}$$

where c_v and c_p are the constant volume and the constant pressure specific heats, respectively. The variability of the specific heats with temperature has been also taken into account.

This theorem is particularly suitable for the present application because, unlike the momentum balance equation, some thermodynamic terms, such as entropy and enthalpy, are explicitly present.

3.3 Non Equilibrium parameters

As the Crocco theorem relies on the hypothesis of equilibrium, one can expect that the difference vector between the terms $\underline{\nabla}H + (\underline{\nabla}\times\underline{V})\times\underline{V}$ and $T\underline{\nabla}s$ increases with non-equilibrium. Then a possible parameter, quantifying non-equilibrium, at every point in the flow field, is defined as the module (δ) of the difference vector:

$$\delta = \left|\underline{\nabla}H + (\underline{\nabla}\times\underline{V})\times\underline{V} - T\underline{\nabla}s\right| \tag{3.8}$$

In principle, using a non dimensional parameter is advisable in every evaluation process, thus δ has been made non-dimensional. Possible quantities, making δ (Energy/Mass/Length) non-dimensional, are the free stream, total, specific enthalpy and a characteristic length of the flow field.

As already said, Bird [12] proposes as thermodynamic non-equilibrium parameters (ϑ_r, ϑ_v), the percentage variation of the rotational (T_r) and vibrational (T_v) temperatures with respect to the translational (T) one:

$$\vartheta_r = \frac{T_r}{T} - 1 \qquad \vartheta_v = \frac{T_v}{T} - 1 \tag{3.9}$$

and, as anisotropy parameter (ϑ_{xy}), the percentage variation of the spatial components (T_x, T_y) of the translational temperature:

$$\vartheta_{xy} = \frac{T_x}{T_y} - 1 \tag{3.10}$$

Generally $T_x > T_y$, $T > T_r$ and $T > T_v$, therefore in order to make comparable anisotropy and thermodynamic non-equilibrium parameters, ϑ_r and ϑ_v have been defined in the present paper as:

$$\vartheta_r = \frac{T}{T_r} - 1 \qquad \vartheta_v = \frac{T}{T_v} - 1 \tag{3.11}$$

A further anisotropy parameter (ϑ_{xz}) has been also introduced:

$$\vartheta_{xz} = \frac{T_x}{T_z} - 1 \tag{3.12}$$

3.4 Rarefaction Parameters

The rarefaction analysis relies on two parameters:

1. overall Knudsen number ($Kn_{\infty L}$), defined as the ratio of the free stream mean free path (λ_∞) to a characteristic dimension (L) of the body under study. According to Moss [28], a general definition of the transitional regime is: $10^{-3} < Kn_{\infty L} < 50$.
2. Local Knudsen number (Kn_G), defined as the ratio of the local mean free path (λ) to the scale factor (L_G) of the gradient of a generic macroscopic quantity G, such as temperature (T), pressure (p), density (ρ) and velocity (V):

$$Kn_G = \frac{\lambda}{L_G} \tag{3.13}$$

L_G is computed as:

$$L_G = \frac{G}{dG/ds} \tag{3.14}$$

where s is an abscissa in the flow direction.

According to Bird [1], the classification of rarefaction, in terms of Kn_G, is:

$Kn_G<0.1$	Continuum with validity of the Navier-Stokes equations,
$0.1<Kn_G<0.2$	Continuum without validity of the Navier-Stokes equations; this regime is called also continuum low density regime,
$Kn_G>0.2$	Non continuum; a molecular approach is necessary.

3.5 Computing Procedure

The computing procedure relies on two codes, working in tandem, a DSMC code and a post-processor code. Using the DSMC method [1, 29] is necessary, in the present application, because the computer tests ran in the whole transitional regime, from continuum to free molecular flow. It is well known that the DSMC method is nowadays the only available method to solve a rarefied flow field [1, 29]. The method is able to overcome the failure, in this regime, of the phenomenological equations of Newton, Fourier, and Fick on which the Navier–Stokes equations rely. DSMC method simulates the evolution of millions of molecules. Each simulated molecule represents a large number of real molecules in the physical space.

The DSMC code, used in the present application, is DS2V. This code can simulate 2-D plane or axial-symmetric flow fields. DS2V is sophisticated and advanced.

The post-processor code elaborates the output from DS2V to compute: δ (Eq. 3.8), ϑ_r, ϑ_v (Eq. 3.11), ϑ_{xy} (Eq. 3.10), ϑ_{xz} (Eq. 3.12) and Kn_G (Eq. 3.13). In the present application, for the computation of L_G (Eq. 3. 14), the derivative d/ds has been replaced by the nabla operator. As the output results from DS2V are related to cells with irregular shape, produced by the DS2V adaptation process, it was necessary to report the values of each thermo-fluid-dynamic quantity onto a rectangular cells system to make feasible the numerical approximation of derivatives along x and y. This task was fulfilled by the kriging routine included in the TECPLOT software [30]. The kriging routine relies on a least square curve fitting procedure.

First order derivatives of the nabla operator, applied to a generic macroscopic quantity, are approximated by a second order, forward or central or backward numerical differentiation scheme, each one where necessary. For example along x, the forward (Eq. 3.15), the central (Eq. 3.16) and the backward (Eq. 3.17) approximations of derivatives are:

$$\left(\frac{dG}{dx}\right)_i = \frac{-G_{i+2} + 4G_{i+1} - 3G_i}{2\Delta x} + O(\Delta x^2) \tag{3.15}$$

$$\left(\frac{dG}{dx}\right)_i = \frac{G_{i+1} - G_{i-1}}{2\Delta x} + O(\Delta x^2) \tag{3.16}$$

$$\left(\frac{dG}{dx}\right)_i = \frac{3G_i - 4G_{i-1} + G_{i-2}}{2\Delta x} + O(\Delta x^2) \tag{3.17}$$

3.6 Test Conditions

Tests have been carried out considering a slab (height=0.04 m, thickness=0.002 m) normal to the free stream velocity. The computing region is a rectangle (length=0.23 m, height=0.1 m). All tests rely on the same free stream temperature and molar fractions (α) of air, met at an altitude of about 80 km: T_∞=200 K, α_{O_2}=0.21, α_{N_2}=0.78, α_O=0.01. Free stream velocity has been kept constant, V_∞=2500 m/s, consequently the Mach number is also constant: Ma_∞=8.78.

The analysis relies on 9 tests. In order to evaluate the effects of rarefaction, the free steam number density has been changed from 10^{18} to 10^{22} 1/m^3. The free stream Knudsen number based on the slab height ($Kn_{\infty h}$), ranges practically in the whole transitional regime: 3.5×10^{-3} to 35. All tests ran with 2×10^7 simulated molecules. The quality of the runs, therefore the reliability of the results, is verified by the average value of mcs/λ that, at the most severe test condition of free stream number density of 10^{22} 1/m^3, is 0.195. The ratio of the simulation time to a reference time, defined as the time necessary to cross the computing region at the free stream velocity (9.2×10^{-5} s), is about 10; thus a steady state condition can be considered reasonably achieved.

The reference quantities, making δ non-dimensional, are the free-stream total enthalpy (H_∞=3.3×10^6 J/kg) and the length of the flow field region. The grid used for the kriging process has been made up of square cells of $10^{-3}\times10^{-3}$ m^2. The spacing of the kriging grid can be considered sufficient; the size of Δx is half of the smallest macroscopic scale of fluid-dynamic system, i.e. the slab thickness; this involves two kriging cells in x direction. The dimensions of the kriging cell made the numerical approximation of derivatives of the order of 10^{-6} m.

3.7 Analysis of Results

In order to show the influence of rarefaction on the shape and extension of the shock wave, Figs. 3.1(a) to (c) and Figs. 3.2(a) to (c) show, respectively, the 2-D maps of the translational temperature and of a local Knudsen number (as per Kn_V) for the tests at $Kn_{\infty h}=3.5\times10^{-3}$, 0.35 and 35. Increasing $Kn_{\infty h}$, the shock wave zone extends up to involving the whole computing dominion and to becoming fuzzy. The shock wave is a rarefied and a non-equilibrium flow field region (Fig. 3.2(a) to (c)); this can be explained by fact that DS2V implements the Variable Hard Sphere model (VHS) [10]. According to this model, the diameter of a molecule and therefore the collision cross section decreases with temperature. This produces an increase of the mean free path and therefore a decrease of the intermolecular collision frequency, finally a decrease of the capability of restoring equilibrium.

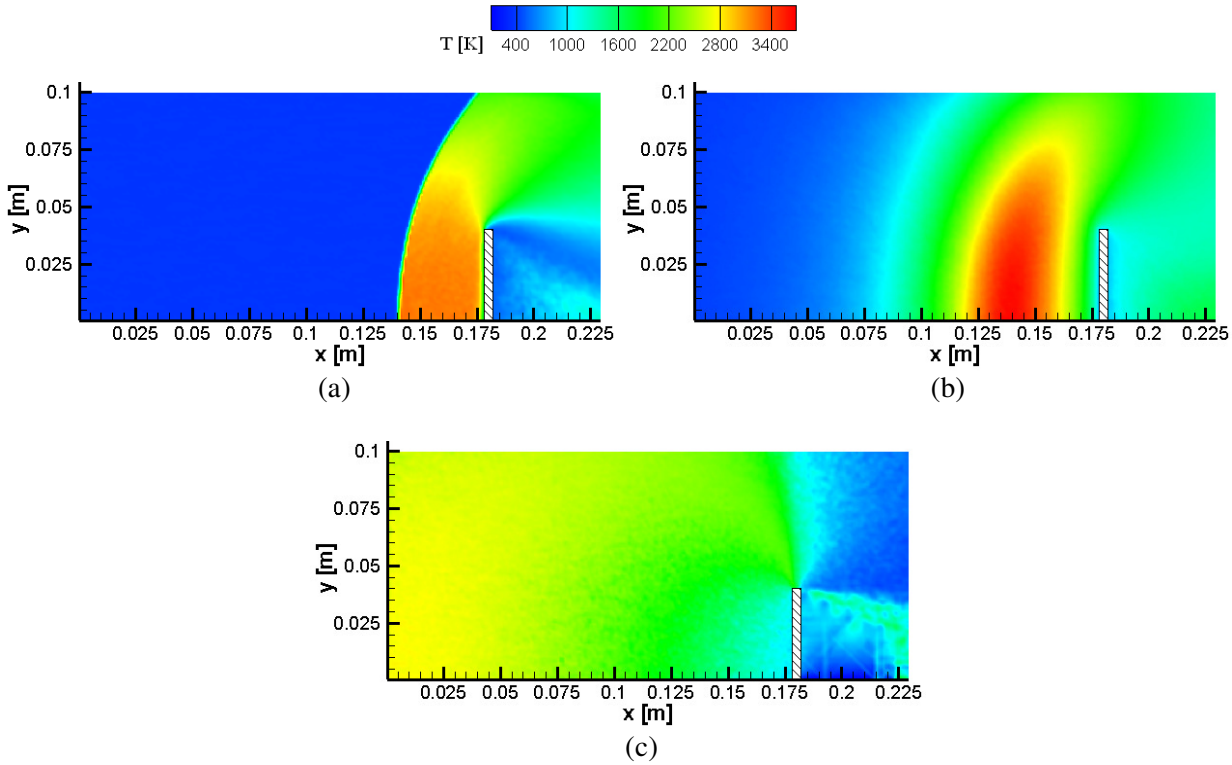

Figure 3.1 2-D maps of the translational temperature (T): $Kn_{\infty h}=3.5\times10^{-3}$ (a), $Kn_{\infty h}=0.35$ (b), $Kn_{\infty h}=35$ (c)

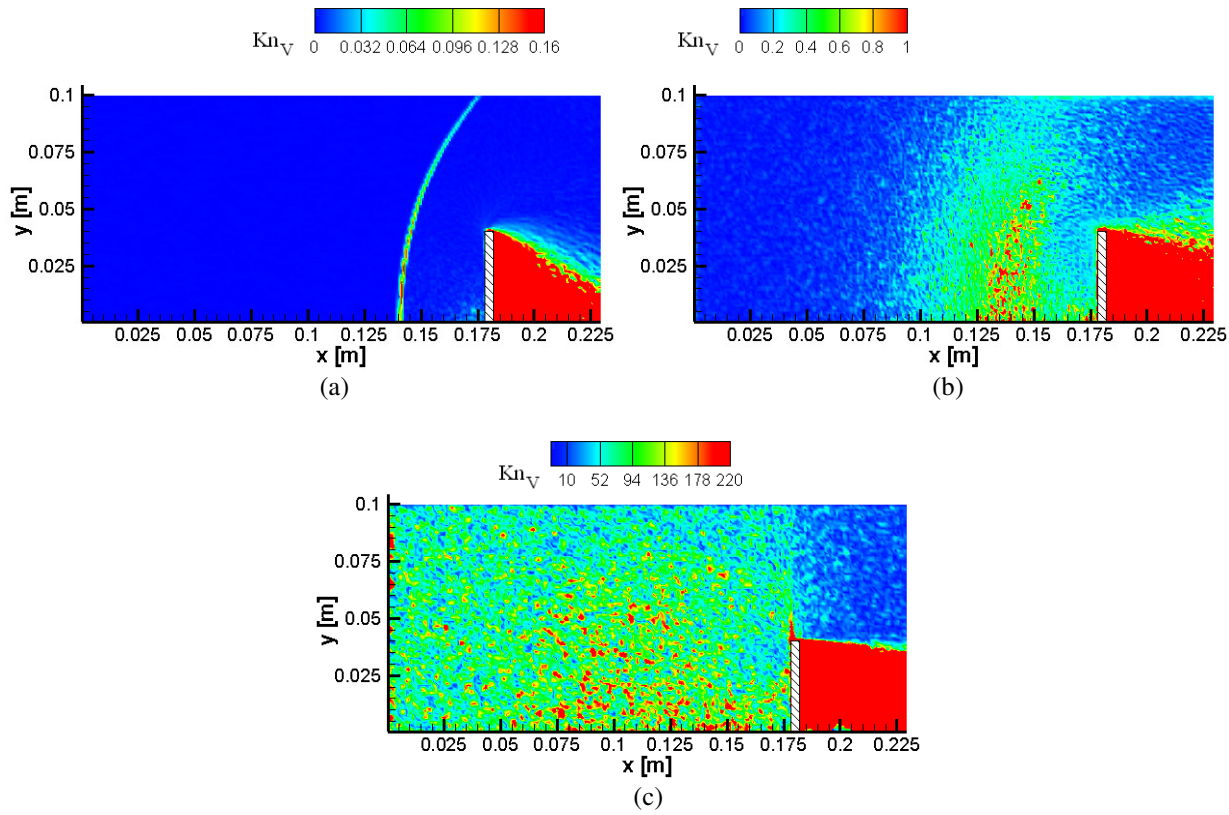

Figure 3.2 2-D maps of the local Knudsen number (Kn_V): $Kn_{\infty h}=3.5\times10^{-3}$ (a), $Kn_{\infty h}=0.35$ (b), $Kn_{\infty h}=35$ (c)

To show the incidence of rarefaction on the terms forming the Crocco theorem, Fig. 3.3 shows the profiles of the modules of the three terms. Also the terms of the Crocco theorem have been made non dimensional by the same reference quantity used for δ. The average of the terms of the Crocco theorem are computed as the arithmetic average on the flow field. The terms of the Crocco theorem increase with rarefaction. This is due to the increment of the gradients of any macroscopic thermodynamic quantities with rarefaction [1, 31].

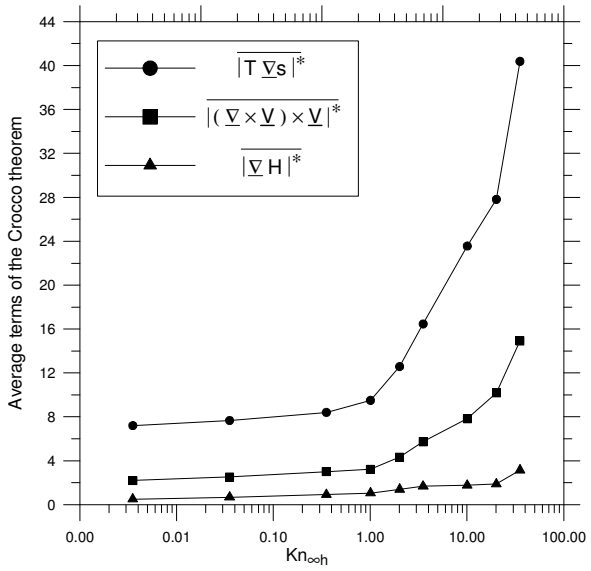

Figure 3.3 Profiles of the modules of the terms of the Crocco theorem averaged on the whole flow field, as a function of the Knudsen number

The 2-D maps of non-dimensional δ (δ*), reported in Fig. 3.4(a) to (c), verify that this parameter is a valid tool for the identification of the non-equilibrium zones. In fact, according to the maps of T and Kn_V, for:

(a) $Kn_{\infty h}=3.5\times10^{-3}$ (Fig. 3.4(a)), the highest values of δ* or the non-equilibrium zone, practically coincides with that of the core of the shock wave and with that of the highest values of Kn_V. All these zones are located at 0.14 m along the stagnation line,

(b) $Kn_{\infty h}=0.35$ (Fig. 3.4(b)), the highest values of δ* are located in the same regions both of the shock wave core and of the highest values of Kn_V. These regions are located roughly between 0.125 and 0.15 m along the stagnation line,

(c) $Kn_{\infty h}=35$ (Fig. 3.4(c)), the region of the highest values of δ* spread practically in the whole computing region, like the maps of temperature and Kn_V.

In addition, as the Crocco theorem is based on the assumption of non diffusive flow field, δ* verifies to be able to take into account non-equilibrium effects linked to the transport phenomena. In fact, δ* is able to identify a non equilibrium region at the top of the slab where, the effect of viscosity amplifies the non uniformity of velocity. This is in agreement with what reported by Smolderen [31]; the non uniformity of any macroscopic quantities (velocity, density, temperature and pressure), is indicative of non-equilibrium. Also the non-equilibrium region at the top of the slab extends with rarefaction just like the non equilibrium region in the shock wave. The maps of δ* show that the intensity of non-equilibrium region, or the maximum value of δ* keeps practically constant (about 100) with rarefaction. This can be explained by the consideration that the intensity of the shock wave (depending only on the free stream parameters as velocity, temperature and gas composition) is the same.

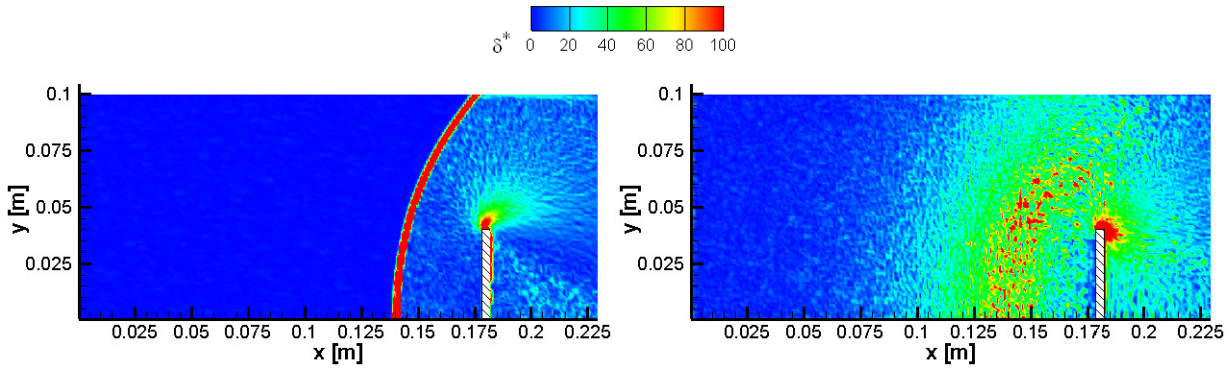

(a) (b)

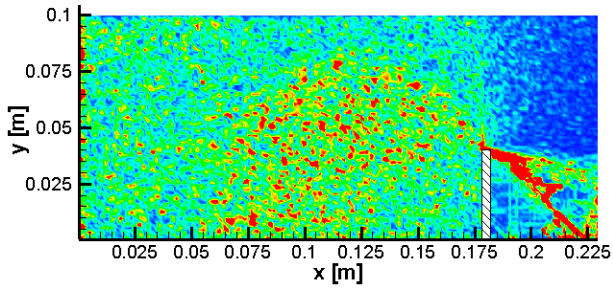

(c)

Figure 3.4 2-D maps of δ*: $Kn_{\infty h}=3.5\times10^{-3}$ (a), $Kn_{\infty h}=0.35$ (b), $Kn_{\infty h}=35$ (c)

Information from δ* is in agreement with the maps of the ϑ-parameters (ϑ_r, ϑ_v, ϑ_{xy} and ϑ_{xz}) for the extreme cases of $Kn_{\infty h}=3.5\times10^{-3}$ and $Kn_{\infty h}=35$. For the intermediate cases (as per the one with $Kn_{\infty h}=0.35$), the ϑ-parameters identify the region of maximum thermo-dynamic non-equilibrium and anisotropy previous to the position indicated by the maps of T, Kn_V and δ*. Figures 3.4(a) to (d) show, for example, the 2-D maps of the ϑ-parameters. The maximum values of these parameters, along the stagnation line, are located between: 0.090 m and 0.125 m for ϑ_r, 0.125 m and 0.135 m for ϑ_v, 0.075 m and 0.125 m for ϑ_{xy} and for ϑ_{xz}. Also ϑ_v and ϑ_{xy} indicate the presence of the non-equilibrium region at the top of the slab but δ* identifies this region in more clear way. This can be verified by the comparison of Fig. 3.4(b) with Figs. 3.5(b),(c).

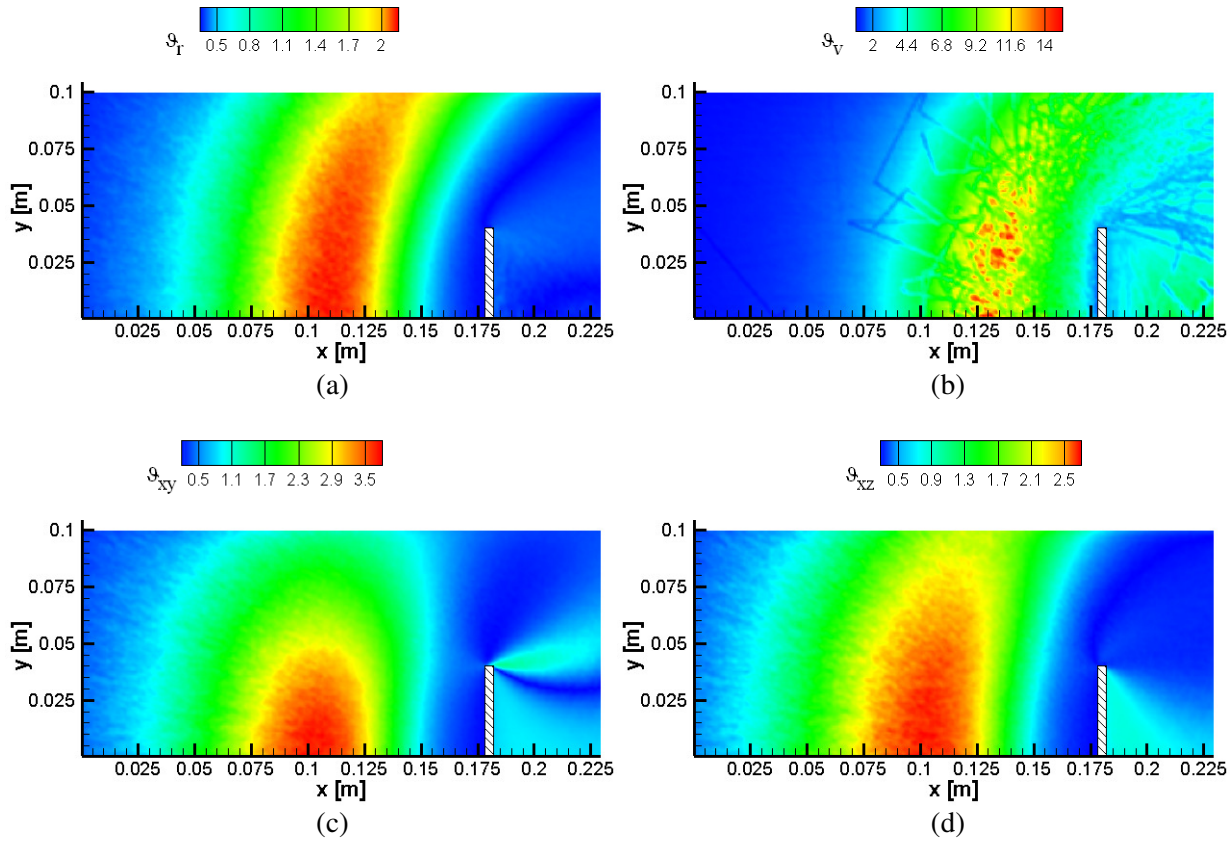

(a) (b)

(c) (d)

Figure 3.5 2-D maps of parameters ϑ_r (a), ϑ_v (b), ϑ_{xy} (c) and ϑ_{xz} (d) for the intermediate case $Kn_{\infty h}=0.35$)

To compare the incidence of rarefaction on δ^* and on the ϑ-parameters, Fig. 3.6 shows the trends of the arithmetic average on the flow field of these quantities ($\overline{\delta^*}$, $\overline{\vartheta_r}$, $\overline{\vartheta_v}$, $\overline{\vartheta_{xy}}$ and $\overline{\vartheta_{xz}}$) as a function of Knuden number. Even though, as already said, the computation of δ relies on the components of these terms of the Crocco theorem, the increase of $\overline{\delta^*}$ with rarefaction can be explained by the trends of the modules of the Crocco theorem terms (Fig. 3.3). More specifically, for $Kn_{\infty h} \leq 1$ the imbalance among the terms is small and then $\overline{\delta^*}$ grows slowly, for values of $Kn_{\infty h}>1$ where the imbalance is greater $\overline{\delta^*}$ grows fast.

The choice of the reference quantity, making δ non-dimensional, turned out to be proper. In fact, as shown in Fig. 3.6, the values $\overline{\delta^*}$ are comparable with the $\overline{\vartheta}$-parameters. The suitability of the reference quantity, making δ non-dimensional, gave rise to the condition that $\overline{\delta^*}$ is always higher than the $\overline{\vartheta}$-parameters; this is agreement with what expected because δ^* includes all non-equilibrium phenomena.

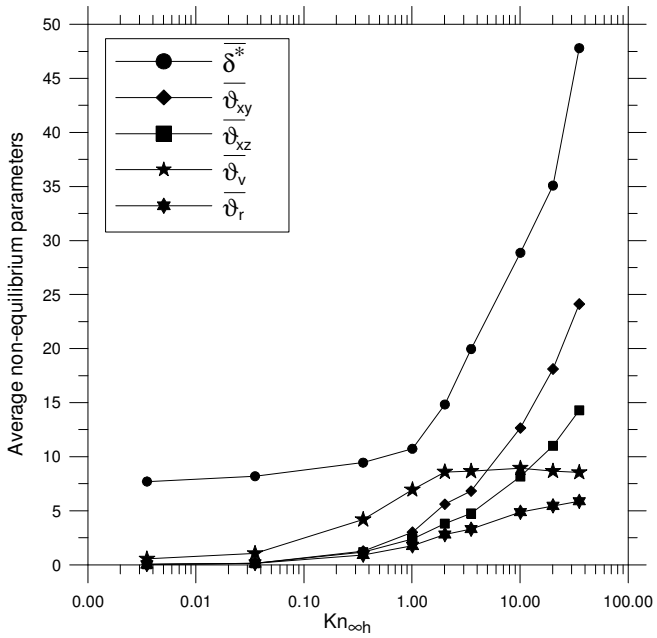

Figure 3.6 Profiles of the non-equilibrium parameters averaged on the whole flow field, as a function of the Knudsen number

It has to be pointed out that, at low Knudsen numbers ($Kn_{\infty h}<1$), $\overline{\delta^*}$ is less sensitive than the $\overline{\vartheta}$-parameters. In fact in the range of $Kn_{\infty h}$ between 3.5×10^{-3} and 1.0, $\overline{\delta^*}$ ranges from 7.7 to 10.7 with a percentage increment of 28%, while $\overline{\vartheta_r}$, $\overline{\vartheta_v}$, $\overline{\vartheta_{xy}}$ and $\overline{\vartheta_{xz}}$ range from 0.029 to 1.746, 0.552 to 6.937, 0.039 to 3.01 and 0.040 to 2.378, respectively; the related percentage increments are of the order of 10^3%. This different behavior between $\overline{\delta^*}$ with respect to the $\overline{\vartheta}$-parameters is due to the fact that, as already said. the highest values of δ^* keeps practically constant, while the ones

of the $\overline{\vartheta}$-parameters tend to decrease with decreasing rarefaction. This can be verified by the comparison of the 2-D maps of ϑ-parameters for $Kn_{\infty h}=3.5\times10^{-3}$ (Fig. 3.7(a) to (d)) with those for $Kn_{\infty h}=0.35$ (Fig. 3.5(a) to (d))

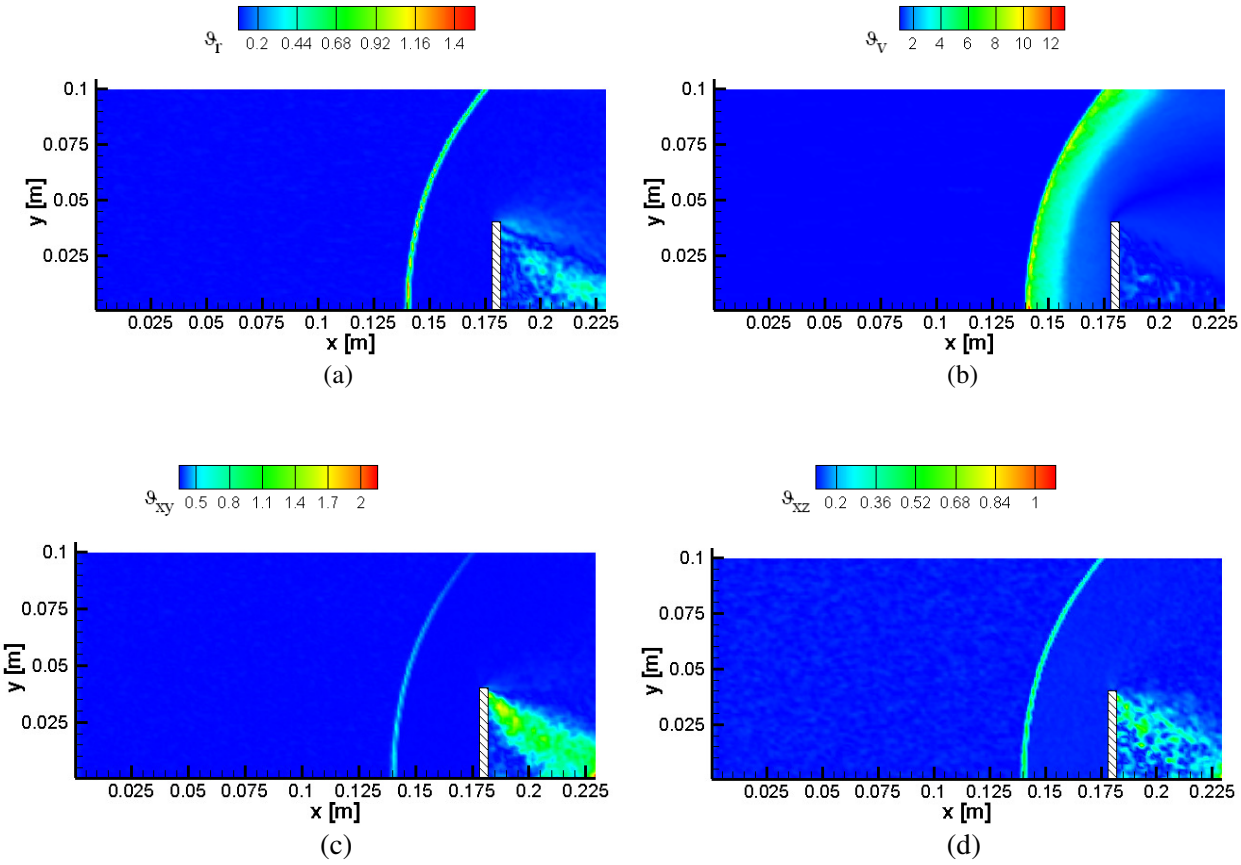

Figure 3.7 2-D maps of parameters ϑ_r (a), ϑ_v (b), ϑ_{xy} (c) and ϑ_{xz} (d): $Kn_{\infty h}=3.5\times10^{-3}$

In the interval of $Kn_{\infty h}$ from 1 to 35, $\overline{\delta^*}$ increases with a rate similar to the ones of $\overline{\vartheta}_{xy}$ and $\overline{\vartheta}_{xz}$. In fact $\overline{\delta^*}$ ranges from 10.7 to 47.8 (the percentage increment is of 347%), $\overline{\vartheta}_{xy}$ and $\overline{\vartheta}_{xz}$ range from 3.01 to 24.13 and 2.38 to 14.28, with a percentage increment of 702% and 500%. The constant trend of $\overline{\vartheta}_v$ for $Kn_{\infty h}>2$ is misleading. It is due to the decrease of the number of collisions that is no longer able to activate molecular vibration and therefore to increase T_v; the number of collisions per second decreases from 4.2×10^{13} for $Kn_{\infty h}=3.5\times10^{-3}$ to 1.9×10^{11} for $Kn_{\infty h}=2$. This can be checked by Fig. 3.8 where the profiles of T_v, along the stagnation line, are shown for some tests. The profile of T_v for test with $Kn_{\infty h}=2$ is close to the one for test with $Kn_{\infty h}=35$.

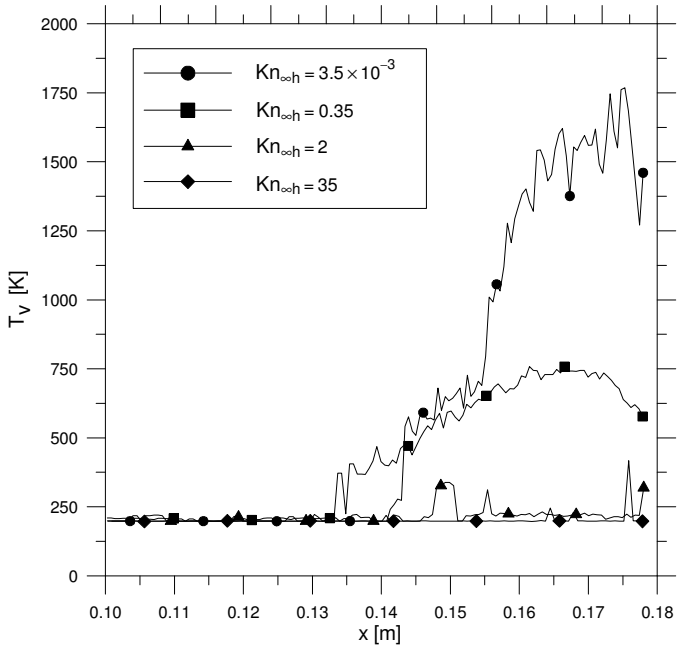

Figure 3.8 Profiles of vibrational temperature along the slab stagnation line

Finally we can say that the proposed parameter verified to be more effective than the parameters based on temperature differences; it seems to be able to identify in a more precise and effective way the non-equilibrium regions both in and outside the shock wave. This encourages going on by the comparison of the results with the ones from the entropy generation rate.

3.8 Conclusions

A new parameter evaluating the non-equilibrium of a flow field has been proposed. The results have been compared with the ones based on the difference of the components of translational temperature, for the quantification of anisotropy, and the ones based on the difference of the translational, rotational and vibrational temperatures, for the quantification of thermodynamic non-equilibrium.

The new parameter considers globally non-equilibrium phenomena like the entropy generation rate that identifies the non equilibrium regions whereas a positive entropy generation exists. The new parameter relies on the formulation of the Crocco theorem, that is valid under the assumption of equilibrium. The basic idea is that a mismatch, between the terms forming the Crocco theorem equation, increases with non-equilibrium.

Computing tests have been carried out in the whole transitional regime by a DSMC code simulating a 2-D flow field past a slab normal to the free stream velocity. The proposed

parameter verified to be more effective than the parameters based on temperature differences; it seems to be able to identify in a more precise and effective way the non-equilibrium regions both in and outside the shock wave. This encourages going on by the comparison of the results with the ones from the entropy generation rate.

CHAPTER IV

Influence of chemical models on computation of thermo-fluid-dynamic parameters

4.1 Introduction

It is well known that the flow field evolution and the momentum/energy exchange of a gas with a body surface is influenced by chemical reactions (dissociation, recombination, exchange) that, besides changing the gas composition, affect the evolution of a flow field from an energetic point of view and produce also surface catalytic effects. For this reason a proper modeling of chemical reactions and therefore a correct evaluation of gas composition is important in all aerodynamic regimes.

In rarefied flows a number of chemical models, relying on different assumptions, has been developed for application to the Direct Simulation Monte Carlo method. Zuppardi and Romano [32] proposed a DSMC implementation of the microscopic model by Fan and Shen [33] and compared it with the phenomenological model by Bird [1, 34]. The main difference between these models is in handling molecular vibration. In fact, the Bird model considers the vibrational energy only as a contribution to the collision energy; therefore it does not consider any process of Vibrational Favored Dissociation (VFD). On the opposite, the Fan-Shen model considers a physical link between vibrational excitation and dissociation/exchange reactions. The VFD process is of great interest in DSMC applications. In fact, also the chemical model, implemented in the advanced SMILE code [14], takes account of vibrational favoring for dissociation and exchange reactions.

In order to compare the Bird and the Fan-Shen models, Zuppardi and Romano [32] wrote a "simple" DSMC code. The code was simple because it was able to compute just the occurrence of a reaction in the collision between two molecules, without considering some important aerodynamic features such as: i) recombination, ii) energy re-distribution between the internal degrees of freedom and the translational one, iii) interaction with the body surface. In order to overcome the limitations of the code and therefore to compare the models in a more realistic simulation, Zuppardi [35] compared the two models in the flow field on a flat plate. Zuppardi provided an evaluation of the influence of a different chemical composition, due to the different

chemical models, on local parameters such as heat flux, pressure and shear stress distributions along the surface, as well as on parameters in the flow field such as Mach number, vibrational and rotational temperatures. The DSMC code was generated by merging two codes by Bird [1]: DSMC2 and DSMC0D and then by implementing the chemical models. The merge was necessary for combining the aerodynamic features of DSMC2, providing the simulation of the flow field of a partially inert gas (i.e. non dissociating, non vibrating, but rotating) on a flat plate, with those of DSMC0D, providing the simulation of a reactive, macroscopically stationary gas.

In the present study the Bird and the Fan-Shen models have been implemented in a DSMC, axis-symmetric code, simulating the hypersonic, rarefied flow field on a bluff (or flat-ended) circular cylinder and also in other fluid-dynamic conditions, characterized by a normal, strong shock wave. As the aim of the present work is the comparison of different DSMC chemical models and the evaluation of their capability to be used in hypersonic, rarefied flow fields, also the "Classic" [1] and the "New" [34] quantic models by Bird have been considered. The "Classic" quantic model was already implemented in the DSMC0D code, while the "New" quantic model has been not yet implemented in the Bird's codes. Once again, following the same approach like that used in [35], the present DSMC code has been generated by merging two codes by Bird [1]: DSMC2A and the above mentioned DSMC0D. DSMC2A, like DSMC2, simulates a partially inert gas in an axis-symmetric flow field, past a bluff cylinder. Furthermore in this study, the DSMC implementation of the Fan-Shen model has been refined with respect to the former version [35].

The simulation of the flow field past a bluff cylinder was proper because this body offers the opportunity to make a comparison between calculated Stanton number at the stagnation point and experimental data, available in literature [36]. The thermo-fluid-dynamic parameters in the shock layer are compared with those computed by DS2V [12] which is a "sophisticated" [11] and advanced DSMC code. When a code is not-sophisticated, it is defined as "basic". DSMC2/2A and DSMC0D are basic codes.

Input data both to the present code and to DS2V reproduced the above mentioned experimental test conditions such as Mach number and Reynolds number downstream the normal shock wave; test gas was Nitrogen. The results showed that the Fan-Shen model is very close to the Bird model. This is very meaningful from a theoretical point of view because these models, as said before and shown later, rely on completely different approaches. Furthermore, the results from both models are closer to the experimental data and to the DS2V results than those from quantic models. Even though the present DSMC implementation of the Fan-Shen model requires further

verifications by sophisticated DSMC codes and then by simulation of other tests conditions, however this model seems to be a viable alternative to the widely accepted Bird model.

4.2 Bird Model

Starting from the kinetic theory of gases and from the phenomenological rate coefficient, Bird [1] proposed a model evaluating the occurrence of a chemical reaction (dissociation or exchange) in a collision between two molecules A and B. The rate coefficient (K), defined by an equation of the Arrhenius form, reads:

$$K(T) = \Lambda T^{\eta} \exp\left(-\frac{E_a}{kT}\right) \tag{4.1}$$

where: T is temperature, Λ and η are constants, k is the Boltzmann constant and E_a is the reaction activation energy.

Necessary condition for the occurrence of a chemical reaction is that the collision energy (E_c), is greater than E_a. E_c is the sum of the relative translational energy (E_t) and the internal energies: rotational (E_r), vibrational (E_v) of both colliding molecules. If $E_c > E_a$, a parameter, called "steric factor", is computed. This parameter, defined as the ratio of the "reaction cross-section" (σ_R) to the total cross-section (σ_T), reads:

$$\frac{\sigma_R}{\sigma_T} = \frac{\sqrt{\pi}\varepsilon\Lambda T_{ref}^{\eta}}{2\sigma_{ref}\left(kT_{ref}\right)^{\eta-1+\omega_{AB}}} \frac{\Gamma\left(\bar{\zeta} - \omega_{AB} + \frac{5}{2}\right)}{\Gamma\left(\bar{\zeta} + \eta + \frac{3}{2}\right)} \sqrt{\frac{m_r}{2kT_{ref}}} \frac{\left(E_c - E_a\right)^{\eta+\bar{\zeta}+1/2}}{E_c^{\bar{\zeta}-\omega_{AB}+3/2}} \tag{4.2}$$

where: ε is the symmetry factor, equal to 1 if the colliding molecules are the same, equal to 2 if the colliding molecules are different, σ_{ref} is the cross-section evaluated at the reference temperature T_{ref}, ω_{AB} is the exponent of the viscosity power law, appropriate to the combination of the species A and B, $\bar{\zeta}$ is the average number of internal degrees of freedom ($\bar{\zeta} = (\zeta_A + \zeta_B)/2$), Γ is the gamma function and m_r is the reduced mass between mass of A (m_A) and mass of B (m_B): $m_r = m_A m_B/(m_A+m_B)$. In [32, 35], as well as in the present computations, $\omega_{AB} = (\omega_A+\omega_B)/2$. It as to be point out that the values of the constant Λ and η are the ones provided by the Gupta model [16].

As the steric factor represents the probability of occurrence of a chemical reaction in a collision, it is subjected to an acceptance/rejection procedure [1]. A reaction occurs if the steric factor is greater than a random number (R): $\sigma_R/\sigma_T>R$.

4.3 Fan-Shen Model

Fan and Shen [29, 33] proposed a microscopic criterion for the occurrence of a chemical reaction (dissociation or exchange) as the result of the breakdown of the chemical bond of a diatomic molecule B, colliding with another molecule A (Fig. 4.1).

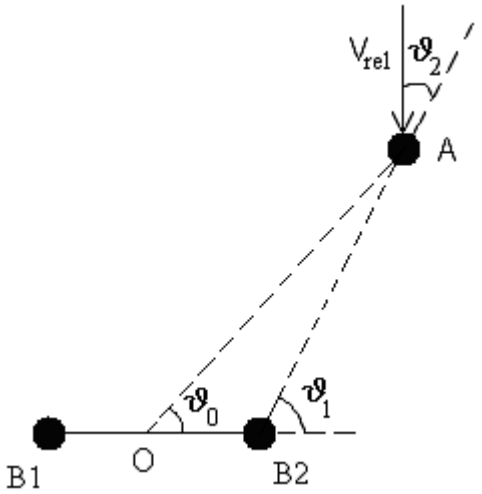

Figure 4.1 Schematic of collision between a diatomic molecule B and a molecule A

Molecule A can be either mono-atomic or diatomic. A dissociation or exchange reaction occurs, in a collision, when the sum of the impact stress (F_i) and the stress acting on B, originated from vibration (F_{vB}), is greater than the dynamic breaking strength of the chemical bond of B (F_{bB}):

$$F_i + F_{vB} \geq F_{bB} \tag{4.3}$$

Considering the expressions of F_i, F_{vB} and F_{bB} [33], Eq. 4.3 reads:

$$\sqrt{1/2\, m_B}\, V_{rel} \cos(\vartheta_1 + \vartheta_2) + \sqrt{E_{vB}}\, \cos(\varphi) \geq a_d \sqrt{E_{dB}} \tag{4.4}$$

where: V_{rel} is the relative velocity between A and B, E_{vB} is the vibration energy of B, φ is the phase angle of vibration, a_d is the dynamic factor and E_{dB} is the dissociation energy of B. Factor

a_d considers the dynamic influence in breaking a chemical bond. As reported by Fan and Shen [33], if the duration of a collision is long then $a_d \rightarrow 1$, if it is short then:

$$a_d \rightarrow \frac{m_{B1} + m_{B2}}{\sqrt{m_{B1} m_{B2}}} \left(\frac{E_{dB} - E^i_{vB} - E^i_{rB}}{E_{dB}} \right)^{1/2} \tag{4.5}$$

where: m_{B1} and m_{B2} are the masses of the atoms of B, E^i_{vB} and E^i_{rB} are the initial (or pre-collision) vibrational and rotational energies of B, respectively. From Eq. 4.4, the microscopic criterion for the reaction occurrence is:

$$V_{rel} \geq \frac{a_d \sqrt{E_{dB}} - \sqrt{E_{vB}} \cos(\varphi)}{\sqrt{1/2\, m_B} \cos(\vartheta_1 + \vartheta_2)} \tag{4.6}$$

Using the sphere-cylinder molecular model should be proper in a DSMC implementation but, according to Bird [1], it is too complicate. In fact, this model requires additional variables such as spatial orientation and angular velocity of molecule B. Therefore, in the former [32, 35] and in the present DSMC implementation, the sphere model is used; molecule B is considered still mono-atomic and located in O (Fig. 4.1). Moreover, being angle ϑ_1 not longer defined, it has been put at zero. In the former version angle ϑ_2 was put also at zero, while in the present version this angle has been computed as the angle between the relative velocity and the line linking A and B. To make possible the DSMC implementation of this model, a parameter Z, was introduced in [32, 35]. It was defined as the ratio of the right to the left term in Eq. 4.6 and reads:

$$Z = \frac{a_d \sqrt{E_{dB}} - \sqrt{E_{vB}} \cos(\varphi)}{V_{rel} \sqrt{1/2\, m_B} \cos(\vartheta_2)} \tag{4.7}$$

As the DSMC implementation of Eq. 4.7 relies on an uniform distribution of the phase angle φ, in [32, 35] and also in the present computations, $\cos(\varphi)$ has been assumed, for each collision, as a random number: $\cos(\varphi)=R$. Necessary condition for the occurrence of a reaction is $Z<1$. Like for the Bird steric factor, the occurrence of a chemical reaction is subjected to an acceptance/rejection procedure; a reaction occurs if Z is greater than a random number: $Z>R$.

Even though the Bird and the Fan-Shen models are basically different, however as reported by the authors [33, 34], both are able to reproduce the conventional rate equations, evaluated experimentally in continuum. Besides what already said about the physical link between vibrational excitation and dissociation/exchange reactions, other differences with the Bird model are:

1. the vibrational and rotational energies are related only to B,
2. the characteristics of A, that can be either monatomic or diatomic, are ignored,
3. the rotational energy contributes to reaction only in the calculation of a_d,
4. the model works in terms of the dissociation energy even for an exchange reaction.

4.4 Classic and New Quantic Models

The quantic models consider dissociation closely linked to the vibrational excitation. Two molecules, involved in a collision, are accepted to or rejected from the relaxation process by the acceptance/rejection procedure. This procedure relies on the relaxation vibrational number Z_v; relaxation is accepted if $1/Z_v>R$. Usually Z_v is a function of the collisional temperature T_c, that is based on the relative translational energy of the colliding molecules A and B and vibrational energy stored in the processed molecule (B) [1]: $E_v=ik\Theta_v$, where "i" is the vibrational quantum level, and Θ_v is the characteristic vibrational temperature.

The "Classic" quantic model [1] evaluates Z_v by:

$$Z_v = \left(C_1 / T_c^{\omega_{AB}}\right)\exp\left(C_2 T_c^{-1/3}\right) \tag{4.8}$$

where C_1 and C_2 are constants (for Nitrogen C_1=9.1, C_2=220).

As C_1 and C_2 have no physical meaning, Bird [11] developed a new and more realistic model. In fact, in this "New" model C_1 and C_2 take into account dissociation and vibration; C_1 and C_2 are computed by Eq. 4.8 using, in lieu of T_c, the characteristic dissociation (Θ_d) and vibrational temperatures (for Nitrogen Θ_v=3395 K, Θ_d=113200 K). Eq. 4.8 finally reads:

$$Z_v = \left(\frac{\Theta_d}{T_c}\right)^{\omega_{AB}}\left[Z_{ref}\left(\frac{\Theta_d}{\Theta_v}\right)^{-\omega_{AB}}\right]^{\left[\left(\frac{\Theta_d}{T_c}\right)^{1/3}-1\right]\Big/\left[\left(\frac{\Theta_d}{\Theta_v}\right)^{1/3}-1\right]} \tag{4.9}$$

where Z_{ref} is computed by Eq. 4.8 using a reference temperature T_{ref} instead of T_c. As suggested by Bird [11], a proper value of T_{ref} is Θ_v.

For both models, if vibrational relaxation occurs (i.e. $1/Z_v>R$), the collision energy E_c is computed as the sum of relative translational energy, vibrational and rotational energies only of the processed molecule. If E_c is greater than the dissociation energy, the vibrational quantic level

"i*", related to E_c, is computed: $i^*=\lfloor E_c/(k\Theta_v)\rfloor$, where symbol $\lfloor . \rfloor$ denotes truncation. A vibrational level "i" is then selected randomly between zero and "i*". The vibrational level "i" is finally processed by the quantic Larsen-Borgnakke probability function distribution:

$$\frac{P}{P_{max}} = \left(1 - \frac{ik\Theta_v}{E_c}\right)^{3/2-\omega_{AB}} \tag{4.10}$$

Vibrational level "i" is accepted if $P/P_{max}>R$, if not so a new value of "i" is again selected randomly between zero and "i*". If the accepted level "i" is greater than the maximum level of vibration "i_{max}", dissociation occurs (for Nitrogen $i_{max}=46$).

4.5 DSMC Codes

The present DSMC code, labeled DS2A0D, was born, as said before, by merging two codes by Bird [1]: DSMC2A and DSMC0D.

1. DSMC2A simulates a 2D axis-symmetric flow field and, more specifically, a flow field past a bluff cylinder. Gas is partially inert. Due to the axis-symmetry of the flow field, only half computing dominion is considered. The x-axis and y-axis lie along the cylinder axis and radius, respectively. Diameter (D) of the cylinder is 0.02 m. The computational domain is a rectangle (0.04×0.03 m^2) in the meridian plane. The domain is divided into (80×60) rectangular cells, each one into (2×2) sub-cells. The cells and sub-cells are uniformly spaced along x and y. This code employs the procedure linked to radial weighting factor; the reference radius is 0.004 m.
2. DSMC0D simulates dissociation and recombination in a uniform gas that is in a macroscopically stationary state. Gas initially consists of molecular Nitrogen and the dissociation reactions are:

$$N_2 + N_2 \rightarrow 2N + N_2 \tag{4.11}$$

$$N_2 + N \rightarrow 2N + N \tag{4.12}$$

These reactions are handled according to the "Classic" quantic model. The code implements:

(a) the procedure by Bird [1] for a termolecular recombination. This relies on a steric factor similar to that of dissociation (Eq. 4.2),

(b) the Larsen-Borgnakke procedure for the redistribution of rotational and translational energies,

(c) a quantum version of Larsen-Borgnakke procedure for the redistribution of vibrational and translational energies.

In DS2A0D, Eqs. 4.11 and 4.12 can be handled also by the Bird, Fan-Shen and "New" quantic models. These models, as well as the condition of inert gas (i.e. not dissociating, not vibrating, not rotating), can be chosen optionally. The geometrical parameters of the original code DSMC2A were kept also in this code.

The DS2V (Ver.4.5) code by Bird [12] simulates 2-D/axis-symmetric flow fields. It implements the Bird model. DS2V is an advanced code. In fact, DS2V, besides being sophisticated, allows the user to evaluate the quality of a run in terms of the adequacy of the number of simulated molecules, by the visualization of the ratio of the molecule mean collision separation (mcs) in the cell on the local mean free path (λ). According to Bird the adequacy of the run is achieved when the maximum value of mcs/λ in the computational dominion is less than 0.2 [12].

4.6 Test Conditions

Input data to DS2A0D and to DS2V reproduced test conditions of the measured heat flux by Coleman et al. [36], such as the free stream Mach number (M_∞) and the Reynolds number behind a normal shock wave, based on the cylinder diameter ($Re_{2,D}$): M_∞ was between 7.5-14 and $Re_{2,D}$ was between 930-0.33. In all tests, wall temperature was about 300 K. Free stream temperature (T_∞) was evaluated by the relation between wall and gas temperatures, provided by Coleman: $T_\infty=T_w/3.15=95$ K. Thus the flow velocity ranged between 1492-2786 m/s.

Preliminary DS2A0D runs verified that, at these experimental conditions, the flow enthalpy, ranging from 1.2 to 4.0 MJ/kg, was too low for the activation of Nitrogen dissociation. In order to evaluate the effects of dissociation, free stream velocity, for all runs, was increased to 7000 m/s and, in order to get a Mach number as close as possible to the experimental one, a free stream temperature of 465 K was used, therefore $M_\infty\cong16$. The flow enthalpy increased to 25 MJ/kg. Using this velocity and this temperature, density was computed to reproduce the experimental Re_{2D}. Wall temperature was evaluated by the above reported relation between T_w and T_∞; $T_w=1464$ K.

4.7 Analysis of the results

Analysis relies on 6 tests. Table 4.1 reports some input data and operative parameters:

(a) free stream number density of molecular Nitrogen ($n_{N2\infty}$); all runs started with $n_{N\infty}=0$ or atomic Nitrogen molar fraction $\alpha_N=0$,
(b) number of real molecules represented by each simulated molecule (FNUM),
(c) simulation time (t_s), iv) free stream Knudsen number ($Kn_{\infty D}=\lambda_\infty/D$),
(d) Reynolds number down-stream a normal shock wave (Re_{2D}).

Table 4.1 Input and operative parameters

Test no.	$n_{N_{2\infty}}$ [m^{-3}]	FNUM	t_s [s]	Kn_D	$Re_{2,D}$
1	3.3285×10^{21}	3×10^{12}	8.6×10^{-3}	2.5×10^{-2}	80
2	6.6571×10^{21}	6×10^{12}	7.7×10^{-3}	1.3×10^{-2}	160
3	1.0818×10^{22}	9.7×10^{12}	6.4×10^{-3}	7.8×10^{-3}	260
4	1.6643×10^{22}	1.5×10^{13}	4.8×10^{-3}	5.1×10^{-3}	400
5	2.0615×10^{22}	2.5×10^{13}	4.4×10^{-3}	4.1×10^{-3}	496
6	2.9125×10^{22}	2.6×10^{13}	3.1×10^{-3}	2.9×10^{-3}	700

For all tests $Kn_{\infty D}$ verifies that the flow field is rarefied and more specifically in continuum low density regime. In fact, according to Moss [28], a general definition of the transitional regime is: $10^{-3}<Kn_\infty<50$. The simulation time indicates that a steady state condition is achieved. In fact, simulation time was about three order of magnitude longer than the time necessary to cross the computation domain at free stream velocity (5.7×10^{-6} s). The number of megabytes (1200), input to DS2V, provided a sufficient accuracy of the runs. In fact, the average values of mcs/λ, in the flow field, range in the interval 0.012, 0.13 from test no.1 to test no.6.

Figures 4.2(a) and (b) show the profiles of α_N along the axis (a) and along the flat surface of the cylinder (b) at an intermediate test condition (test no.4).

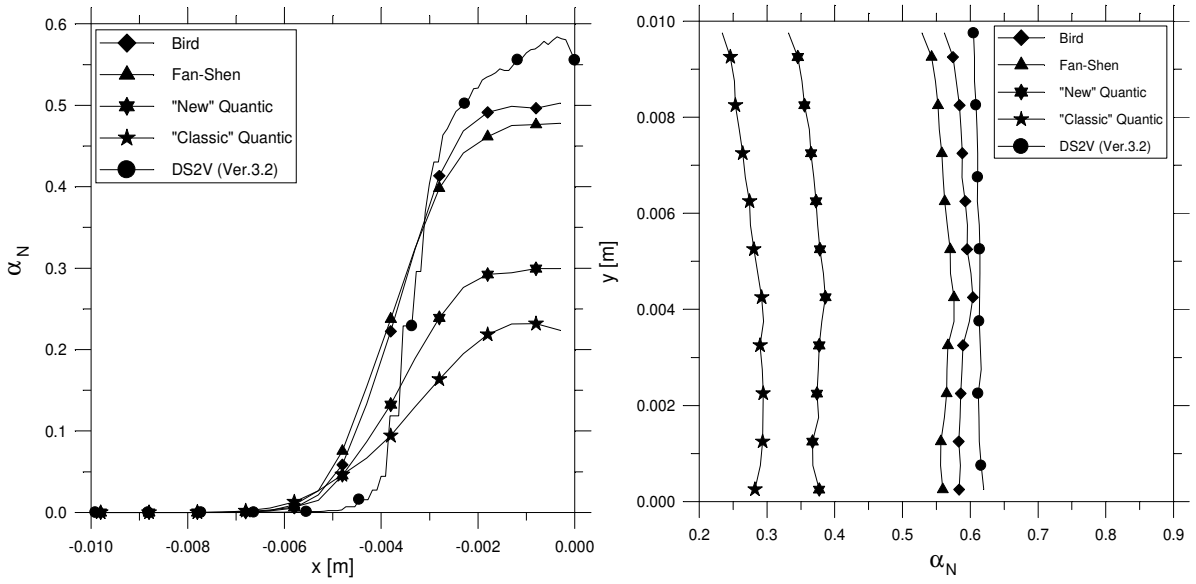

Figure 4.2 Profiles of the atomic Nitrogen molar fraction along the axis (a) and along the cylinder flat surface (b): test no.4

In order to quantify the influence of the chemical models, Table 4.2 reports the average values of α_N in the flow field along the cylinder axis for all tests and for all chemical models. The atomic molar fraction can be considered as a measure of the reactivity level; the higher is α_N the more reactive is the model.

Table 4.2 Average values of α_N in the flow field along the cylinder axis

Test no.	DS2V	Bird	Fan-Shen	"New" Quantic	"Classic" Quantic
1	8.29×10^{-2}	4.81×10^{-2}	5.90×10^{-2}	2.03×10^{-2}	1.73×10^{-2}
2	8.85×10^{-2}	7.53×10^{-2}	7.55×10^{-2}	3.62×10^{-2}	2.54×10^{-2}
3	8.71×10^{-2}	8.34×10^{-2}	8.44×10^{-2}	4.62×10^{-2}	3.23×10^{-2}
4	8.96×10^{-2}	9.09×10^{-2}	8.90×10^{-2}	5.45×10^{-2}	4.12×10^{-2}
5	8.88×10^{-2}	9.06×10^{-2}	9.06×10^{-2}	5.64×10^{-2}	4.48×10^{-2}
6	8.68×10^{-2}	9.11×10^{-2}	9.11×10^{-2}	6.25×10^{-2}	5.17×10^{-2}

In order to provide a synoptic view of α_N in the whole flow field, Figures 4.3(a) to (d) show the 2-D maps of α_N, computed by the four chemical models.

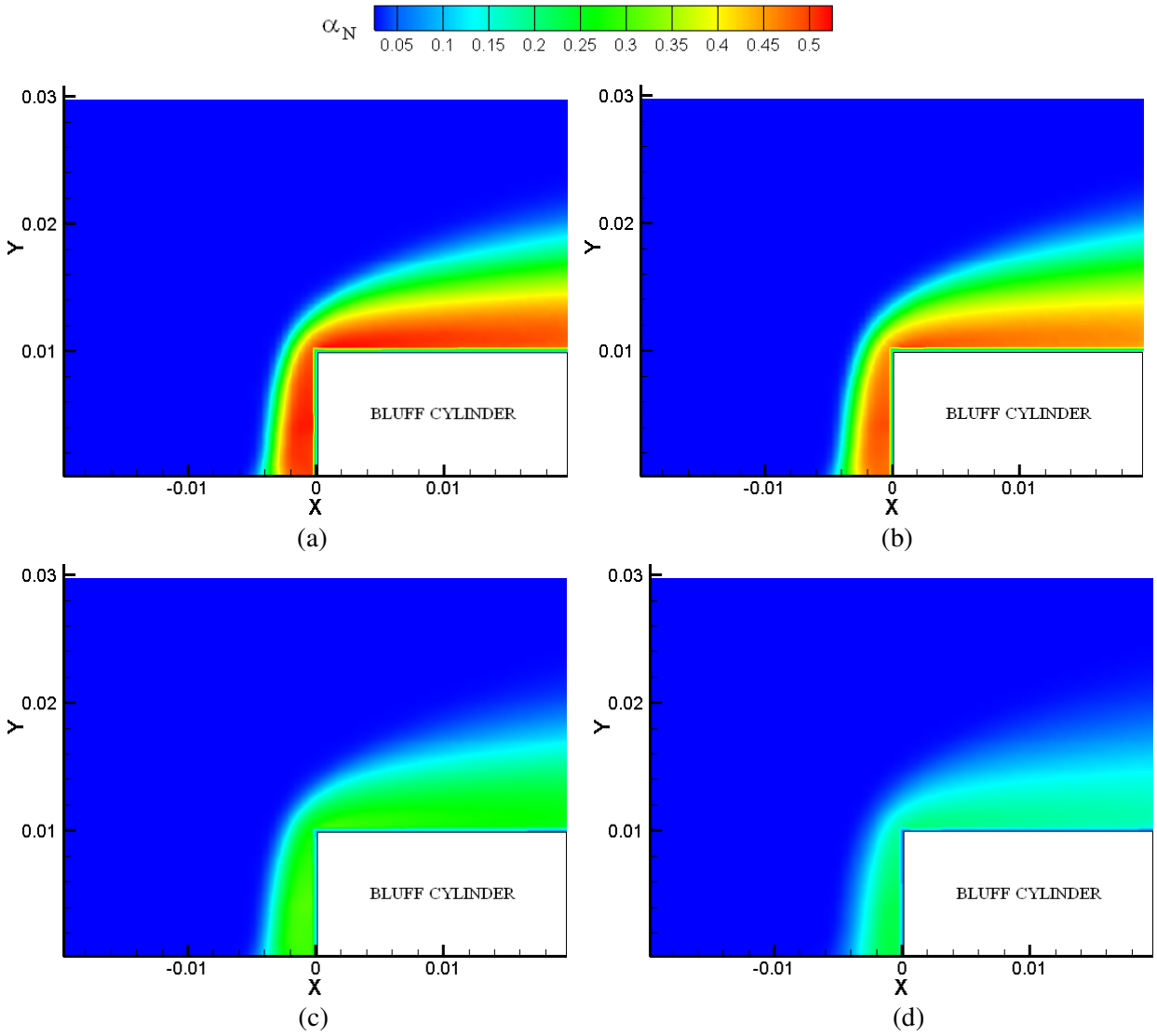

Figure 4.3 Maps of the atomic Nitrogen molar fraction (α_N) in the flow field by the Bird (a), Fan-Shen (b), "New" quantic (c) and "Classic" quantic models (d): test no.4

Figure 4.4 reports the profiles of the Stanton number at the cylinder stagnation point (St(0)) as functions of $Re_{2,D}$. For providing further reference data, both in this plot and in the following ones, parameters calculated on the assumption of inert gas are reported. Both experimental data and computed results show the same trend. The comparison of the results verifies what is well known, i.e. the higher is the reactivity level the lower is the Stanton number. This agrees with the consideration that, due to endothermicity of dissociation, the higher is the reactivity level the lower is the energy that can be exchanged with the body surface. As expected, the match of the results by DS2V with the experimental data is excellent. Therefore, the DS2V results will be taken into account for the comparison of other parameters for which experimental comparison data are not available.

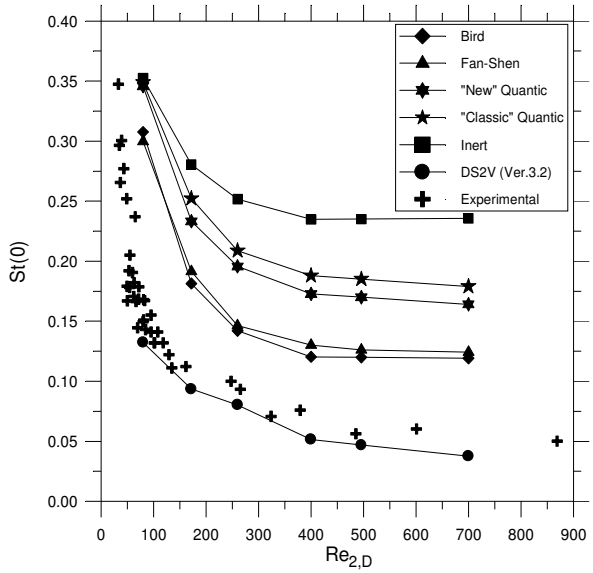

Figure 4.4 Profiles of the Stanton number at the stagnation point of a bluff cylinder as a function of the Reynolds number downstream a normal shock wave

Figures 4.5(a) to (d) show the influence of different gas composition on translational temperature (a), rotational temperature (b), velocity (c) and Mach number (d) in the flow field, along the cylinder axis. The translational temperature, computed on the assumption of inert gas, is the highest, as well as, due to endotermicity of dissociation, the translational and rotational temperatures are higher for the less reactive models. Velocity is higher by the energy conservation. The profiles of Mach number change accordingly.

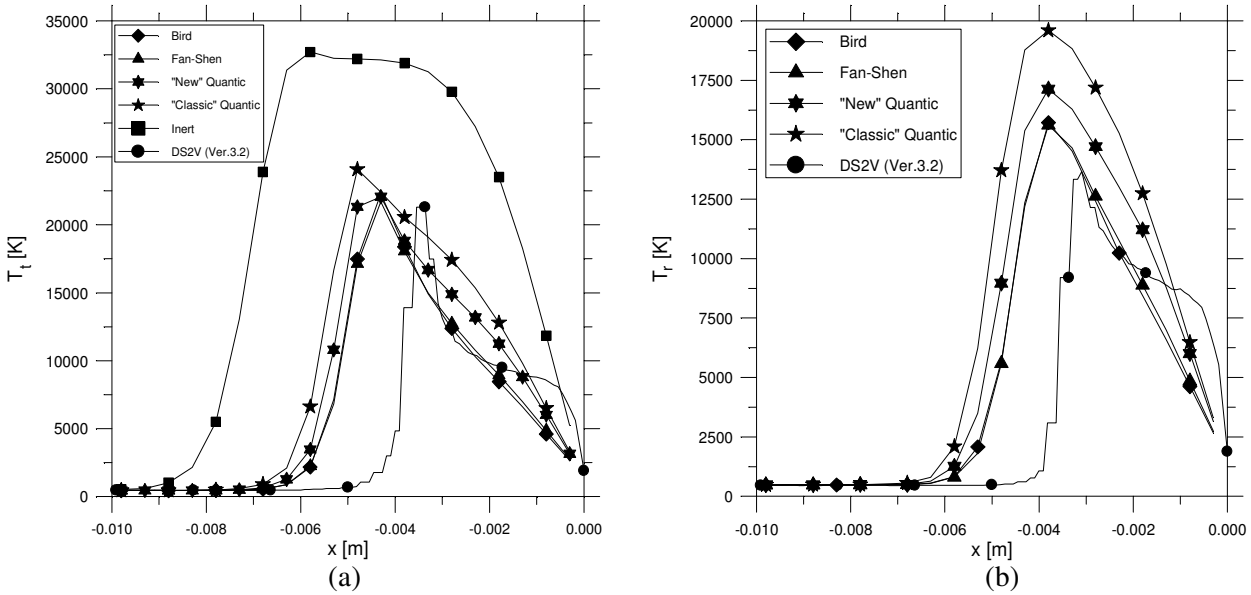

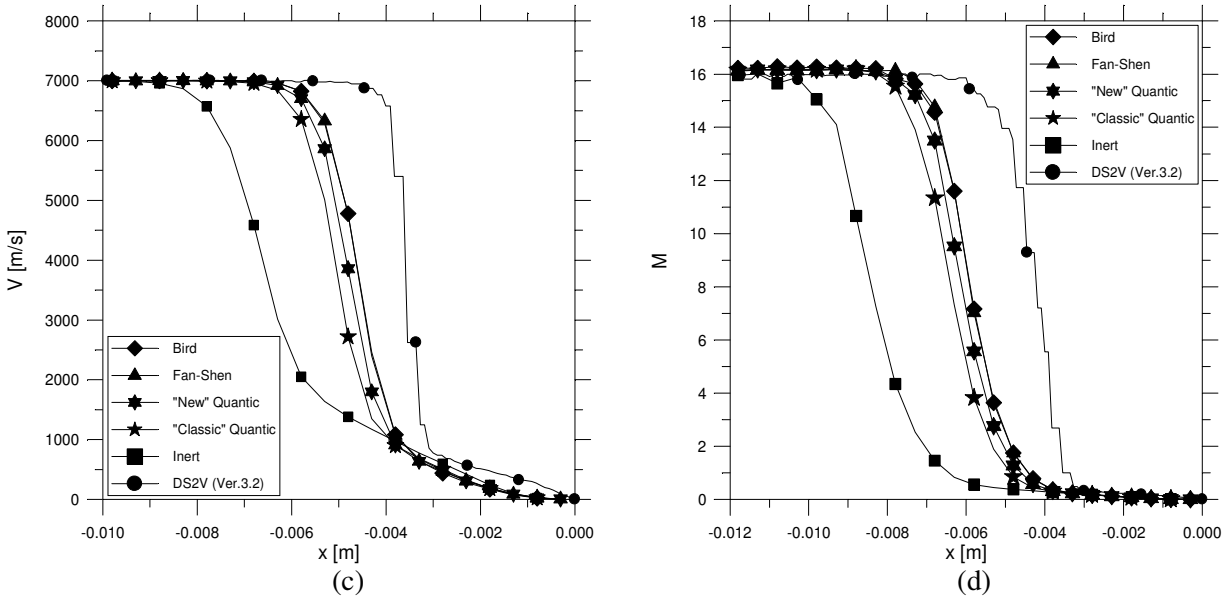

Figure 4.5 Profiles of translational temperature (a), rotational temperature (b), velocity (c) and Mach number (d) along the axis by the Bird, Fan-Shen, "New" quantic, "Classic" quantic models and DS2V code: test no.4

Furthermore, in order to quantify the influence of the chemical models on fluid-dynamic parameters, Table 4.3 reports the average values of translational temperature in the flow field along the cylinder axis for all tests and for all chemical models.

Table 4.3 Average values of translational temperature in the flow field along the cylinder axis

Test no.	DS2V	Bird	Fan-Shen	"New" Quantic	"Classic" Quantic	Inert
1	4834	6543	6275	6742	7031	11478
2	3444	4823	4726	5287	5824	10501
3	2724	3985	3935	4534	5129	9997
4	2563	3514	3533	4105	4739	9893
5	2270	3456	3481	4127	4710	9837
6	2054	3119	3094	3753	4330	9700

Figures 4.6(a) and (b) report the pressure coefficient and Stanton number distributions along the flat surface of the cylinder. These profiles agree with what above said about velocity, i.e. the higher is the reactivity level, the higher is velocity, therefore the higher is the exchanged momentum with the surface and, finally, the higher is pressure. As well as, the Stanton number profile is lower for the more reactive model.

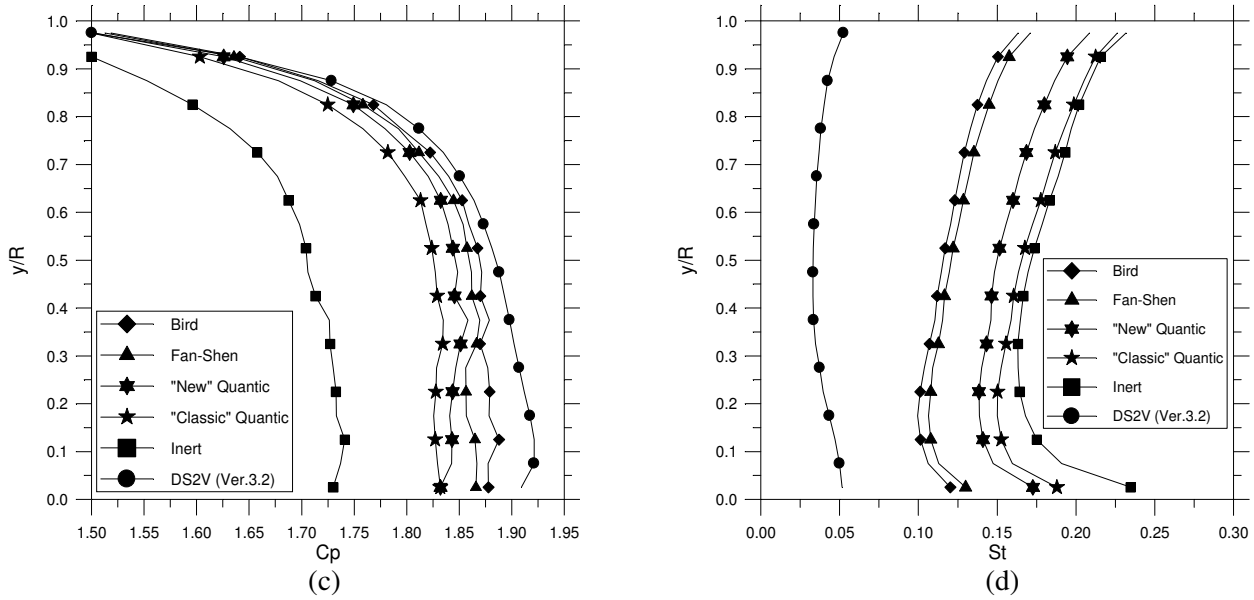

Figure 4.6 Profiles of pressure coefficient (a) and Stanton number (b) along the cylinder flat surface by the Bird, Fan-Shen, "New" quantic, "Classic" quantic models and DS2V code: test no.4

Also in this case, in order to quantify the influence of the chemical models on the surface parameters, Table 4.4 reports the average values of pressure coefficient along the cylinder flat surface. The results both in the flow field and along the surface agree qualitatively with what could be expected from a physical point of view, verifying the validity of computations.

Table 4.4 Average values of pressure coefficient along the cylinder flat surface

Test no.	DS2V	Bird	Fan-Shen	"New" Quantic	"Classic" Quantic	Inert
1	1.8359	1.7838	1.7863	1.7830	1.7768	1.7021
2	1.8292	1.7853	1.7852	1.7774	1.7660	1.6722
3	1.8534	1.8016	1.7959	1.7872	1.7688	1.6677
4	1.8418	1.8224	1.8118	1.7974	1.7798	1.6657
5	1.8399	1.8186	1.8161	1.8026	1.7825	1.6664
6	1.8411	1.8294	1.8287	1.8138	1.7923	1.6726

The Bird and the Fan-Shen models are closer both to the experimental data and to DS2V results. The distance could be due to the different DSMC approaches; DS2A0D is basic, DS2V is sophisticated. The consideration that DS2V implements the Bird model supports this analysis.
It is meaningful that, even though based on different approaches, the results from the Fan-Shen model are very close to those from the Bird model. Thus the Fan-Shen model could be considered as a possible alternative to the Bird model.

The "New" quantic model does not show any substantial differences with the "Classic" model. Furthermore even though these models were born for molecular application and therefore for a DSMC approach, their results appear to be not very reliable. A definitive evaluation of the DSMC implementation of the Fan Shen model and of the quantic model should be deepened by using these models in advanced DSMC codes, e.g. the above-mentioned SMILE [14] or DS3V [13] or DAC [15], making possible the simulation of more complex flow fields and therefore the comparison with the other experimental data.

4.8 Conclusions

Four different chemical models (Bird, Fan-Shen, "Classic" and "New" quantic) have been implemented in a DSMC code, simulating the hypersonic, rarefied flow field past a bluff cylinder. This code was born by merging two basic codes by Bird. The results have been compared both with experimental data and with those from the advanced DS2V code. The aim of the work was the evaluation of the capability of the Fan-Shen model and quantic models to be implemented in a DSMC code.

The results of all models were qualitatively correct. Those from the Bird and Fan-Shen models were close both to the experimental data and to the DS2V results. The mismatch in the values is probably due to the fact that the used code is basic. On the opposite, the quantic models look to be not suitable.

It is meaningful that, even though based on different approaches, the results from the Fan-Shen model are very close to those from the Bird model. Thus the Fan-Shen model could be considered as a possible alternative to the Bird model

As a further check of validity of the DSMC implementation of the Fan-Shen model, it should be implemented in a more advanced DSMC code, making possible the simulation of the flow field around more complex geometries and fluid-dynamic conditions such as those met by spacecraft during the re-entry.

CHAPTER V

Expert and Orion Capsules

5.1 Expert – The ESA experimental re-entry test-bed

EXPERT (European eXPErimental Reentry Test-bed) capsule [37], funded by ESA and supported by a number of European research centers, was designed to provide the scientific community with quality data on critical aero-thermodynamic phenomena encountered during hypersonic flights as well as to provide industry with system experience of re-entry vehicle manufacturing and development of hypersonic instrumentation. To this regard it important to point out that the aerodynamic know-how needed to design and safely fly future hypersonic space vehicles is obtained via computational predictions, ground-based experimental simulations, and flight extrapolation methodologies. The best approach to improve confidence in aerothermodynamics design tools is to validate them against flight experiments. Flight experimentation is however limited due to high costs and risks associated to fly reentry hypersonic vehicles.

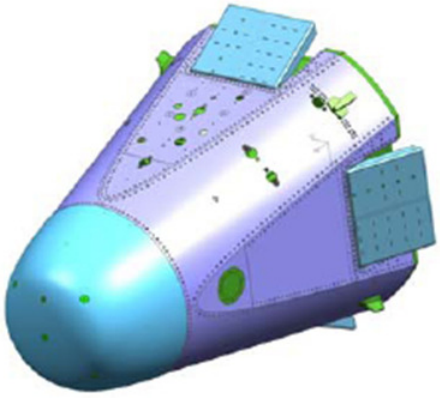

Figure 5.1 Rendering of Expert

EXPERT is equipped with 14 experiments provided by several scientific institutions all around Europe. The experiments address the following phenomena: TPS material characterization, surface catalysis and oxidation, plasma spectroscopy, laminar to turbulent transition, flow separation and reattachment, shock-boundary layer interactions, base flow characteristic and aerodynamic characterization of flap control surfaces.

EXPERT will fly a suborbital ballistic trajectory from the Pacific Ocean to a landing site located on the peninsula of Kamchatka as shown in Fig. 5.2 The re-entry speed selected at the entry gate of 100km altitude is 5 km/s. Such a speed is

Figure 5.2 EXPERT mission trajectory

compatible with the conditions that can be achieved on ground facilities, allowing therefore extensive comparison between flight and ground data which is of primary importance to validate mathematical models and establish ground to flight extrapolations. EXPERT will be launched with a Russian Volna rocket (Fig. 5.3) from a submarine. EXPERT is housed inside the second stage tank, in an upside down configuration with the nose pointing downwards, as shown in Fig. 5.4. After the re-entry phase EXPERT will be slowed down using a 3 stage parachute system that will allow a landing speed lower than 10 m/s. The recovery will be done via helicopters that will track the signal of an on board beacon. EXPERT is equipped with a crash proof and redundant memory unit in order to protect the data in case of a crash landing.

Figure 5.3 VOLNA Launcher

EXPERT is injected with a velocity of 5km/s at the entry gate which is defined at an altitude of 100 km. In this initial condition the flight path angle is -5.5 deg. The EXPERT flight will last 140 seconds before the drogue parachute is opened. The flight duration is about ten minutes.

The shape of EXPERT and the location of the center of gravity has been chosen such that EXPERT is inherently stable in order to maintain a small angle of attack (AoA), lower than 3 deg, in the experimental phase and up till the last portion of flight, till M=2. At such Mach number it is expected that the AoA will tend to diverge. The onset of the instability drives the triggering of the drogue parachute.

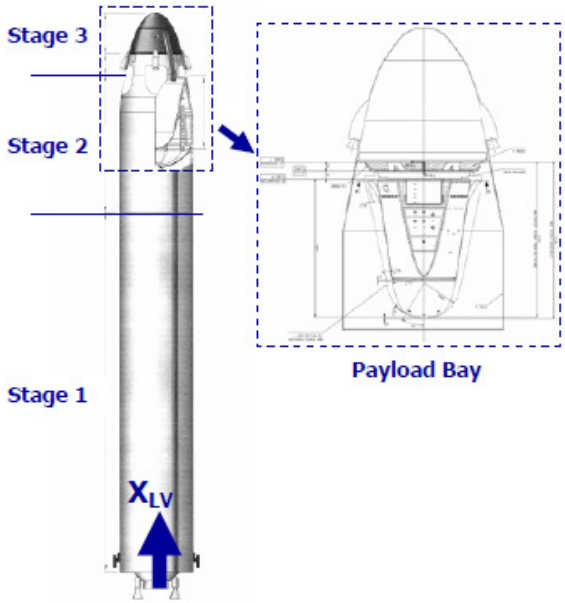

Figure 5.4 EXPERT inside VOLNA second stage tank

Extensive aerothermodynamics simulations [38, 39] and wind tunnel tests have been performed to characterize the aerodynamic behavior in the different regions of the atmosphere: free molecular flow, transitional and continuum regime. This led to the compilation of an aerothermodynamics database [40]. Bridging functions have been used to compute the coefficients in the transitional region. Such values have been also cross checked with DSMC simulations [41].

The flight data acquired by EXPERT will be distributed to several European Institutes and Industries and is expected to bring a much needed boost to the European competence in the strategic field of re-entry. The launch windows is scheduled for April-October 2011.

5.2 Orion – NASA's Constellation Program

In August 22 2006, NASA announced that its new crew exploration vehicle will be named Orion [42].

Orion is the vehicle NASA's Constellation Program is developing to carry a new generation of explorers back to the moon and later to Mars. Orion will succeed the space shuttle as NASA's primary vehicle for human space exploration.

Figure 5.5 Artist's rendering of Orion crew exploration vehicle and service module geometry

Orion is named for one of the brightest, most familiar and easily identifiable constellations. "Many of its stars have been used for navigation and guided explorers to new worlds for centuries," said Orion Project Manager Skip Hatfield (NASA). In June 2006, NASA announced the launch vehicles under development by the Constellation Program have been named Ares, a synonym for Mars. The booster that will launch Orion will be called Ares I, and a larger heavy-lift launch vehicle will be known as Ares V.

Orion will be capable of transporting cargo and up to six crew members to and from the International Space Station. It can carry four crewmembers for lunar missions. Later, it can support crew transfers for Mars missions.

Orion borrows its shape from space capsules of the past, but takes advantage of the latest technology in computers, electronics, life support, propulsion and heat protection systems. The capsule's conical shape is the safest and most reliable for re-entering the Earth's atmosphere, especially at the velocities required for a direct return from the moon.

Orion will be 5.03 meter in diameter and have a mass of about 25 tons. Inside, it will have more than 2.5 times the volume of an Apollo capsule. The spacecraft will return humans to the moon to stay for long periods as a testing ground for the longer journey to Mars.

Building upon the best of Apollo and shuttle-era design, the Orion spacecraft includes both crew and service modules, a spacecraft adaptor, and a revolutionary launch abort system that will significantly increase crew safety (Fig. 5.6).

The launch abort system, positioned on a tower atop the crew module, activates within milliseconds to propel the crew module to safety in the event of an emergency during launch or climb to orbit. The system also protects the crew module from dangerous atmospheric loads and heating,

The crew module is the transportation capsule that provides a safe habitat for the crew, provides storage for consumables and research instruments, and serves as the docking port for crew transfers. The crew module is the only part of Orion that returns to Earth after each mission.

The service module supports the crew module from launch through separation prior to reentry. It provides in-space propulsion capability for orbital transfer, attitude control, and high altitude ascent aborts. When mated with the crew module, it provides the water, oxygen and nitrogen needed for a habitable environment, generates and stores electrical power while on-orbit, and maintains the temperature of the vehicle's systems and components. This module can also transport unpressurized cargo and scientific payloads.

The spacecraft adapter connects the Orion Crew Exploration Vehicle to the launch vehicle and protects service module components.

(a) (b)

Figure 5.6 The test vehicle is readied for launch at White Sands Missile Range's Launch Complex 32E (a). Orion crew exploration vehicle in its parts (b)

The Ares launch vehicles, named for the Greek god associated with Mars, will carry into orbit astronauts, cargo, and the components needed to go to the moon and later to Mars. Ares I will be an in-line, two-stage rocket topped by the Orion crew vehicle and its launch abort system. Ares V cargo launch vehicle will be the heavy lifter of America's next-generation space fleet. The two-stage, vertically stacked launch system will have a 206-ton capacity to low-Earth orbit and 78-ton capacity to lunar orbit.

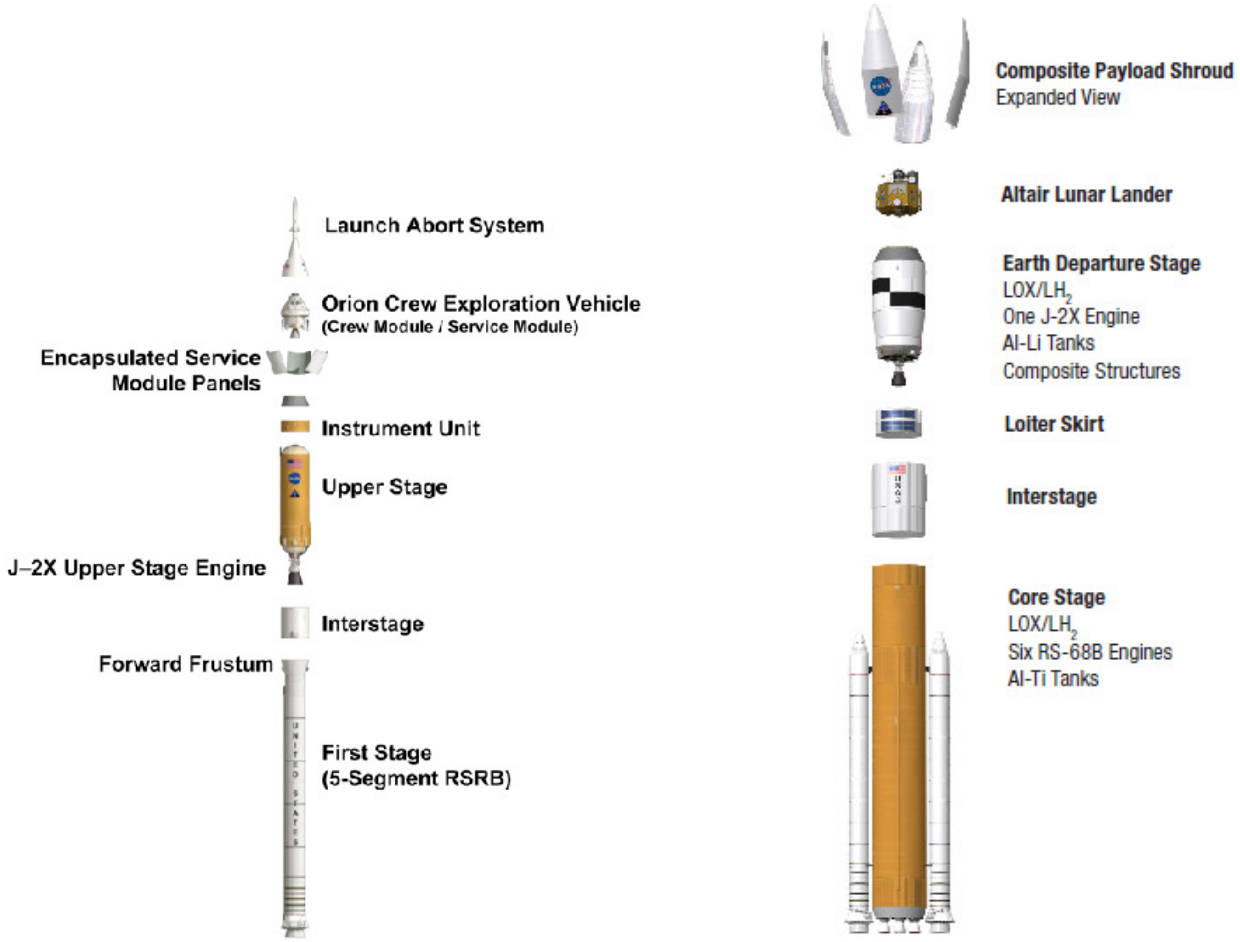

(a) (b)

Figure 5.7 Concept image of Ares I (a) and Ares V (b) elements

The Altair lunar lander (Fig. 5.8) will be capable of landing four astronauts on the moon, providing life support and a base for week-long initial surface exploration missions, and returning the crew to the Orion spacecraft that will bring them home to Earth. Altair will launch aboard an Ares V rocket into low-Earth orbit, where it will rendezvous with the Orion crew vehicle.

The first crewed flight of Orion is planned for no later than 2015, with crew transportation to the space station following within the same decade and the first lunar mission scheduled for the 2020 timeframe.

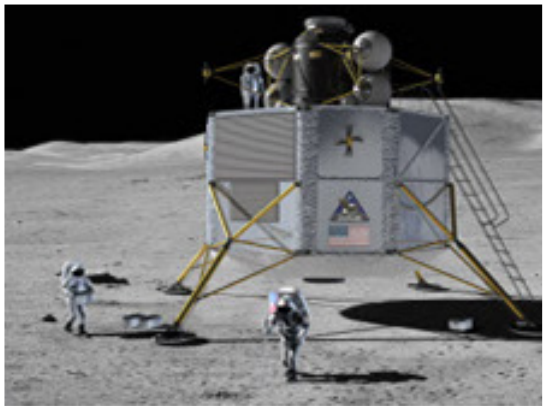

Figure 5.8 Three crew members work in the area of their lunar lander on the lunar surface in this NASA artist's rendering.

5.3 Re-entry Trajectory of EXPERT and ORION

Figure 5.9 shows the re-entry trajectories of both capsules. In the altitude interval here considered for EXPERT (65.2-104.5 km), velocity does not change strongly, ranging from 5038 to 4992 m/s [37, 40], the Mach number ranges from 16.1 to 17.0 (the maximum value of 18.3 is met at h=88 km). The free stream Reynolds number ($Re_{D\infty}$) ranges from 7.3×10^{4} to 82 and the free stream Knudsen number ($Kn_{D\infty}$) ranges from 3.2×10^{-4} to 3.1×10^{-1}.

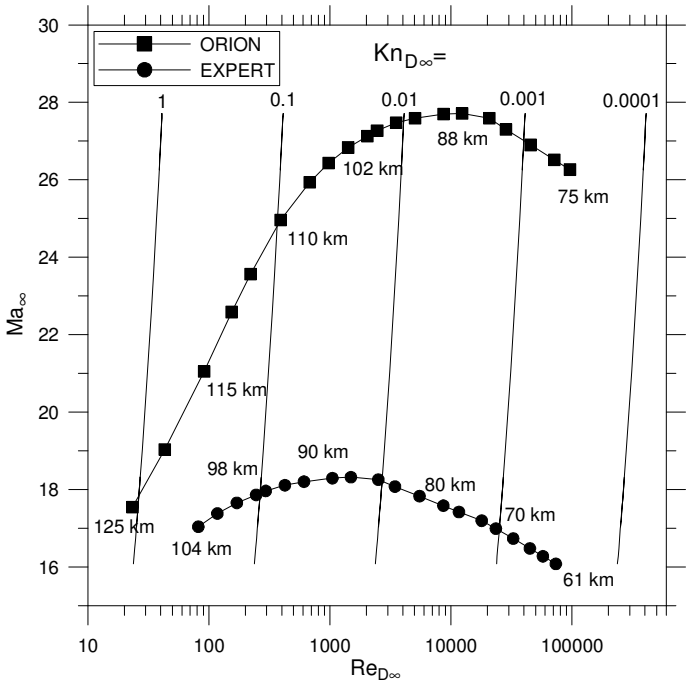

Figure 5.9 EXPERT and ORION re-entry trajectories

The present test conditions for ORION are related to the re-entry from ISS in the altitude interval 75.0-125.0 km. Velocity is 7600 m/s at all altitudes [43], the Mach number ranges from 17.5 to 26.3 (the maximum value of 27.7 is met at h=88 km). The related $Re_{D\infty}$ and $Kn_{D\infty}$ range from 9.62×10^4 to 23.3 and from 4.04×10^{-4} to 1.11, respectively.

According to Moss [28], a general definition of the transitional regime is: $10^{-3}<Kn_{L\infty}<50$. EXPERT is in transitional regime in the altitude interval 80.4-104.5 km, where $Kn_{D\infty}$ ranges from 4.8×10^{-3} to 33. At lower altitudes or in the interval 61.2-80.4 km, EXPERT is in continuum low density regime. In fact, $Kn_{D\infty}=3.2\times10^{-4}$ at h=61.2 km. ORION is in transitional regime in the altitude interval 83.0-125.0 km, where $Kn_{D\infty}$ ranges from 1.4×10^{-3} to 1.1. At lower altitudes or in the interval 75.0-83.0 km, ORION is in continuum low density regime. In fact, $Kn_{D\infty}=4.04\times10^{-4}$ at h=75.0 km.

CHAPTER VI

Aerodynamic Analysis of Expert

6.1 Introduction

A number of papers have been already written about EXPERT with different aims, from the evaluation of the aerodynamic behavior to the description of tests and experiments to be made during the re-entry (see [40] and related references). Preliminary computations of aero-thermo-dynamic data base at high altitudes were provided by approximate engineering methods or bridging formulae [44]. The aim of the present work is making an additional analysis and, hopefully, a better characterization of the aerodynamic data base in rarefied regime.

The present chapter is focused on the analysis of the aerodynamic behavior of the capsule in high altitude flight, between 80 and 105 km. The computations are performed using a DSMC approach by means of the "sophisticated" and advanced DS3V code [13]; at each altitude the range of angle of attack is 0-60 deg.. Furthermore, as the presence of four open flaps makes the flow field, at angle of attack, depending on the rolling angle φ, the effect of φ is evaluated by computations both at φ=0 and φ=45 deg.. The analysis will focus on global aerodynamic coefficients, on longitudinal stability and on fluctuation of the position of pressure center. As reported by Ivanov [44], the reference surface and the reference length, necessary for reducing the forces and the pitching moment to the related coefficients, are 1.1877 m^2 and 1.55 m, respectively

6.2 Test conditions

For the DS3V simulations, an unstructured surface grid (Figs. 6.1(a) and (b)) is used to define the body surface, where the number of surface triangles are 6384. Note that the numerical simulations take advantage of the problem symmetry in that the flow is computed about only half of the vehicle. The computational domain of DS3V was a parallelepiped: x=2.4 m, y=2.3 m, z=1.1 m (Fig. 6.2). For all 3-D runs, simulation time was longer than 25 times the time necessary to cross the computing region along the x direction at the free stream velocity ($\cong 5\times10^{-4}$ s). This

simulation time can be considered long enough for stabilizing all thermo-aerodynamic parameters. The number of simulated molecules was about 2.0×10^7. This number of molecules provided: for 3-D tests, at the most severe test condition of 80.4 km, an average value of mcs/λ of about 1.1, thus the results at this altitudes are not fully reliable.

All aerodynamic tests by DS3V were made in the range of angle of attack 0-60 deg. with a step of 5 deg.. The aerodynamic forces were evaluated on the assumption of non-reactive surface. Free stream thermodynamic parameters were provided by the U.S. Standard Atmosphere 1976.

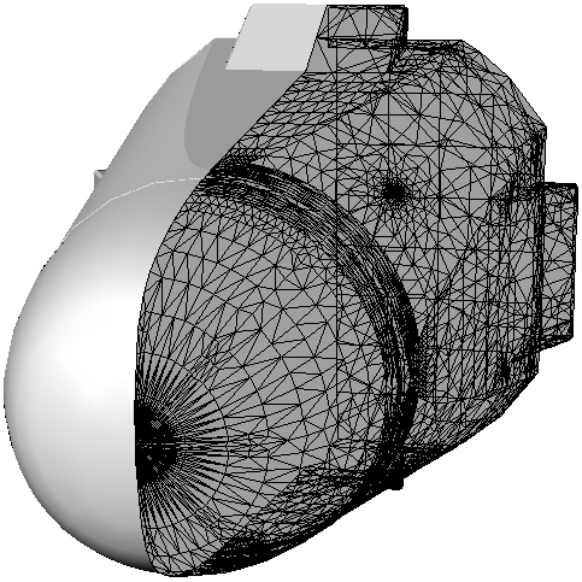

(a) Frontal view

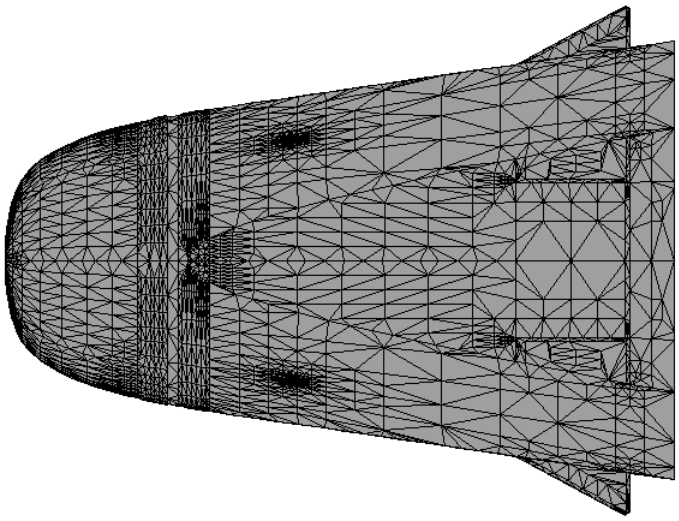

(b) Side view

Figure 6.1 EXPERT unstructured body grid used in present DS3V simulations

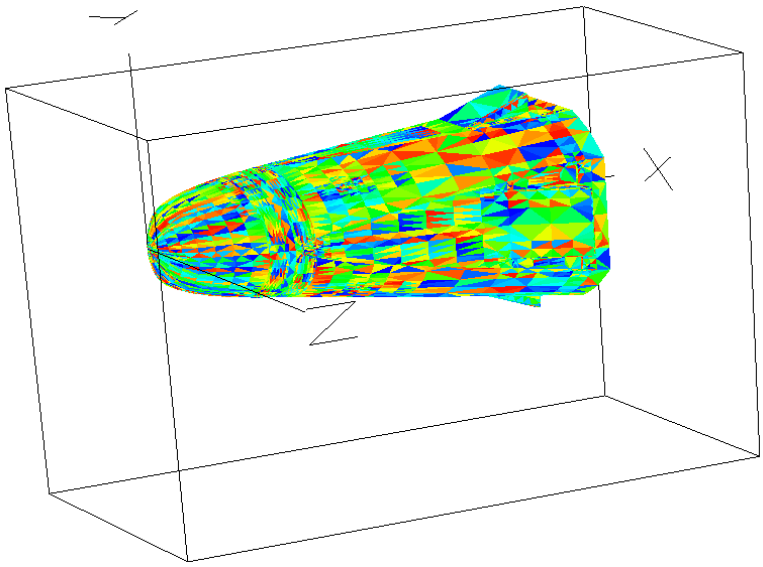

Figure 6.2 DS3V computational domain

6.3 Analysis of the results

The high altitude, aerodynamic behavior of EXPERT is shown in Figs. 6.4(a) and (b) where the profiles of the axial (C_A) and the normal (C_N) force coefficients are reported as functions of the angle of attack α, in the altitude interval 80.4-104.5 km. Most of computations have been made with φ=0. In order to evaluate the influence of the rolling angle, only two sets of tests with φ=45 deg. have been made at h=80.4 and h=104.5 km (Figures 6.5). Figures 6.4(a) and (b) show that, in this altitude interval, the influence of φ is negligible. Very slight difference is detectable at high angle of attack (say α>40 deg.), therefore, considering that, as said before, the angle of attack of EXPERT is not higher than 5 deg., the influence of the rolling angle is practically irrelevant.

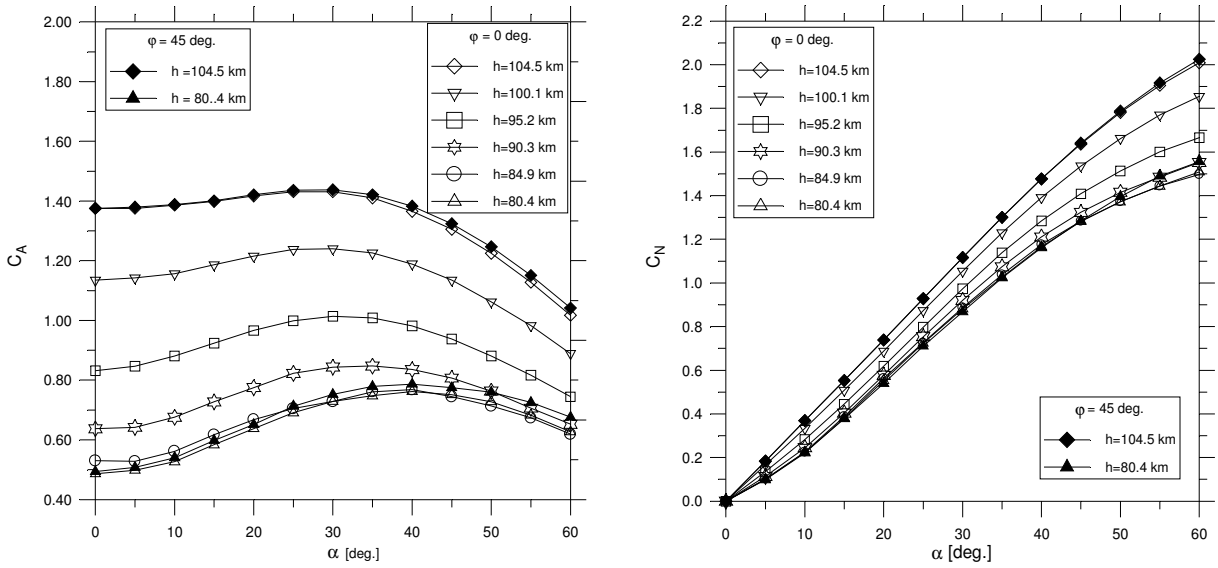

Figure 6.4 Profiles of axial (a) and normal (b) force coefficients of EXPERT in the altitude interval 80.4-104.5 km

The capsule is longitudinally stable. A measure of stability is provided by the profiles of the pitching moment around the gravity center (C_{Mcg}) and by the location of the pressure center (x_{cp}) along the axis, reported in Figs. 6.6(a) and (b), respectively. The longitudinal equilibrium ($dC_{Mcg}/d\alpha<0$), with a trim angle up to about 40 deg., is kept at all altitudes. The pressure center is, at least, at 0.14 m behind the center of gravity (x_{cg}). Also the longitudinal stability and the position of the pressure center practically are not influenced by the rolling angle.

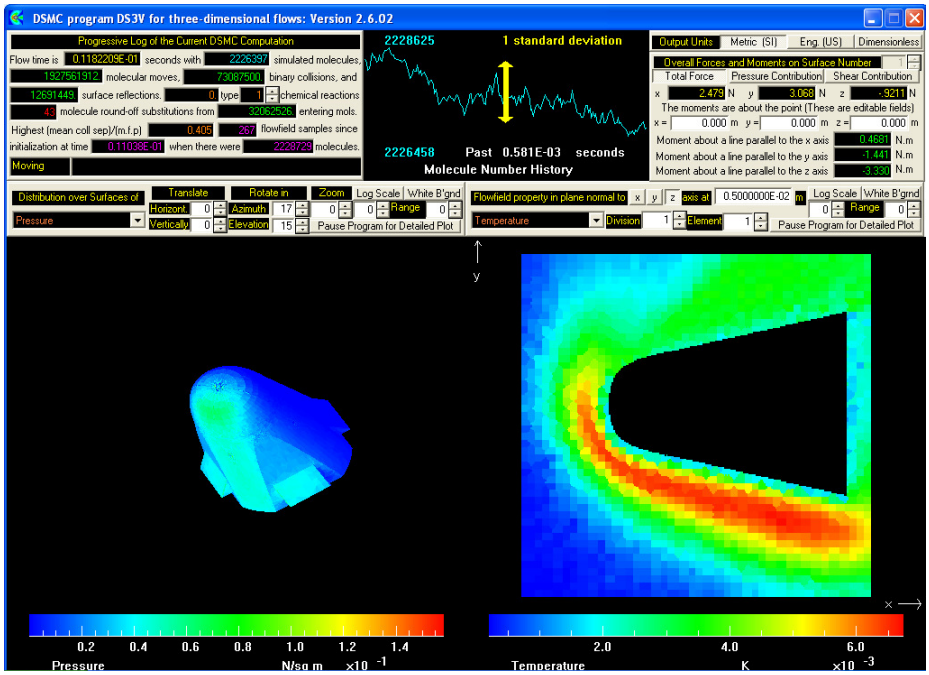

Figure 6.5 DS3V program interface during a run at $\alpha = 60$ deg. and $\varphi = 45$ deg.

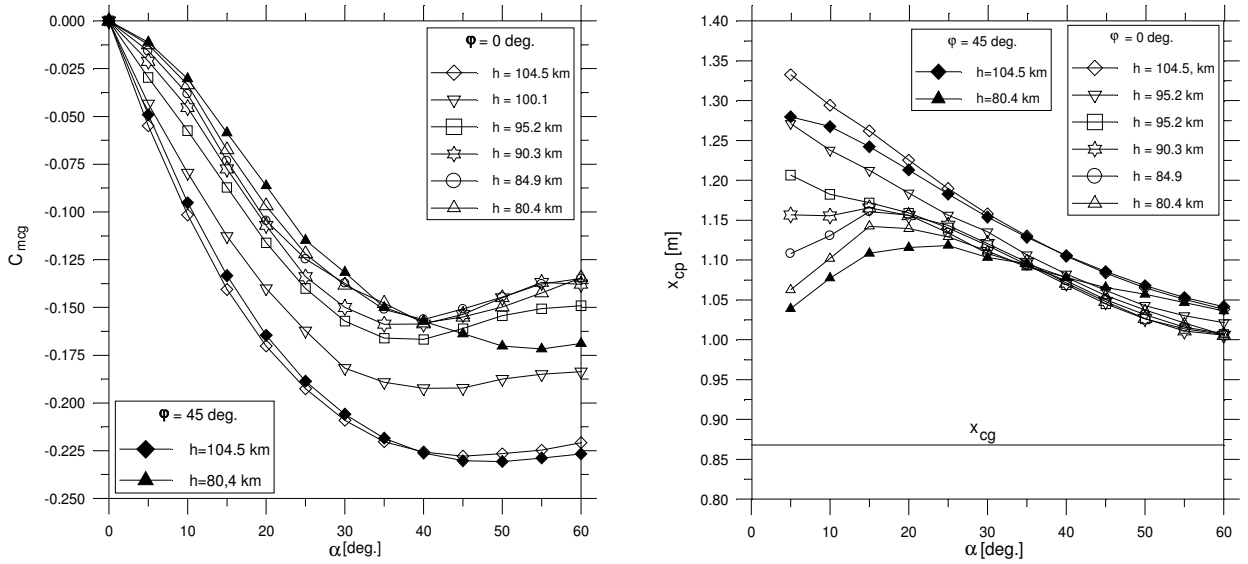

(a) (b)

Figure 6.6 Profiles of pitching moment coefficient (a) and position of pressure center along the axis of EXPERT in the altitude interval 80.4-104.5 km

6.4 Conclusions

The data base of the EXPERT capsule has been broadened by computations in the altitude interval 80-105 km by 3-D DSMC code. The work involved aerodynamic parameters (axial and normal force coefficients), longitudinal stability (pitching moment coefficient and fluctuation of position of pressure center along the axis). The capsule showed good stability behavior in the whole altitude interval up to an angle of attack of about 40 deg.. It has been also verified that, when the capsule is at an angle of attack, the effect of non-symmetry of the flow field is practically irrelevant.

CHAPTER VII

Analysis of Bridging Formulae in transitional regime

7.1 Introduction

In the past, several bridging formulae have been used to compute the aerodynamic forces of a spacecraft at first stage of a design (Phase A). There are two kinds of bridging formulae: global and local. The basic difference is that the global formulae rely on knowledge of the spacecraft aerodynamic force coefficients in continuum and free molecular flow, while the local formulae take directly into account the geometry of the vehicle and calculate pressure and skin friction distribution on the body surface. Then, the global aerodynamic coefficients are computed by integration of pressure and skin friction distributions on the body surface.

The aim of this work (chapter) is to analyze the local formulae by Kotov, Lychkin, Reshetin and Schelkonogov [45] (here called Kotov formula) and by Potter and Peterson [46] (here called Potter formula), through the comparison of the results with the ones from the widely accepted DSMC code DS2V [12]. To this purpose, a simple body, like a sphere, has been considered. This comparison pointed out that the Kotov formula showed good match of the pressure coefficient at high altitudes, while some corrections were necessary at lower altitudes. These corrections have been applied to the Potter formula. For the skin friction coefficient, both formulae showed pretty good results at high altitudes but the results were not satisfactory in continuum low density regime. To obtain a satisfactory agreement with the DS2V results, changing the methodology of the skin friction coefficient computation was proper. Once again, the Potter formula has been chosen for the corrections. Therefore a "new" methodology (here called "new" bridging formula) has been developed. This relies, at low altitudes, on the use of the corrected Potter formula and, at higher altitudes, on the merge of the corrected Potter formula, for the computation of the skin friction coefficient, and of the Kotov formula, for the computation of the pressure coefficient.

The ultimate purpose of this work is to apply the "new" formula to more complex bodies, such as EXPERT and ORION capsules, along the re-entry path. These capsules have been chosen because characterized by completely different shapes. More specifically, ORION is "Apollo like" or sphere-cone shape, EXPERT is a blunted pyramidal shape, consisting of a body of revolution with an ellipse-clothoid-cone 2D longitudinal profile. For these capsules, in rarefied flow, pressure, skin friction and axial force coefficients, computed by the "new" bridging formulae, agree with the

results by DS2V and DS3V [13] codes. On the opposite, in continuum low density regime, these coefficients over-estimate the DS2/3V results.

Finally, for these capsules, the global bridging formula by Wilmoth, Mitcheltree and Moss [47] (here called Wilmoth formula) has been also considered. By tuning the adjustable parameters, the axial force coefficient is in a very good agreement with the DS2/3V results in the whole transitional regime.

7.2 Local Bridging Formula by Kotov, Lychkin, Reshetin and Schelkonogov

Kotov, Lychkin, Reshetin and Schelkonogov [45] proposed a semi-empirical approximate method based on both numerical calculation data and experimental results for numerical calculations of aerodynamic characteristics of complex geometry bodies.

The pressure coefficient, C_P, and friction coefficient, C_f , for a surface element with a local angle of incidence α_{loc} were presented in the following rather general form:

$$C_f = \tau_0 \cos\alpha_{loc} + \tau_1 \cos\alpha_{loc} \sin\alpha_{loc} \qquad (7.1) \qquad C_p = P_0 + P_1 \sin\alpha_{loc} + P_2 \sin^2\alpha_{loc} \qquad (7.2)$$

where P_0, P_1, P_2, τ_0 and τ_1 (called "regime coefficients") depend in the general case on similarity parameters, such as Reynolds number ($Re_0=\rho_\infty V_\infty L/\mu_0$, where μ_0 is the viscosity at the stagnation point), Mach number (M_∞), ratio of specific heats ($\gamma=c_p/c_v$), temperature ratio ($t_w=T_w/T_0$, where T_w is the wall temperature and T_0 is the stagnation temperature), and some parameter of a streamlined body.

In the range of intermediate Reynolds number, Re_o, the dependence of the regime coefficients on the main flow parameters for the general case can be presented as:

$$P_0 = P_0^{id} + \left(P_0^{fm} - P_0^{id}\right)F_{P_0} \qquad \tau_0 = \tau_0^{fm} F_{\tau_0}$$

$$P_1 = P_1^{fm} F_{P_2} \qquad \tau_1 = \tau_1^{fm} F_{\tau_1}$$

$$P_2 = P_2^{id} + \left(P_2^{fm} - P_2^{id}\right)F_{P_2}$$

Superscripts "fm" and "id" refer to the free-molecular and ideal-continuum regimes, respectively. More specifically, the free molecular terms depend on the normal and tangential components of momentum, exchanged between gas and surface. The ideal-continuum terms depend on pressure

coefficient at the stagnation point. A particular form of the functions $F_{\tau 0}$, $F_{\tau 1}$, F_{P0}, F_{P1} and F_{P2} is obtained by a semi-empirical procedure. This relies on the results from numerical calculations and experimental data about different bodies and at different test conditions.

It follows from the free-molecular theory of convex body flow that for the free-molecular limit

$$P_0^{fm} = \frac{2-\sigma_n}{\gamma M_\infty^2}\left(1+\mathrm{erf}(z)\right) + \frac{\sigma_n}{\gamma M_\infty^2}\sqrt{t_w \frac{\gamma-1}{2}}e^{-z^2} \qquad \tau_0^{fm} = \sigma_t e^{-z^2}\frac{1}{M_\infty^2}\sqrt{\frac{2}{\pi\gamma}}$$

$$P_1^{fm} = \frac{\sigma_n}{2}\sqrt{t_w \frac{\pi(\gamma-1)}{\gamma}}\left(1+\mathrm{erf}(z)\right) + \frac{2-\sigma_n}{M_\infty^2}\sqrt{\frac{2}{\pi\gamma}}e^{-z^2} \qquad \tau_1^{fm} = \sigma_t\left(1+\mathrm{erf}(z)\right)$$

$$P_2^{fm} = (2-\sigma_n)\left(1+\mathrm{erf}(z)\right) \qquad \text{with} \qquad z = \sqrt{\frac{\gamma}{2}}M_\infty^2 \sin\alpha_{loc}$$

In the limiting case of supersonic ideal gas flow $Re_0 \to 0$ the regime coefficients are presented as

$$P_0^{id} = \begin{cases} 0, & \text{for } \sin\alpha_{loc} \geq 0.73 \\ P_\alpha\left(1-\dfrac{\sin\alpha_{loc}}{0.73}\right), & \text{for } 0 \leq \sin\alpha_{loc} \leq 0.73 \end{cases}$$

$$P_\alpha = \begin{cases} \dfrac{8}{(\gamma-1)(\gamma+3)M_\infty^2}, & \text{for the wedge} \\ \dfrac{1}{(\gamma-1)M_\infty^2}, & \text{for the cone} \end{cases}$$

$$P_2^{id} = \begin{cases} C_p, & \text{for } \sin\alpha_{loc} \geq 0.73 \\ C_p + (P_k - C_p)\left(1-\dfrac{\sin\alpha_{loc}}{0.73}\right), & \text{for } 0 \leq \sin\alpha_{loc} \leq 0.73 \end{cases}$$

$$P_k = \begin{cases} \gamma+1, & \text{for the wedge} \\ \dfrac{2(\gamma+1)(\gamma+7)}{(\gamma+3)^2}, & \text{for the cone} \end{cases}$$

Here Cp is expressed by the Rayleigh's formula:

$$C_p = \frac{\gamma+1}{\gamma}\left(\frac{(\gamma+1)^2 M_\infty^2}{4\gamma M^2 - 2(\gamma-1)}\right)^{\frac{1}{\gamma-1}} - \frac{2}{\gamma M_\infty^2}$$

The analysis of experimental and calculation data shows that the functions F_{P1}, F_{P2} and $F_{\tau 1}$ vary monotonically depending on the parameter Re_o, while the function F_{P0} and $F_{\tau 0}$ are non-monotonic in the character of changing depending on Re_o and depend considerably on M_∞ and t_w.

$$F_{P_0} = \left[a\sqrt{Re_0} + \exp(-b\,Re_0)\right]^{-1}, \qquad \text{where}$$

$$a = \frac{(\gamma-1)\sqrt{t_w} + M_\infty^{-1}\sqrt{2(\gamma-1)}}{(0.56+1.2t_w)(M_\infty+2.15)}, \qquad b = 0.20 + 0.005M_\infty$$

$$F_{P_1} = F_{P_2} = \exp\left[-(0.125+0.078t_w)Re_0\,10^{-1.8(1-\sin\alpha_{loc})^2}\right]$$

$$F_{\tau_0} = \left[a_1\,Re_0 + \exp(-b_1\,Re_0)\right]^{-3/4} \qquad \text{where}$$

$$a_1 = \frac{\gamma-1}{2}\left[\sqrt{\frac{\pi\gamma}{2}}M_\infty(0.208+0.341t_w)\right]^{3/4}$$

$$b_1 = 0.213 - 0.133t_w$$

$$G_{\tau_1} = (0.75t_w + 0.25)^{-2/3}\,Re_0$$

$$G_x = G_{\tau_1}\cdot 10^{\left(-0.24(1-\sin\alpha_{loc})^3\right)}$$

$$F_{\tau_1} = 1\Big/\sqrt{0.145\cdot G_x + \exp(G_y)}$$

$$G_y = G_x\cdot\left(7.2\cdot 10^{-3} - 1.6\cdot 10^{-5}\cdot G_x\right)$$

7.3 Local Bridging Formula by Potter and Peterson

The values of skin friction (C_f) and pressure (C_p) coefficients are based on correlation of these quantities as computed for sphere by the DSMC method in transitional regime:

Transitional Skin friction

It is possible to demonstrate [46] that the ratio between the skin friction coefficient in transitional regime and the skin friction coefficient in free molecular flow (C_{ffm}) can be correlated to the Z parameter that reads:

$$Z = f(\vartheta)\frac{\left[M_\infty/\sqrt{Re_\infty}\right]\,(T_\infty/T_W)^{(1-\omega)/2}\,(80H_W/H_0)^y}{\sin\vartheta} \tag{7.3}$$

where:

- $y = V^{2.7}/\left(V^{3.1}+180\right)$,
- $V = M_\infty/\sqrt{Re_\infty}$,
- $f(\vartheta)$ is a function correlating the DSMC data, for sphere $f(\vartheta)=1+\sin\vartheta$ and ϑ is the angle between the local surface normal and the free stream velocity.

Potter and Peterson computed C_f by a DSMC code and C_{ffm} by the well known Maxwell equation [1]:

$$C_{ffm} = \tau_{fm}/(p_\infty S_\infty^2) \tag{7.4}$$

$$\tau_{fm}/p_\infty = [(1-E)S_\infty \sin\theta/\sqrt{\pi}]\left\{\exp(-S^2\cos^2\theta)+\sqrt{\pi}S_\infty\cos\theta[1+\mathrm{erf}(S_\infty)]\right\} \tag{7.5}$$

where:

- E is the fraction of molecules specularly reflected
- $S_\infty = M_\infty\sqrt{\gamma/2}$ is the molecular speed ratio at the free stream conditions

They obtained two correlation equations for $\vartheta \leq 75$ deg:

$$\text{if} \quad Z > 1 \quad \text{then} \qquad C_f/C_{ffm} = \left[0.24/\left(0.24+Z^{1.3}\right)\right]^{1.25} \tag{7.6}$$

$$\text{if} \quad Z \leq 1 \quad \text{then} \qquad C_f/C_{ffm} = 0.1284\ Z \tag{7.7}$$

In the interval $75<\vartheta\leq 90$ deg., C_f/C_{ffm} is computed by linear interpolation between the value of C_f/C_{ffm} at $\vartheta=75$ deg. by equations (9) or (10), and the value at $\vartheta=90$ deg., by multiplying the right hand side of equation (9) by the factor

$$1+887.5/(7.46+Z^{1.14})^2 \qquad \text{if } Z\geq 1,$$

or multiplying the right hand side of equation (10) by the factor

$$1+12Z^2 \qquad \text{if } Z<1.$$

These multipliers have been chosen in order to fit the DSMC calculation for sphere when $\theta = 90$ deg.

Transitional Pressure Ratio

Rather arbitrarily, Potter and Peterson have chosen to correlate p/p_{fm} as a function of M_∞/Re_∞ for the purpose of estimating the variation of p/p_∞ in the transitional regime.

When $p_i \leq p_{fm}$, the approximation used is

$$p/p_{fm} = 1-(1-p_i/p_{fm})/[1+(0.6+\theta)^4(M_\infty/Re_\infty)^{1/2}] \tag{7.8}$$

where θ is expressed in radians. When $p_i > p_{fm}$, the following equation is used:

$$p/p_{fm} = 1+(p_i/p_{fm}-1)/[1+0.6(M_\infty/Re_\infty)^{1/2}] \tag{7.9}$$

where p_i is the pressure corresponding to inviscid flow and p_{fm} is the free molecular. Pressure p_{fm} is computed from the ratio p_{fm}/p_∞ that is computed by the well known Maxwell equation [1]:

$$\begin{aligned} p_{fm}/p_\infty = {} & [(1+E)S_\infty(1/\sqrt{\pi})\cos\theta)+0.5(1-E)\sqrt{T_w/T_\infty}] \\ & \times\exp(-S_\infty^2\cos^2\theta)+[(1+E)(0.5+S_\infty^2\cos^2\theta) \\ & +0.5(1-E)\sqrt{T_w/T_\infty}\sqrt{\pi}S_\infty\cos\theta][1+\mathrm{erf}(S_\infty\cos\theta)] \end{aligned}$$

The pressure corresponding to inviscid flow is computed from the ratio p_i/p_∞ that is approximated by

$$p_i/p_\infty = 1+1.895S_\infty^2(1+0.191\vartheta-2.143\vartheta^2+1.564\vartheta^3-0.334\vartheta^4) \tag{7.10}$$

this equation is a curve fit based on a method of characteristics solution for hypersonic flow over a sphere.

7.4 Global Bridging Formula by Wilmoth, Mitcheltree and Moss

The global bridging formula, proposed by Wilmoth, Mitcheltree and Moss [47] to compute the aerodynamic force coefficients, as per the axial force coefficient C_A, is:

$$C_A = C_{A,cont} + \left(C_{A,fm} - C_{A,cont}\right)\sin^2(\phi) \tag{7.11}$$

where: subscript "cont" is for continuum, $\phi=\pi(a_1+a_2\log_{10}Kn_\infty)$, a_1 and a_2 are constants. These constants are determined by choosing the Knudsen numbers corresponding to continuum and free molecular limits. For example, choosing $Kn_{cont}=10^{-3}$ and $Kn_{fm}=10$ one obtains $a_1=3/8$ (=0.375) and $a_2=1/8$ (=0.175). Furthermore, as the constants a_1 and a_2 are simply adjustable parameters, proper values may be chosen giving the best overall description of the transitional flows when additional data are available. Expressions similar to equation (14) can be used for other aerodynamic coefficients: lift, drag and so on.

7.5 Codes and Test Conditions

The DS2V computational domain was a rectangle in the meridian plane: i) x=2.4 m, y=1.5 m for SPHERE (diameter 1.6 m), ii) x=2.4 m, y=2.3 m for EXPERT (length 1.55 m, base diameter 0.918 m), iii) x=6 m, y=3.5 m for ORION (length 3.3 m, base diameter 2.51 m). The DS3V computational domain for EXPERT was a parallelepiped: x=2.4 m, y=2.3 m, z=1.1 m.

The number of simulated molecules was about 2.0×10^7. This number of simulated molecules, for the DS2V runs at the most severe test conditions, in terms of altitude, provided an average value of mcs/λ: of about 0.39 for SPHERE (70 km), of about 0.25 for EXPERT (69.8 km), of about 0.1 for ORION (85 km). For the DS3V runs (EXPERT), at the most severe test conditions (80.4 km), the average value of mcs/λ was 1.1.

For all runs, the simulation time was longer than 25 times the time necessary to cross the computing region along the x direction at the free stream velocity: 7500 m/s for sphere, 5000 m/s for EXPERT and 7600 m/s for ORION, therefore this time was of the order of 10^{-4} s. This simulation time can be considered long enough for stabilizing all thermo-fluid-dynamic parameters.

The working gas was simulated air made up of 5 chemical species: O_2, N_2, O, N and NO in chemical non-equilibrium. A fully accommodate gas-surface interaction model was used. In agreement with Potter [46], the wall temperature of SPHERE was 350 K. While wall temperature of

capsules was 300 K. Free stream thermodynamic parameters were provided by the U.S. Standard Atmosphere 1976.

7.6 Analysis of Results for Sphere

The first stage of the analysis of the results is related to the pressure and skin friction coefficient distributions on a sphere. Figures 7.1 show, as typical examples, the pressure coefficient distributions (a) at h=75 km ($Kn_{D\infty}\cong 1.7\times10^{-3}$). The profiles of C_p both by Kotov and by Potter show good agreement with the DS2V results. However, it has to be pointed out that the values of C_p from both formulae slightly overestimate the ones by DS2V. In fact the average values of C_p by Potter, Kotov and DS2V are 0.947, 0.937 and 0.909, respectively. As shown in Figures 7.2(a) to (d) this condition is verified also at other altitudes up to 95 km ($Kn_{D\infty}\cong 3.6\times10^{-2}$). At higher altitudes, the Kotov formula provides a good match with DS2V, while the Potter formula slightly underestimates DS2V, see Figures 7.3(a) to (d). Therefore, correcting the C_p computational procedure for $Kn_{D\infty}<3.6\times10^{-2}$ is proper.

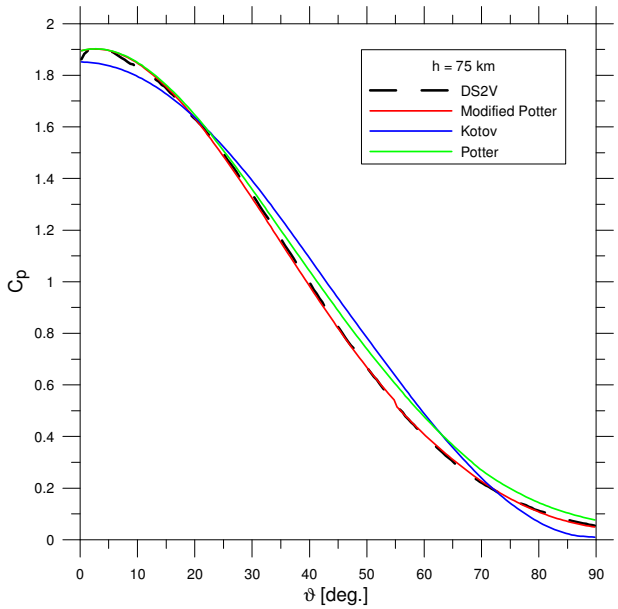

Figure 7.1 Profiles of pressure coefficient at h=75

The Potter formula has been chosen for this correction, therefore, equations (7.8) and (7.9) have been modified and read:

if $p_i \le p_{fm}$ then

$$p/p_{fm} = 1 + \frac{(p_i/p_{fm}\alpha - 1)}{1+\beta(M_\infty/Re_\infty)^{1/2}} \tag{7.12}$$

if $p_i > p_{fm}$ then

$$p/p_{fm} = 1 + \frac{(p_i/p_{fm}\alpha - 1)}{1+\beta(M_\infty/Re_\infty)^{1/2}} \tag{7.13}$$

where:

- $\alpha=0.8, \beta=1$ if $Kn_{D\infty} \leq 1.1\times10^{-3}$,
- $\alpha=0.9, \beta=5$ if $1.1\times10^{-3} < Kn_{D\infty} < 5.2\times10^{-3}$,
- $\alpha=0.8, \beta=10$ if $Kn_{D\infty} \geq 5.2\times10^{-3}$.

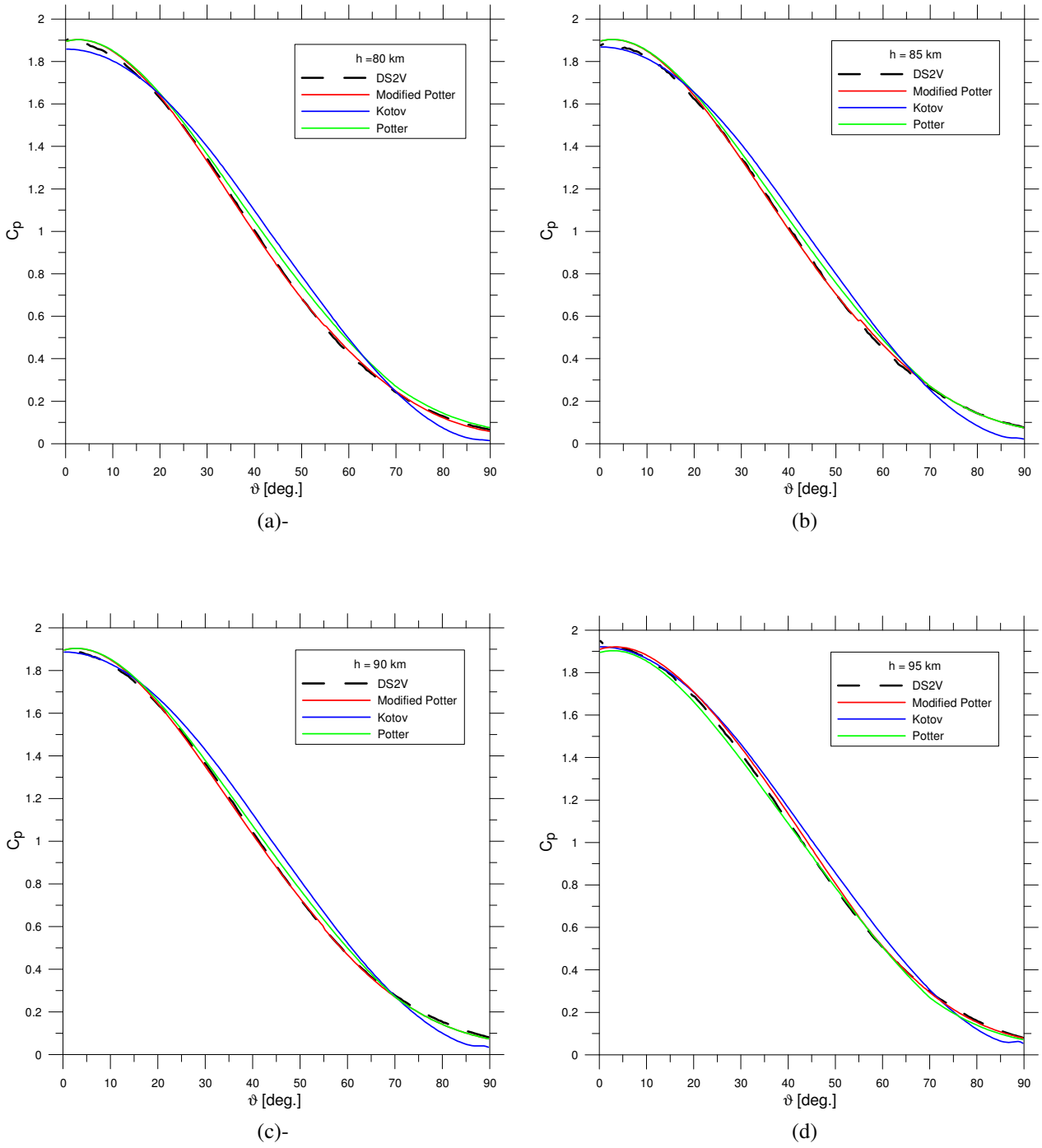

Figure 7.2 Profiles of pressure coefficient at h=80 km (a), h=85 km (b), h=90 km (c), h=95 km (d)

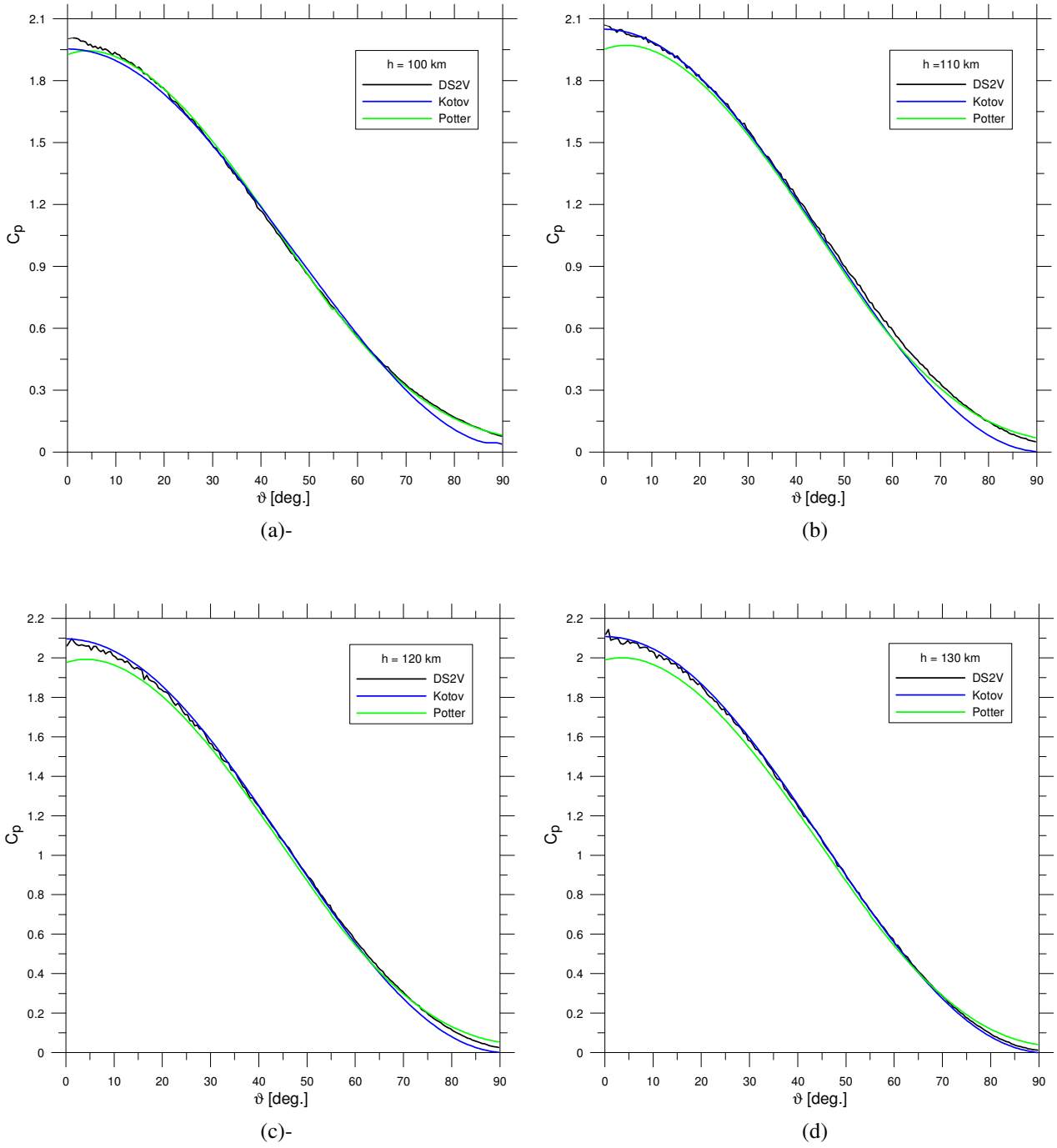

Figure 7.3 Profiles of pressure coefficient at h=100 km (a), h=110 km (b), h=120 km (c) and h=130 km (d)

The profiles of C_f do not show a satisfactory agreement with DS2V. As shown in Figs 7.4(a) to (l) this mismatch decreases at high altitudes (h>100 km), but amplifies at lower altitudes.

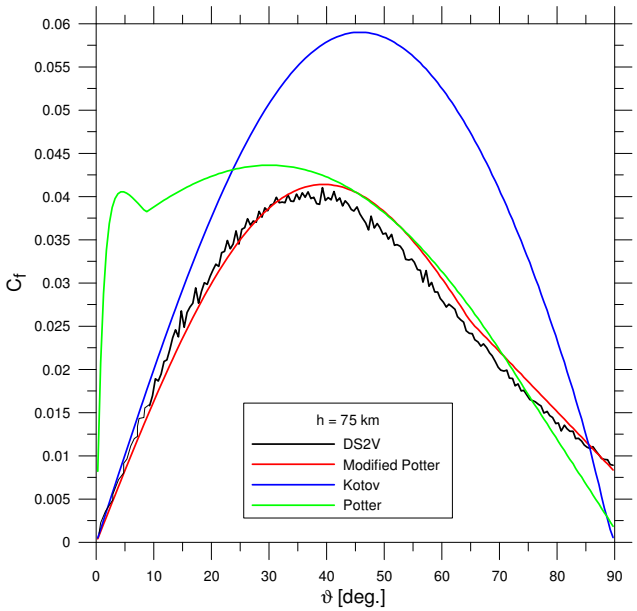

(a)-

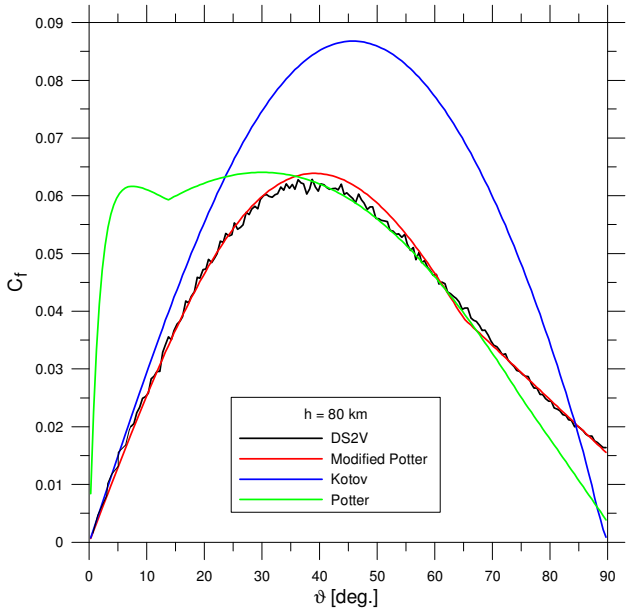

(b)

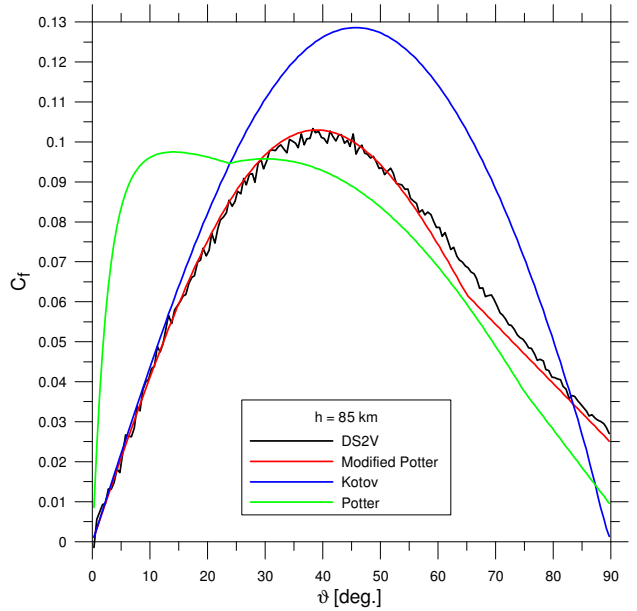

(c)-

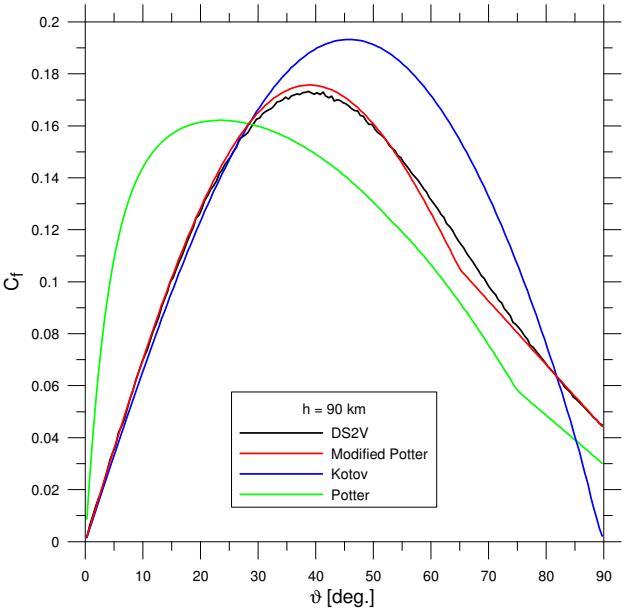

(d)

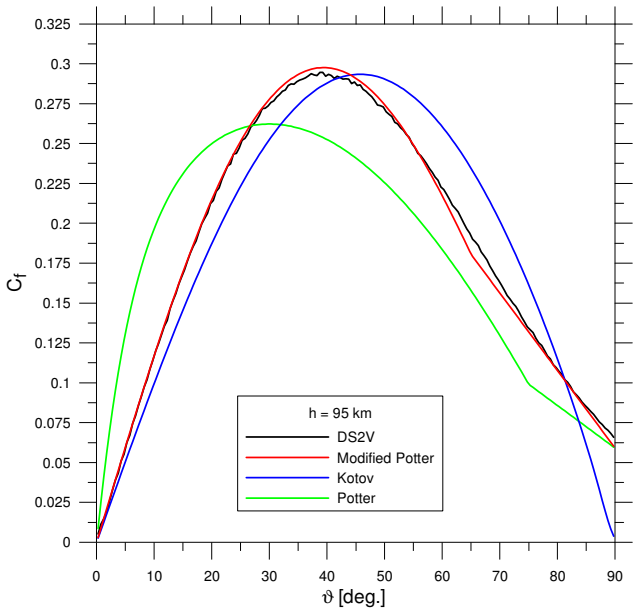
h = 95 km
DS2V
Modified Potter
Kotov
Potter
Cf
ϑ [deg.]

(e)-

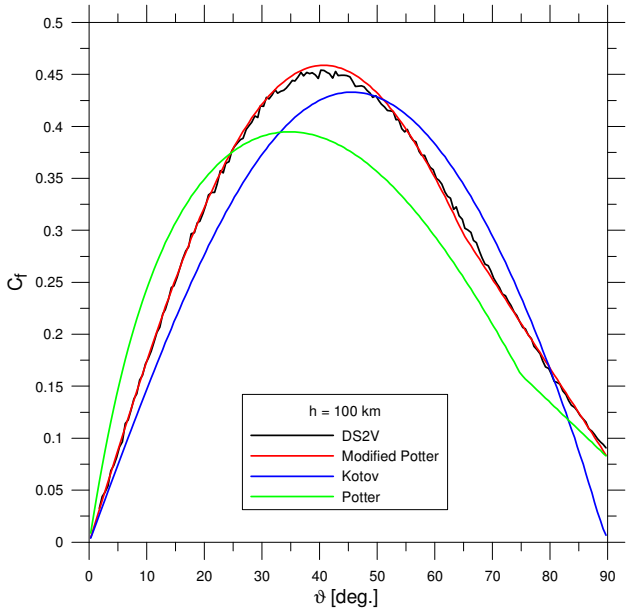
h = 100 km
DS2V
Modified Potter
Kotov
Potter
Cf
ϑ [deg.]

(f)

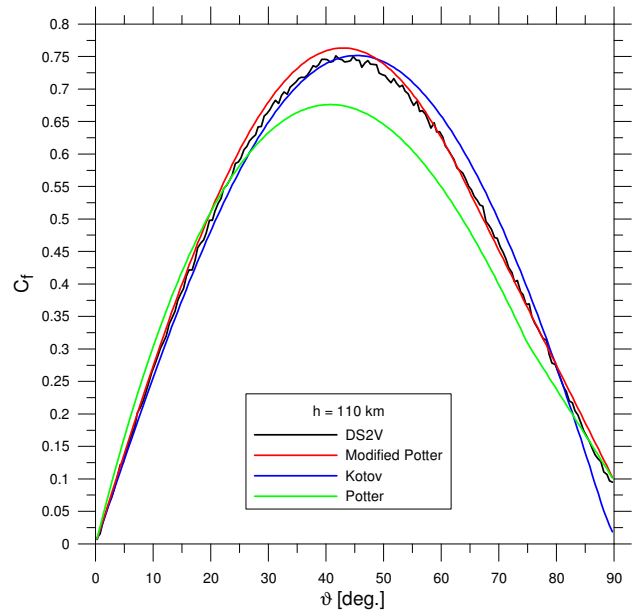
h = 110 km
DS2V
Modified Potter
Kotov
Potter
Cf
ϑ [deg.]

(g)-

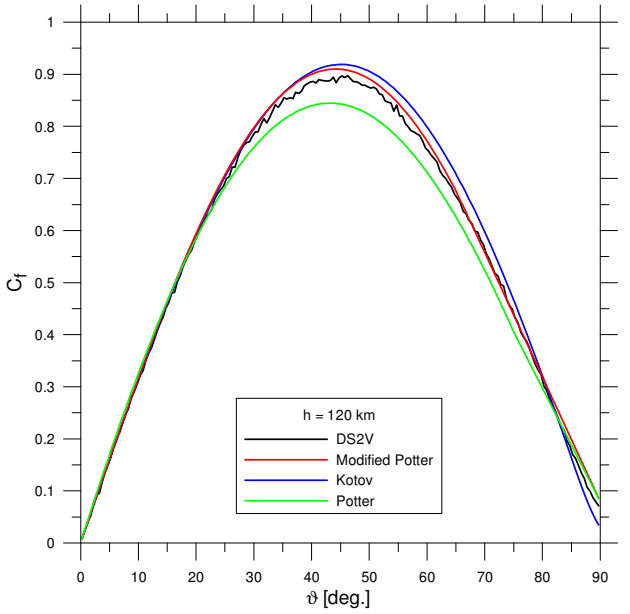
h = 120 km
DS2V
Modified Potter
Kotov
Potter
Cf
ϑ [deg.]

(h)

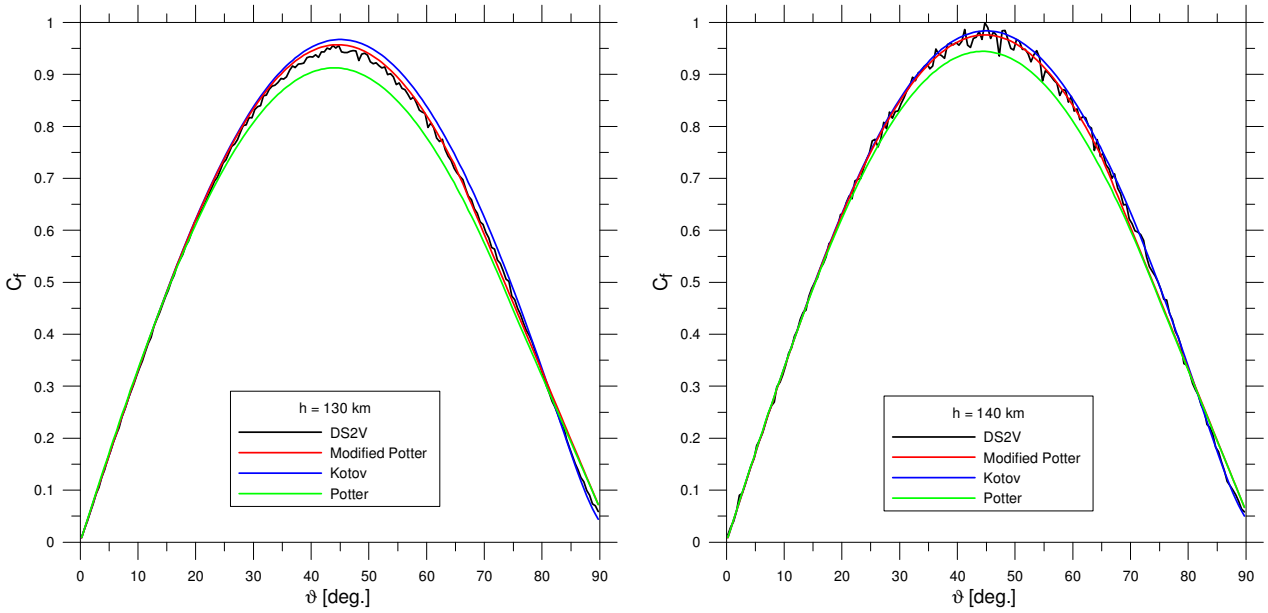

(i)- (l)

Figure 7.4 Profiles of skin friction at h=75 km (a), h=80 km (b), h=85 km (c), h=90 km (d), h=95 km (e) h=100 km (f), h=110 km (g), h=120 km (h), h=130 km (i), h=140 km (l)

Therefore improvement to the computation of C_f is necessary. Once again the Potter formula has been selected for the corrections. These are related to:

1. exponents in equation (9); these have been put at -1.6 and 0.85 instead of -1.3 and 1.25.
2. Ratio C_f/C_{ffm}; this has been correlated with parameter Z* instead of Z. Z* reads:

$$Z^* = \left[M_\infty / \sqrt{Re_\infty}\right] \left(T_\infty / T_w\right)^{(1-\omega)/2} \left(1+\cos\vartheta\right) \left(80 H_w / H_0\right)^y \qquad (7.14)$$

   this parameter has been obtained by using the correlation function $f(\vartheta)=(1+\cos\vartheta)\sin\vartheta$ instead of $f(\vartheta)=(1+\sin\vartheta)$. This new function $f(\vartheta)$ has been obtained correlating new DSMC data, in-house computed.
3. The switch value; this has been put at 1.56 instead of 1.

Finally, the modified equations (9) and (10) read:

if $Z^* > 1.56$ then

$$C_f / C_{ffm} = \left[0.24 / \left(0.24 + (Z^*)^{-1.6}\right)\right]^{0.85} \qquad (7.15)$$

if $Z^* \le 1.56$ then

$$C_f / C_{ffm} = 0.0026 + 0.1392(Z^*) + 0.1480(Z^*)^2 - 0.0523(Z^*)^3 + 0.0008(Z^*)^4 \qquad (7.16)$$

Exponents in equation (7.15) and coefficients of the polynomial in the equation (7.16) have been fixed by interpolating the values of C_f/C_{ffm} computed by DS2V.

In Figs. 7.5(a) and (b) the results of the modified and of the original Potter formulae are compared with DS2V. The agreement of the modified Potter formula with DS2V is better than the one from the original formula. It has to be pointed out that the mismatch of the modified formula and DS2V, at each altitudes for ϑ>65 deg., has been overcome by a linear interpolation between the values of C_f/C_{ffm} at ϑ=65 deg., computed by equations (7.15) and (7.16), and the values at ϑ=90 deg., computed by the following equations:

if $Z^* \geq 1$ then

$$C_f / C_{ffm} = \left[0.24 / \left(0.24 + (2Z^*)^{-1.6}\right)\right]^{0.85} (1 + 887.5/(7.46 + (2Z^*)^{1.14})^2 \qquad (7.17)$$

if $Z^*<1$ then

$$C_f / C_{ffm} = [0.0026 + 0.1392(Z^*) + 0.1480(Z^*)^2 - 0.0523(Z^*)^3 + 0.0008(Z^*)^4]K \qquad (7.18)$$

where:

- $K=8+1.0078(Z^*-0.38)$ if $0.38<Z^*<1.0$
- $K=5.5+12.26$ if $Z^* \leq 0.38$

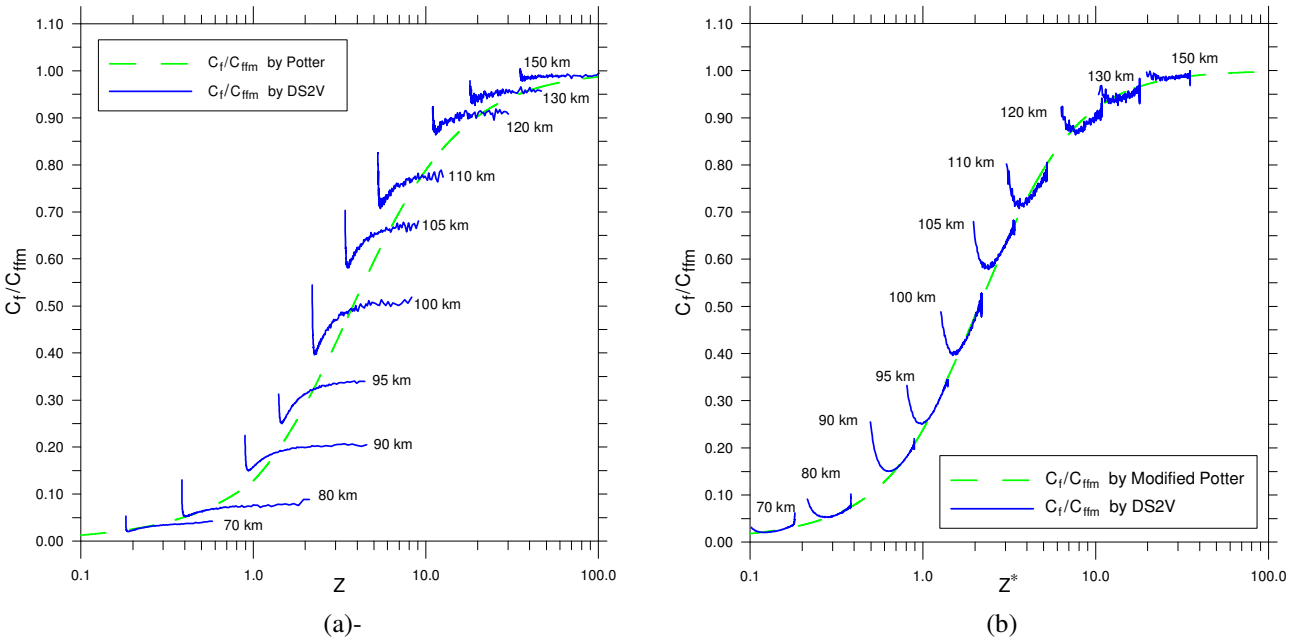

Figure 7.5 Correlation curves of friction coefficients from the Potter formula (a) and modified Potter formula (b), compared with the DS2V results

Figures 7.2(a) to (d) and 7.4(a) to (l) show the comparison, with DS2V, of the C_p and of C_f profiles on from the modified Potter, the original Potter and the Kotov formulae. The improvement of the modified Potter formula is evident.

As reported in Fig. 7.6, the corrections on C_p and C_f influence favorably the computation of C_A. In fact, the better agreement of the values of C_A from the "new" bridging formula with the ones from DS2V, compared with the results from the original Potter and Kotov formulae, is well apparent.

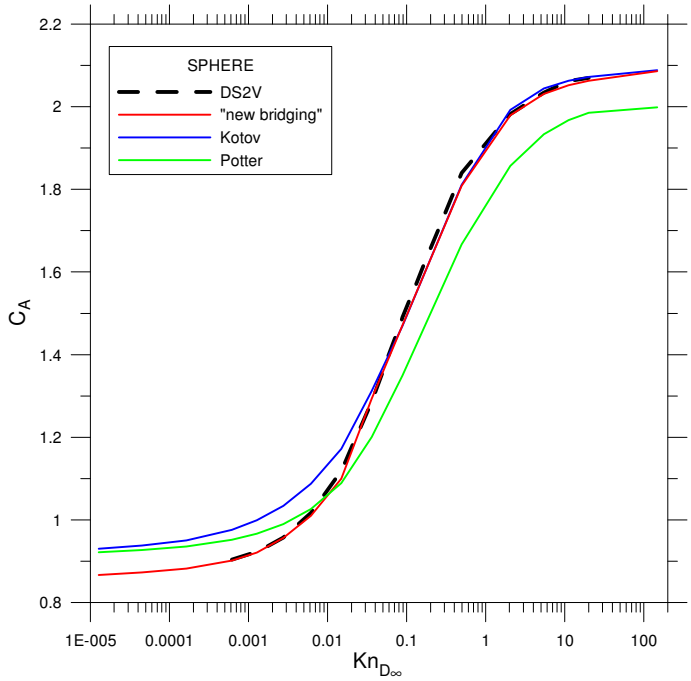

Figure 7.6 Profiles of axial force coefficient as function of Knudsen number

7.7 Analysis of Results for Capsules

Figures 7(a) and (b) show the profiles of pressure and skin friction coefficients for ORION as a function of the curvilinear abscissa (s) at the altitude of 130 km ($Kn_{D\infty}$=1.7). As expected, considering that $Kn_{D\infty}>3.6\times10^{-2}$, the agreement of C_p by Kotov with DS2V is better than the one by Potter (Fig. 7.7(a)). As for as the skin friction coefficient, the modified Potter and Kotov formulae are in excellent agreement with DS2V (Fig. 7.7(b)).

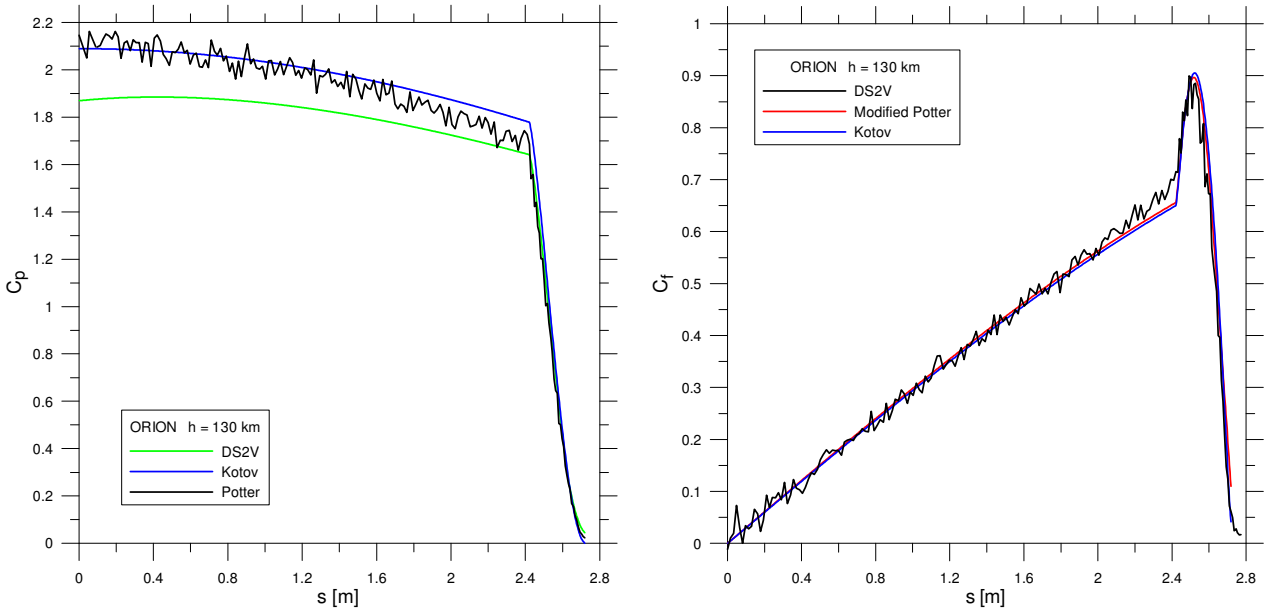

(a)- (b)

Figure 7.7 Profiles of pressure (a) and of skin friction (b) coefficients along ORION surface at h=130 km

Figures 7.8(a) and (b) show the profiles of pressure and skin friction coefficients at the altitude of 90 km ($Kn_{D\infty}$=0.0047); the bridging formulae are not able to evaluate satisfactory both C_p and C_f. This is probably due to the failure of the panel method, that increases with decreasing altitude.

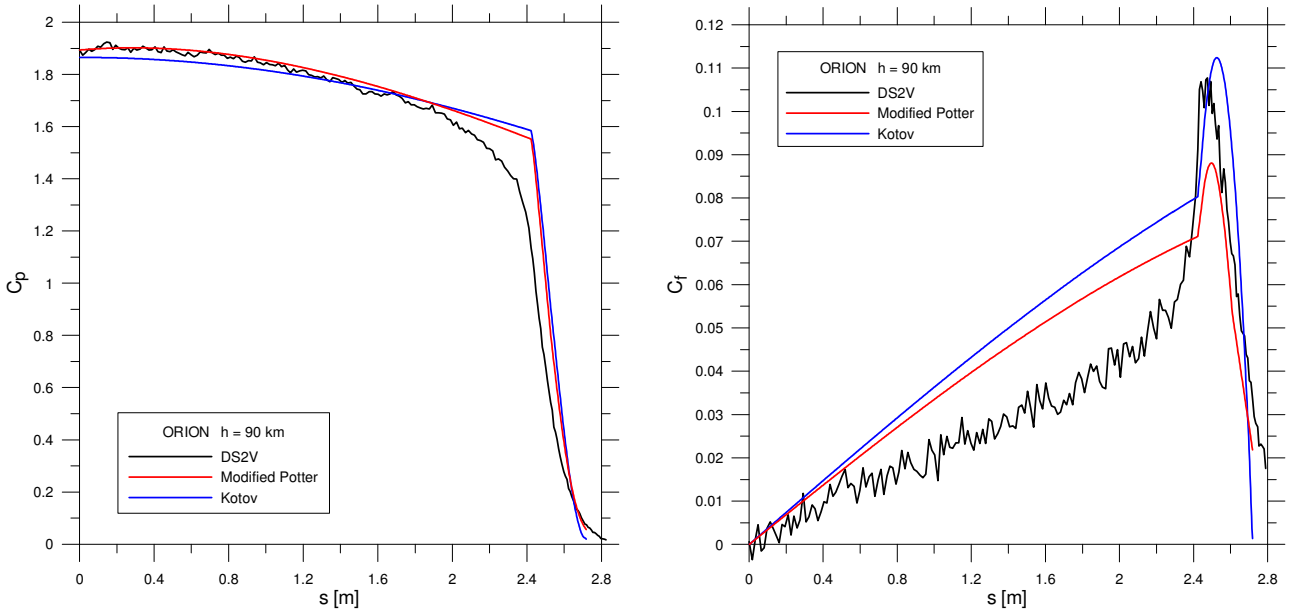

(a)- (b)

Figure 7.8 Profiles of pressure (a) and of skin friction (b) coefficients along ORION surface at h=90 km

Figures 7.9(a) and (b) show the profiles of pressure and skin friction coefficients for EXPERT at 104.5 km ($Kn_{D\infty}$=0.37). Figures show an over prediction of pressure and skin friction coefficients on the flap.

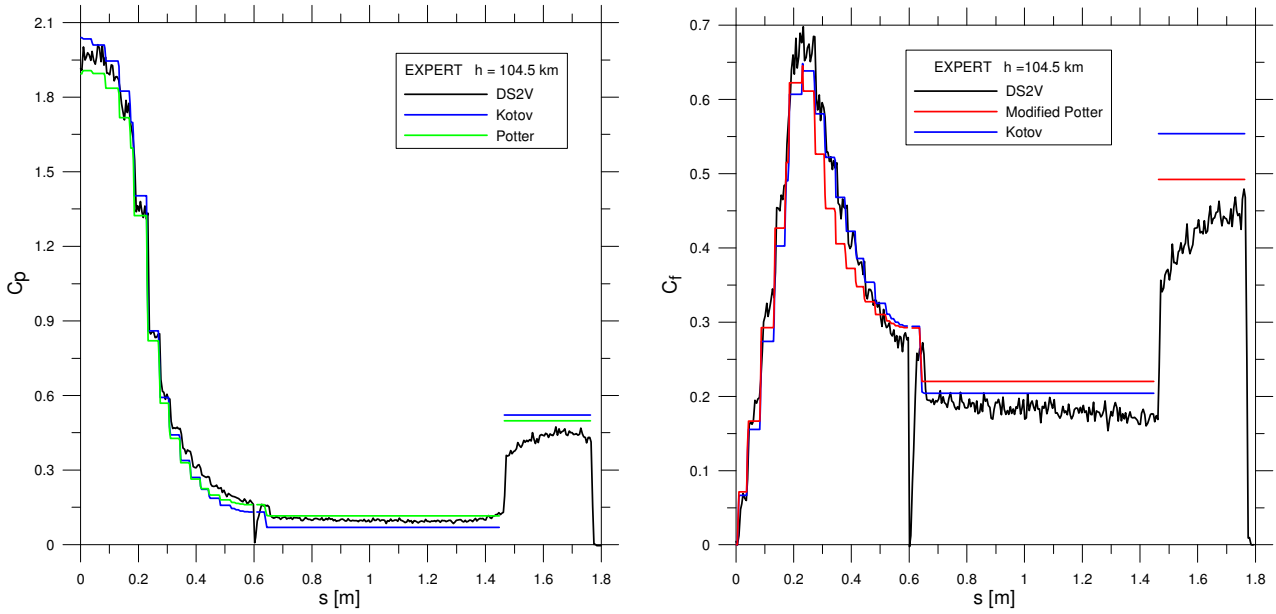

(a)- (b)

Figure 7.9 Profiles of pressure (a) and of skin friction (b) coefficients along EXPERT surface at h=104.5 km

As already pointed out by Ivanov [44], the flaps are exposed to a flow that is very different from the free stream one, input to the bridging formulae (see Fig. 7.10). For example, near the flap, the Mach number and the flow angle, computed by DS3V, range roughly between 2.5 and 3 and between 10 and 12 deg., respectively, while the free stream Mach number and the free stream flow angle, input to the bridging formulae, are 18 and 0 deg., respectively.

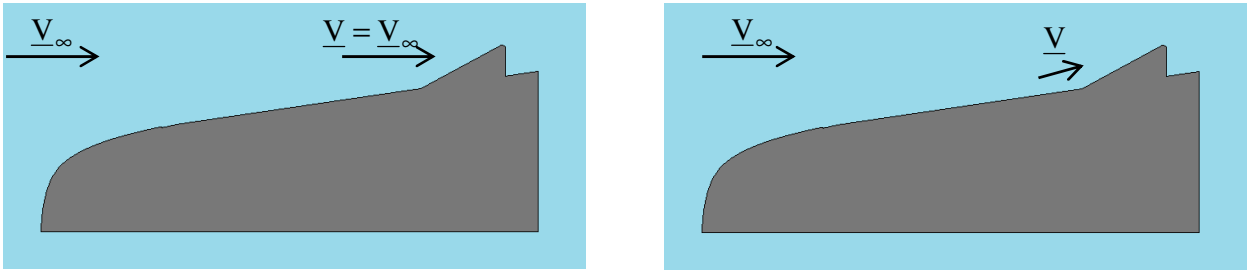

(a) (b)

Figure 7.10 Velocity vector, in the region close to the flap, considered by the local bridging formulae (a) and by the DSMC (b)

Figures 7.11(a) and (b) show the profiles of axial force coefficient as function of the Knudsen number for ORION and for EXPERT, respectively. The match is pretty good at high altitudes ($Kn_{D\infty}$>0.5 for ORION and $Kn_{D\infty}$>2.0 for EXPERT), but at lower altitudes, the local bridging

formulae do not match satisfactory DS2/3V; the percentage differences of C_A from the "new" bridging formula with respect to DS2/3V are 5% and 19% for ORION and EXPERT, respectively. However, as already pointed out by Ivanov [44], an uncertainty of 20% is acceptable in the Phase A of design of a re-entry vehicle. The agreement of the results from the Wilmoth formula with the ones from DS2/3V is excellent in the whole transitional regime. It has to be pointed out that, in this case, parameters a_1 and a_2 have been tuned for each capsule; for ORION a_1=0.333 and a_2=0.143, for EXPERT a_1=0.353 and a_2=0.133.

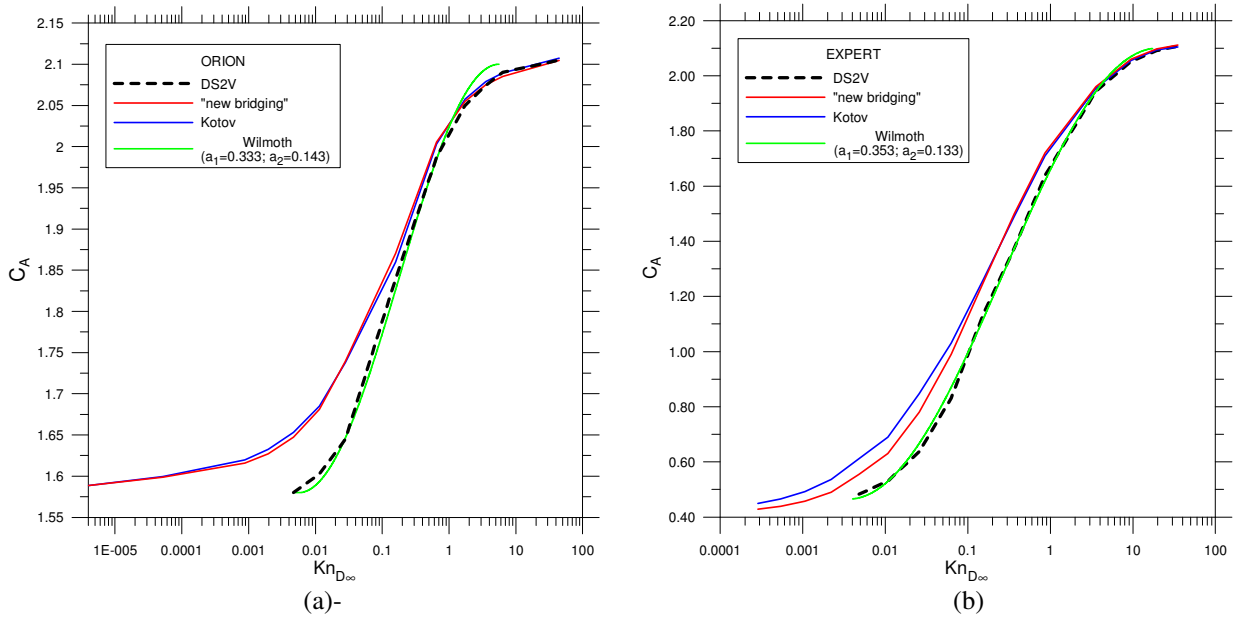

Figure 7.11 Profiles of axial force coefficient as functions of the Knudsen number for ORION (a) and for EXPERT (b)

7.8 Conclusions

The local bridging formulae by Kotov and by Potter have been analyzed using a sphere. The comparison with the results from DS2V led to the corrections or modifications of the bridging formulae. For this purpose, the Potter formula has been chosen. A "new" bridging formula was obtained by the merge of the modified Potter formula and the Kotov formula. The "new" formula was used to compute the pressure and the skin friction distributions on two current capsules: EXPERT and ORION. The comparison of the local and global aerodynamic coefficients with the DS2/3V results verified that the "new" bridging formula is excellent at high altitudes but at low altitudes do not match satisfactory the DS2/3V results; this is probably due to a failure of the panel method. Also the global bridging formula by Wilmoth was applied to these capsules. For this formula, thanks to proper values of the adjustable parameters, the axial force coefficient was in a very good agreement with the DS2/3V results in the whole transitional regime.

CHAPTER VIII

Analysis of Heat Fluxes for EXPERT and ORION

8.1 Introduction

It is well known that one of the most important problems in the design of a capsule is the evaluation of heat flux during the re-entry. This evaluation has to provide information about the design of the Thermal Protection System (TPS). Such an analysis should be carried on experimentally in thermal tunnels but, as well known, studying experimentally any aerodynamic problem in hypersonic, rarefied flow is very difficult and expensive. For this reason, computational methods play an important role and are subjected to continuous improvements. A number of papers have been already written about aero-thermo-dynamic behavior both of EXPERT [40, 44, 48] and of ORION [43, 49]. The aims of the present work are: a) the comparison of the heat flux computations, in high altitude flight, by two codes based on different approaches or direct simulation Monte Carlo (DSMC) and computational fluid dynamics (CFD), b) the evaluation of the influence of the related chemical models on the heat flux.

The analysis has been carried out by the DSMC code DS2V [12] at high altitudes and by the CFD code H3NS [17] at low altitudes; DS2V ran between 70-105 km for EXPERT and 85-125 for ORION. H3NS ran between 65-75 km for EXPERT and 75-95 for ORION. Tests considered both non-reactive and fully-catalytic surface. The results from the two codes have been compared at the overlapping altitudes of 70 km for EXPERT and of 85 km for ORION.

Considering different capsules is proper for the purposes of the present analysis. In fact, these capsules generate different fluid-dynamic conditions, produced by different shock wave intensity. This is due both to different radius of the nose of EXPERT (0.6 m) and of the cap of ORION (6.04 m) and to different free stream Mach numbers. For example, at the lowest altitudes of 70 km for EXPERT and 85 km for ORION, the Mach number is 17 and 28, respectively.

Even though the ionization process of air occurs during the re-entry path, in the present application it has been neglected. In fact, the aim of the present study is to compare the two chemical models in their basic aspects or in dissociation, recombination and exchange reactions. Therefore, both codes considered air as made up of five species: O_2, N_2, O, N and NO, relying on 17 forward/reverse chemical reactions. DS2V implements the Gupta chemical model [16] while

H3NS implements the Park chemical model [18, 19, 20]. The results showed that the heat flux by DS2V is always higher than the one by H3NS. The reason is that the two codes compute a different chemical composition. Therefore, a sensitivity analysis of the chemical models has been carried out. More specifically, the Park model has been implemented also in the DS2V code and the related results have been compared with those by the Gupta model.

8.2 The Gupta and the Park Chemical Models for neutral species

As said before, in the present study the ionization process has been neglected. The five chemical species (O_2, N_2, O, N and NO) react according to 17 forward/reverse chemical reactions by the Gupta and the Park models.

For the Gupta model, both the forward (k_f) and the reverse (k_r) rate coefficients are expressed in terms of the Arrhenius-like equation:

$$k_{f,r} = C_{f,r} T^{n_{f,r}} \exp\left(-\frac{E_{a_{f,r}}}{kT} \right) \tag{8.1}$$

where: C is the pre-exponential factor, n is the temperature exponent, E_a is the specific activation energy, k is the Boltzmann constant, subscripts f and r stand for forward and reverse reactions. The reactions are reported in Table 8.1 and Table 8.2 together with the reaction rate coefficients, the ratios of activation energies and the Boltzmann constant. The reactions are 15 dissociations/recombinations (Table 8.1) and 2 exchanges (Table 8.2).

Table 8.1 Gupta kinetic model for dissociation/recombination reactions

No	Reactions	C_f [m^3/molecule/s]	n_f	E_{af}/k [K]	C_r [m^6/$molecule^2$/s]	n_r	E_{ar}/k [K]
1	$O_2+N \leftrightarrow O+O+N$	5.99×10^{-12}	-1	59500	8.30×10^{-45}	-0.5	0.0
2	$O_2+NO \leftrightarrow O+O+NO$	5.99×10^{-12}	-1	59500	8.30×10^{-45}	-0.5	0.0
3	$O_2+N_2 \leftrightarrow O+O+N_2$	1.20×10^{-11}	-1	59500	1.66×10^{-44}	-0.5	0.0
4	$O_2+O_2 \leftrightarrow O+O+O_2$	5.39×10^{-11}	-1	59500	7.47×10^{-44}	-0.5	0.0
5	$O_2+O \leftrightarrow O+O+O$	1.50×10^{-10}	-1	59500	2.07×10^{-43}	-0.5	0.0
6	$N_2+O \leftrightarrow N+N+O$	3.18×10^{-13}	-0.5	113200	3.01×10^{-44}	-0.5	0.0
7	$N_2+O_2 \leftrightarrow N+N+O_2$	3.18×10^{-13}	-0.5	113200	3.01×10^{-44}	-0.5	0.0
8	$N_2+NO \leftrightarrow N+N+NO$	3.18×10^{-13}	-0.5	113200	3.01×10^{-44}	-0.5	0.0
9	$N_2+N_2 \leftrightarrow N+N+N_2$	7.97×10^{-13}	-0.5	113200	7.51×10^{-44}	-0.5	0.0
10	$N_2+N \leftrightarrow N+N+N$	6.90×10^{-8}	-1.5	113200	6.42×10^{-39}	-1.5	0.0
11	$NO+N_2 \leftrightarrow N+O+N_2$	6.59×10^{-10}	-1.5	75500	2.78×10^{-40}	-1.5	0.0
12	$NO+O_2 \leftrightarrow N+O+O_2$	6.59×10^{-10}	-1.5	75500	2.78×10^{-40}	-1.5	0.0
13	$NO+NO \leftrightarrow N+O+NO$	1.32×10^{-8}	-1.5	75500	5.57×10^{-39}	-1.5	0.0

14	NO+O↔N+O+O	1.32×10^{-8}	-1.5	75500	5.57×10^{-39}	-1.5	0.0
15	NO+N↔N+O+N	1.32×10^{-8}	-1.5	75500	5.57×10^{-39}	-1.5	0.0

Table 8.2 Gupta kinetic model for exchange reactions

No	Reactions	C_f [m^3/molecule/s]	n_f	E_{af}/k [K]	C_r [m^3/molecule/s]	n_r	E_{ar}/k [K]
16	NO+O↔O_2+N	5.28×10^{-21}	1.0	19220	1.60×10^{-18}	0.5	3580
17	N_2+O↔NO+N	1.12×10^{-16}	0.0	38400	2.49×10^{-17}	0.0	0.0

Park provides the forward reaction rate coefficients expressed in the Arrhenius-like equation:

$$k_f = C_f T_c^{n_f} \exp\left(-\frac{E_{a_f}}{kT_c}\right) \tag{8.2}$$

where T_c is the temperature controlling the reaction. This temperature takes into account the influence of the vibrational temperature on the rates of reaction. Park assumes that T_c is a function of the geometrical mean temperature between transitional and vibrational temperatures:

$$T_c = T^{\phi} T_v^{(1-\phi)} \tag{8.3}$$

according to Park [18], ϕ=0.5 for dissociation/recombination reactions and ϕ=1.0 for exchange reactions.

The reverse rate coefficient (k_r) is computed by the ratio of the forward rate coefficient (k_f) and the equilibrium constant (K_e): $k_r=k_f/K_e$. For reactions 1 to 10 and for reactions 16 and 17, the equilibrium constant is computed by [18]:

$$K_e(T) = \exp[A_1 / Z + A_2 + A_3 \ln(Z) + A_4 Z + A_5 Z^2] \tag{8.4}$$

For reactions 11 to 15, the equilibrium constant is computed by [19]:

$$K_e(T) = \exp[A_1 + A_2 \ln(Z) + A_3 Z + A_4 Z^2 + A_5 Z^3] \tag{8.5}$$

where Z=10000/T. Table 8.3 reports the pre-exponential factors, the temperature exponents, the ratios of activation energies and the Boltzmann constant and the equilibrium constant coefficients.

Table 8.3 Park kinetic model for dissociation/recombination and exchange reactions

No	Reactions	C_f [m^3/molecule/s]	n_f	E_{af}/k [K]	A_1	A_2	A_3	A_4	A_5
1	$O_2+N \leftrightarrow O+O+N$	1.66×10^{-8}	-1.5	59500	2.855	0.988	-6.181	-0.023	-0.001
2	$O_2+NO \leftrightarrow O+O+NO$	3.32×10^{-9}	-1.5	59500	2.855	0.988	-6.181	-0.023	-0.001
3	$O_2+N_2 \leftrightarrow O+O+N_2$	3.32×10^{-9}	-1.5	59500	2.855	0.988	-6.181	-0.023	-0.001
4	$O_2+O_2 \leftrightarrow O+O+O_2$	3.32×10^{-9}	-1.5	59500	2.855	0.988	-6.181	-0.023	-0.001
5	$O_2+O \leftrightarrow O+O+O$	1.66×10^{-8}	-1.5	59500	2.855	0.988	-6.181	-0.023	-0.001
6	$N_2+O \leftrightarrow N+N+O$	4.98×10^{-8}	-1.6	113200	1.858	-1.325	-9.856	-0.174	0.008
7	$N_2+O_2 \leftrightarrow N+N+O_2$	1.16×10^{-8}	-1.6	113200	1.858	-1.325	-9.856	-0.174	0.008
8	$N_2+NO \leftrightarrow N+N+NO$	1.16×10^{-8}	-1.6	113200	1.858	-1.325	-9.856	-0.174	0.008
9	$N_2+N_2 \leftrightarrow N+N+N_2$	1.16×10^{-8}	-1.6	113200	1.858	-1.325	-9.856	-0.174	0.008
10	$N_2+N \leftrightarrow N+N+N$	4.98×10^{-8}	-1.6	113200	1.858	-1.325	-9.856	-0.174	0.008
11	$NO+N_2 \leftrightarrow N+O+N_2$	8.30×10^{-15}	0.0	75500	0.792	-0.492	-6.761	-0.091	0.004
12	$NO+O_2 \leftrightarrow N+O+O_2$	8.30×10^{-15}	0.0	75500	0.792	-0.492	-6.761	-0.091	0.004
13	$NO+NO \leftrightarrow N+O+NO$	1.83×10^{-13}	0.0	75500	0.792	-0.492	-6.761	-0.091	0.004
14	$NO+O \leftrightarrow N+O+O$	1.83×10^{-13}	0.0	75500	0.792	-0.492	-6.761	-0.091	0.004
15	$NO+N \leftrightarrow N+O+N$	1.83×10^{-13}	0.0	75500	0.792	-0.492	-6.761	-0.091	0.004
16	$NO+O \leftrightarrow O_2+N$	1.39×10^{-17}	0.0	19400	-1.840	-1.768	-4.759	1.154	-0.239
17	$N_2+O \leftrightarrow NO+N$	9.46×10^{-18}	0.42	42938	-3.032	0.078	-7.693	1.411	-0.517

The handling of the chemical processes in a DSMC code is different from the one in a CFD code, in fact a DSMC code does not rely on the rate equation (Eq. 8.1) but uses only the pre-exponential factor ($C_{f,r}$) and the temperature exponent ($n_{f,r}$) to calculate the reaction probability (or steric factor [1]). For this reason, in order to implement the reverse reaction rates of the Park model in DS2V or to define $C_{f,r}$ and n_r, the curves, best-fitting the values k_f/K_e as a function of temperature, have been evaluated in the form of Eq. 8.1. Tables 8.4 and 8.5 report the pre-exponential factors and the exponent coefficients of the fitting curves. Figs. 8.2(a) to (e) show the comparison of the present curves with the ones from the Park reverse reaction rate in the temperature interval 3000-13000 K.

For a direct comparison of the Gupta and Park models, Figs.8.3(a) to (f) show the profiles of forward and backward reaction rates for some reactions as a function of temperature in the interval 3000-13000 K. These reactions have been chosen because are the most frequent in the present runs. Figures show that: a) the reaction rate coefficients are comparable, b) neither the Gupta model nor the Park model is always prevalent with respect to the other one.

Table 8.4 Reaction rate coefficients of the reverse (recombination) equations approximating the Park model

No	Reactions	C_r [m^6/molecule^2/s]	n_r	E_{ar}/k [K]
1	$O_2+N \leftrightarrow O+O+N$	4.41×10^{-42}	-0.8	0.0
2	$O_2+NO \leftrightarrow O+O+NO$	8.82×10^{-43}	-0.8	0.0
3	$O_2+N_2 \leftrightarrow O+O+N_2$	8.82×10^{-43}	-0.8	0.0
4	$O_2+O_2 \leftrightarrow O+O+O_2$	8.82×10^{-43}	-0.8	0.0
5	$O_2+O \leftrightarrow O+O+O$	4.41×10^{-42}	-0.8	0.0
6	$N_2+O \leftrightarrow N+N+O$	1.01×10^{-38}	-1.7	0.0
7	$N_2+O_2 \leftrightarrow N+N+O_2$	2.35×10^{-39}	-1.7	0.0
8	$N_2+NO \leftrightarrow N+N+NO$	2.35×10^{-39}	-1.7	0.0
9	$N_2+N_2 \leftrightarrow N+N+N_2$	2.35×10^{-39}	-1.7	0.0
10	$N_2+N \leftrightarrow N+N+N$	1.01×10^{-38}	-1.7	0.0
11	$NO+N_2 \leftrightarrow N+O+N_2$	2.76×10^{-40}	-1.5	0.0
12	$NO+O_2 \leftrightarrow N+O+O_2$	2.76×10^{-40}	-1.5	0.0
13	$NO+NO \leftrightarrow N+O+NO$	5.51×10^{-39}	-1.5	0.0
14	$NO+O \leftrightarrow N+O+O$	5.51×10^{-39}	-1.5	0.0
15	$NO+N \leftrightarrow N+O+N$	5.51×10^{-39}	-1.5	0.0

Table 8.5 Reaction rate coefficients of the reverse (exchange) equations approximating the Park model

No	Reactions	C_r [m^3/molecule/s]	n_r	E_{ar}/k [K]
16	$NO+O \leftrightarrow O_2+N$	4.32×10^{-15}	-0.5	3580
17	$N_2+O \leftrightarrow NO+N$	4.65×10^{-20}	0.75	0.0

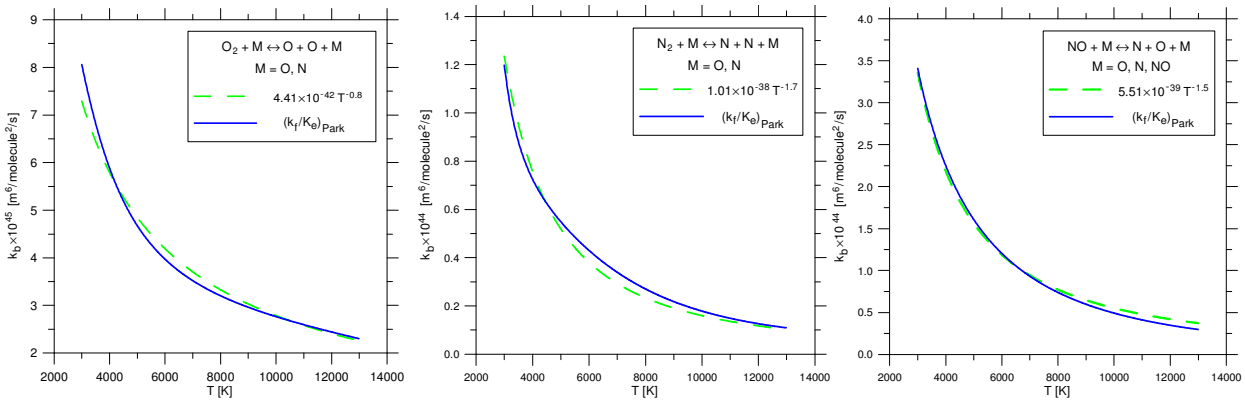

(a) (b) (c)

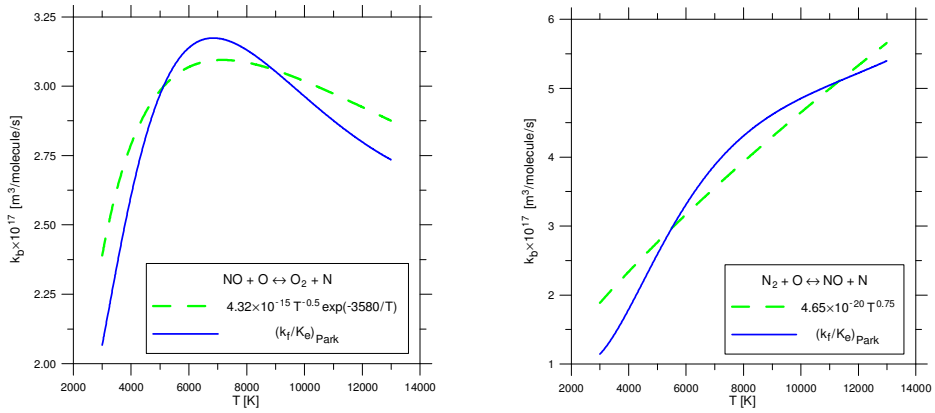

(d) (e)

Figure 8.2 Profiles of reverse reaction rate coefficients:
(a) $O_2 + M \leftrightarrow O + O + M$ (M=O, N), (b) $N_2 + M \leftrightarrow N + N + M$, (M=O, N),
(c) $NO + M \leftrightarrow N + O + M$ (M=O, N, NO), (d) $NO + O \leftrightarrow O_2 + N$,
(e) $N_2 + O \leftrightarrow NO + N$

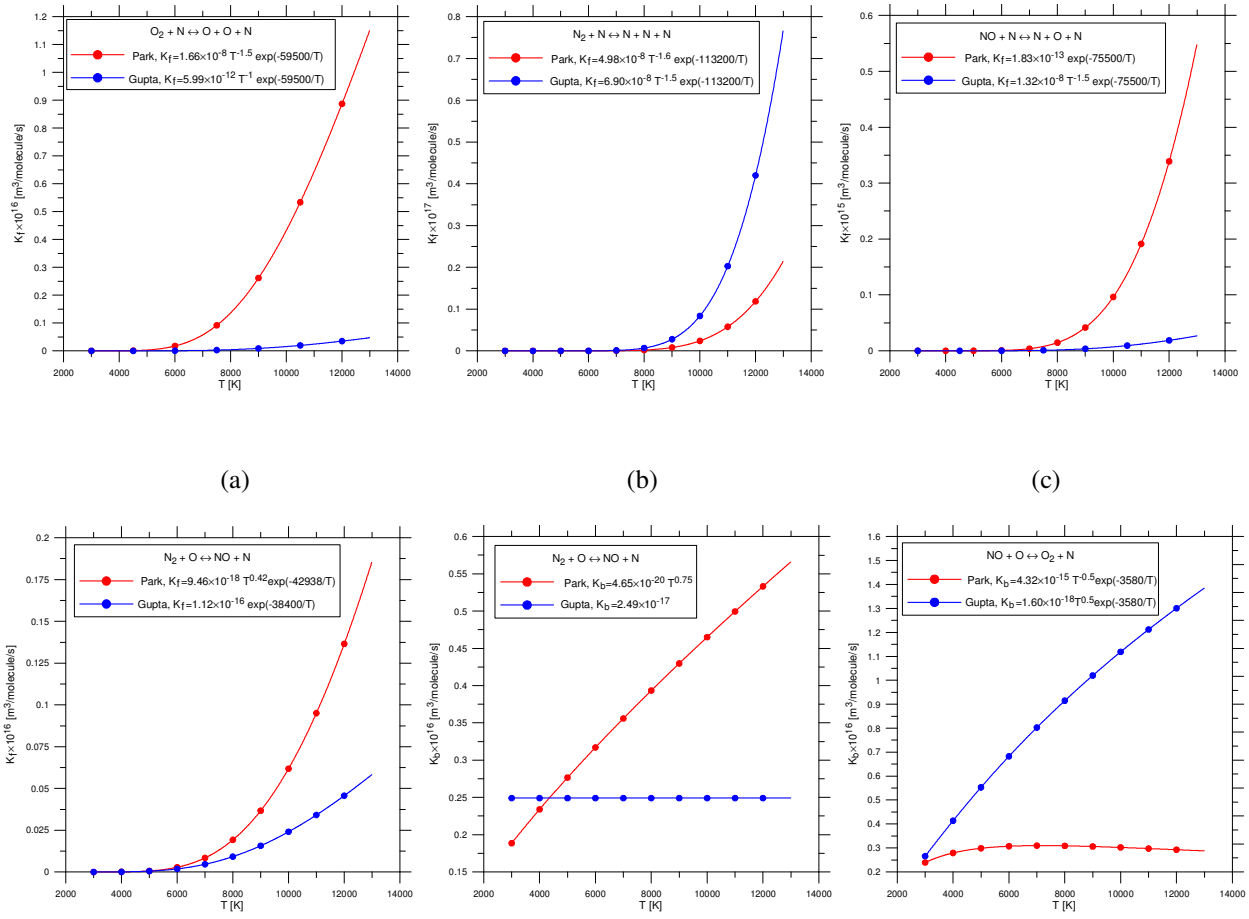

(a) (b) (c)

(d) (e) (f)

Figure 8.3 Profiles of the forward (a,b,c,d) and backward (e,f) of some reactions by the Gupta and the Park models

8.3 Test Conditions

Tables 8.6 and 8.7 report the input data to both codes for EXPERT and for ORION. The free stream thermodynamic parameters are provided by the US standard Atmosphere. According to the test matrices the wall temperature of EXPERT is 300 K in the whole altitude interval 65.2-104.5 km [40], of ORION ranges from 1464 to 494 K in the altitude interval 75.0-125.0 km [43]. The surface recombination reactions, implemented in both codes, are: $O+O \rightarrow O_2$, $N+N \rightarrow N_2$ and $N+O \rightarrow NO$.

Table 8.6 Input data for EXPERT

H [km]	T_∞ [K]	n_∞ [1/m^3]	α_{O_2}	α_{N_2}	α_O	V_∞ [m/s]	T_w [K]
65.2	233	3.30×10^{21}	0.2095	0.7808	0.0097	5045	300
69.8	220	1.77×10^{21}	0.2095	0.7808	0.0097	5047	300
74.9	209	8.42×10^{20}	0.2095	0.7808	0.0097	5043	300
84.9	189	1.74×10^{20}	0.2095	0.7808	0.0097	5028	300
95.2	189	2.81×10^{19}	0.1983	0.7766	0.0251	5009	300
104.5	208	5.48×10^{18}	0.1544	0.7731	0.0725	4992	300

Table 8.7 Input data for ORION

H [km]	T_∞ [K]	n_∞ [1/m^3]	α_{O_2}	α_{N_2}	α_O	V_∞ [m/s]	T_w [K]
75.0	208	8.30×10^{20}	0.2095	0.7808	0.0097	7600	1464
85.0	189	1.71×10^{20}	0.2095	0.7808	0.0097	7600	1184
95.0	189	2.92×10^{19}	0.1988	0.7767	0.0245	7600	951
105.0	210	5.03×10^{18}	0.1516	0.7729	0.0755	7600	760
115.0	299	9.81×10^{17}	0.1001	0.7490	0.1509	7600	618
125.0	416	3.03×10^{17}	0.0777	0.7085	0.2138	7600	494

The computational domain of DS2V was a rectangle in the meridian plane: for EXPERT L_x=3.3 m and L_y=1.8 m, for ORION L_x=6.0 m and L_y=4.5 m. For all runs, the simulation time was longer than 5 times the time necessary to cross the computing region along the x direction at the free stream velocity ($\cong7\times10^{-4}$ s for EXPERT and $\cong8\times10^{-4}$ s for ORION). This simulation time can be considered long enough for stabilizing all thermo-aerodynamic parameters. In order to satisfy the condition that mcs/λ is less that 0.2, a 64-bit version of DS2V was used, making possible simulations with a number of about 50 millions of molecules.

The computation domain of H3NS was a grid, following the shock wave profile. The grid was obtained by subsequent grid refinement until the solution stabilized, i.e. did not show any

meaningful variation. The grid for EXPERT was made up of 5200 cells, the one for ORION of 42400 cells. The convergence of solution was obtained when the maximum and the average residuals were stabilized and when the heat flux, that is the most sensitive variable, did not change during the iterations. Figs. 8.4(a) and (b) show the CFD optimal computational grids for EXPERT and ORION, respectively.

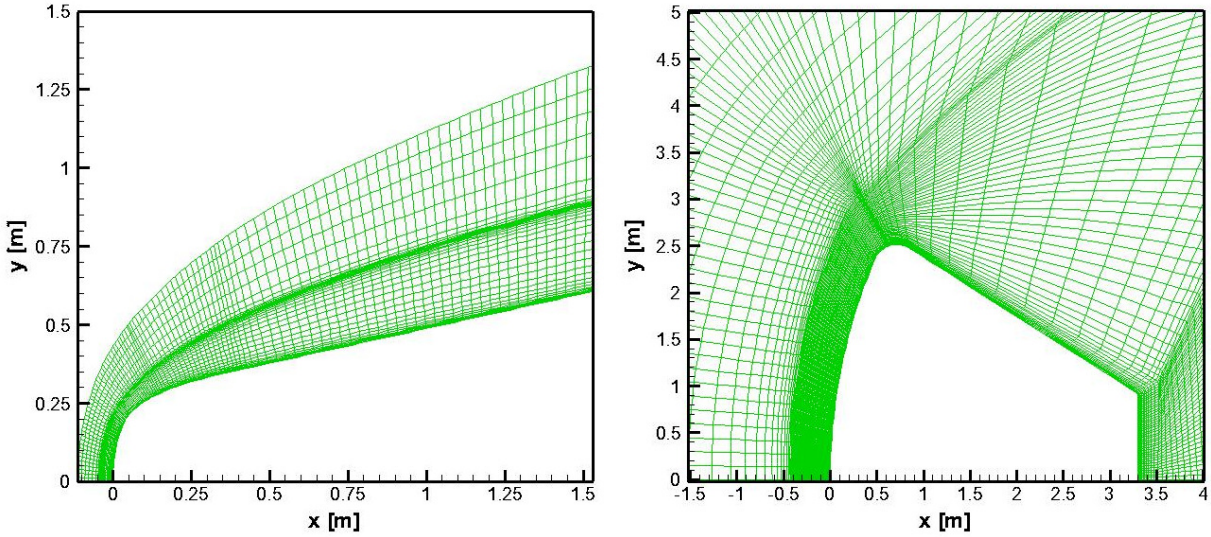

(a) (b)

Figure 8.4 CFD computational grid for EXPERT (a) and for ORION (b)

8.4 Analysis of Results

A. Comparison between the results from DS2V and H3NS

As the chemical effects increase with decreasing rarefaction, considering the lowest altitudes for EXPERT (h=69.8 km) and for ORION (h=85.0 km) is proper. At these altitudes the two capsules are at different Mach numbers (17 for EXPERT and 28 for ORION), this produces for ORION a stronger shock wave and therefore a stronger dissociation. On the other hand, the related Knudsen numbers are comparable: 1.1×10^{-3} for EXPERT, 2.0×10^{-3} for ORION. Thus the rarefaction similarity is achieved.

Figures 8.5(a) and (b) show the profiles of heat flux by DS2V and H3NS, considering both non-reactive and fully catalytic surface, along the EXPERT nose (a) and along the ORION surface (b). It must be pointed out that in the present study, the slip corrections, besides being very small, seem to be not proper. In fact, as shown in Fig. 8.5(b), for the case of fully catalytic

surface, the slip corrections amplify instead of reducing the deviation of the H3NS results from the DS2V ones. Similar condition was obtained also for other cases. For this reason, the comparison with the DS2V results relies on those obtained without slip corrections. On the other hand, as verified by Votta et al. [43], the slip effects are proper only for the correction of primary quantities such as pressure, temperature and so on.

The profiles of heat flux are in agreement with what expected by the different geometries or with the different aspect ratios of both capsules. The profile on the EXPERT nose is typical of slender bodies, i.e. heat flux decreases quickly on the first part of the body (roughly up to x=0.4 m) and then keeps practically constant. The profile on ORION is typical of blunt bodies, i.e. heat flux is about constant along the cap surface. Furthermore for ORION, a peak of heat flux is predicted by H3NS in the shoulder region. The peak is probably linked to a strong expansion and therefore to an high skin friction. On the opposite, DS2V seems to be not able to predict clearly the heat flux peak.

For both capsules and for both surface conditions, heat flux computed by DS2V is always higher than the one computed by H3NS. The mismatch between the two codes decreases for fully catalytic surface. For instance at the stagnation point, the percentage differences are 38% for EXPERT and 87% for ORION for non-reactive surface, the differences are 7% for EXPERT and 12% for ORION for fully catalytic surface. This can be justified because the fully catalytic surface reduces the differences of gas composition generated in the flow field, thus only the differences related to the different approach of the two codes exist.

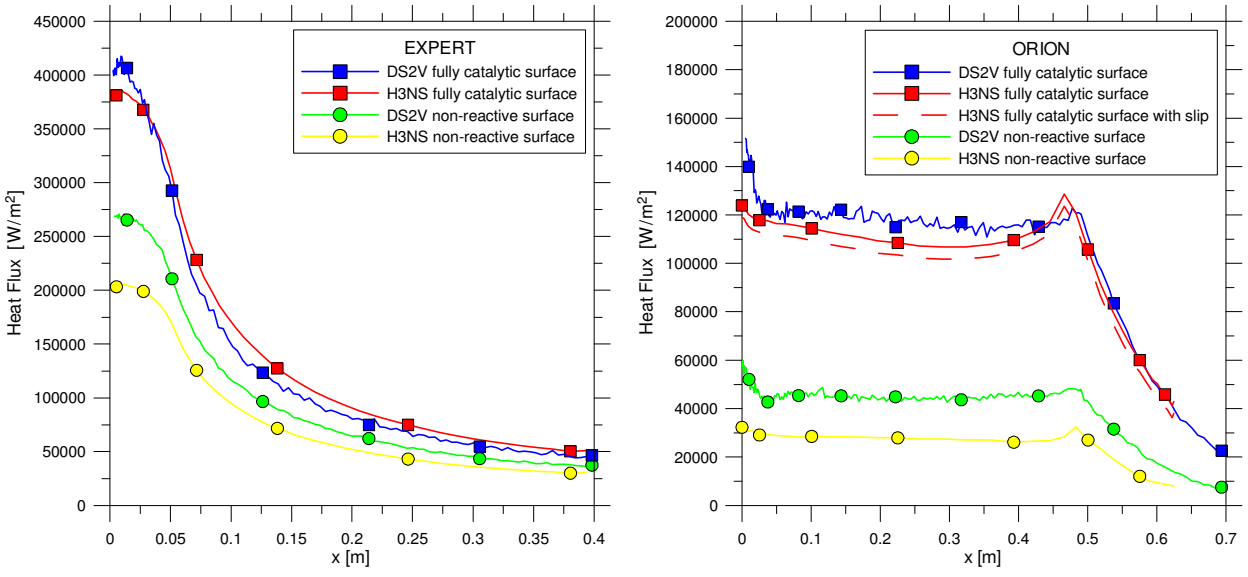

(a) (b)

Figure 8.5 Heat flux profiles along the EXPERT nose at 69.8 km (a) and along the ORION surface at 85 km (b)

It is important to point out that, for fully catalytic surface, DS2V is characterized by a lower recombination capability with respect to H3NS. In fact, as shown in Figs. 8.6(a) and (b), near the surface the molar fraction of N_2 computed by DS2V is pretty similar to the one computed by H3NS, but the molar fraction of O_2 computed by DS2V is less than the one computed by H3NS. This is typical of a DSMC approach. In fact, the surface recombination occurs when two possible recombining atoms impact the surface at the same time and at the same point but, if the impinging particles are a molecule and an atom, the atom is re-emitted from the surface without recombining. The higher formation of NO (Fig. 8.6(c)) is not enough to compensate the lower recombination of O_2 and N_2. In fact, as shown in Fig.8.8, even though the surface has been set as fully catalytic, along the surface the molar fractions of O and N are not zero.

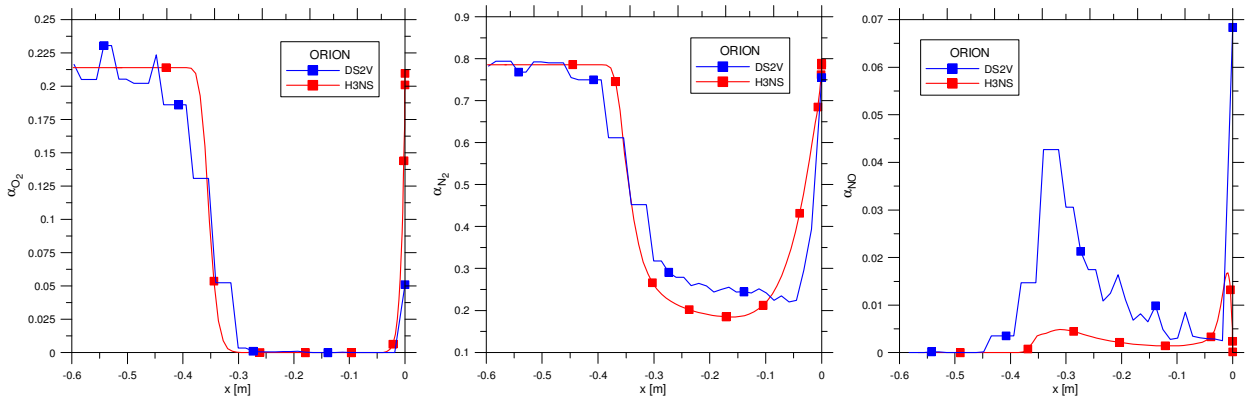

(a) (b) (c)

Figure 8.6 Molar fraction of O, N and NO along the stagnation line of ORION: fully catalytic surface, h=85 km

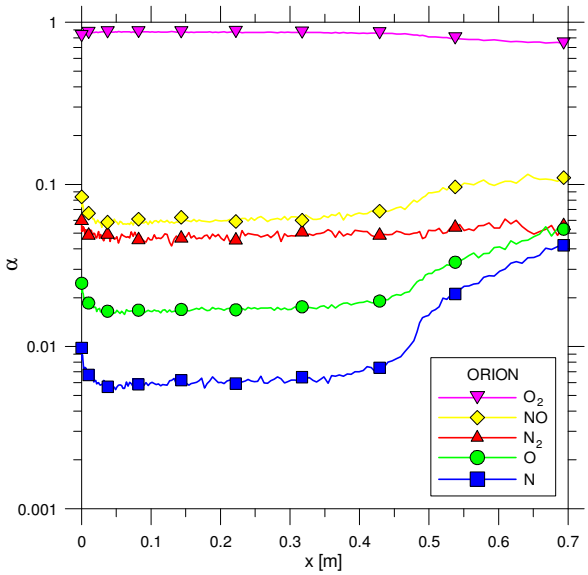

Figure 8.7 Molar fractions along the ORION surface: fully catalytic surface, h=85 km

The overestimation of heat flux (Figs. 8.5(a) and (b)), for non-catalytic surface by DS2V is due mostly to a lower dissociation of O_2 and N_2. In fact, as shown in Figs. 8.8(a) and (b), the molar fraction of O and N along the stagnation line of EXPERT at h=69.8 km computed by H3NS are higher than the ones computed by DS2V. This involves that a larger amount of energy is spent for dissociation, thus a lower amount of energy is exchanged with the surface. At the same time, DS2V computes a slightly higher molar fraction of NO (Fig. 8.8(c)), therefore a slightly higher amount of energy is recovered by the formation of this species.

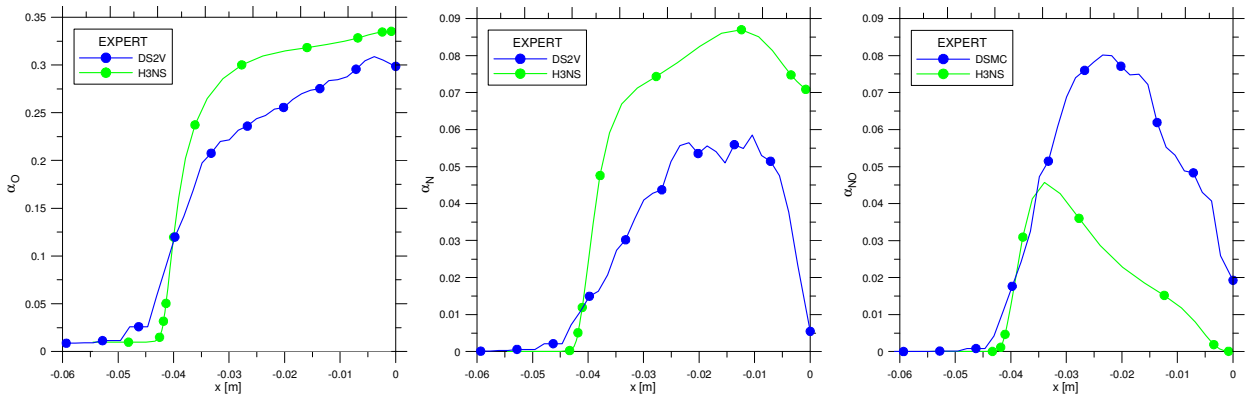

(a) (b) (c)

Figure 8.8 Molar fraction of O, N and NO along the stagnation line of EXPERT: non-reactive surface, h=69.8 km

The condition that the heat flux, computed by DS2V, is higher than the one computed by H3NS is met also at other altitudes. Figs. 8.9(a) and (b) show the heat flux at the stagnation point of EXPERT (a) and of ORION (b). For both codes, the effect of catalyticity increases with decreasing altitude. This can be explained, from a physical point of view because, with increasing density, dissociation in the flow and recombination on the surface increase.

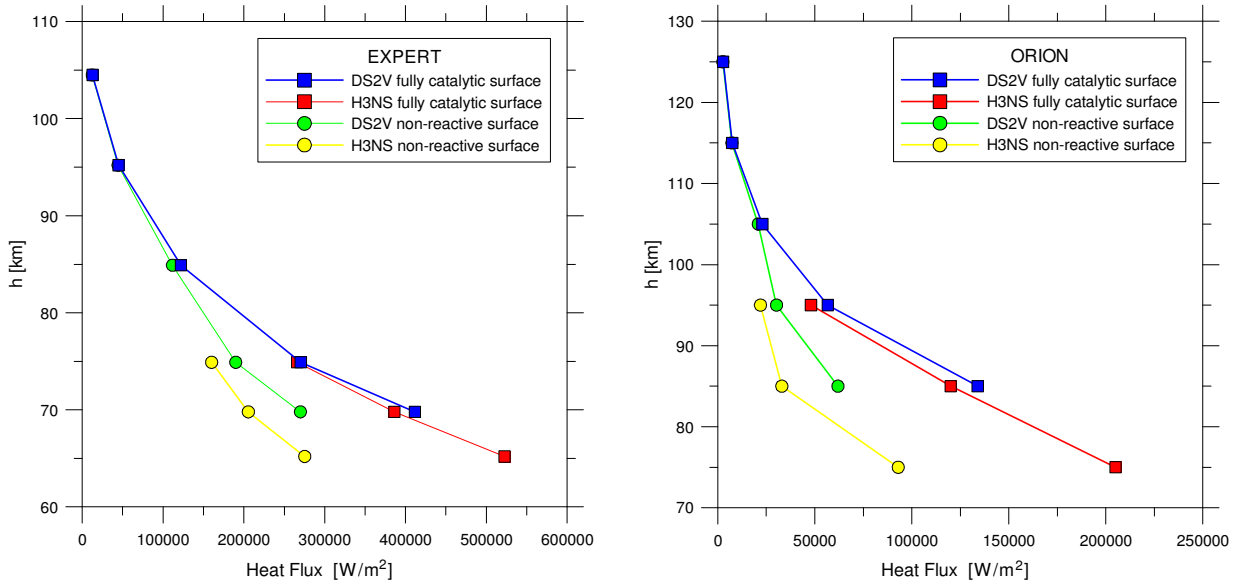

(a) (b)

Figure 8.9 Heat flux at the stagnation point vs altitude for EXPERT (a) and for ORION (b)

B. Comparison between the DS2V results using the Gupta and the Park chemical models

As shown before, the heat flux computed by DS2V, both for non-reactive and fully catalytic surface, is higher than the one computed by H3NS. Therefore, verifying the incidence of the different chemical models is proper. To this aim, the Park model has been implemented also in DS2V.

Figures 8.10(a) to (f) show the profiles of molar fraction of O, N and NO along the stagnation lines across the shock layer of the two capsules, computed by the two chemical models. The two models at the fluid-dynamic condition or temperature in the shock wave of EXPERT (maximum temperature is about 10000 K) and of ORION (maximum temperature is about 23000 K) compute a different composition in the flow field. In fact, the percentage variation of the absolute value of the molar fractions of O, N and NO, averaged along the stagnation line across the shock layer, computed by the two chemical models, are: 36%, 33% and 43% for EXPERT and 112%, 93 % and 110% for ORION. However, using the Park model in DS2V does not generate any match of the molar fractions of O, N and NO with the ones computed by H3NS. This is well apparent for the EXPERT capsule by the comparison of the Figures 8.10(a) to (c) with the Figures 8.8(a) to (c).

However, air composition, computed by the two models at the stagnation point of both capsules are not very different (see Tables 8.8 and 8.9). This can be justified because, as already shown in

Figs. 8.3(a) to (f), decreasing temperature the difference of rate coefficients by both models tend to reduce. For this reason, the chemical models do not influence meaningfully the computation of heat flux. In fact, as shown in Figs. 8.11(a) and (b), the heat flux, computed by the two models along the nose of EXPERT and along the surface of ORION, are practically the same. However, it has to be pointed out that, for an unknown reason, the runs of DS2V by Park were able to reach a steady state condition more quickly compared with the runs by Gupta. Furthermore it look that the profiles of heat flux by Park appear to be more smooth than the ones by Gupta (Fig. 8.11(a) and (b)).

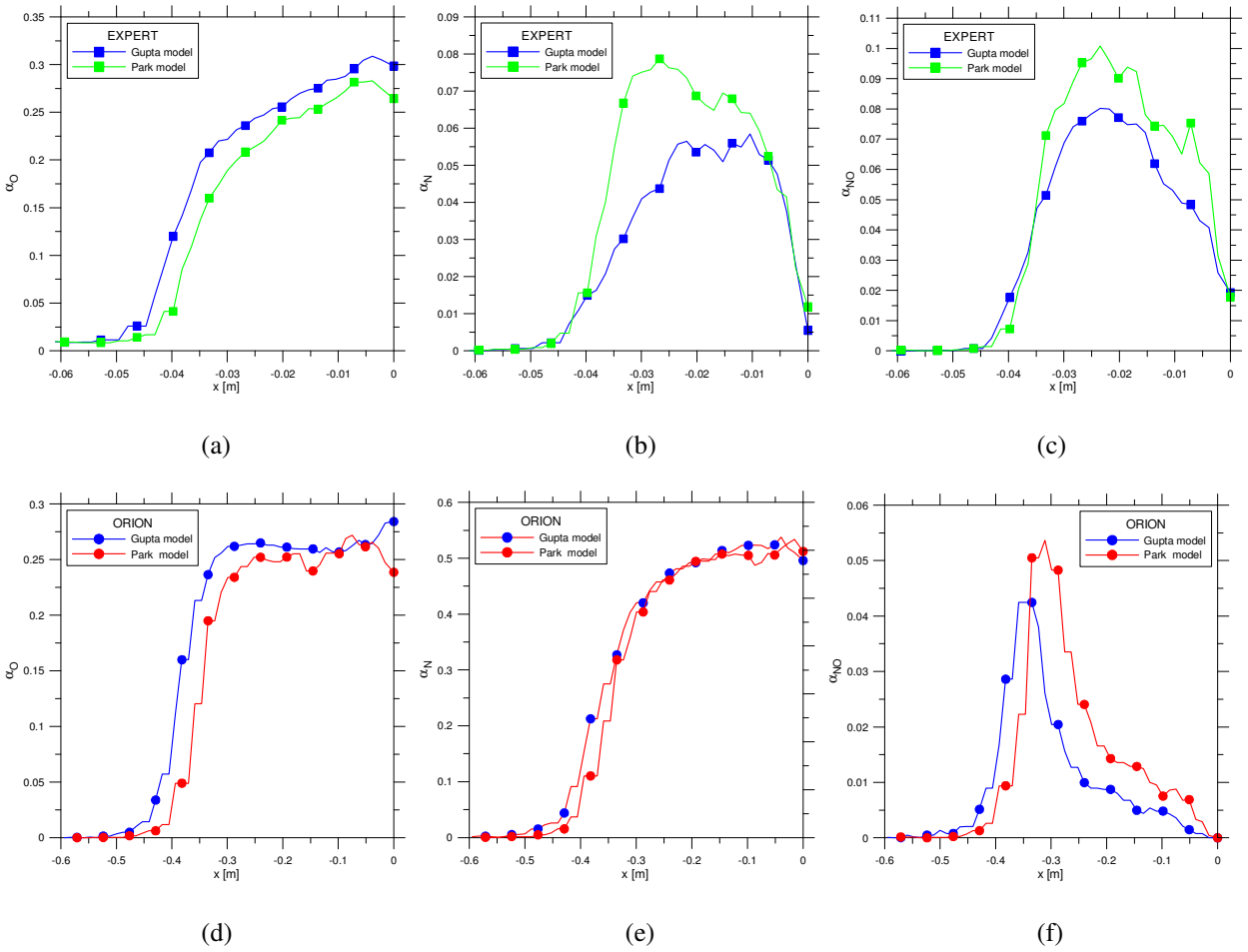

Figure 8.10 Molar fraction of O, N and NO along the stagnation line of EXPERT (a) to (c) (h=69.8 km) and ORION (d) to (f) (h=85.0 km): non-reactive surface

Table 8.8 Molar fractions at the stagnation point of EXPERT: h=69.8 km, non-reactive surface

Chemical Model	α_{O_2}	α_{N_2}	α_O	α_N	α_{NO}
Gupta	0.0038	0.6305	0.3459	0.0096	0.0102
Park	0.0032	0.6223	0.3429	0.0116	0.0200

Table 8.9 Molar fractions at the stagnation point of ORION: h=85.0 km, non-reactive surface

Chemical Model	α_{O_2}	α_{N_2}	α_O	α_N	α_{NO}
Gupta	0	0.1868	0.2748	0.5384	0
Park	0	0.2202	0.2492	0.5306	0

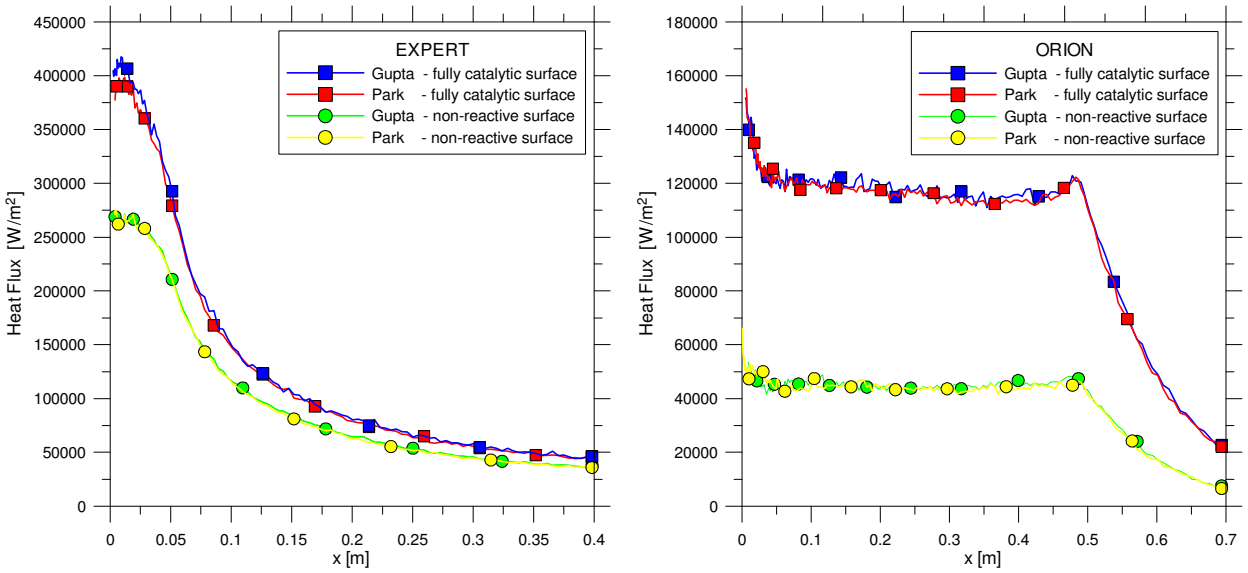

(a) (b)

Figure 8.11 Heat Flux profile along the EXPERT nose (a) and the ORION surface (b) by DS2V with the Park and the Gupta models

C. Influence of dissociation

As shown, DS2V and H3NS compute different composition both in the flow field and on the surface, even implementing the same chemical model (Park). The difference in the computation of heat flux can be attributed to the different approaches but mostly to the different handling of the chemical process that produces higher dissociation of O_2 and N_2 by H3NS with respect to DS2V. The influence of the higher level of dissociation can be verified when DS2V implements only the forward reactions. This condition can be considered as a limit case in which no recombination occurs, therefore the level of dissociation is maximum. As shown in Figures 8.12(a) and (b), when DS2V implements only the forward reactions, the profiles of heat flux, for both capsules, are closer to the ones by H3NS and the profiles by DS2V, implementing Park, even overlap the ones by H3NS. It is also shown (Fig. 8.12(a) and (b)) that, considering only the forward reactions, the difference in the computation of heat flux between Gupta and Park models is highlighted.

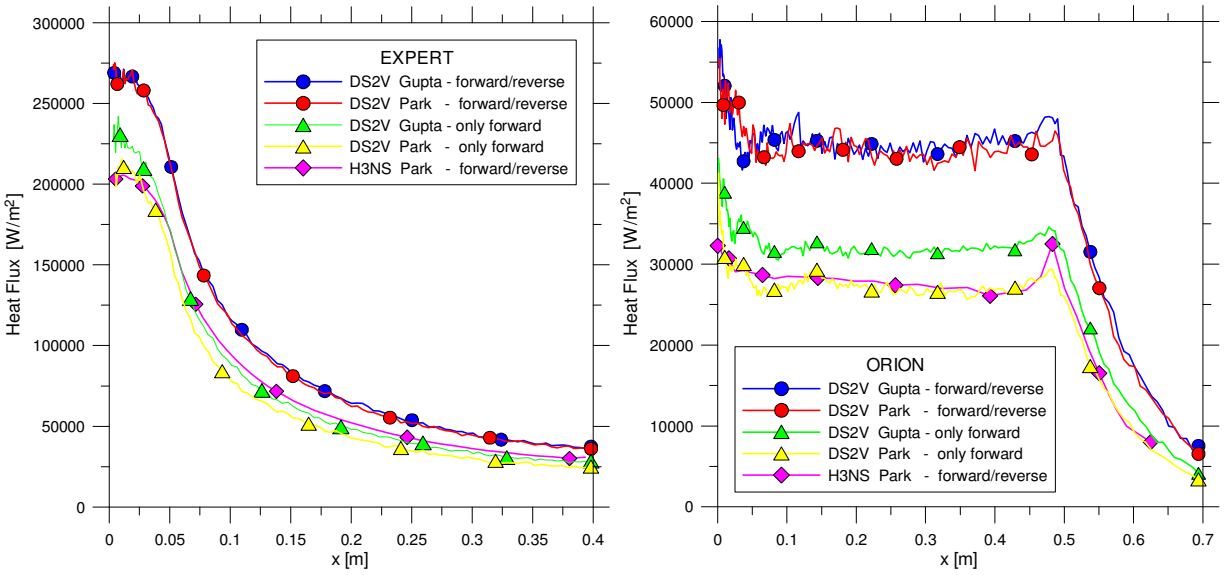

(a) (b)

Figure 8.12 Heat Flux profile along the EXPERT nose (a) and the ORION surface (b) by H3NS, implementing forward and reverse reactions and by DS2V, implementing only the forward reactions by the Park and the Gupta models

8.5 Conclusions

In order to deepen the comparison of heat flux, at high altitude flight, by two codes based on different approaches, the computation of heat flux on EXPERT and on ORION capsules, has been carried out by a direct simulation Monte Carlo code (DS2V) and by a computational fluid dynamic code (H3NS), considering both non-reactive and fully catalytic surface. DS2V and H3NS rely on the Gupta and on the Park chemical models, respectively. The capsules have been chosen because characterized by completely different shapes and re-entry trajectories, therefore by different fluid-dynamic conditions as per the Mach number.

Heat flux was evaluated in the altitude interval 65-105 km for EXPERT and 75-125 km for ORION. Heat flux by DS2V is always higher than the one by H3NS, but the mismatch between the two codes decreases for fully catalytic surface. This is justified because the fully catalytic surface reduces the differences of chemical model and keeps only the ones related to the different approach on which the two codes rely. On the other hand the overestimation of heat flux by DS2V, for non-reactive surface, is due mostly to a lower dissociation of O_2 and N_2 and to an higher formation of NO.

To assess the incidence of the chemical models, the Park model was implemented also in DS2V. The results showed that the two chemical models compute a different composition in the flow field but the same composition on the surface and therefore the same heat flux. However, using the Park model in DS2V does not generate any match of the molar fractions of O, N and NO with the ones computed by H3NS. Therefore DS2V and H3NS compute a different composition both in the flow field and on the surface, even implementing the same model (Park). For this reason the difference in the computation of heat flux between DS2V and H3NS can be attributed to the different approaches but mostly to the different handling of the chemical process.

CHAPTER IX

Analysis of Transport Properties for Gupta and Park without ionization

9.1 Introduction

The present chapter is the natural completion of the chapter 8 in which the effects of the chemical models by Gupta [16] and by Park [18, 19, 20] were evaluated on the computation of heat flux on the EXPERT and ORION capsules along the high altitude re-entry path. The analysis was fulfilled by implementing also the Park model in the DS2V [12] code that uses, in its original version, the Gupta model. Computer tests were carried out between 70-105 km for EXPERT and 85-125 km for ORION and by both non-reactive and fully-catalytic surface. The results showed that the two models compute different compositions in the flow field but practically the same composition on the surface, therefore practically the same heat flux.

In the present study the effects of the different compositions as well as of the different thermo-dynamic quantities, by the two chemical models, are evaluated on: non-equilibrium parameters, local mean free path and local Knudsen numbers, local transport coefficients and local characteristic numbers of Prandtl, Lewis and Schmidt. As well known, these numbers play an important role in the diffusion process of energy and therefore in the heat flux.

Tests, already ran for the purpose of the chapter 8 and here processed, are those at h=70 km for EXPERT and at h=85 km for ORION, where both capsules are in continuum, low density regime. These altitudes have been chosen because low enough to highlight the chemical effects. The choice of EXPERT and ORION was proper for the purposes of both the present and the former analysis. In fact, these capsules generate completely different fluid-dynamic conditions, produced by different shock wave intensities, due both to different radius of the nose of EXPERT (0.6 m) and of the cap of ORION (6.04 m) and to different free stream Mach numbers. In fact, at h=70 km and h=85 km, the Mach numbers are 17 for EXPERT and 28 for ORION, producing maximum temperatures in the shock wave of about 10000 K and 23000 K, respectively. Furthermore, at these altitudes the capsules are characterized by comparable free stream Knudsen numbers therefore by practically the same overall rarefaction level.

Even though the ionization process occurs during the re-entry path, in the former application it was neglected. The aim of that paper, in fact, was to compare the two chemical models in their basic aspects or in dissociation, recombination and exchange reactions. Therefore, air was considered as made up of five species: O_2, N_2, O, N and NO, relying on 17 forward/backward chemical reactions. Furthermore, the tests considered in the present study are related to non-catalytic surface. This is because the condition of fully catalytic surface reduces the difference in the chemical composition in the flow field close to the surfaces. The transport parameters are computed by the Chapman-Enskog method [50] for temperatures less than 1000 K and by the Gupta-Yos-Thompson method [16] for temperatures greater than 1000 K.

The effects of the chemical models are analyzed qualitatively by the comparison of the profiles of the thermo-fluid-dynamic quantities along the stagnation line across the shock layer and quantified by the maximum values and by the absolute percentage variation of each quantity computed by the Gupta and by the Park model, averaged along the stagnation line.

9.2 Diffusion Characteristic Numbers and Transport Coefficients

The diffusion characteristic numbers of Prandtl (Pr_{mix}), Lewis (Le_{mix}) and Schmidt (Sc_{mix}) are computed considering the transport coefficients of the mixture:

$$Pr_{mix} = \frac{c_{pmix}\mu_{mix}}{K_{mix}}, \qquad Le_{mix} = \frac{\rho D_{mix} c_{pmix}}{K_{mix}}, \qquad Sc_{mix} = \frac{\rho D_{mix}}{\mu_{mix}}$$

In the present study two models, computing the transport coefficients both of each single species and of the mixture have been implemented: the Chapman-Enskog [50] and the Gupta-Yos-Thompson models [16]. Palmer and Wright [51] suggest to use the Gupta's mixing rule for high speed and high temperature flows therefore, in this application, the Chapman-Enskog model is used for T<1000 K and the Gupta-Yos-Thompson model is used for T≥1000 K.

Chapman-Enskog Model

Viscosity μ [kg/m/s] of the i^{th} species is computed, as a function of temperature, by:

$$\mu_i = 2.6693\times10^{-6}\frac{\sqrt{M_i T}}{\sigma_i^2 \Omega_{ii}^{(2,2)}} \tag{9.1}$$

where: M_i is the molecular mass [kg/kmoles] , σ_i is the collision diameter (in Å), $\Omega_{ii}^{(2,2)}$ is the viscosity collision integral, function of T/ε_i, ε_i is the Lennard-Jones parameter. Viscosity of a mixture is evaluated by the Wilke rule [50]:

$$\mu_{mix} = \sum_{i=1}^{n} \frac{\alpha_i \mu_i}{\sum_{j=1}^{n} \alpha_j \Phi_{i,j}} \tag{9.2}$$

where: α_i is the molar fraction of the i^{th} species and Φ is the dimensionless function:

$$\Phi_{i,j} = \frac{1}{\sqrt{8}} \left(1 + \frac{M_i}{M_j} \right)^{-1/2} \left[1 + \left(\frac{\mu_i}{\mu_j} \right)^{1/2} \left(\frac{M_j}{M_i} \right)^{1/4} \right]^2 \tag{9.3}$$

The thermal conductivity K_i [W/m/K] is linked to μ_i by the Eucken formula:

$$K_i = \frac{15}{4} R_i \mu_i \qquad \text{for mono-atomic gases} \tag{9.4}$$

$$K_i = \left(c_{p_i} + \frac{5}{4} R_i \right) \mu_i \qquad \text{for poly-atomic gases} \tag{9.5}$$

where: R_i and c_{pi} are the constant and the specific heat at constant pressure of the i^{th} species, respectively. The thermal conductivity of a mixture (K_{mix}) relies on the Wilke rule (Eq. 8.2).

Diffusivity [m^2/s] of species i with respect to specie j is computed by:

$$D_{ij} = 1.8583 \times 10^{-3} \frac{\sqrt{T^3 \left(\frac{1}{M_i} + \frac{1}{M_j} \right)}}{p \sigma_{ij}^2 \Omega_{ij}^{(1,1)}} \tag{9.6}$$

where: $\sigma_{ij} = (\sigma_i + \sigma_j)/2$, $\Omega_{ij}^{(1,1)}$ is the diffusion collision integral, function of T/ε_{ij} ($\varepsilon_{ij} = \sqrt{\varepsilon_i \varepsilon_j}$) and p is the pressure in atmosphere. Tabulated values of $\Omega_{ij}^{(1,1)}$, $\Omega_{ij}^{(2,2)}$, σ_i and ε_i are reported in reference [50].

The self-diffusion coefficient of the mixture (D_{mix}) is computed by Eq. 9.6 considering for the parameters, the average values weighted with respect to the mixture composition:

$$M_{mix} = \sum_i \alpha_i M_i , \qquad \sigma^2_{mix} = \sum_i \alpha_i \sigma_i^2 , \qquad \varepsilon_{mix} = \sum_i \alpha_i \varepsilon_i$$

and

$$D_{mix} = 1.8583\times10^{-3} \frac{\sqrt{T^3\left(\frac{2}{M_{mix}}\right)}}{p\sigma^2_{mix}\Omega^{(1,1)}_{mix}} \tag{9.7}$$

Gupta-Yos-Thompson Model

The Gupta-Yos-Thompson model provides the viscosity and thermal conductivity of a mixture by:

$$\mu_{mix} = \sum_i \frac{\frac{M_i}{N_A}\alpha_i}{\sum_j \alpha_j \Delta^{(2)}_{ij}} \tag{9.8}$$

and

$$K_{mix} = \frac{15}{4} k \sum_i \left(\frac{\alpha_i}{\sum_j \beta_{ij}\alpha_j \Delta^{(2)}_{ij}} \right) \tag{9.9}$$

where: N_A is the Avogadro number, $\Delta^{(2)}_{ij}$ is a collision term defined by:

$$\Delta^{(2)}_{ij} = \frac{16}{5}\sqrt{\frac{2}{\pi N_A kT}\frac{M_i M_J}{M_i + M_j}}\pi\sigma^2_{ij}\Omega^{(2,2)}_{ij} \tag{9.10}$$

β_{ij} are the stoichiometric coefficients for reactants, defined by:

$$\beta_{ij} = 1 + \frac{[1-(M_i/M_j)][0.45-2.54(M_i/M_j]}{[1+(M_i/M_j)]^2} \tag{9.11}$$

$\pi\sigma^2\Omega^{(2,2)}_{ij}$ is computed by a best fit curve as a function of temperature:

$$\pi\sigma^2_{ij}\Omega^{(2,2)}_{ij} = e^{D_{\sigma^2_{ij}\Omega^{(2,2)}_{ij}} T\left[B_{\sigma^2_{ij}\Omega^{(2,2)}_{ij}} \ln T + C_{\sigma^2_{ij}\Omega^{(2,2)}_{ij}}\right]} \tag{9.12}$$

coefficients $B_{\sigma_{ij}^2\Omega_{ij}^{(2,2)}}$, $C_{\sigma_{ij}^2\Omega_{ij}^{(2,2)}}$ and $D_{\sigma_{ij}^2\Omega_{ij}^{(2,2)}}$ are reported in [2].

Also in this case, D_{mix} is computed by Eq. 9.7 considering for the involved parameters, the average values weighted with respect to the mixture composition:

$$\sigma_{mix}^2\Omega_{mix}^{(1,1)} = \sum_i \alpha_i(\sigma_{ii}^2\Omega_{ii}^{(1,1)}) \tag{9.13}$$

Gupta computes $\sigma_{ii}^2\Omega_{ii}^{(1,1)}$ by:

$$\pi\sigma_{ii}^2\Omega_{ii}^{(1,1)} = e^{D_{\sigma_{ii}^2\Omega_{ii}^{(1,1)}} T\left[B_{\sigma_{ii}^2\Omega_{ii}^{(1,1)}} \ln T + C_{\sigma_{ii}^2\Omega_{ii}^{(1,1)}}\right]} \tag{9.14}$$

Also the coefficients $B_{\sigma_{ij}^2\Omega_{ij}^{(1,1)}}$, $C_{\sigma_{ij}^2\Omega_{ij}^{(1,1)}}$ and $D_{\sigma_{ij}^2\Omega_{ij}^{(1,1)}}$ are reported in [16].

9.3 Post-processor code and Test Conditions

The post-processor code processes the output from DS2V along the stagnation line to compute the transport coefficients and the diffusion characteristic numbers of the mixture (Pr_{mix}, Le_{mix} and Sc_{mix})..

Table 9.1 reports some input data and some operative parameters. The choice of these altitudes, for the present application, is proper; apart from the very different free stream Mach numbers, the overall Reynolds and Knudsen numbers are comparable. The values of $Kn_{D\infty}$ indicate that at these altitudes the flow fields past both capsules are in continuum low density regime.

Table 9.1 Input data for EXPERT and for ORION

	h [km]	T_∞ [K]	N_∞ [1/m^3]	$\alpha_{\infty O_2}$	$\alpha_{\infty N_2}$	$\alpha_{\infty O}$	V_∞ [m/s]	T_w [K]	Ma_∞	$Re_{\infty D}$	$Kn_{\infty D}$
EXPERT	70	220	1.77×10^{21}	0.2095	0.7808	0.0097	5047	300	17	2.35×10^{4}	1.07×10^{-3}
ORION	85	189	1.71×10^{20}	0.2095	0.7808	0.0097	7600	1184	28	2.08×10^{4}	1.96×10^{-3}

9.4 Analysis of Results

The analysis relies both on a qualitative (or graphical) and a quantitative evaluation of the effects of the chemical models on the thermo-fluid-dynamic quantities. For a direct graphical comparison, the plots for ORION and for EXPERT are drawn, where possible, in the same scale. Quantification relies both on the comparison of the maximum values of a generic thermo-fluid-dynamic quantity (G_{max}^{Gupta}, G_{max}^{Park}) and on the absolute percentage variation ($\Delta G\%$) of the values of G, computed by the Gupta model with respect to those computed by the Park model, averaged along the stagnation line:

$$\Delta G\% = \frac{1}{n_p} \sum_{i}^{n_p} \frac{\left|(G_i^{Gupta} - G_i^{Park})\right|}{G_i^{Park}} \times 100 \qquad (9.15)$$

In the present application, the lengths of the stagnation line (L_s) and the related number of computing points (n_p) are: L_s=0.6 m, n_p=53 for ORION, L_s=0.06 m, n_p=39 for EXPERT. The analysis will involve both "basic" quantities, or quantities computed by DS2V, and quantities computed by the post-processor.

Results from DS2V

Figures 9.1(a) and (b) show the profiles of atomic Oxygen, atomic Nitrogen and Nitrogen-Oxide along the stagnation line of ORION and of EXPERT. Both chemical models compute a complete dissociation of Oxygen for both capsules. The much stronger shock wave for ORION produces higher dissociation of Nitrogen; the maximum molar fraction for both models is about 0.53 for ORION and about 0.08 for EXPERT. Dissociation by Gupta model is a little bit higher than dissociation by Park; the molar fractions of N and O by Gupta are always higher than the ones by Park. This condition is not verified for the dissociation of Nitrogen for EXPERT.

Figures 9.2(a) and (b) show the profiles of temperature. These plots indicate clearly that the cores of the shock waves, identified by the maximum values of temperature, are located for the two models at x ≅ -0.38 m (T_{max}^{Gupta} = 23082 K), x ≅ -0.35 m (T_{max}^{Park}=22355 K) for ORION and at x ≅ -0.043 m (T_{max}^{Gupta}=13230 K), x ≅ -0.038 m (T_{max}^{Park}=11849 K) for EXPERT. The condition that temperature, that as well known is representative of the translational energy, is higher for Gupta, even though this model produces higher dissociation, is probably due to the fact that

energy for a di-atomic molecule is stored also in the rotational and vibrational degrees of freedom, while for the two atoms, produced by dissociation, is stored only in the translational degree of freedom.

The influence of the two chemical models produces, for both capsules, a slight variation in the shock stand-off distance; the variations for ORION and for EXPERT are only about 0.04 m and 0.005 m, respectively. Even though the maximum values of temperature by the two models are comparable for each capsule, the variation of the stand-off distance produces locally strong effects. For example, for ORION at the position x≅-0.41 m, temperatures by Gupta and by Park are 12032 K and 4172 K (the percentage variation is 188%); for EXPERT at the position x≅-0.041 m, temperatures by Gupta and by Park are 11957 and 10431 (the percentage variation is 15%).

Figures 9.3(a) and (b) show the profiles of the percentage variations between the two models of the molar fraction of O, N and NO. As expected, these variations are higher in the core of the shock wave, where temperature is higher and for ORION. Air compositions, computed by the two models near the stagnation point (x=0) of both capsules, are pretty similar; the percentage variation is practically zero. As already pointed out in the chapter 8, this can be justified because the difference of rate coefficients by both models tends to reduce by decreasing temperature.

According to the Variable Hard Sphere (VHS) model [1], the profiles of the mean free path (Figs. 9.4(a) and (b)) reproduce those of temperature. The maximum values are: $\lambda_{max}^{Gupta} \cong 0.025$ m and $\lambda_{max}^{Park} \cong 0.020$ for ORION and $\lambda_{max}^{Gupta} \cong 0.0016$ m, $\lambda_{max}^{Park} \cong 0.0006$ m for EXPERT. For completeness, Figs. 9.5(a), (b) and 8.6(a), (b) show the profiles of velocity and pressure, respectively. The change of the stand-off distance appears clearly also in these figures.

Table 9.2 reports the average percentage variation ($\Delta G\%$) of some basic parameters for both capsules. As expected, these percentage variations for ORION are higher than the ones for EXPERT.

Table 9.2 Percentage variations of molar fractions of O, N and NO, temperature, velocity, pressure and mean free path averaged along the stagnation line across the shock layer for EXPERT and for ORION

	$\Delta\alpha_O\%$	$\Delta\alpha_N\%$	$\Delta\alpha_{NO}\%$	$\Delta T\%$	$\Delta\lambda\%$	$\Delta V\%$	$\Delta p\%$
ORION	112	93	110	57	23	22	61
EXPERT	36	33	43	46	19	17	40

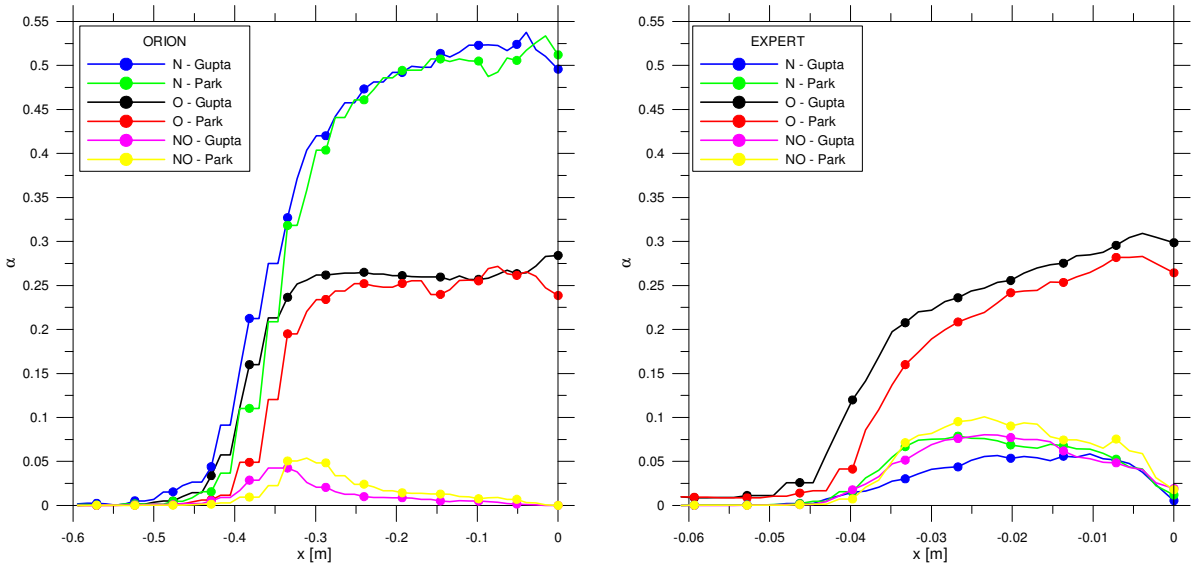

(a) (b)

Figure 9.1 Profiles of molar fraction of N, O, NO along the stagnation line across the shock layer of ORION (a) at h=85 km and of EXPERT (b) at h=70 km

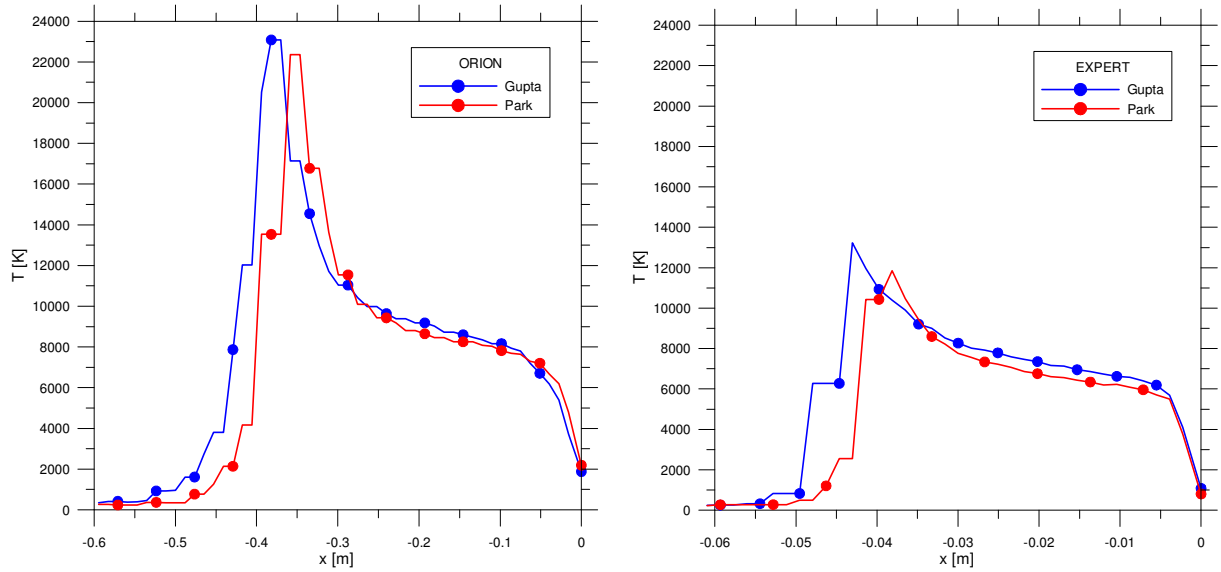

(a) (b)

Figure 9.2 Profiles of temperature along the stagnation line across the shock layer of ORION (a) at h=85 km and of EXPERT (b) at h=70 km

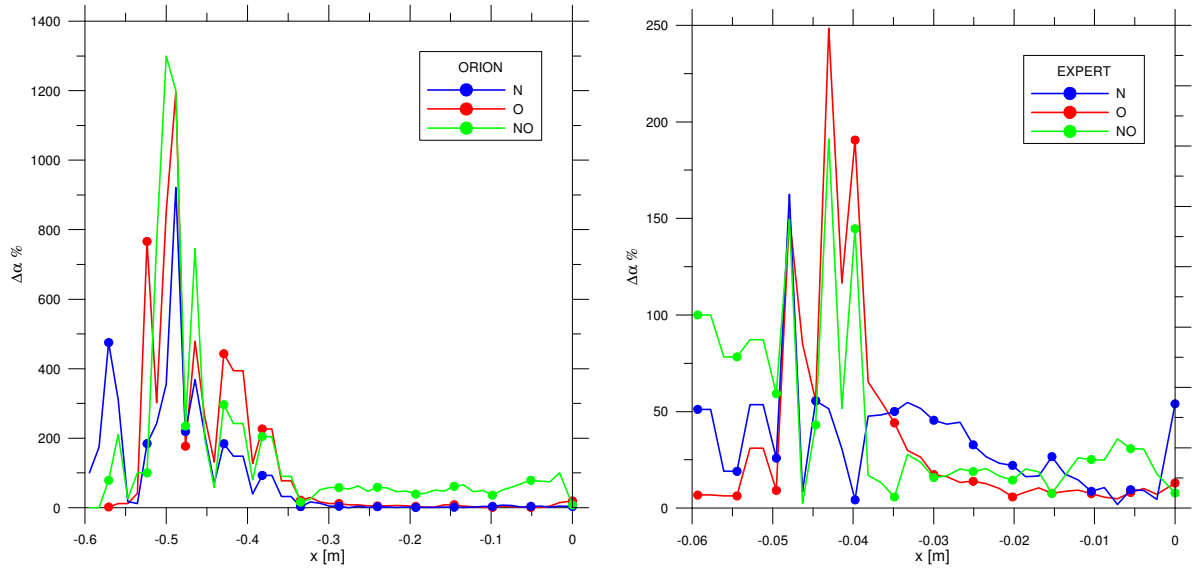

(a) (b)

Figure 9.3 Profiles of the percentage variation between two models of the molar fractions of N, O, NO along the stagnation line across the shock layer of ORION (a) at h=85 km and of EXPERT (b) at h=70 km

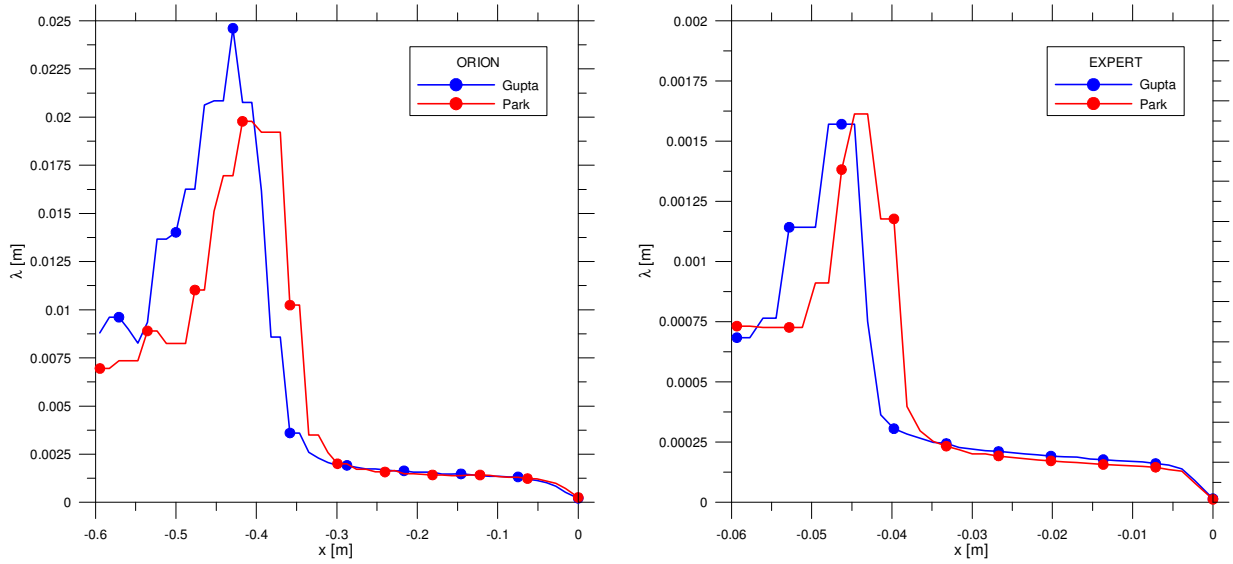

(a) (b)

Figure 9.4 Profiles of the mean free path along the stagnation line across the shock layer of ORION (a) at h=85 km and of EXPERT (b) at h=70 km

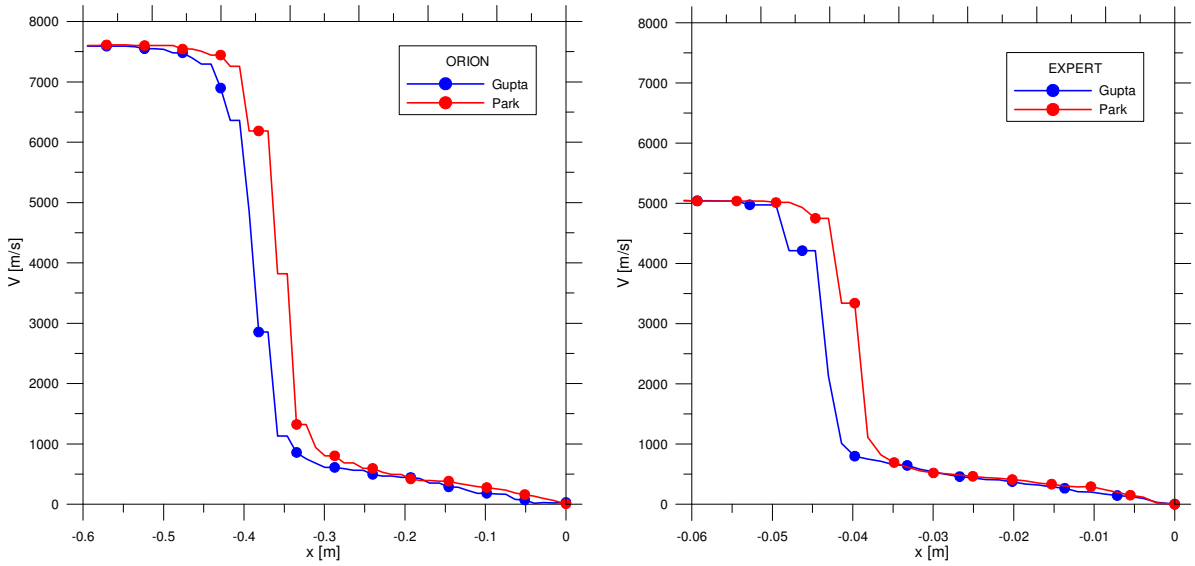

(a) (b)

Figure 9.5 Profiles of velocity along the stagnation line across the shock layer of ORION (a) at h=85 km and of EXPERT (b) at h=70 km

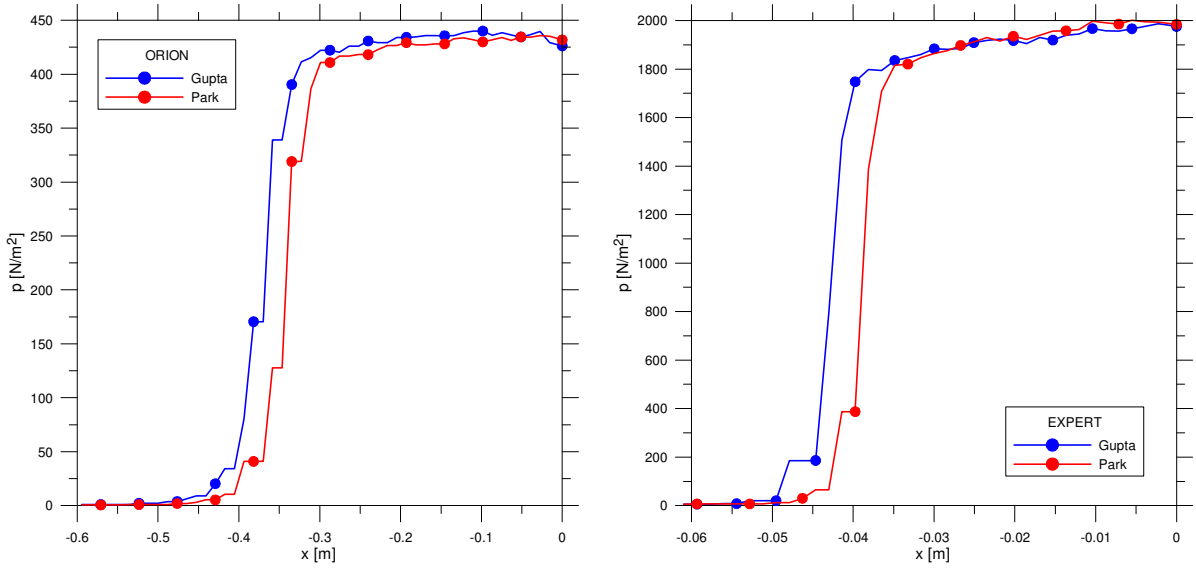

(a) (b)

Figure 9.6 Profiles of pressure along the stagnation line across the shock layer of ORION (a) at h=85 km and of EXPERT (b) at h=70 km

Results from the post-processor

For both chemical models and for both capsules the profiles of the transport coefficients of the mixture μ_{mix} (Figs. 9.7(a) and (b)). K_{mix} (Figs. 9.8(a) and (b)), D_{mix} (Figs. 9.9(a) and (b)) reproduce those of temperature. For example, for ORION at position x≅-0.41 m, μ_{mix}, K_{mix} and D_{mix} by Gupta are 2.51×10^{-4} [kg/m/s], 0.31 [W/m/K] and 26.6 [m^2/s], those by Park are 1.1×10^{-4} [kg/m/s], 0.12 [W/m/K] and 16.3 [m^2/s]; the related percentage variations are 128%, 158% and

63%, respectively. The maximum values of the diffusion parameters as well as of the Prandtl (Pr_{mix}, Figs. 9.10(a) and (b)), Lewis (Le_{mix}, Figs. 9.11(a) and (b)) and Schmidt (Sc_{mix}, Figs. 9.12(a) and (b)) numbers of the mixture, computed by the two chemical models for both capsules, are comparable. For example, for ORION $Pr_{max}^{Gupta} \cong 1.74$, $Le_{max}^{Gupta} \cong 1.62$, $Sc_{max}^{Gupta} \cong 2.11$ and $Pr_{max}^{Park} \cong 1.73$, $Le_{max}^{Park} \cong 1.61$, $Sc_{max}^{Park} \cong 2.12$. The influence of the chemical models is just a little bit stronger for EXPERT, in this case: $Pr_{max}^{Gupta} \cong 1.61$, $Le_{max}^{Gupta} \cong 1.98$, $Sc_{max}^{Gupta} \cong 1.80$ and $Pr_{max}^{Park} \cong 1.45$, $Le_{max}^{Park} \cong 1.75$, $Sc_{max}^{Gupta} \cong 1.81$.

As already verified for the basic parameters, also for the processed parameters the differences linked to the two models tend to disappear toward the surface of the capsules. The same remarks are also for the transport coefficients and the diffusion characteristic numbers. The latter, from Table 9.3, appear to be the least sensitive.

Table 9.3 Percentage variations of viscosity, conductivity, diffusivity, Prandtl, Lewis and Schmidt numbers of the mixture, averaged along the stagnation line across the shock layer for EXPERT and for ORION

	$\Delta\mu_{mix}$ %	ΔK_{mix} %	ΔD_{mix} %	ΔPr_{mix} %	ΔLe_{mix} %	ΔSc_{mix} %
ORION	33	33	35	7	13	9
EXPERT	26	29	28	6	9	5

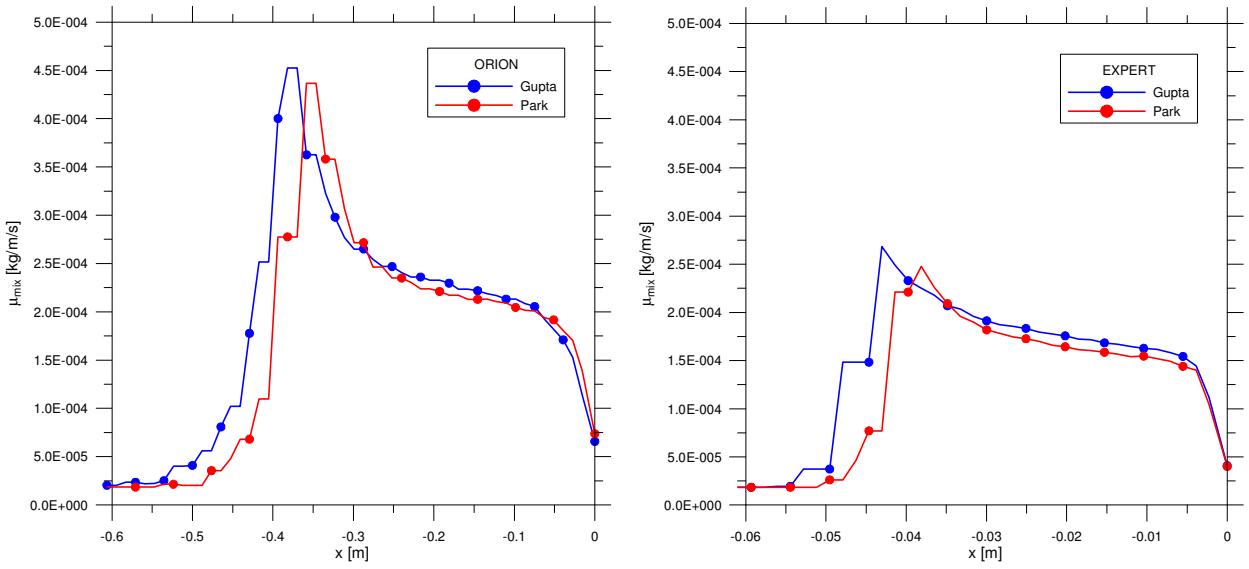

(a) (b)

Figure 9.7 Profiles of the mixture viscosity along the stagnation line across the shock layer of ORION (a) at h=85 km and of EXPERT (b) at h=70 km

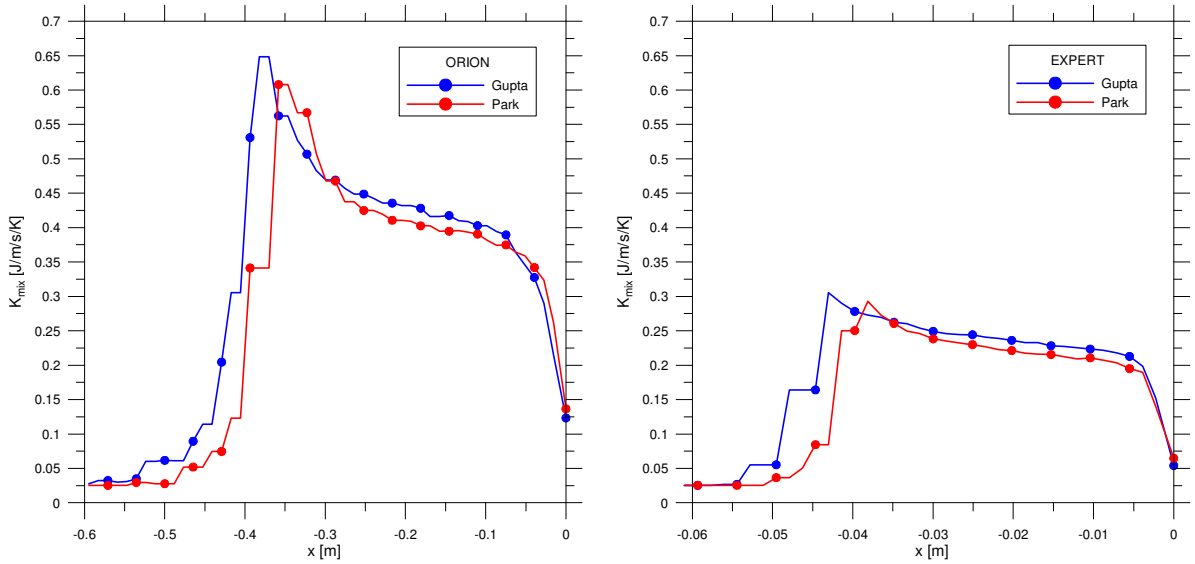

(a) (b)

Figure 9.8 Profiles of the mixture thermal conductivity along the stagnation line across the shock layer of ORION (a) at h=85 km and of EXPERT (b) at h=70 km

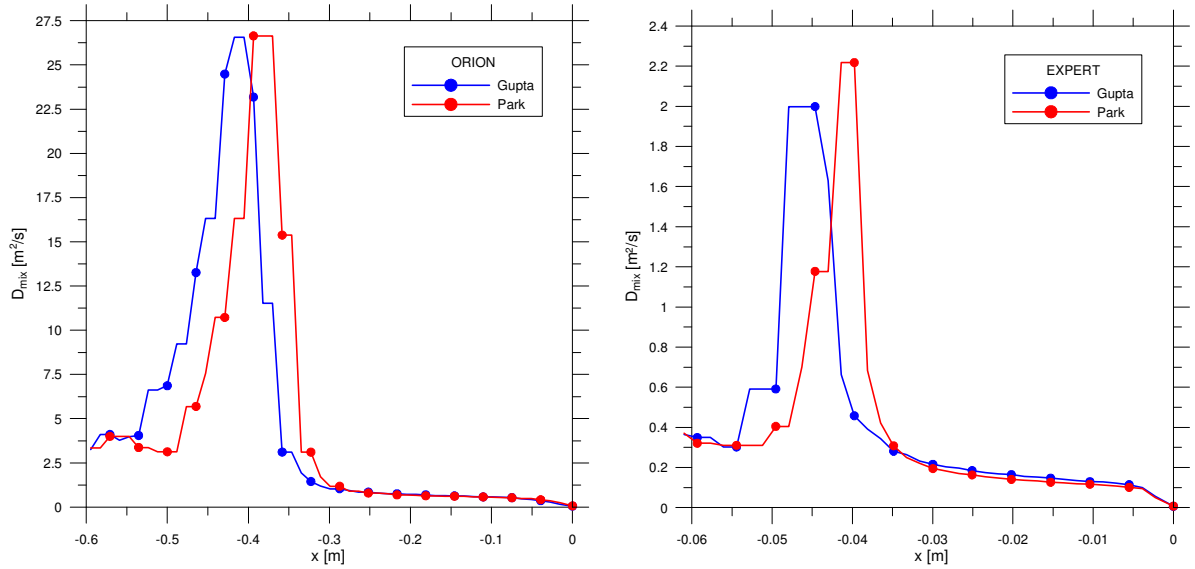

(a) (b)

Figure 9.9 Profiles of the mixture self-diffusivity along the stagnation line across the shock layer of ORION (a) at h=85 km and of EXPERT (b) at h=70 km

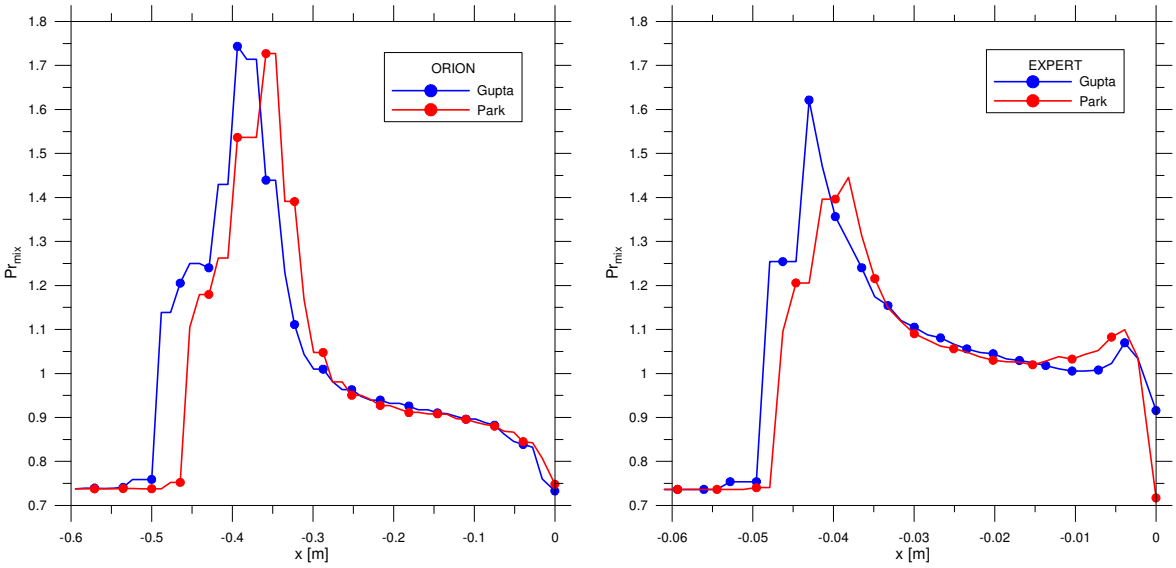

(a) (b)

Figure 9.10 Profiles of the mixture Prandtl number along the stagnation line across the shock layer of ORION (a) at h=85 km and of EXPERT (b) at h=70 km

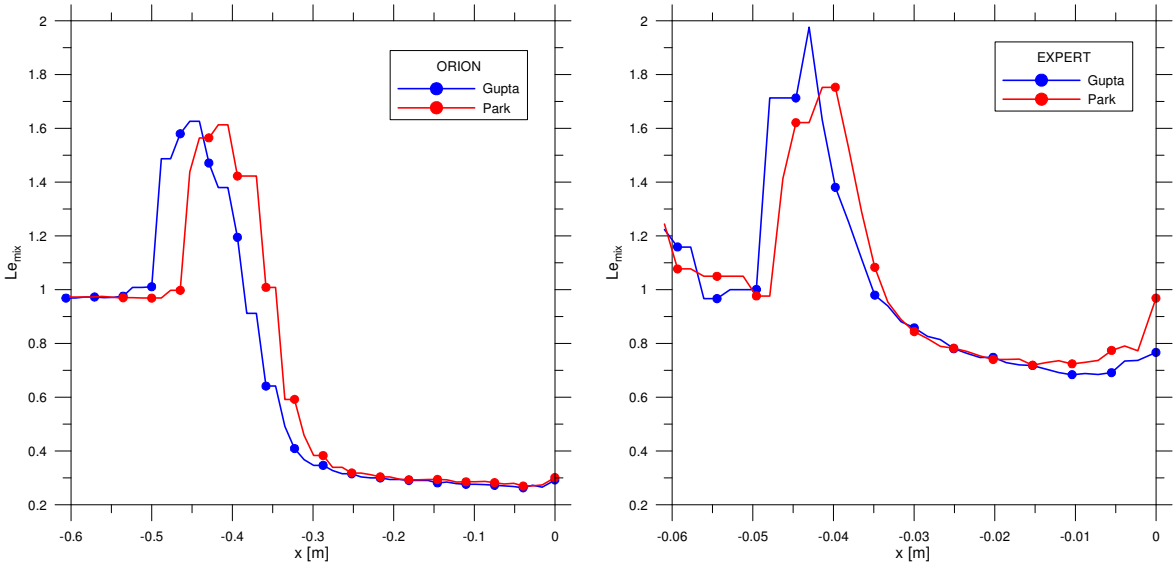

(a) (b)

Figure 9.11 Profiles of the mixture Lewis number along the stagnation line across the shock layer of ORION (a) at h=85 km and of EXPERT (b) at h=70 km

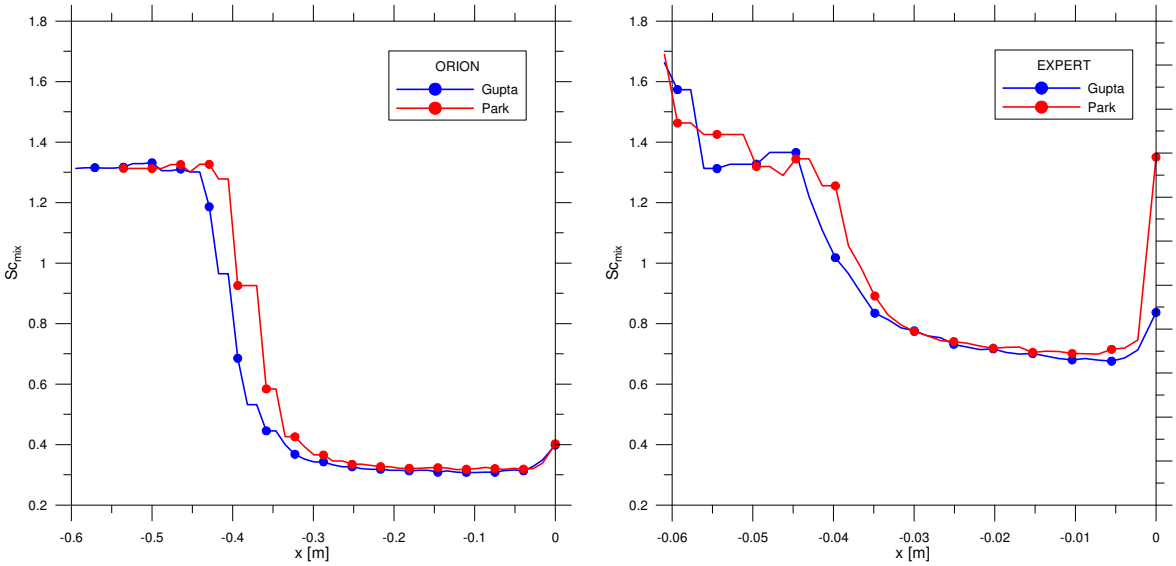

Figure 9.12 Profiles of the mixture Schmidt number along the stagnation line across the shock layer of ORION (a) at h=85 km and of EXPERT (b) at h=70 km

9.5 Conclusions

As seen in the chapter 8 the influence of the chemical models by Gupta and by Park were analyzed and quantified on the heat flux of the EXPERT and ORION capsules. In this chapter a similar analysis has been carried out considering parameters in the flow fields such as basic fluid-dynamic parameters as well as non equilibrium, rarefaction and diffusion parameters and related characteristic numbers.

The output data at the altitudes of 70 km for EXPERT and 85 km for ORION, generated for the purpose of the chapter 8, have been processed along the stagnation line in the shock layer. These altitudes have been chosen because, being the lowest ones of that analysis, the influence of chemistry is the strongest one. Furthermore, the flow fields past the capsules are characterized by similar overall Knudsen and Reynolds numbers and therefore by the same free stream rarefaction level.

The most relevant effect, due to the chemical models, is the change of the stand-off distance, producing locally strong effects on the computation of thermo-fluid-dynamic quantities. More specifically, the stand-off distance computed by the Park model is slightly shorter than the one by the Gupta model. As expected, due to a much stronger shock wave, the average percentage variation of each thermo-fluid-dynamic quantity is stronger for ORION than for EXPERT.

CHAPTER X

Influence of Ionization for the Gupta and the Park Chemical models

10.1 Introduction

The present work is a step forward of the chapters 8 and 9 in which the effects of the chemical models by Gupta and by Park on heat flux and on thermo-fluid-dynamic quantities have been analyzed and quantified. In those chapters tests were carried out considering EXPERT and ORION capsules during the high altitude re-entry path in the interval 70-105 km for EXPERT and 85-125 km for ORION, where both capsules are in transitional regime. The choice of these capsules was proper because characterized by different shapes and re-entry trajectories, therefore by completely different fluid-dynamic conditions. For example, the Mach number at the altitude of 70 km is 17 for EXPERT, and at the altitude of 85 km is 28 for ORION.

The effects of the two chemical models were evaluated on the heat flux and on some thermo-fluid-dynamic parameters (local Knudsen numbers, transport coefficients, Prandtl and Lewis numbers and so on). In those applications, ionization process was neglected because the velocities of the capsules (about 5000 m/s for EXPERT and 7600 m/s for ORION) were not high enough to activate meaningful ionization process. On the other hand the aim of those studies was to compare the two chemical models in their basic aspects or in dissociation, recombination and exchange reactions.

The conclusions were that the two models compute for both capsules different compositions in the flow field but only very slight different compositions on the surface. For this reason, the chemical models did not influence meaningfully the computation of heat flux. In addition, the effect due to the chemical models was the change of the stand-off distance, producing locally strong effects. More specifically, the stand-off distance computed using the Park model is slightly shorter than the one using the Gupta model.

The aim of the present chapter is to check the incidence of ionization linked to the chemical models by Gupta and by Park both on heat flux and on the fluid-dynamic parameters. For this purpose, runs simulating the re-entry of ORION have been considered. This capsule has been

chosen for the present application because, thanks to the possibility of returning from interplanetary missions, it can achieve velocity high enough to produce meaningful ionization.

Computer tests have been carried out by the direct simulation Monte Carlo (DSMC) code DS2V [12], considering an altitude of 85 km and velocities between 7600 and 12000 m/s. The altitude of 85 km has been chosen because it satisfies a good compromise between the amplification of chemical effects, requiring high density level of the gas, and quality of the runs by a DSMC code, requiring low density level. As well as, the interval of velocity has been selected to highlight the effects of ionization. On the other hand, all selected values of velocity are compatible with the missions of ORION.

The analysis of the results will rely both on a qualitative (or graphical) and a quantitative evaluation of the effects of ionization on each and between the chemical models. The quantification will consider both basic quantities, i.e. quantities computed by DS2V, and quantities such as transport coefficients and related characteristic number, computed by a code processing the DS2V results. The influence of ionization on the heat flux computation by the two chemical models will be also carried out.

10.2 Gupta and Park Ionization Chemical Model

The chemical models by Gupta [16] and by Park [18, 19, 20], here reported, are related to the 11 constituent chemical species of air: O_2, N_2, O, N, NO, O_2^+, N_2^+, O^+, N^+, NO^+ and e^-. For the Gupta model, both the forward (k_f) and the backward (k_b) rate coefficients are expressed in terms of the Arrhenius-like equation:

$$k_{f,b} = C_{f,b} T^{n_{f,b}} \exp\left(-\frac{E_{a_{f,b}}}{kT} \right) \tag{10.1}$$

where C is the pre-exponential factor, n is the temperature exponent, E_a is the specific activation energy (subscripts f and b stand for forward and backward reactions, respectively), k is the Boltzmann constant, the ratio $E_{af,b}/k$ is the characteristic temperature of the reaction (in K). These coefficients for neutral species are reported also in chapter 8. The reactions whose coefficients are reported in Table 10.1 are related just to the ionization process.

Table 10.1 Gupta kinetic models for ionization reactions

No	Reactions	C_f [m^3/molecule/s]	n_f	E_{af}/k [K]	C_r [m^3/molecule/s]	n_r	E_{ar}/k [K]
1	$N + O \leftrightarrow NO^+ + e^-$	1.50×10^{-20}	0.5	32400	2.99×10^{-11}	-1.0	0.0

2	$O + e^- \leftrightarrow O^+ + e^- + e^-$	5.98×10	2.91	158000	3.65×10^{10}	-4.5	0.0
3	$N + e^- \leftrightarrow N^+ + e^- + e^-$	1.83×10^{-10}	-3.14	169000	3.65×10^{10}	-4.5	0.0
4	$O + O \leftrightarrow O_2^+ + e^-$	2.66×10^{-13}	-0.98	80800	1.33×10^{-8}	-1.5	0.0
5	$O + O_2^+ \leftrightarrow O_2 + O^+$	4.85×10^{-12}	-1.11	28000	1.30×10^{-18}	0.5	0.0
6	$N_2 + N^+ \leftrightarrow N + N_2^+$	3.35×10^{-19}	0.81	13000	1.30×10^{-18}	0.5	0.0
7	$N + N \leftrightarrow N_2^+ + e^-$	2.32×10^{-17}	0	67800	2.49×10^{-8}	-1.5	0.0
8	$O + NO^+ \leftrightarrow NO + O^+$	6.03×10^{-15}	-0.6	50800	2.49×10^{-17}	0.0	0.0
9	$N_2 + O^+ \leftrightarrow O + N_2^+$	5.65×10^{-11}	-2	23000	4.12×10^{-11}	-2.2	0.0
10	$O_2 + NO^+ \leftrightarrow NO + O_2^+$	2.99×10^{-15}	0.17	33000	2.99×10^{-17}	0.5	0.0
11	$O + NO^+ \leftrightarrow O_2 + N^+$	2.23×10^{-17}	0.31	77270	1.66×10^{-16}	0.0	0.0
12	$O_2 + N_2 \leftrightarrow NO + NO^+ + e^-$	2.29×10^{-10}	-1.84	141000	1.66×10^{-6}	-2.5	0.0
13	$NO + O_2 \leftrightarrow NO^+ + e^- + O_2$	3.65×10^{-15}	-0.35	108000	3.65×10^{-4}	-2.5	0.0
14	$NO + N_2 \leftrightarrow NO^+ + e^- + N_2$	3.65×10^{-15}	-0.35	108000	3.65×10^{-4}	-2.5	0.0
15	$N + NO^+ \leftrightarrow NO + N^+$	1.66×10^{-11}	-0.93	61000	7.97×10^{-16}	0.0	0.0

Also Park provides the forward reaction rate coefficients expressed in the Arrhenius-like equation:

$$k_f = C_f T_c^{n_f} \exp\left(-\frac{E_{a_f}}{kT_c}\right) \tag{10.2}$$

where T_c is the temperature controlling the reaction. This temperature takes into account the electron temperature T_e and the translational temperature. Park assumes that T_c is the geometrical mean temperature between the electron and the transitional temperatures:

$$T_c = T_e^{\phi} T^{(1-\phi)} \tag{10.3}$$

In the present work, to implement the Park model in DS2V, the value of ϕ=0 has been used.

Table 10.2 Park kinetic model for ionization reactions

No	Reactions	C_f [m^3/molecule/s]	n_f	E_{af}/k [K]	C_r [m^3/molecule/s]	n_r	E_{ar}/k [K]
1	$N + O \leftrightarrow NO^+ + e^-$	8.80×10^{-18}	0.0	31900	1.79×10^{-7}	-1.65	0.0
2	$O + e^- \leftrightarrow O^+ + e^- + e^-$	$6.47 \times 10^{+3}$	-3.78	158500	$1.63 \times 10^{+31}$	-5.2	0.0
3	$N + e^- \leftrightarrow N^+ + e^- + e^-$	$4.15 \times 10^{+4}$	-3.82	162000	$1.86 \times 10^{+12}$	-5.2	0.0
4	$O + O \leftrightarrow O_2^+ + e^-$	1.86×10^{-17}	0.0	80600	1.45×10^{-4}	-2.412	0.0
5	$O + O_2^+ \leftrightarrow O_2 + O^+$	6.64×10^{-18}	-0.09	18000	4.99×10^{-18}	-0.001	0.0
6	$N_2 + N^+ \leftrightarrow N + N_2^+$	1.66×10^{-18}	0.5	12200	2.34×10^{-14}	-0.610	0.0
7	$N + N \leftrightarrow N_2^+ + e^-$	7.31×10^{-23}	1.5	67500	$1.793 \times 10^{+08}$	-0.58	0.0
8	$O + NO^+ \leftrightarrow NO + O^+$	4.57×10^{-17}	0.01	50800	$2.32 \times 10^{+15}$	0.5	2500
9	$N_2 + O^+ \leftrightarrow O + N_2^+$	1.51×10^{-18}	0.36	22800	$1.98 \times 10^{+18}$	0.109	0.0
10	$O_2 + NO^+ \leftrightarrow NO + O_2^+$	3.99×10^{-17}	0.41	32600	2.99×10^{-08}	0.5	0.0
11	$O + NO^+ \leftrightarrow O_2 + N^+$	1.95×10^{-16}	0.0	35500	1.66×10^{-16}	0.0	0.0
12	$N_2 + O_2^+ \leftrightarrow O_2 + N_2^+$	1.64×10^{-17}	0.0	40700	4.59×10^{-18}	-0.037	0.0
13	$O + NO^+ \leftrightarrow N + O_2^+$	1.20×10^{-17}	0.29	48600	8.92×10^{-13}	-0.969	0.0
14	$NO + O^+ \leftrightarrow O_2 + N^+$	2.32×10^{-25}	1.9	26600	2.44×10^{-26}	2.102	0.0
15	$N + NO^+ \leftrightarrow N_2 + O^+$	5.65×10^{-17}	-1.08	12800	7.97×10^{-18}	-0.71	0.0

The backward rate coefficient (k_b) is computed by the ratio of the forward rate coefficient (k_f) to the equilibrium constant (K_e): $k_b=k_f/K_e$. K_e, provided by Park, is computed at a number of values of temperature (between 3000 and 15000 K) and then interpolated by polynomial fitting curves [19, 20].

As DS2V uses the pre-exponential factor ($C_{f,b}$) and the temperature exponent ($n_{f,b}$) in the evaluation of reaction probability (or steric factor [1]), in order to implement the Park backward reaction rates in DS2V defining C_b and n_b is necessary. Boyd [52] obtained these values for all equations, except for reactions 2, 3 and 8. For these equations, the values of C_b and n_b have been obtained by curves, in the form of Eq. 10.1, best-fitting the values k_f/K_e as a function of temperature. The accuracy of the curves can be evaluated from Figs. 10.2(a) to (c).

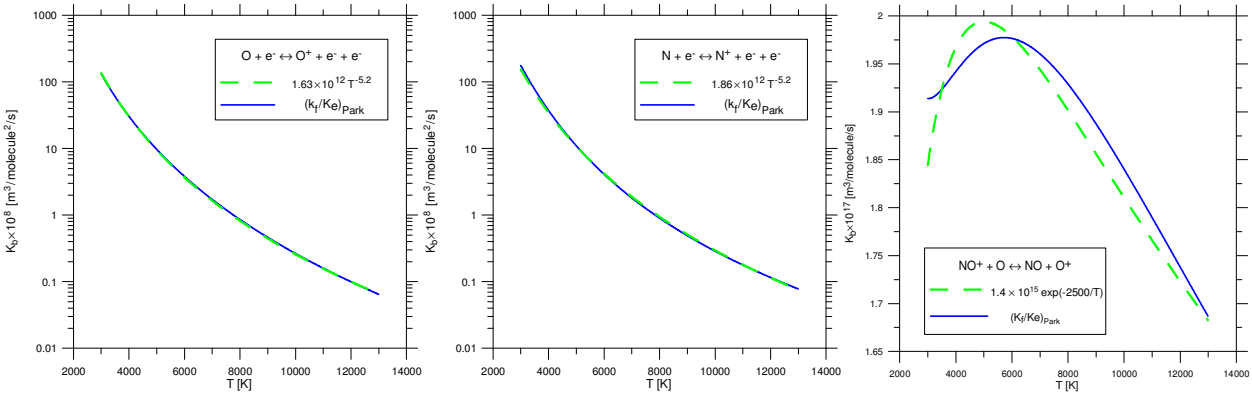

(a) (b) (c)

Figure 10.2 Profiles of the backward rate coefficient of some reactions by the Park models

For reactions 2 and 3 the equilibrium constant is computed by [19]:

$$K_e(T) = \exp[A_1/Z + A_2 + A_3\ln(Z) + A_4 Z + A_5 Z^2] \tag{10.4}$$

For reaction 8 the equilibrium constant is computed by [20]:

$$K_e(T) = \exp[A_1 + A_2\ln(Z) + A_3 Z + A_4 Z^2 + A_5 Z^3] \tag{10.5}$$

where Z=10000/T and the equilibrium constant coefficients are reported in Table 10.3.

Table 10.3 Park kinetic model for dissociation/recombination and exchange reactions

No	Reactions	A_1	A_2	A_3	A_4	A_5
2	$O + e^- \leftrightarrow O^+ + e^- + e^-$	0.614	-6.755	-0.774	-16.003	0.006
3	$N + e^- \leftrightarrow N^+ + e^- + e^-$	0.201	-3.966	-0.042	-18.063	0.126
8	$O + NO^+ \leftrightarrow NO + O^+$	0.148	-1.011	-4.121	-0.132	0.006

10.3 Computing Codes

The DSMC code, used in the present application, is DS2V (Ver.4.5) [12]. DS2V is able to consider a number of built-in gases, including also air plasma. The built-in, air plasma is considered made up of eleven chemical species: neutral O_2, N_2, O, N, NO, related ions O^+_2, N^+_2, O^+, N^+, NO^+ and electron e^- in thermo-chemical non-equilibrium.

Post-processor code handles the output from DS2V along the stagnation line to compute the mixture transport coefficients and the mixture diffusion characteristic numbers of Prandtl ($Pr_{mix} = c_{pmix}\,\mu_{mix}/K_{mix}$) and of Lewis ($Le_{mix} = \rho_{mix}\,D_{mix}\,c_{pmix}/K_{mix}$). In the present paper two models, computing the transport coefficients both of a single species and of a mixture have implemented: the Chapman-Enskog model [50] and the Gupta-Yos-Thompson model [16]. Palmer and Wright [51] suggest to use the Gupta's mixing rule for high speed and high temperature flows, therefore, in this application, the Chapman-Enskog model is used for T<1000 K while the Gupta-Yos-Thompson model is used for T≥1000 K.

10.4 Analysis of the Results

Tests have been carried out considering the free stream parameters met at an altitude of 85 km ($N_\infty=1.71\times10^{20}$ 1/m^3, $T_\infty=189$ K, $\alpha_{O2\infty}=0.21$, $\alpha_{N2\infty}=0.79$); the overall Knuden number, based on the capsule diameter ($Kn_{D\infty}$), is about 1.3×10^{-3}, therefore the flow field can be considered in continuum low density regime in fact, according to Moss [28], a general definition of the transitional regime is: $10^{-3}<Kn_{\infty D}<50$. The free stream velocity ranges between 7600 and 12000 m/s, therefore the Mach number (Ma_∞) between 28 and 43. At velocities of 7600 and 12000 m/s the kinetic energies are 2.9×10^7 and 7.2×10^7 J/kg. Therefore at the velocity of 7600 the flow energy is not high enough to activate a meaningful ionization. In fact, the ionization energies for air components are: 3.3×10^7 J/kg for Oxygen, 5.4×10^7 J/kg for Nitrogen, 8.2×10^7 J/kg for atomic Oxygen, 1.0×10^8 J/kg for atomic Nitrogen and 3.0×10^7 J/kg for Nitric Oxide. The analysis will focus on the results at the intermediate velocity of 10000 m/s. Quantification of difference between two chemical models with and without ionization is provided by the percentage variation averaged along the stagnation line across the shock layer. In the present application, the length of the stagnation line (L_s) and the related number of computing points (n_p) are $L_s=0.6$ m, $n_p=52$. Quantification of heat flux is related to the capsule stagnation point.

A. Thermo-fluid-dynamic parameters

Figures 10.3(a) and (b) show the profiles of molar fraction of ionized species; the molar fractions of ionized species by the two models are completely different and the Park model is more reactive from an ionization point of view. The different behavior of the two models is due, besides to the different rate coefficients, also to fact that the reactions from 11 though 15 are different. Figures 4(a) and (b) verify the influence of ionization on the dissociation. In fact the molar fraction of neutral species of O, N and NO are pretty close to each other with no ionization and very different with ionization. As shown in Figs. 5(a) and (b), the maximum value of temperature by the Gupta model is less than the one by the Park model because, as already found in chapter 8, the Gupta model is more reactive than the Park model from a dissociation point of view. On the opposite, in the region close to the surface (-0.2 m<x<0 m) where ionization is strong (see Figs. 10.3(a) and (b)), temperature by Park is less than the one by Gupta because, as already pointed out, the Park model is more reactive from the ionization point of view.

According to what already found in chapter 9 the stand-off distance computed by Gupta is greater than the one by Park; in fact if one considers the point of the maximum value of temperature as the core of the shock wave, these positions are located at x=-0.41 m and x=-0.39 m for Gupta and for Park respectively, therefore the difference of the stand-off distance is 0.02 m. Ionization reduces the stand of distance; in fact position of the shock wave is at x=-0.34 for Gupta and -0.27 for Park; the difference is 0.07.

Table 10.4 reports the averaged absolute percentage variation of velocity, pressure, temperature and molar fractions of neutral species. Letters G and P stand for quantity computed by Gupta and by Park, respectively. Subscripts I and N, identify the condition of computation with or without ionization reactions. The presence of ionization increases the difference of the models (see the first and second line in Table 10.4). The influence of ionization is stronger for yhe Park model (compare third and forth lines in Table 10.4).

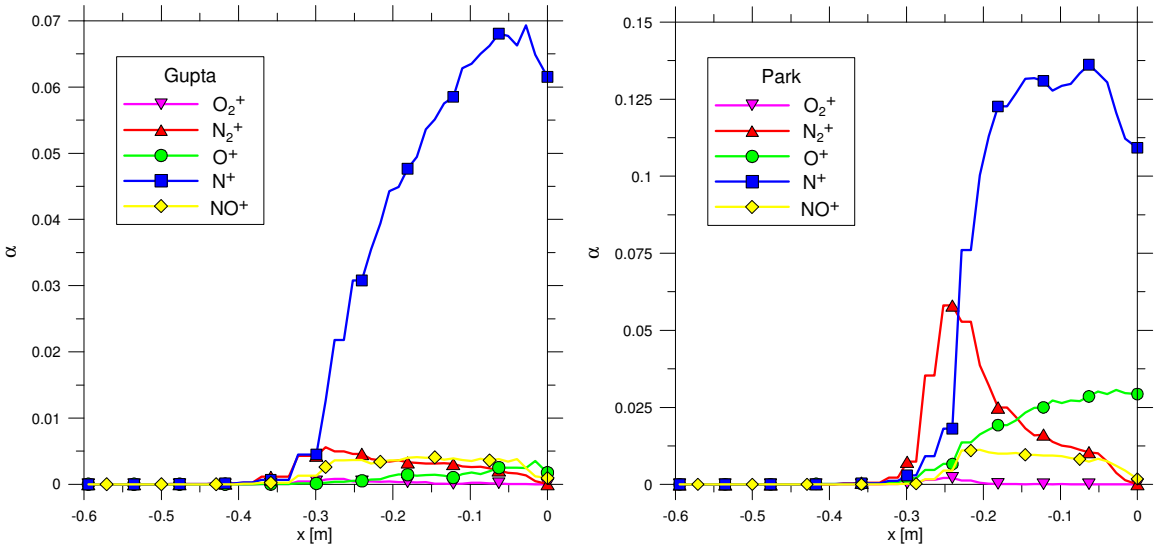

(a) (b)

Figure 10.3 Molar fractions of ionized species along the stagnation line across the shock layer by Gupta (a) and by Park (b): V_∞=10000 m/s

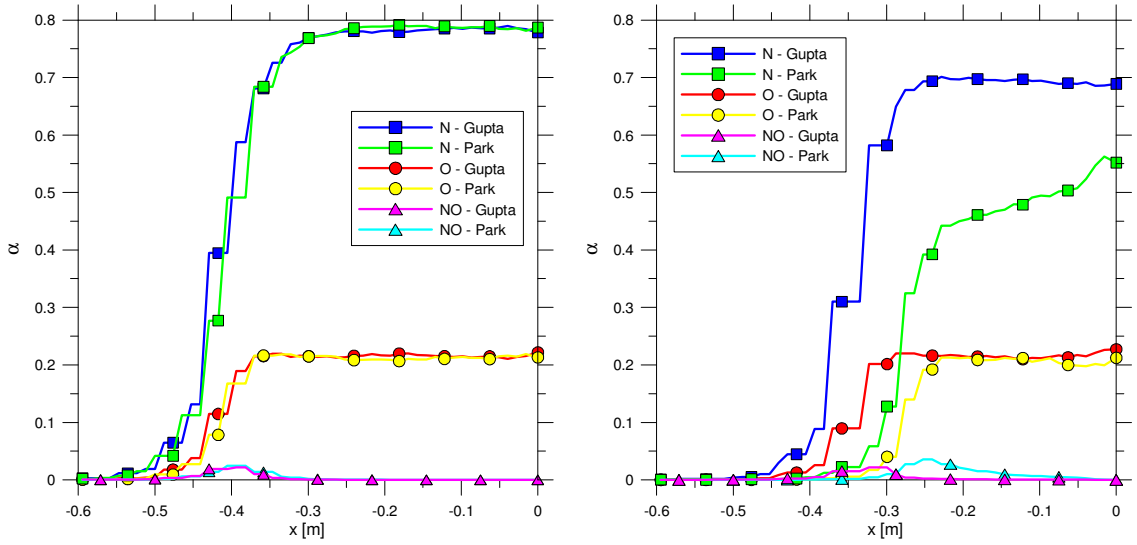

(a) (b)

Figure 10.4 Molar fractions of neutral species of O, N and NO along the stagnation line across the shock layer by Gupta and by Park without (a) and with (b) ionization reactions: V_∞=10000 m/s

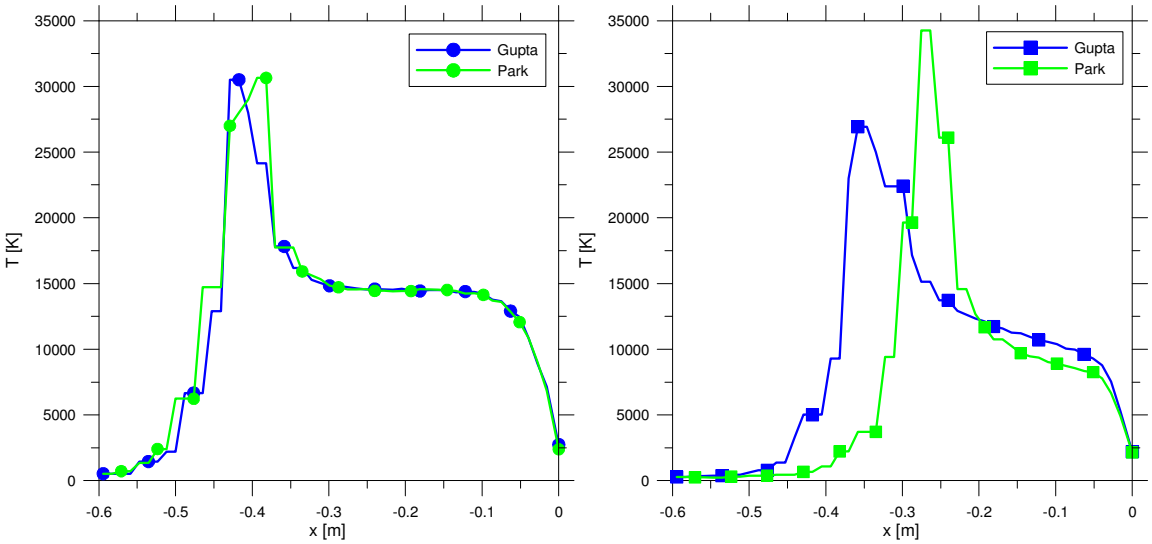

(a) (b)

Figure 10.5 Temperature along the stagnation line across the shock layer by Gupta (a) and by Park (b): V_∞=10000 m/s

Table 10.4 Average percentage variation along the stagnation line across the shock layer of thermo-fluid-dynamic quantities and molat fractions of neutral species: V_∞=10000 m/s

	V	p	T	α_{O_2}	α_{N_2}	α_O	α_N	α_{NO}
$\frac{G_N - P_N}{P_N}$ %	12.8	9.8	7.8	72.1	17.0	20.1	13.5	51.1
$\frac{G_I - P_I}{P_I}$ %	24.1	328.2	154.8	37.1	47.9	545.6	476.2	1172.2
$\frac{G_N - G_I}{G_I}$ %	23.7	292.4	144.6	62.5	66.7	244.5	253.9	693.7
$\frac{P_N - P_I}{P_I}$	35.4	2201.7	684.0	64.3	67.9	2644.9	2391.0	2896.3

B. Transport coefficients

As already found in chapter 9, the influence of the two chemical models, without ionization, generates a meaningful effect in the core of the shock wave, but this difference tends to disappear toward surface. The difference between the two models increases in the shock wave and keeps toward surface when ionization reactions are considered. As an example of the influence of ionization on the transport coefficient, Figures. 10.6(a) and (b) show the profiles of the mixture viscosity without and with ionization reactions, Figures 10.7(a), (b) and 8(a), (b) the profiles of the Prandtl and Lewis numbers.

In order to quantify the influence of ionization on the difference of the chemical models, Table 10.5 reports the average percentage variations of viscosity, thermal conductivity and self-diffusivity, Prandt and Lewis numbers. Quantification shows, once again, that ionization increases the distance between the two models and, more specifically in the present case, of about one order of magnitude and that the effect of ionization is stronger for Park.

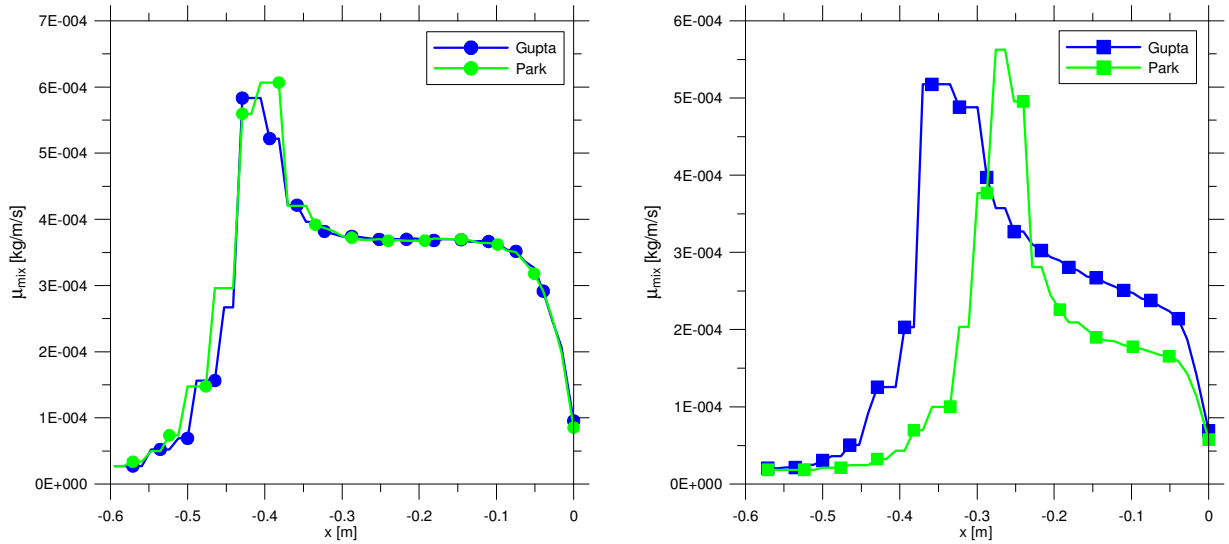

Figure 10.6 Profiles of mixture viscosity along the stagnation line across the shock layer without (a) and with (b) ionization reactions: V_∞=10000 m/s

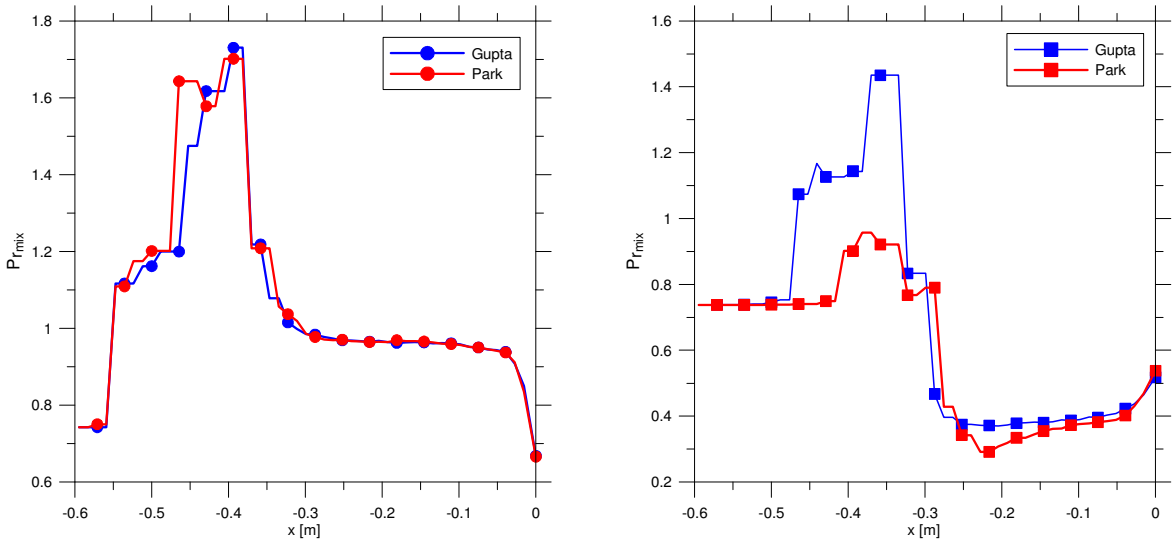

Figure 10.7 Profiles of Prandtl number along the stagnation line across the shock layer without (a) and with (b) ionization reactions: V_∞=10000 m/s

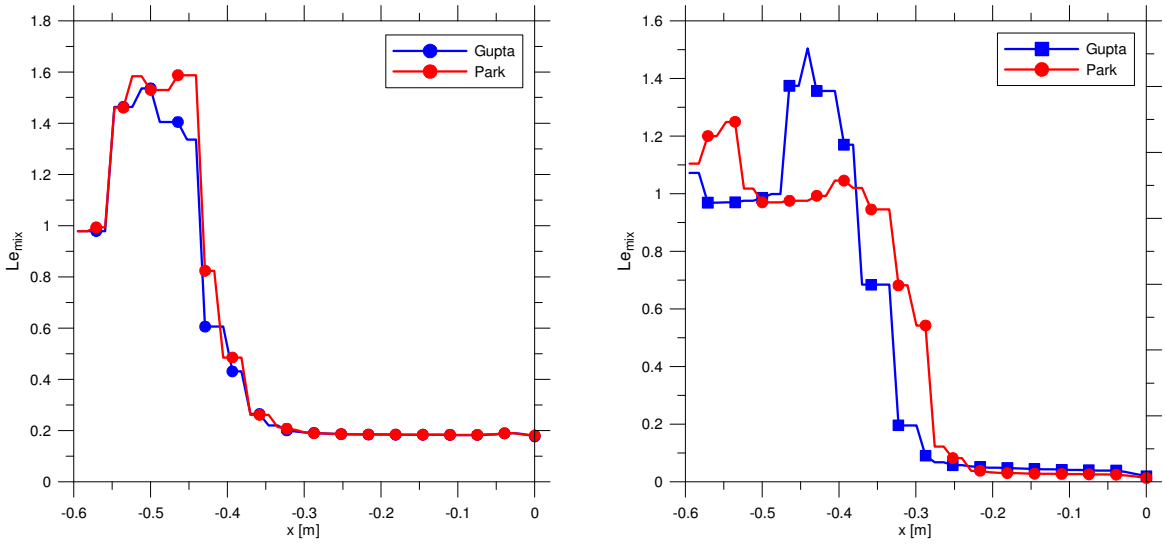

Figure 10.8 Profiles of Lewis number along the stagnation line across the shock layer without (a) and with (b) ionization reactions: V_∞=10000 m/s

Table 10.5 Average percentage variation along the stagnation line across the shock layer of transport coefficients and diffusion characteristic numbers: V_∞=10000 m/s

	μ_{mix}	K_{mix}	D_{mix}	Pr_{mix}	Le_{mix}
$\frac{G_N - P_N}{P_N}\%$	5.8	6.3	12.7	2.0	4.1
$\frac{G_I - P_I}{P_I}\%$	99.6	114.6	109.4	16.2	38.8
$\frac{G_N - G_I}{G_I}\%$	92.6	105.5	169.0	84.1	179.4
$\frac{P_N - P_I}{P_I}\%$	318.2	323.3	437.1	103.6	272.1

C. Heat Flux

Figures 10.8(a) and (b) show the profiles of heat flux along the ORION surface by the two chemical models at the extreme velocities with and without implementing ionization reactions. As expected, the effect of ionization is practically negligible at the velocity of 7600 m/s; the reduction, due to ionization, of heat flux at the stagnation point by the two chemical models are about -3% for the Gupta model and about -2% for the Park model. The effects of ionization are much stronger at the velocity of 12000 m/s. The heat fluxes reduce of about -53% and of about -59% for the Gupta and the Park model, respectively. The present results confirmed what already found in [1], namely the two models are practically equivalent when ionization is not implemented. For instance, at V_∞=7600 m/s the percentage variations between the heat flux computed by the Gupta model with respect that computed by the Park model without ionization is about -0.4%, with ionization is about -2%. On the opposite at V_∞=12000 m/s the percentage

variations increase; it ranges from -2% to about 18%. Figure 10.9 shows the profiles of the stagnation point heat flux as a function of free stream velocity. The figure shows that increasing free stream velocity the difference between the two models when ionization is taken into account amplifies. In fact, at V_∞=9000 m/s the percentage difference between the models is 5% at V_∞=12000 m/s is 18%.

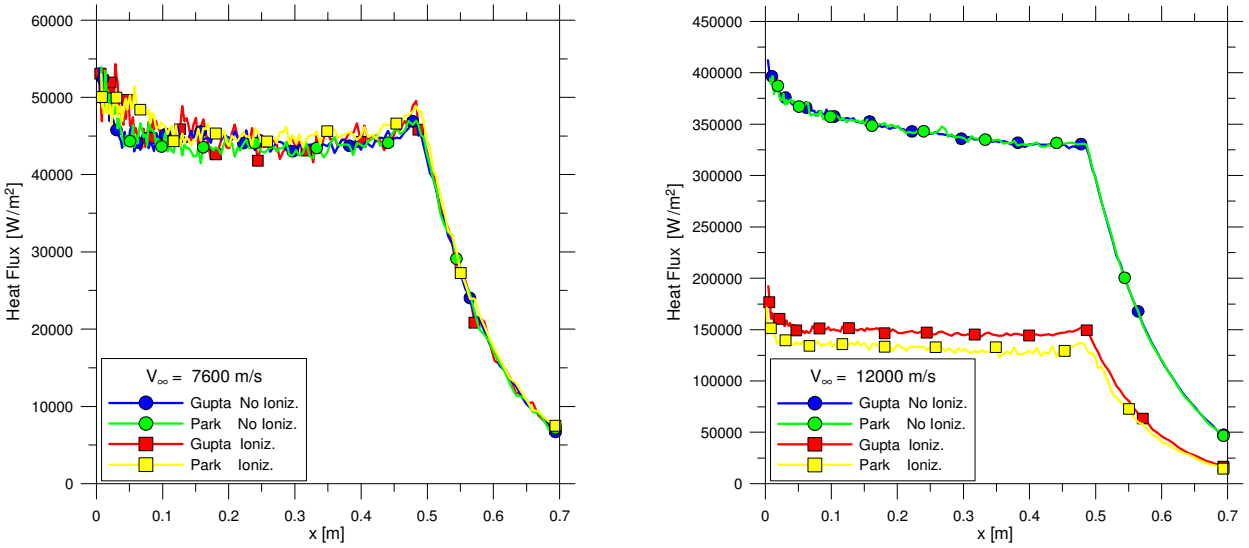

Figure 10.8 Heat flux profiles along the ORION surface at V_∞=7600 m/s (a) and at V=12000 m/s (b)

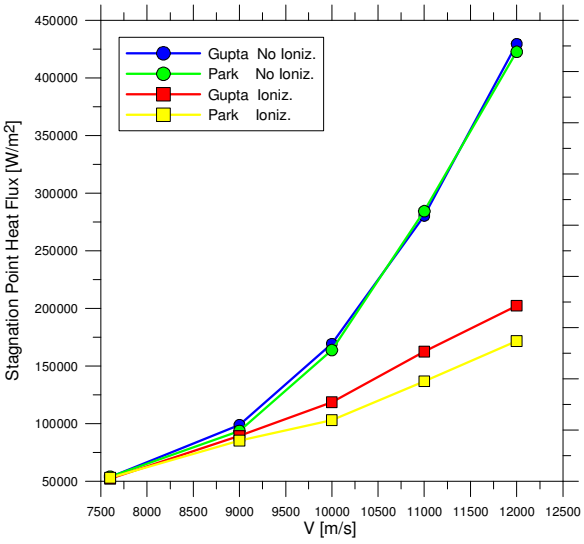

Figure 10.9 Heat flux profiles at the ORION stagnation point as function of velocity

10.5 Conclusion

The effects of ionization on the chemical models by Gupta and by Park have been analyzed on the gas composition, on the heat flux and on some thermo-fluid-dynamic parameters, including transport coefficients and related characteristic numbers. Computer tests by the DS2V code have been carries out on the ORION capsule at the altitude of 85 km in the velocity interval between 7600 to 12999 m/s.

The results showed that when ionization is not considered the chemical models compute a slight different composition in the core of the shock wave and practically the same composition on the surface, therefore the same heat flux. On the opposite when ionization is considered, the chemical models compute different composition in the whole shock layer and on the surface. More specifically, Park model is more reactive from an ionization point of view therefore, as a consequence the heat flux computed by Park is less than the one by Gupta.

The different behavior of the chemical models has been quantified by the percentage variation of some thermo-fluid-dynamic quantity, averaged along the stagnation line across the shock layer. The variation of each quantity increases when ionization is considered.

CHAPTER XI

The Fast 20XX project

11.1 Introduction

The aim of the present study is the demonstration and validation of the numerical tools able to predict aero-thermal loads acting on a space re-entry vehicle at high altitude conditions. This goal is carried out by the characterization of the DLR low density wind tunnel V2G (Fig. 10.1) and by an aerodynamic analysis of the available model of a lifting body (Figs. 11.2(a) and (b)) for realizing a comparison between computational results and experimental data. This can be considered a preliminary phase in the FAST20XX project (described in the next section) because in the V2G tunnel a model of the Spaceliner vehicle will be tested.

Figure 11.1 V2G Facility: Hypersonic blow down wind tunnel

All simulations of the present work are performed using as test gas molecular nitrogen. Two DSMC codes have been used in this study: DS2V and DS3V for studying two-dimensional flowfield and three-dimensional flow field, respectively.

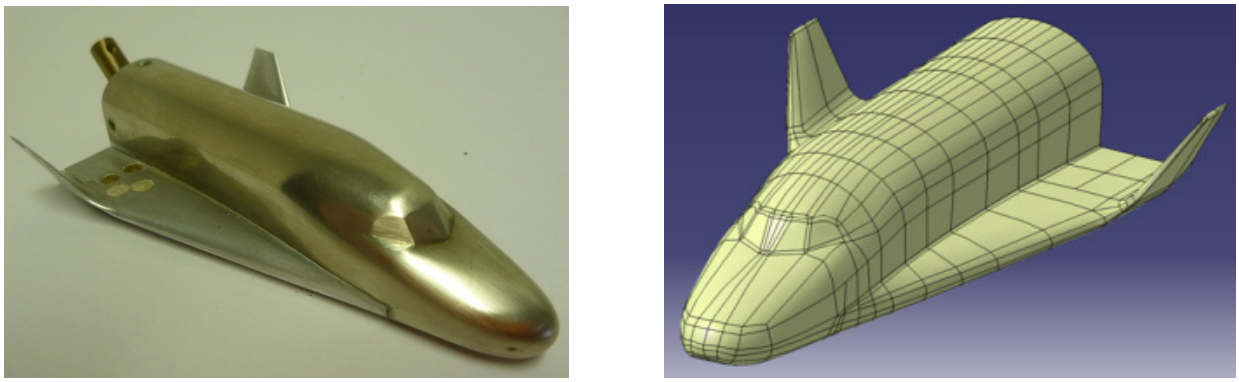

(a) (b)

Figure 11.2 Model of a lifting body (a) and its CAD rapresentation (b): length 0.0964 m; hight 0.0316 m, open wing 0.0208 m;

The main results of this work can be divided in two parts. For the first one, the DSMC two-dimensional simulation of the nozzle has been compared with the CFD simulation (by CIRA). Comparison between the continuum approach (CFD with slip flow boundary conditions) and the particle one (DSMC) in low density continuum regime, where both modeling could be used, produced similar results. So, when in future studies with a too low density (for example in transition flow regime) for using CFD code it will be possible to use DSMC method confidently. The second part of the main results is about three-dimensional simulations of a vehicle in the test chamber. A comparison between 3D simulations taking as input the exit conditions of the nozzle:

- Nominal exit conditions
- CFD exit conditions

has been made. A pre-test aerodynamic characterization of the lifting body model has been carried out, finding out that nozzle rarefaction effects can cause a not negligible difference in aerodynamic efficiency prediction.

DLR provided a test matrix with nominal test chamber conditions (based on the anticipated flight trajectory). In the present thesis has been simulated all these conditions for the lifting body. A comparison between computational results and experimental data has been already scheduled in a near future

11.2 Future high-Altitude high-Speed Transport (FAST) 20XX

The FAST20XX project [53] aims at providing a sound technological foundation for the industrial introduction of advanced high-altitude high-speed transportation in the medium term (5-10 years) and in the longer term (second part of this century), defining the most critical Research, Technology & Development associated building blocks to achieve this goal. XX in FAST20XX stands then for a number of about 5-10 for the concept in the medium term, while XX stands for much larger numbers in the case of the remaining futuristic higher-energy concepts. Among the most important scientific and technological objectives of the project is to evaluate essentially two novel concepts for high-altitude high-speed transportation. All concepts aim to satisfy the

Figure 11.3 Phoenix single stage reusable vehicle comparable to ALPHA

desire of humans to leave the atmosphere and view the earth from space, without going into orbit.

The first, ALPHA (Airplane Launched PHoenix Aircraft), is based on the shape of Phoenix (Fig. 11.3) and is launched from a carrier plane, ignites a hybrid rocket motor to climb out of the atmosphere, and then glides back to earth (like SpaceShipOne). While the main ideas of the carrier launch were based on carrying the space plane on top or below the carrier plane, the new idea of ALPHA is to release the suborbital vehicle from the cargo bay of the carrier plane, typically a huge freighter such as the largest military Antonov plane, via the rear cargo hatch (Fig 11.4(a)). This would avoid special structural changes for the carrier plane, and thus avoid certification procedures as a special plane. However, other solutions such as "piggy-back" (Fig 11.4(b)) will be considered in this project as well, and a choice will be made early. Alpha-concept is envisaged in the medium term of five to ten years

(a)

(b)

Figure 11.4 The artist's view of Phoenix leaving the cargo plane's rear end (a) and Space Shuttle testing for approach and landing after separation (b).

SpaceLiner (Fig. 11.5), a high-energy concept, is intended to achieve a step change in ultra-fast long-haul passenger and freight transport. The SpaceLiner is defined to be capable of transporting about 50 people at high altitudes over very long distances (e.g. Europe – Australia) in no more than 90 minutes while at the same time releasing less exhaust gases into the atmosphere than today's commercial airliners. This environmentally benign concept is possible because the all-rocket LOX-LH2 propulsion is not burning the oxygen of the air and because the flight is mostly at high altitudes with almost no noise impact on ground. Nevertheless, the deposition of water in different altitudes remains to be investigated with respect to the environmental influences. Although the basic performance data of the vertically launching and horizontally landing two-stage vehicle are undisputable, the eventual commercial realization is facing quite a lot of technical and operational challenges. The most important challenges are:

- High reliability and safety of hypersonic passenger flight
- Long life staged combustion cycle rocket engines
- Transpiration cooling to safely withstand a challenging aerothermal environment
- Fast turn-around times currently unknown in the launcher business

(a)

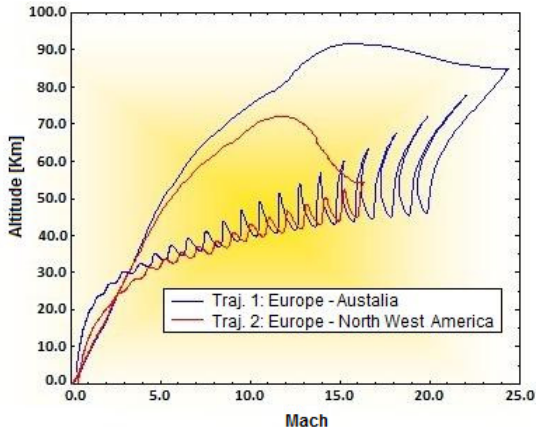

(b)

Figure 11.5 Artistic rendering of SpaceLiner (a) and its possible trajectories (b)

During the transportation phase both concepts would allow people to have a view of Earth and space at the same time

11.3 Test Matrix

Table 11.1 reports the text matrix provided from the DLR.

Table 11.1 Text matrix

M	p_0 [Pa]	T_0 [K]	Re/m	Kn	h [km]
12	5.00E+04	470	6.60E+04	8.60E-03	93
12	2.00E+05	510	1.80E+05	3.40E-03	88
16	2.00E+05	530	8.60E+04	9.80E-03	93
16	1.00E+06	780	2.10E+05	4.10E-03	89
22	1.00E+06	790	9.40E+04	1.20E-03	94
22	4.00E+06	880	2.40E+05	5.50E-03	90

These values, defined “Nominal Conditions”, as shown in Fig. 11.6, are close to the conditions that Spaceliner could met in the range of altitude between 80 and 100 km.

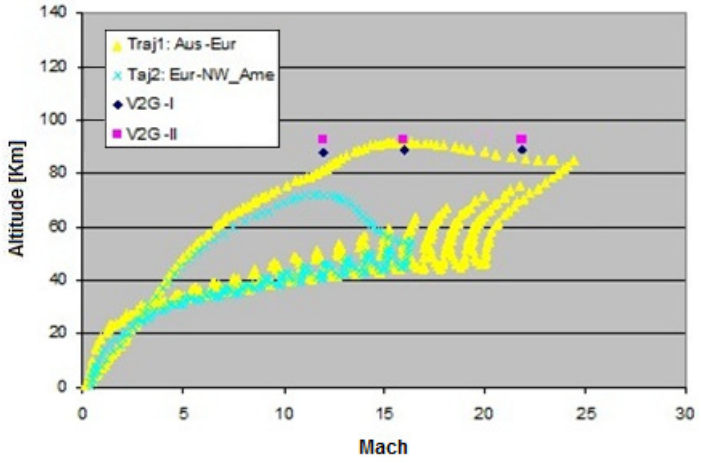

Figure 11.6 Point of trajectory SpaceLiner simulated in V2G

All of test in V2G nozzle will be carried on with molecular nitrogen. The vales reported in Table 111 has been elaborated to make possible to run with DSMC. From the stagnation temperature it is possible to obtain the free stream temperature:

$$T_0 = T_\infty\left(1+\frac{\gamma-1}{2}M_\infty^2\right) \Rightarrow T_\infty = \frac{T_0}{\left(1+\frac{\gamma-1}{2}M_\infty^2\right)} \tag{11.1}$$

Therefore the speed of sound in the free stream conditions (with γ=1.4):

$$a_\infty = \sqrt{\gamma R_{N_2} T_\infty} \tag{11.2}$$

From the knowledge of Mach number we can compute the free steam velocity:

$$V_\infty = a_\infty \cdot M_\infty \tag{11.3}$$

The free stream pressure can be computed from the stagnation pressure:

$$P_0 = P_\infty\left(1+\frac{\gamma-1}{2}M_\infty^2\right)^{\frac{\gamma}{\gamma-1}} \Rightarrow P_\infty = \frac{P_0}{\left(1+\frac{\gamma-1}{2}M_\infty^2\right)^{\frac{\gamma}{\gamma-1}}} \tag{11.4}$$

Thanks to the equation of state for an ideal gas it is possible to compute the density:

$$\rho_\infty = \frac{P_\infty}{R_{N_2} T_\infty} \tag{11.5}$$

and therefore the number density:

$$n_\infty = \frac{\rho_\infty}{m_{N_2}} \tag{11.6}$$

For a zero angle of attack and considering that molecular weight of nitrogen is $m_{N_2} = 4.65 \cdot 10^{-26}\,\mathrm{Kg}$ and the constant of gas for nitrogen is $R_{N_2} = 296.77\ {}^{J}\!/_{KgK}$, we have:

Table 11.2 Free stream nominal parameters

M	p_0 [Pa]	T_0 [K]	λ_∞ [m]	Re	Kn	T_∞ [K]	V_∞ [m/s]	n_∞ [1/m^3]	ρ_∞ [Kg/m^3]
12	5.00E+04	470	4.74E-04	3421	4.91E-03	15.77	971.34	1.59E+21	7.39E-05
12	2.00E+05	510	1.31E-04	12394	1.36E-03	17.11	1011.88	5.86E+21	2.73E-04
16	2.00E+05	530	4.87E-04	4433	5.05E-03	10.15	1039.19	1.39E+21	6.46E-05
16	1.00E+06	780	1.57E-04	13695	1.63E-03	14.94	1260.68	4.72E+21	2.19E-04
22	1.00E+06	790	6.62E-04	4493	6.90E-03	8.08	1274.50	9.69E+20	4.51E-05
22	4.00E+06	880	1.89E-04	15728	1.96E-03	9.00	1345.14	3.48E+21	1.62E-04

The Reynolds and the Knudsen numbers are evaluated by using as reference length the length of the fuselage ($l_x = 0.0965$ m). For the Reynolds number $\left(\mathrm{Re} = \frac{\rho V_\infty l_x}{\mu} \right)$ was necessary to compute the viscosity from the value at T=20°C=293K ($\mu_{20} = 1.76 \cdot 10^{-5}$ Kg/ms):

$$\mu = \mu_{20} \left(\frac{T}{293} \right)^{\omega} \tag{11.7}$$

where ω is the *viscosity index*, for the molecular nitrogen is 0.74.

Considering that the gas is composed of a single gas species, the mean free path can be calculated by the following expression:

$$\lambda_\infty = \frac{1}{\sqrt{2}\pi n d^2} \tag{11.8}$$

where *n* is the *number density* and *d* is the molecular diameter.

11.4 CFD Simulation of the Nozzle

The CFD Simulation of the Nozzle was carried out by the H3NS code [17]. In order to take into account the effects of rarefaction, H3NS ran implementing as slip boundary conditions the ones proposed by Kogan [21]. The computation domain of H3NS was a grid made up of 12000 cells (Fig. 11.7). The numerical simulations took advantage of the axi-symmetry of the nozzle, therefore the flow was computed about only half of the nozzle.

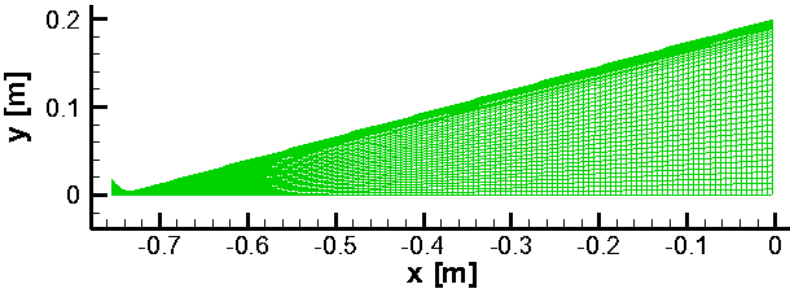

Figure 11.7 CFD computational grid

Here are reported the characteristic dimension of the nozzle:

- Length = 0.72 m;
- Throat diameter = 0.01 m;
- Diameter of the input section = 0.03 m
- Diameter of the output section = 0.40 m.

Figures 11.8(a) to (d) show same results from numerical simulation related to the conditions of the firs case in Table 11.2.

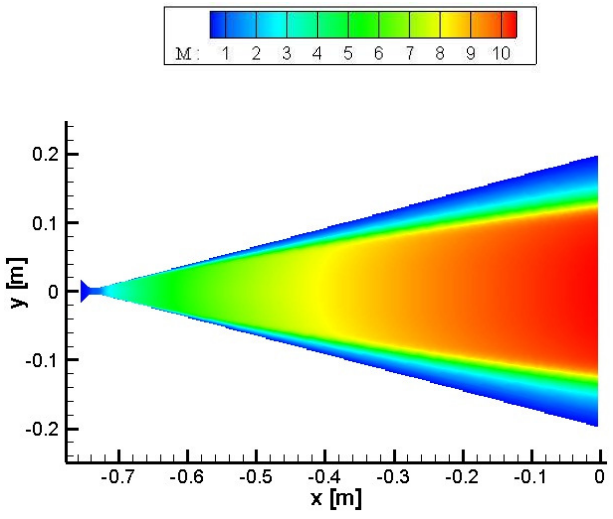

(a)

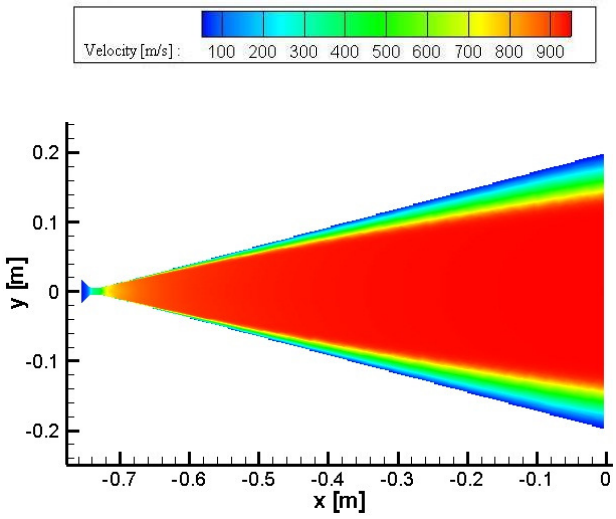

(b)

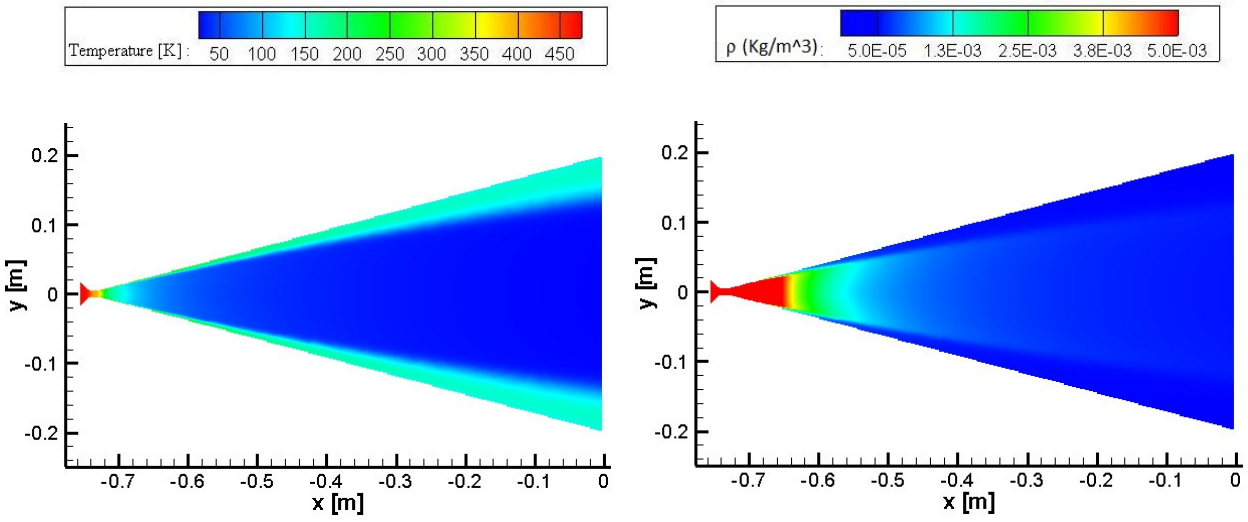

(c) (d)

Figure 11.8 2D maps of Mach number (a), velocity (b), temperature (c) and density (d)

11.5 Rarefaction Analysis of the Nozzle

Considering that in this nozzle takes part a strong expansion, to establish if is necessary a molecular approach is proper. Therefore a rarefaction analysis is carried out in diverging part of the nozzle.

Bird [1] correlates the occurrence of the breakdown of the continuum model in gaseous expansion with the "breakdown parameter", defined as:

$$P = \frac{\sqrt{\pi}}{2} S \frac{\lambda}{\rho} \left| \frac{d\rho}{dx} \right| \tag{11.9}$$

where S is the speed ratio:

$$S = \frac{V_\infty}{\sqrt{2RT_\infty}} \tag{11.10}$$

The initial breakdown starts with a value of *P* of approximately 0.02. Therefore we have:

- P<0.02 Continuo
- P>0.02 Continuum Breakdown

As shown in Fig. 11.9 for the conditions related to the firs case in Table 11.2 it is not required a molecular approach. In fact everywhere in the flow field the breakdown parameter is less than

0.02. However was decised to carried out a run with DS2V in order to compare its results from the ones by H3NS.

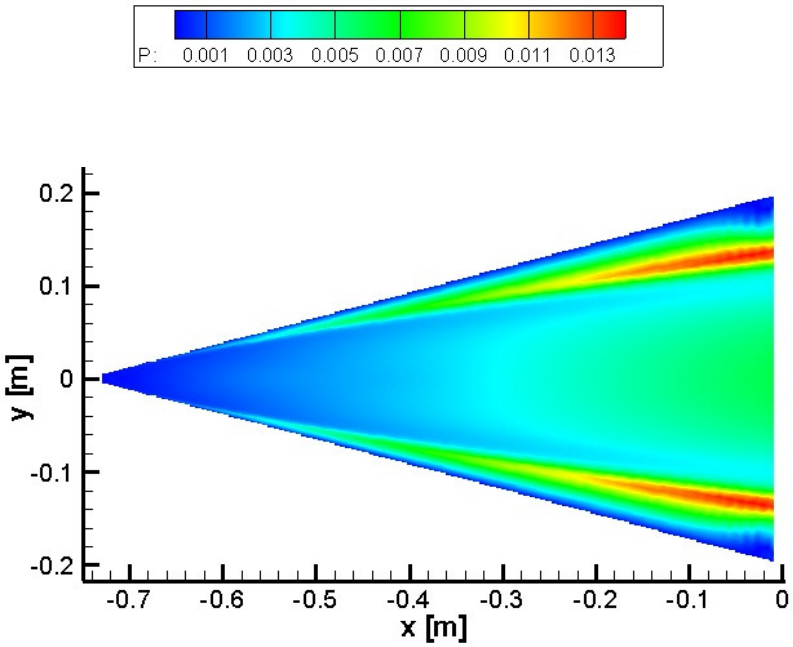

Figure 11.9 2D map of the Bird parameter in the diverging part of the nozzle

11.6 DSMC Simulation of the Nozzle

To run with DS2V were chosen the last 0.04 m of the nozzle where the number density of the gas is not so less (>10^{24} particle/m^3). As input in the DS2V simulation was set the values by H3NS at the section at x = - 0.04 m.

Figures 11.11(a) and (b) show the 2D map by H3NS and by DS2V. As well apparent, the results from the two codes are really close. To have a more accurate comparison between the results from DS2V and H3NS Figures 11.12(a) to (d) show the profile of the most important termo-fluido-dynamic quantities at the exit section of the nozzle. As shows the values of the quantities in the "core" of the flow are pretty close; for instance the Mach computed on the axis by the H3NS is 10.91, the one computed by the DS2V is 11.04. On the contrary toward the surface the results from the two codes are different.

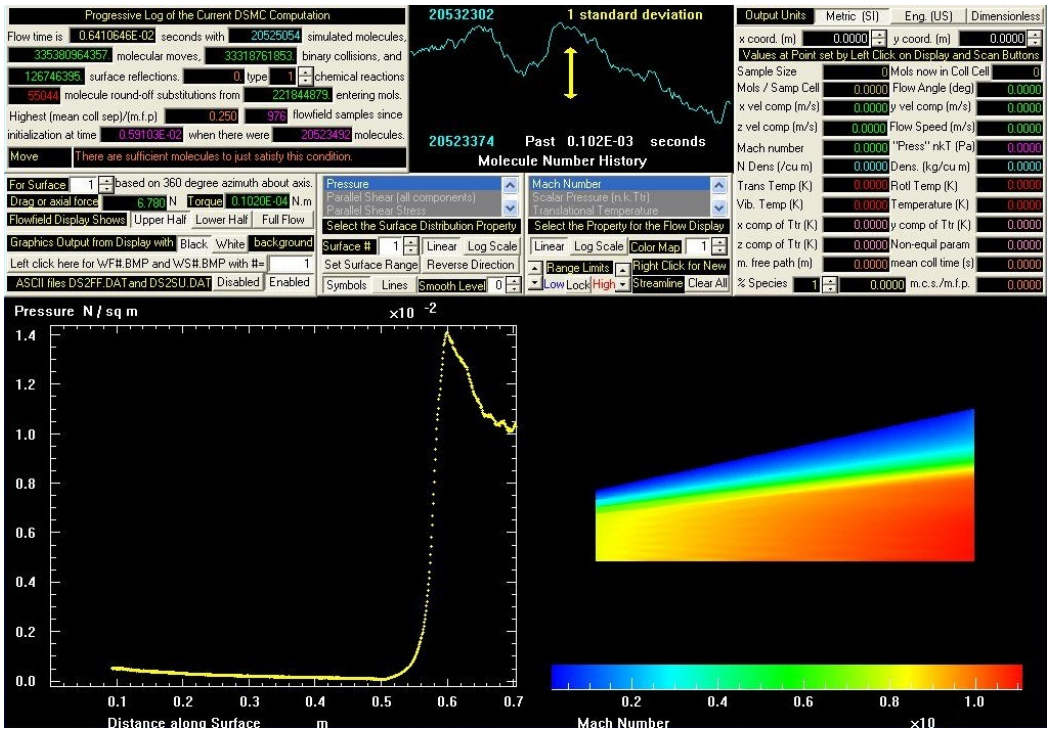

Figure 11.10 DS2V program interface during the run of the nozzle

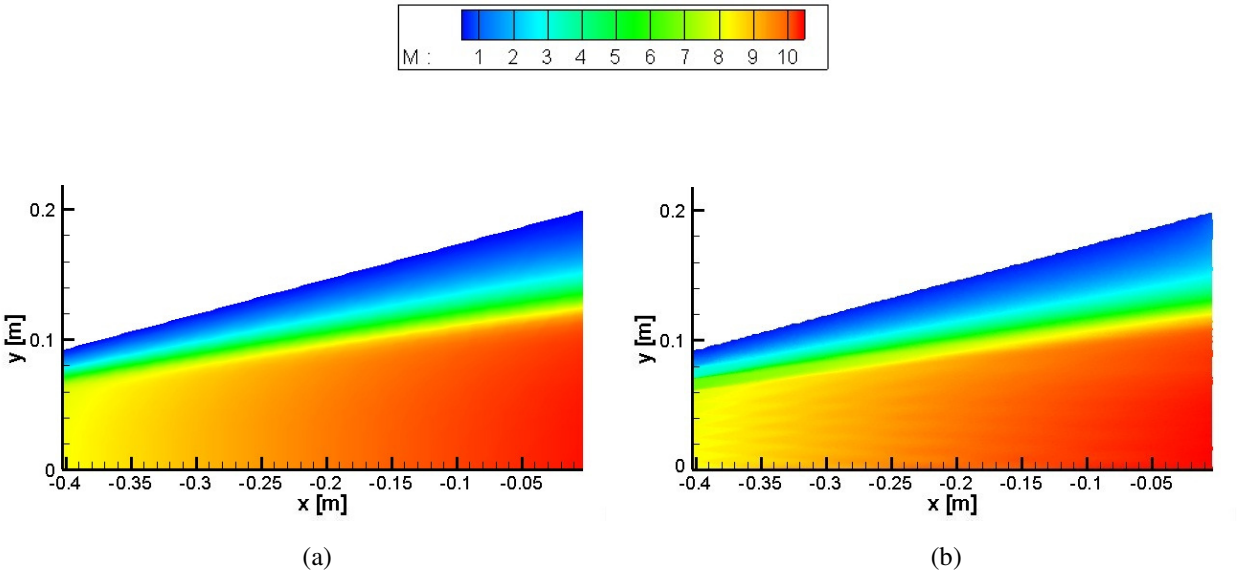

Figure 11.11 2D maps of Mach number by H3NS (a) and by DS2V (b) in the last 0.4 m of the nozzle

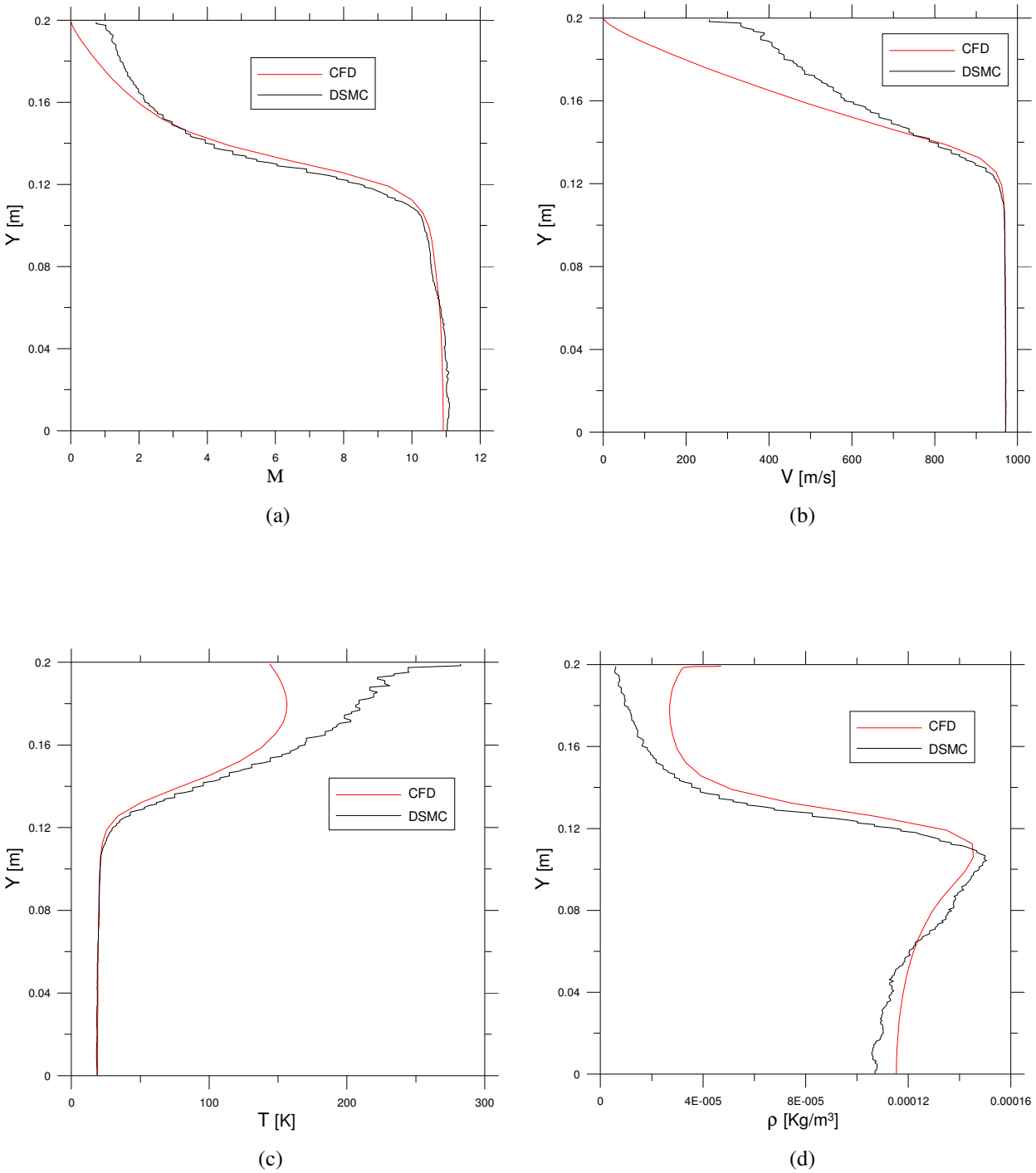

Figure 11.12 Profiles of Mach number (a), velocity (b), temperature (c) and density (d) at the exit section of the nozzle

11.7 3D Runs

For the DS3V simulations, an unstructured surface grid (Figs. 11.13(a) and (b)) is used to define the body surface, where the number of surface triangles are 8824. Note that the numerical simulations take advantage of the problem symmetry in that the flow is computed about only half of the vehicle. The computational domain of DS3V was a parallelepiped: x=0.15 m, y=0.09 m, z=0.045 m (Fig. 11.14). For all 3-D runs, simulation time was longer than 50 times the time necessary to cross the computing region along the x direction at the free stream velocity ($\cong 10^{-5}$ s). This simulation time can be considered long enough for stabilizing all thermo-aerodynamic parameters. The number of simulated molecules was always above of 1.8×10^{7}. This number of molecules provided for all simulation an average value of mcs/λ of about 1.0, thus the results can be considered reliable.

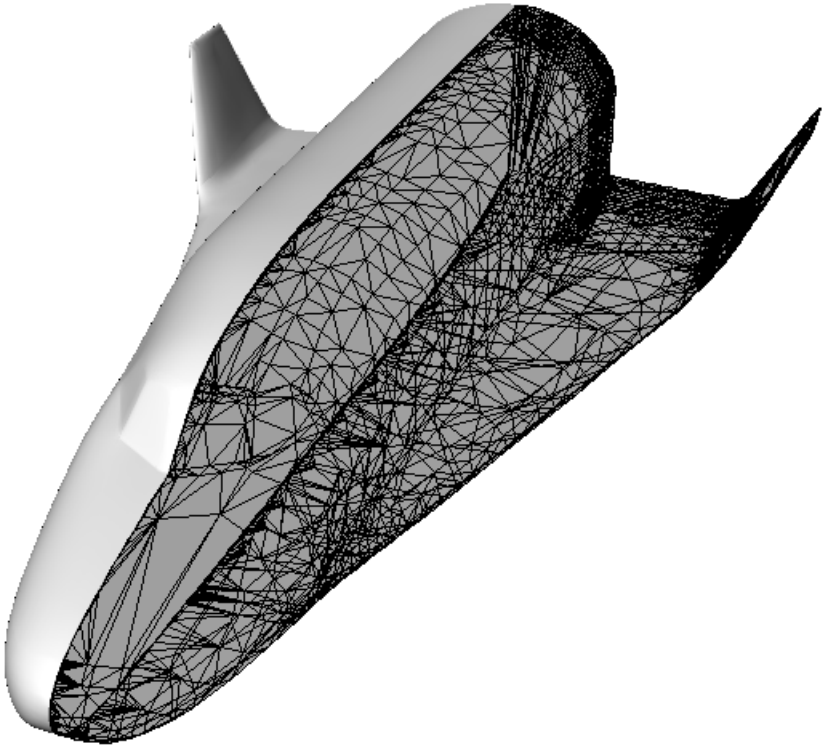

(a) Frontal view

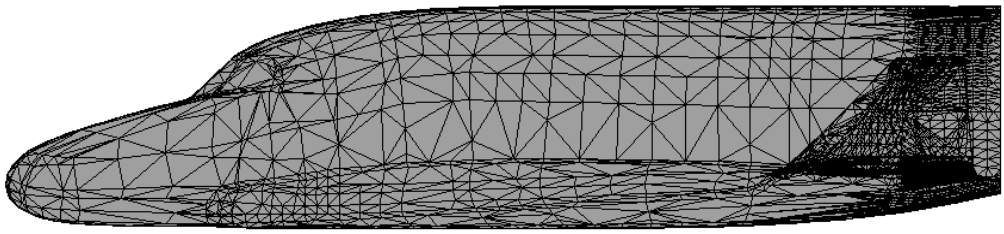

(b) Side view

Figure 11.13 Unstructured body grid used in present DS3V simulations

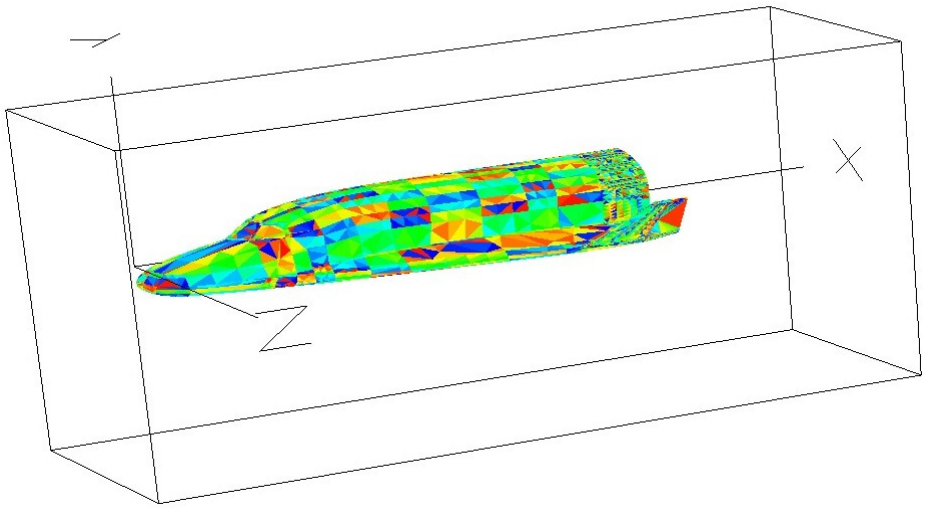

Figure 11.14 DS3V computational domain

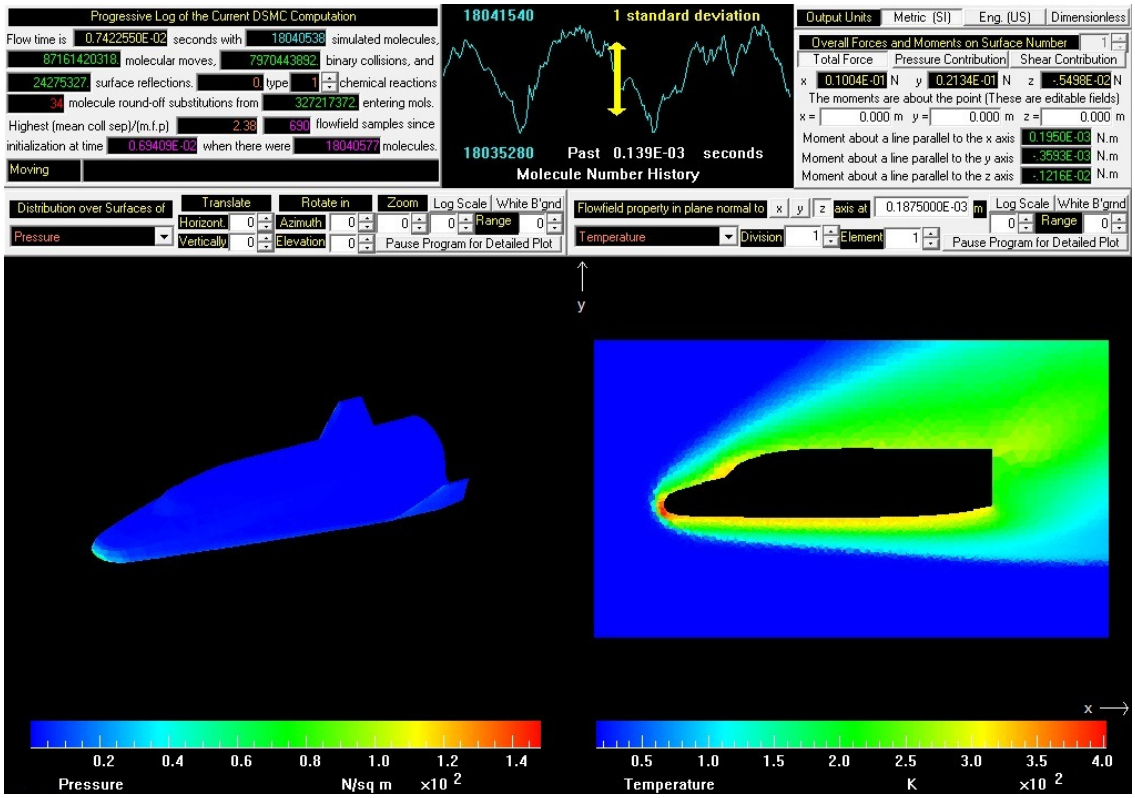

Figure 11.15 DS3V program interface during the run at M=12, Re=3421 ed α=25°

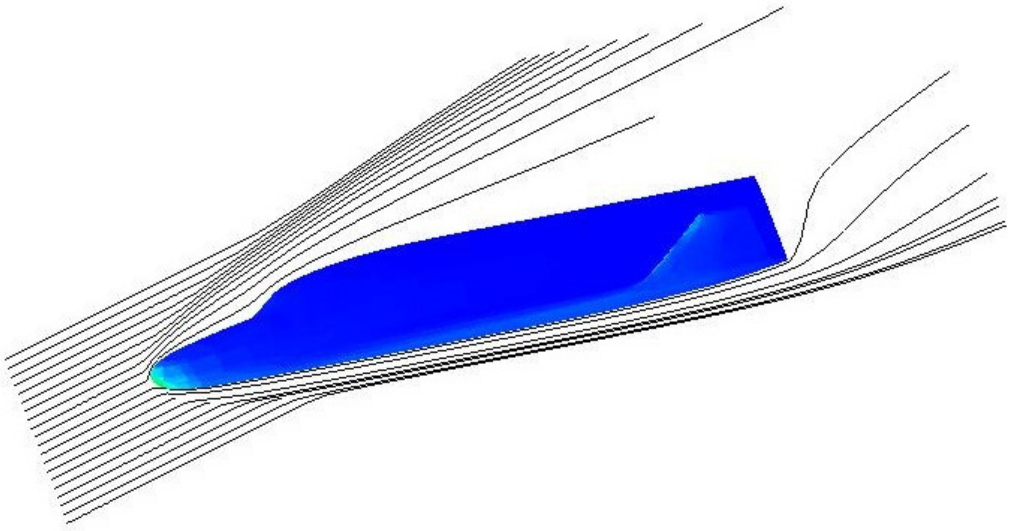

Figure 11.16 Streamlines for the simulation at M=16, Re=13695 and α=20°

Before carried out the entire analysis of the Test matrix, the just for the first case of the Test matrix a comparison of the DSMC 3D simulation results was provided considering as input data the ones provided by DLR and the ones provided by CFD simulations. The input data to compare of the two cases are reported Table 11.3. Figures 11.17(a) and (b) reports the reference surface ($S_{rif} = 1369.55 \cdot 10^{-6} m^2$) and length ($l_x$=0.0965 m) respectively used to compute the aerodynamics coefficients.

Table 11.3 Input values for DS3V run from the Nominal condition and from the Numerical Simulation

Exit Conditions	M_∞	Re_∞	Kn_∞	T_∞ [K]	n_∞ [1/m^3]	$V_{\infty x}$ [m/s]
Nominal	12	3421	4.91×10^{-3}	15.77	1.59×10^{-21}	971.34
CFD	10.91	4526	3.32×10^{-3}	19.72	2.48×10^{-21}	971.09

As expected, considering that the input values are not so different, also the DS3V results obtained from the Nominal condition and from the Numerical Simulation, shown in Fig. 11.18, are not so different. More specifically a small effect between nominal and calculated (CFD slip flow hypothesis) results is predicted on C_L and C_D aerodynamic coefficients (Figs 11.18(a) to (c)). On the other an higher effect is predicted on the maximum value of the aerodynamic efficiency (about 7%) (Fig. 11.18(d)). For this reason for the other cases reported in Table 11.2 was decided to run using as input data the nominal ones.

The results are shown in couple, keeping the same Mach number and considering two values for the Renolds number:

- in Figure 11.19 are shown the results for Mach = 12 and Reynolds = 3421 and 12394;
- in Figure 11.20 are shown the results for Mach = 16 and Reynolds = 4433 and 13695;
- in Figure 11.21 are shown the results for Mach = 12 and Reynolds = 4493 and 15728;

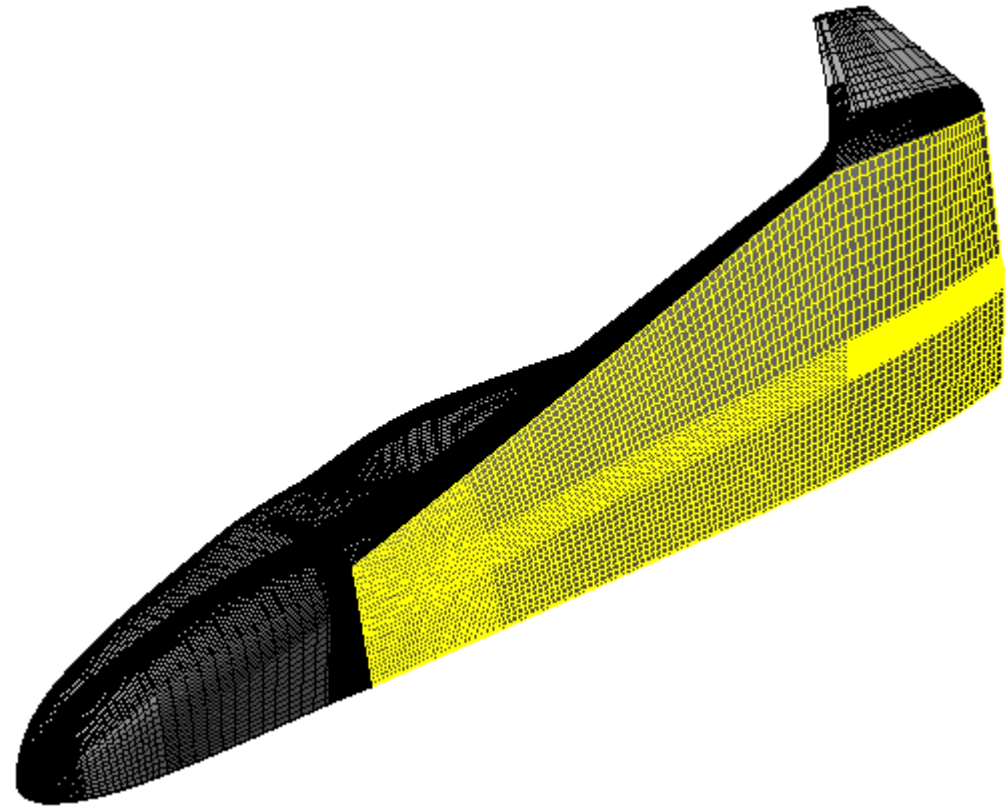

(a)

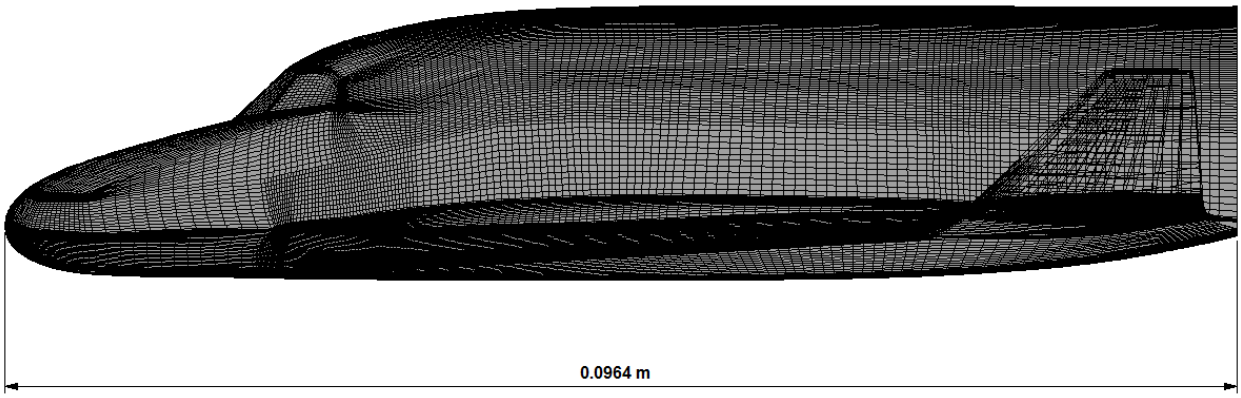

(b)

Figure 11.17 Refernce Surface (a) and Length (b)

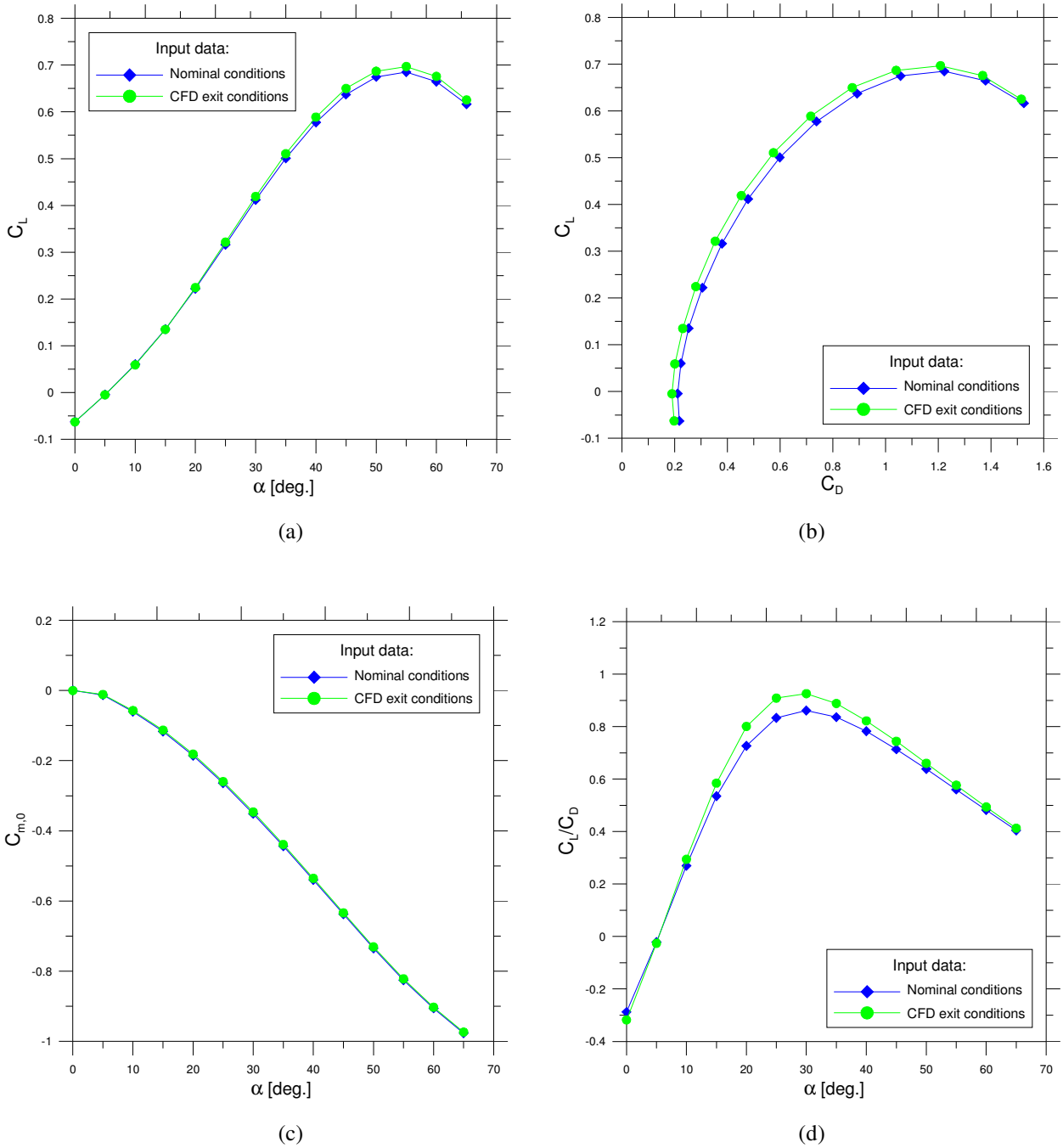

Figure 11.18 Profiles Lift force coefficient C_L versus angle of attack α (a), Lift force coefficient C_L versus Drag force coefficient C_D (b), Pitching moment coefficient around nose $C_{m,0}$ versus angle of attack α (c), Aerodynamic efficiency $C_L\backslash C_D$ versus angle of attack α (d), obtained considering as input values the ones provided from the Nominal condition and the ones from the numerical simulation

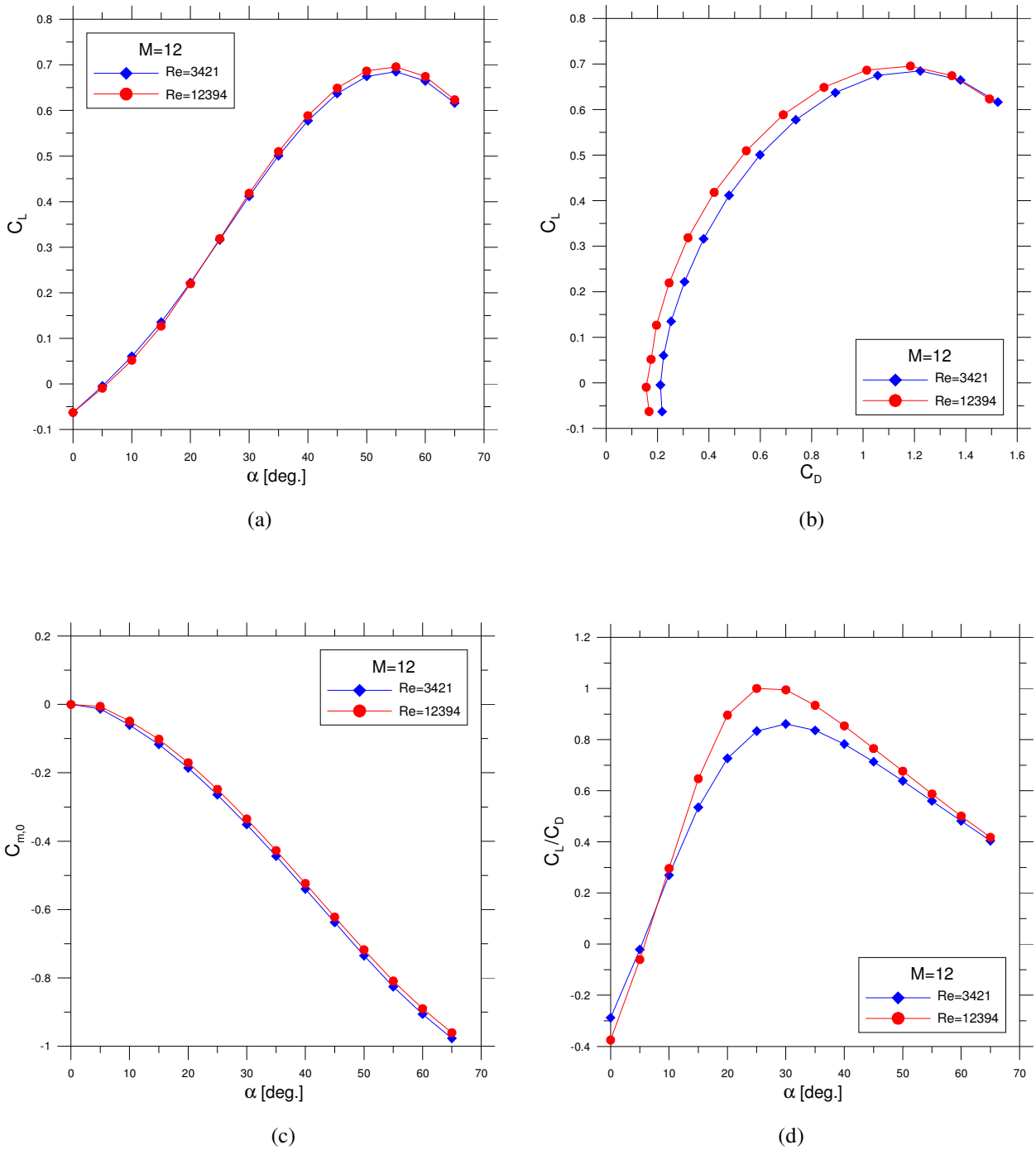

Figure 11.19 Profiles Lift force coefficient C_L versus angle of attack α (a), Lift force coefficient C_L versus Drag force coefficient C_D (b), Pitching moment coefficient around nose $C_{m,0}$ versus angle of attack α (c), Aerodynamic efficiency $C_L\backslash C_D$ versus angle of attack α (d), at Mach = 12 and Reynolds = 3421 and 12394.

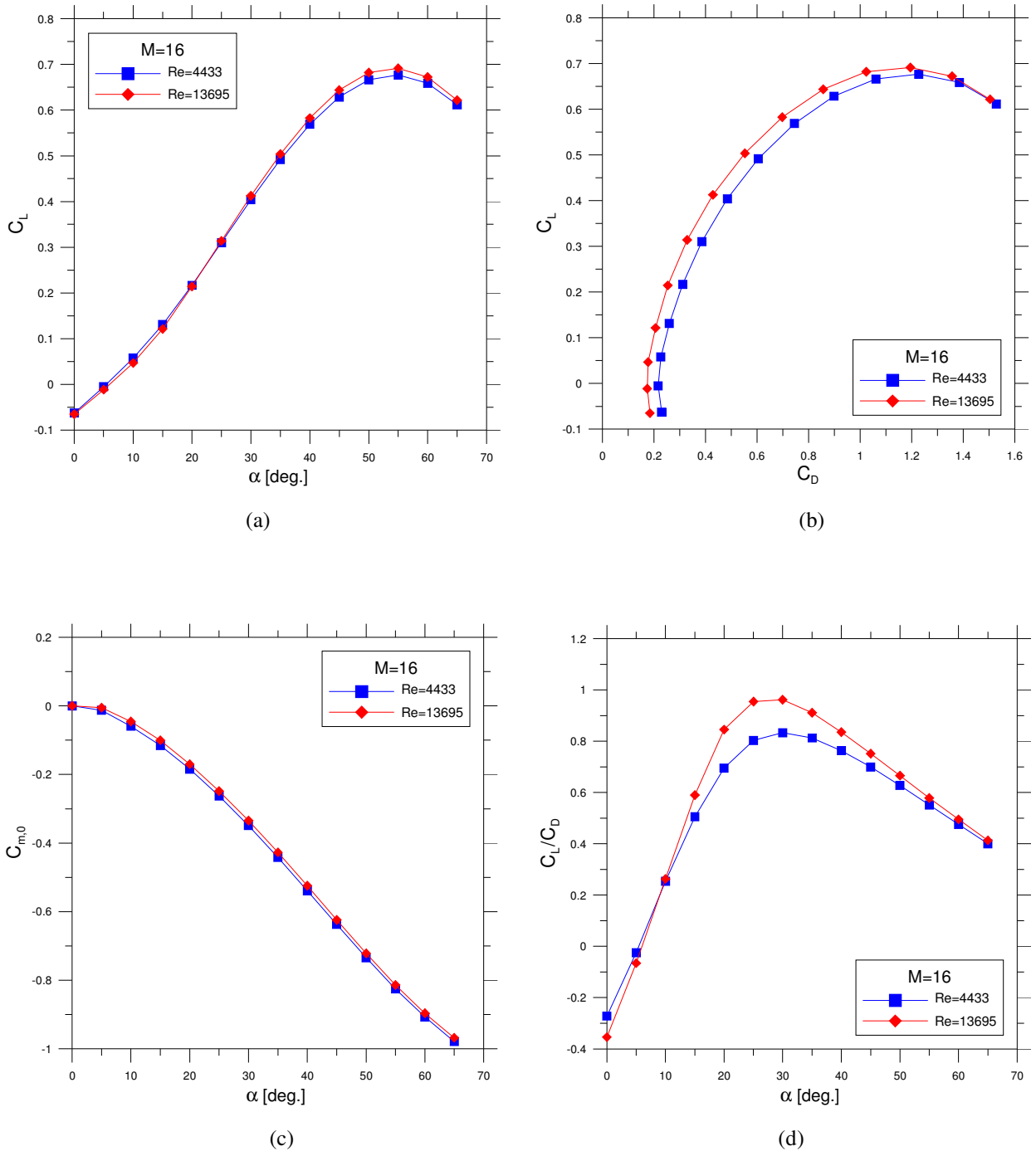

Figure 11.20 Profiles Lift force coefficient C_L versus angle of attack α (a), Lift force coefficient C_L versus Drag force coefficient C_D (b), Pitching moment coefficient around nose $C_{m,0}$ versus angle of attack α (c), Aerodynamic efficiency $C_L\backslash C_D$ versus angle of attack α (d), at Mach = 16 and Reynolds = 4433 and 13695.

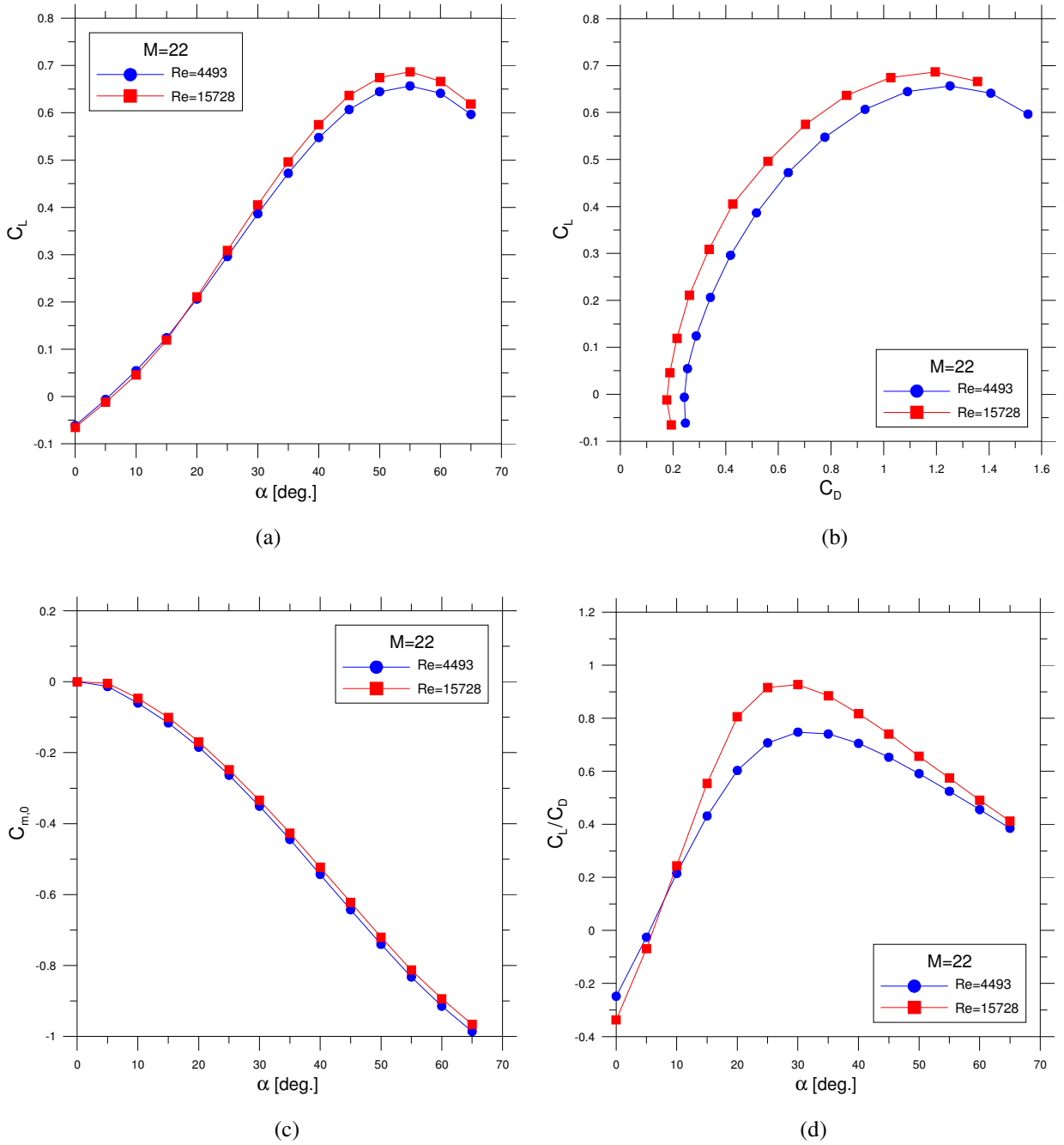

Figure 11.21 Profiles Lift force coefficient C_L versus angle of attack α (a), Lift force coefficient C_L versus Drag force coefficient C_D (b), Pitching moment coefficient around nose $C_{m,0}$ versus angle of attack α (c), Aerodynamic efficiency $C_L\backslash C_D$ versus angle of attack α (d), at Mach = 22 and Reynolds = 4493 and 15728.

11.8 Conclusions

The aim of the study was the demonstration and validation of the numerical tools able to predict aero-thermal loads acting on a space re-entry vehicle at high altitude conditions. This study can be considered a preliminary phase in the ESA FAST20XX project. The most important objectives of the project is to evaluate essentially novel concepts for high-altitude high-speed transportation. The most important concept is definitely SpaceLiner, that is defined to be capable of transporting about 50 people at high altitudes over very long distances (e.g. Europe – Australia) in no more than 90 minutes. In the V2G tunnel a model of the Spaceliner vehicle will be tested.

Two DSMC codes have been used in this study: DS2V and DS3V for studying two-dimensional flow field and three-dimensional flow field, respectively. The DSMC two-dimensional simulation of the nozzle has been compared with the CFD simulation. The Comparison between these two codes showed that the codes produced similar results. So, when in future studies with a too low density (for example in transition flow regime) for using CFD code it will be possible to use DSMC method confidently. DLR provided a test matrix with nominal test chamber conditions (based on the anticipated flight trajectory). These values, defined “Nominal Conditions”, are close to the conditions that Spaceliner could met in the range of altitude between 80 and 100 km. In the present thesis has been simulated all these conditions for the lifting body. The next step in this study will be made a comparison between computational results and experimental data.

Conclusions

The most relevant results of the thesis are here reported:

The new parameter based on the Crocco theorem can be considered a good tool in the identifications of the non-equilibrium regions.

A new parameter evaluating the non-equilibrium of a flow field has been proposed. The new parameter relies on the formulation of the Crocco theorem. The results have been compared with the ones based on the difference of the components of translational temperature, for the quantification of anisotropy, and the ones based on the difference of the translational, rotational and vibrational temperatures, for the quantification of thermodynamic non-equilibrium. The proposed parameter verified to be more effective than the parameters based on temperature differences; it seems to be able to identify in a more precise and effective way the non-equilibrium regions both in and outside the shock wave.

The "new" bridging formula looked to be better than the former formulae.

A "new" methodology to compute aerodynamic force coefficients at a first stage of design (phase A) of a re-entry vehicle has been obtained by the merge of the modified Potter and the Kotov formulae. This methodology, called "new" bridging formula, has been successfully tuned to sphere. The "new" formula has been used to compute the pressure and the skin friction distributions on two current capsules: EXPERT and ORION. The comparison of the local and global aerodynamic coefficients with the DS2/3V results verified that the "new" bridging formula is excellent at high altitudes but at low altitudes do not match satisfactory the DS2/3V results; this is probably due to a failure of the panel method. However the results by the "new" bridging formula are better than the one by the original formulae and the mismatch with the DS2/3V results is within 20% that is acceptable in a phase A of a design.

The Fan-Shen model could be considered a possible alternative to the Bird model.

As well known in the sophisticated and advanced DSMC codes the criterion evaluating the occurrence of a chemical reaction relies on the computation of a parameter, called "steric factor", that represents the probability of occurrence of a chemical reaction. This parameter was obtained by Bird, though mathematical steps, from the kinetic theory of gases and from the phenomenological rate coefficient, defined by an equation of the Arrhenius form. Therefore the steric factor is a macroscopic criterion for the evaluation of the occurrence. On the other hand

Fan and Shen compute the occurrence of a chemical reaction as the result of the breakdown of the chemical bond. Therefore the parameter that Zuppardi obtained from the Fan-Shen relation is a microscopic criterion. The runs proposed in this thesis proved that the results from the Fan-Shen model are very close to those from the Bird model. Thus the Fan-Shen model could be considered as a possible alternative to the Bird model. Furthermore this is meaningful because, as pointed out, the two chemical model are based on different approaches.

The difference in the computation of heat flux between DS2V and H3NS can be attributed mostly to the different handling of the chemical process.

The Gupta and Park chemical model, without ionization, in DSMC compute a different composition in the flow field but the same composition on the surface and therefore the same heat flux.

In order to deepen the comparison of heat flux, at high altitude flight, by two codes based on different approaches, the computation of heat flux on EXPERT and on ORION capsules, has been carried out by DS2V and by a computational fluid dynamic code (H3NS). DS2V and H3NS rely on the Gupta and on the Park chemical models, respectively.

Heat flux by DS2V was always higher than the one by H3NS, but the mismatch between the two codes decreases for fully catalytic surface. This is justified because the fully catalytic surface reduces the differences of chemical model and keeps only the ones related to the different approach on which the two codes rely. On the other hand the overestimation of heat flux by DS2V, for non-reactive surface, is due mostly to a lower dissociation of O_2 and N_2 and to an higher formation of NO.

To assess the incidence of the chemical models, the Park model was implemented also in DS2V. The results showed that the two chemical models compute a different composition in the flow field but the same composition on the surface and therefore the same heat flux. However, using the Park model in DS2V does not generate any match of the molar fractions of O, N and NO with the ones computed by H3NS. Therefore DS2V and H3NS compute a different composition both in the flow field and on the surface, even implementing the same model (Park). For this reason the difference in the computation of heat flux between DS2V and H3NS can be attributed to the different approaches but mostly to the different handling of the chemical process.

The difference between the Gupta and the Park chemical model, without ionization, in DSMC is the change of the stand-off distance.

The effects of the different compositions as well as of the different thermo-dynamic quantities, by the chemical models of Gupta and Park with no ionization, are evaluated in DSMC on: non-equilibrium parameters, local mean free path and local Knudsen numbers, local transport coefficients and local characteristic numbers of Prandtl, Lewis and Schmidt. The most relevant effect, that it is observed, is the change of the stand-off distance, that produces locally strong effects on the computation of thermo-fluid-dynamic quantities. More specifically, the stand-off distance computed by the Park model is slightly shorter than the one by the Gupta model.

When ionization is considered, the chemical models by Gupta and by Park compute different composition in the whole shock layer and on the surface.

To check the incidence of the ionization reactions computer tests by the DS2V code have been carries out on the ORION capsule at the altitude of 85 km in the velocity interval between 7600 to 12000 m/s.

The results showed that when ionization is not considered the chemical models compute a slight different composition in the core of the shock wave and practically the same composition on the surface, therefore the same heat flux. On the opposite when ionization is considered, the chemical models compute different composition both in the flow filed and on the surface. More specifically, Park model is more reactive from an ionization point of view therefore, as a consequence the heat flux computed by Park is less than the one by Gupta.

The analysis of the DLR low density wind tunnel V2G and the study of the aerodynamic analysis of the available model of a lifting body have been successfully carried out by DSMC.

The aim of the study was the demonstration and validation of the numerical tools able to predict aero-thermal loads acting on a space re-entry vehicle at high altitude conditions. This study can be considered a preliminary phase in the ESA FAST20XX project. The DSMC two-dimensional simulation of the nozzle has been compared with the CFD simulation. The Comparison between these two codes showed that the codes produced similar results. So, when in future studies with a too low density (for example in transition flow regime) for using CFD code it will be possible to use DSMC method confidently. In the present thesis has been simulated all these conditions for the lifting body with DSMC codes. A comparison between computational results, obtained in this thesis, and experimental data has been already scheduled in a near future.

Bibliography

[1] **Bird, G.A.** *Molecular gas dynamics and Direct Simulation Monte Carlo*, 1998 (Clarendon Press, Oxford (Great Britain)).

[2] **Wagner, W.**, "A Convergence Proof of Bird's Direct Simulation Monte Carlo Method for the Boltzmann Equation," Journal of Statistical Physics, Vol. 66, No. 3/4, 1992, pp. 1011–1044.

[3] **Vincenti, W. G.** and **Kruger, C. H.**, Introduction to Physical Gas Dynamics, Krieger Publishing Company, 1965.

[4] **Eggers J, Beylich AE**. 1995. Development of a hybrid scheme and its application to a flat plate flow. In *Proc. Int. Symp. Rarefied Gas Dynamics, 19th, Oxford*, ed. J Harvey, G Lord, 2:1216–22. New York: Oxford Univ. Press

[5] **Schwartzentruber, T.E., Scalabrin, L.C., Boyd, I.D.**, "Hybrid Particle-Continuum Simulations of Non-Equilibrium Hypersonic Blunt Body Flow Fields". Paper 2006-3002, AIAA, June 2006. 9th AIAA/ASME Joint Thermophysics and Heat Transfer Conference 5 - 8 June 2006, San Francisco, California

[6] **Cercignani, C.**, "Rarefied Gas Dynamics", Cambridge University Press, 2000

[7] **Cercignani, C.**, "Mathematical Methods in Kinetic Theory", Plemum Press, 1990 (second edition)

[8] **Chapman S.** and **Cowling T.G.**, "The Mathematical Theory of Non-uniform Gases", Cambridge Mathematical Library, Cambridge, 1991 (third edition)

[9] **Zhong X.**, "On numerical Solution of Burnett Equations for Hypersonic Flow Past 2-D Circular Blunt Leading Edges in Continuum Transition Regime", AIAA 24th Fluid Dynamics Conference, Orlando, July 1993

[10] **Bird, G.A.**, *Sophisticated Versus Simple DSMC*, Proceedings of the 25th International Symposium on Rarefied Gas Dynamics, Saint-Petersburg (Russia), July 2006

[11] **Bird, G.A.**, *Sophisticated DSMC*, Notes from a Short Course held at the DSMC07 Conference, Santa Fe (USA), Sep. 30- Oct. 3, 2007

[12] **Bird, G.A.**, "Visual DSMC Program for Two-Dimensional Flows," *The DS2V Program User's Guide Ver. 4.5*, G.A.B. Consulting Pty Ltd, Sydney (Aus.), June 2006, URL: http://gab.com.au.

[13] **Bird, G.A.**, "Visual DSMC Program for Three-Dimensional Flows," *The DS3V Program User's Guide Ver. 3.6*, G.A.B. Consulting Pty Ltd, Sydney (Aus.), June 2006, URL: http://gab.com.au.

[14] **Ivanov, M.S., Markelov, G.N.,** and **Gimelshein, S.F.**, *Statistical Simulation of Reactive Rarefied Flows: Numerical Approach and Applications*, AIAA Paper 98-2669, June 1998.

[15] **LeBeau, G.J.**, A User Guide for the DSMC Analysis Code (DAC) Software for Simulating Rarefied Gas Dynamic Environments," Revision DAC97-G, Jan. 2002.

[16] **Gupta, R.N., Yos J.M.** and **Thompson R.A.**, "A Review of Reaction Rates and Thermodynamic Transport Properties for an 11-Species Air Model for Chemical and Thermal Non-Equilibrium Calculations to 30,000 K," NASA TM 101528, February 1989

[17] **Ranuzzi G., Borreca S.**, "H3NS: Code Development Verification and Validation," CIRA-CF-06-1017, Capua, Italy, 2006

[18] **Park C.** and **Lee S.H.**, "Validation of Multi-temperature Nozzle Flow Code NOZNT," *AIAA 28th Thermophysics Conference*, Orlando, USA, 1993

[19] **Park C., Jaffe R.L.** and **Partridge H.**, "Chemical-Kinetic Parameters of Hyperbolic Earth Entry," *Journal of Thermophysics and Heat Transfer*, Vol.15, N.1, Jan-March 2001

[20] **Gnoffo P.A:, Gupta R.N.** and **Shinn J.L.**, "Consevation Equation and Physical Models for Hypersonic Air Flows in Thermal and Chemical Nonequilibrium,". NASA TP 2867, February 1989

[21] **Kogan N.M.**, *Rarefied Gas Dynamic*, Plenum, New York, USA, 1969

[22] **Chigullapalli, S., Venkattraman, A., Ivanov, M.S., Alexeenko**, A.A, Entropy considerations in numerical simulations of non-equilibrium rarefied flows. *Journal of Computational Physics*, 229 (2010) 2139-2158

[23] **Candler, G.V.** and **Boyd, I.D.** A multiple translational temperature gas dynamic model *Phys. Fluids*, **6** (11), (1994) 3776-3786.

[24] **Zuppardi, G.** Evaluating anisotropy and thermodynamic non-equilibrium in hypersonic transitional regime. In Proceedings of the 24th International Symposium on Rarefied Gas-Dynamics (RGD24), 2004, Monopoli (Italy).

[25] **Hirschel, E.H.** *Basics of Aerothermodynamics*, 2005 (Springer-Verlag Berlin (Germany))

[26] **Shu, F.H**. *The Physics of Astrophysics – Gas Dynamics (Vol.II)*, 1992 (University Science Books Sausalito (USA))

[27] **Greitzer, E.M**., **Tan, C.S.** and **Graf, M.B.** *Internal Flow, Concepts and Applications*, 2004 (Cambridge University Press (United Kingdom))

[28] **Moss, J.N.**, Rarefied Flows of Planetary Entry Capsules, AGARD-R-808, NATO Advisory Group for Aerospace Research and Development, 1997, paper no 5.

[29] **Shen, C.**, *Rarefied Gas Dynamic: Fundamentals, Simulations and Micro Flows*, 2005, Springer-Verlag, Berlin, Germany,

[30] *Tecplot*. Version 11.0–1-125. Software Package, CD-ROM Computer software. Tecplot Inc. Bellevue, WA, 2006.

[31] **Smolderen, J.J.** The Evolution of the Equations of Gas Flow at Low Density, Progress in Aeronautical Science, Vol.6 , 1965, (Pergamon Press, Oxford (Great Britain)).

[32] **Zuppardi, G.** and **Romano, F.**, DSMC Comparison between Two Different Models Evaluating the Occurrence of Chemical Reactions, DSMC07 Conference, 2007, Santa Fe, USA.

[33] **Fan, J.** and **Shen, C.**, A Sterically Dependent Chemical Reaction Model, Proceedings of the 19th Rarefied Gas-Dynamic Symposium, 1994, Oxford, 448-454.

[34] **Bird, G.A.**, New Chemical Reaction Model for Direct Simulation Monte Carlo Studies, Progr. in Astro. and Aero. 159, 1994, 185-196.

[35] **Zuppardi, G.**, Comparing the Chemical Models by Fan-Shen and by Bird through a 2D DSMC Code, Proceedings of the 26th Rarefied Gas-Dynamic Symposium, 2008, Kyoto, Japan, 347-352.

[36] **Coleman, G.T., Metcalf, S.C.** and **Berry, C.J.**, Heat transfer to Hemisphere Cylinders and Bluff Cylinders between Continuum and Free Molecular Flow Limits, Proceedings of the 10th Rarefied Gas-Dynamic Symposium, 1976, Aspen, USA, 393-404.

[37] URL: http://www.esa.int/esaHS/SEMC9A7JT2G_index_1.html

[38] **J. Muylaert** et al., "Aerothermodynamic Environment of EXPERT and Flight Measurement Technique Integration", IAC-05-2363, 2005.

[39] **H. Ottens** et al., "Aerothermodynamic Flight Measurement Techniques and Environment Issues of EXPERT", IPPW-3, Anavysos, 2005

[40] **A. Schettino** et al., "Aerodynamic and aerothermodynamic data base of Expert capsule", West-East High Speed Flow Conference, November 2007, Moscow, Russia

[41] **P.V. Vashchenkov** and **M.S. Ivanov**, "Numerical analysis of high altitude aerothermodynamics of Expert Re-entry vehicle" , Institute of Theoretical and Applied Mechanics SB RAS, ICMAR, July 2002, Novosibirsk, Russia

[42] URL: http://www.nasa.gov/mission_pages/constellation/orion/index.html

[43] **Votta R., Schettino A., Ranuzzi G.** and **Borrelli S.**, "Hypersonic Low-Density Aerothermodynamics of Orion-Like Exploration Vehicle," *Journal of Spacecraft and Rockets*, Vol. 46, No. 4, July–August 2009

[44] **M. Ivanov, P. Vashchenkov** and **A. Kashkowsky,** Numerical Investigation of the EXPERT Reentry Vehicle Aerothermodynamics Along the Descent Trajectory, 39th AIAA thermophysics Conference, Miami, June 2007

[45] **V.M. Kotov**, **E.N. Lychkin**, **A.G. Reshetin**, **A.N. Schelkonogov**, *Proc. of 13th Symp. of Rarefied Gas Dynamics*, Plenum Press, New York, 1982, pp. 487-495

[46] **J.L. Potter**, **S. W. Peterson**, *Journal of Spacecraft and Rockets*, 3, 344-351 (1992)

[47] **R.G. Wilmoth**, **R.A. Mitcheltree** and **J.N. Moss**, *Journal of Spacecraft and Rockets*, 3, 436-441 (1999)

[48] **Zuppardi G., Morsa L., Schettino A., Votta R.**, "Analysis of Aero-Thermodynamic Behavior of EXPERT Capsule in Transitional Regime," *Proceedings of the 27th International Symposium on Rarafied Gas Dynamics*, Pacific Grove, USA, 2010

[49] **Moss J. N., Boyles K. A.** and **Greene F.A.**, "Orion Aerodynamics for Hypersonic Free Molecular to Continuum Conditions," *14th AIAA International Space Planes and Hypersonic Systems and Technologies Conference*, AIAA Paper 2006-8081, Canberra, Australia, 2006.

[50] **Bird R.B.**, **Stewart W.E.**, **Lighthfoot E.N.**,"Transport Phenomena", John Wiley & Sons, Inc., New York, 1960

[51] **Palmer G.E.** and **Wright M.J.**, "Comparison of Methods to Compute High-Temperature Gas Thermal Conductivity," *36th AIAA Thermophysics Conference*, AIAA-2003-3913, Orlando, USA, 2003

[52] **Boyd, I. D.**, "Modeling Backward Chemical Rate Processes in the Direct Simulation Monte Carlo Method," Physics

[53] URL: http://www.esa.int/esaMI/Space_Engineering/SEMV0FXRA0G_0.html